Institute of Safety Research

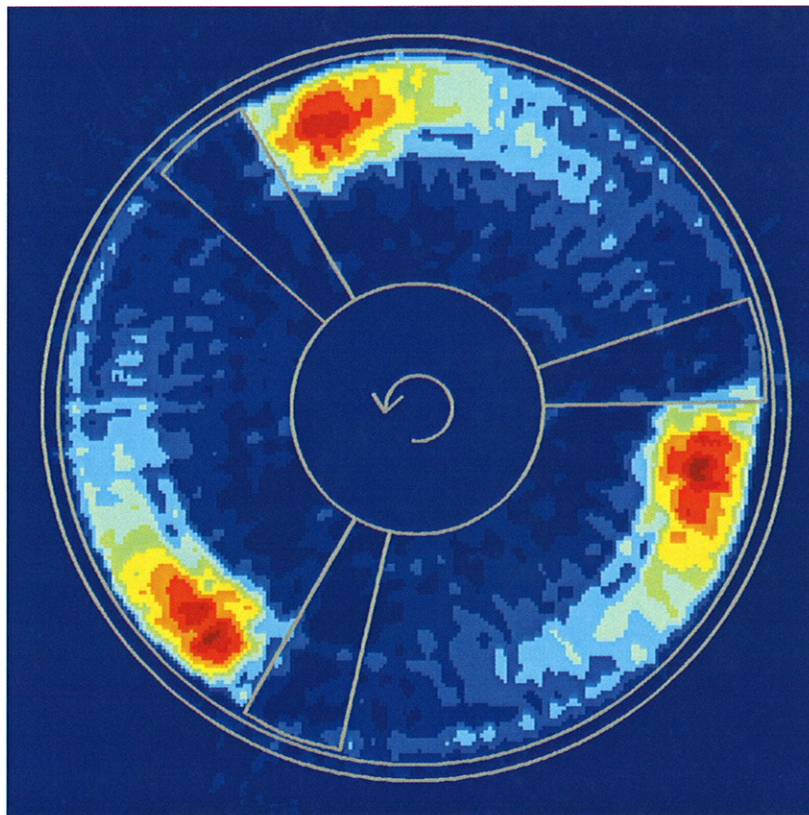# Annual Report 2000

FORSCHUNGSZENTRUM ROSSENDORF FZR

WISSENSCHAFTLICH-TECHNISCHE BERICHTE

FZR-316

April 2001

Annual Report 2000

Institute of Safety Research

Editors:

Prof. Dr. F.-P. Weiß

PD Dr. U. Rindelhardt

CONTENTS

Preface

Preface

The Institute of Safety Research (ISR) is one of the five scientific institutes of Forschungszentrum Rossendorf e. V.. The Forschungszentrum Rossendorf is a member of the "Wissenschaftsgemeinschaft Gottfried Wilhelm Leibniz". As such it is funded by the Federal Ministry of Education and Research and by the Saxon Ministry of Science and Arts with 50% each.

The work of the institute is directed to the assessment and enhancement of the safety of large technical plants and to the increase of the effectiveness and environmental sustainability of those facilities. Subjects of investigations are equally nuclear plants and installations of process industries. To achieve the above mentioned goals, the institute is engaged in two scientific fields, i. e. thermo-fluid dynamics including magneto-hydrodynamics (MHD) and materials/components safety.

To analyse thermo-fluid dynamic phenomena during normal plant operation and during accidents, basic physical models and computer codes are developed for one and two-phase flows, and for the space and time dependent heat release (neutron kinetics and chemical reaction kinetics.). That theoretical work is based on experimental investigations of chemical reaction kinetics including runaway reactions, and of transient two-phase flows. The institute has started the construction of the multi-purpose TOPFLOW (Transient, Two-Phase Flow) experimental facility. It shall be the specificity of TOPFLOW that it applies advanced two-phase measuring techniques which are developed in the ISR and which allow deep insight into the flow characteristics over a wide range of the void content and flow velocities.

MHD is relevant to flows of electrically conducting fluids, reaching from liquid metals to salt water, when there are inherent electromagnetic fields or when they can externally be imposed. The understanding and modeling of MHD effects offers technological and safety related applications in crystal growth, metallurgy, and other areas. However, the Rossendorf MHD department also deals with basic effects like the self-excitation of the magnetic field of the earth. For that, the Institute of Physics in Riga together with the Rossendorf group designed and constructed a sodium flow experiment in Riga. The first experiments of November 1999 showing the self excitation of a magnetic field in a suitable liquid metal flow could be proved by repeated experiments in July 2000. Beyond self-excitation the flow could be driven up to saturation of the magnetic field.

In materials safety, the institute is specialised to the investigation of irradiated nuclear reactor materials. The susceptibility of the mechanical properties against neutron and gamma irradiation and the effect of thermal annealing is evaluated by mechanical tests. The microstructural mechanisms of materials degradation are studied by highly resolving methods of structural analyses like TEM and SAXS and by more integrating methods like SANS.
Monte Carlo methods for radiation field calculation have been developed and validated to get reliable information about the fluences to which the components have been exposed. Improved covariance analysis and spectrum adjustment methods are used to adjust the calculated fluences to activation measurements.
Starting from the estimated accident loads (pressure, temperature) and from the mechanical and thermal properties of the concerned components structural models are developed to assess the integrity of those components in the considered scenario. One scenario that particularly has attracted interest is the in vessel retention of molten corium in LWR. Together with the Royal Institute of Technology (RIT) in Stockholm where the experiments are being

performed, a finite element model was worked out that allows the prediction of the failure mode and the failure time of the reactor vessel.

The ISR together with the Dresden University of Technology and Hochschule für Technik, Wirtschaft und Sozialwesen (HTWS) Zittau/Görlitz constitutes one of the German centres of competence for nuclear energy and nuclear safety. As such it also takes care for the conservation and promotion of expertise in nuclear engineering.

In 2000, the work of the ISR and of the whole research centre was assessed by a commission of the German Scientific Council (Deutscher Wissenschaftsrat). As a result, the main fields of research and the general orientations of ISR were positively evaluated. The non-nuclear activities shall be reinforced by strengthening the work on magneto-hydrodynamics and on two-phase flows. Nevertheless, the institute shall and will go on to play its role as centre of competence in nuclear engineering in the framework of the German Association for Nuclear Competence.

The following graphs give an overview about the sources and deployment of funding between the different research tasks. In 2000 35% of the total budget came from external sources, with 28% from public research grants and with 7% from research orders mainly by the industry.

Distribution of funding sources 2000
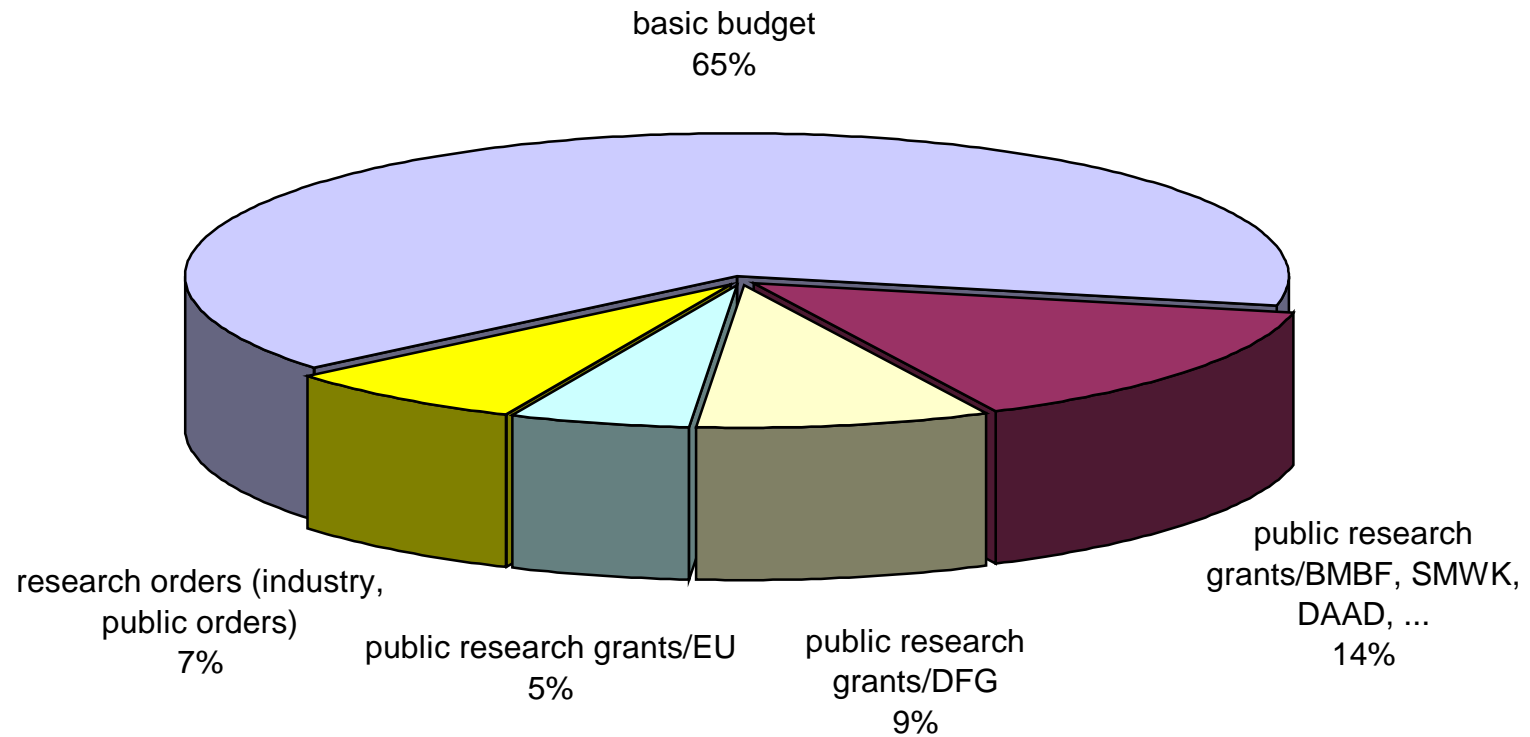
Deployment of funding on the tasks/projects 2000

thermo-fluiddynamics
38%

safety and efficiency of
chemical processes
9%

materials and
components safety
16%

accident analysis
11%

magneto-hydrodynamics
of electrically conducting
fluids
19%

simulation of particle and
radiation transport
7%
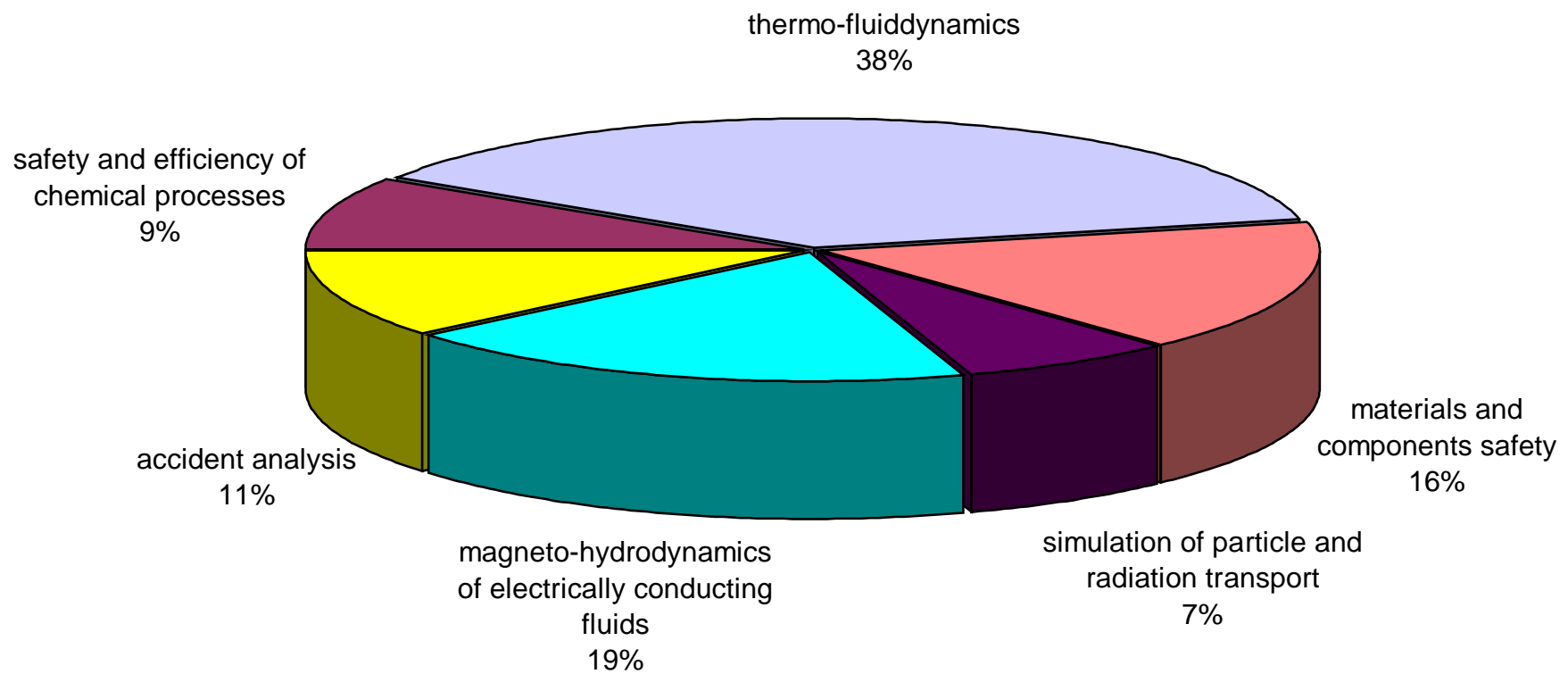
Selected reports

PRACTICABILITY OF LINEAR SUPERPOSITION TECHNIQUES FOR COOLANT MIXING STUDIES FOR PRESSURIZED WATER REACTORS

Gerhard Grunwald, Thomas Höhne, Sören Kliem and Horst-Michael Prasser

1. Introduction

In hypothetical accident scenarios connected with asymmetric perturbations in the primary circuit of a nuclear power plant (NPP) like overcooling of one loop due to a steam line break or local boron dilution events, 3D effects have to be considered. Usually, the computational analysis of such scenarios is performed within three off-line coupled steps, each of them carried out independently. First of all, a thermohydraulic analysis of the transient is carried out by means of an advanced thermohydraulic system code. From that calculation, boundary conditions are derived for an analysis of the 3D mixing processes inside the reactor pressure vessel (RPV) using a computational fluid dynamics (CFD) code. The results of this calculation (temperature or boron concentration distribution at the core inlet) are used in a 3D neutron kinetics analysis of the reactor core behaviour.

Recently, 3D neutron kinetics core models have been coupled with advanced thermohydraulic system codes. To be able to turn from the above described three step off-line approach to a fully coupled analysis of the whole process, the implementation of a model is necessary, which links the thermohydraulics of the system code with the thermohydraulics of the core model, simulating the 3D mixing effects in the RPV in a realistic way. Due to the large computation time, a direct coupling with CFD-codes is presently not practical. Therefore, the realisation of a simplified mixing model is the preferred way to describe the coolant mixing in an appropriate manner.

In this paper, the practicability of a linear superposition technique as a basis for the simplified mixing model is investigated.

2. Derivation of the simplified coolant mixing model

In general, the RPV from the inlet nozzles through the downcomer and the lower plenum up to the core inlet presents itself as a highly non-linear system with multiple inputs and outputs. The input signals are time-dependent values for the coolant velocity, enthalpy and boron concentration at each of the inlet nozzles, which generally can behave in an independent manner. The output signals are the same quantities at each fuel element position together with bypass positions. The geometrical and constructional details of the RPV determine the transfer properties of the system in a dominant manner. The only chance to derive a suitable model for the description of the coolant mixing, meeting the requirements for use in coupled codes, is the conversion of the described system into a simplified system with linear transfer properties.

The elimination of the influence of geometry and construction by concentrating on one reactor type simplifies the work. In the first step, only the processes during the start-up of the first main coolant pump after flow stagnation will be considered. For that special case the number of inputs to the system reduces to one. The splitting of the system into subsystems

(for each fuel element position one) creates a group of systems with one input and one output, but different transfer properties.

The disturbance of such a system by a Dirac impulse is an appropriate method for the determination of these unknown transfer properties. A disturbance of the system by a function of any form (for instance: a plug of coolant with lower boron concentration) can be represented by a linear combination of a sequence of such Dirac impulses. Assuming linearity of the transfer, the same linear combination can be applied to the reconstruction of the answer at the output of the system.

The transfer properties can be determined experimentally or analytically. In this work, an experimental approach has been applied. For that purpose, experiments at the ROCOM test facility [1] were carried out. This experimental facility was designed and built especially for the investigation of coolant mixing phenomena in the downcomer and the lower plenum of the German 1300 MW KONVOI reactor. The facility is a 1:5 linearly scaled model equipped with four loops with fully controllable coolant pumps. Beginning from the cold leg 1 m (corresponding to 5 m in the original) before the entry into the RPV, the inlet nozzle, the downcomer, the lower plenum, the perforated drum up to the core support plate including the corresponding penetrations, the model represents the original reactor with all constructional details in the given scale. The facility is operated with water at room temperature and is equipped with different wire-mesh sensors. The working principle of these sensors is based on the measurement of the conductivity. Water with different conductivity simulates the differences in the boron content or temperature. Particularly, the measurements of two sensors are used for the determination of the transfer functions of the above introduced systems. One is located in the reactor inlet nozzle of one loop (pos. 1, fig. 1), the other one measures the concentration at each fuel element inlet position at the lower core support plate (pos. 2). From the data provided by the sensors dimensionless mixing scalars can be derived with a time resolution of 0.05 s. These scalars are defined as

follows: $\theta_i = \dfrac{\sigma_i - \sigma_0}{\sigma_P - \sigma_0}$, where i is the current measurement position; σ_i the conductivity at that

position, σ_0 the conductivity of the water before the experiment and σ_P the conductivity in the injected plug.

Fig. 1 Sectional view of the ROCOM RPV-model with the positions of the wire-mesh sensors

For the derivation of the transfer functions, experiments were carried out, where water with a high conductivity over a short time (nearly 0.1 s) was injected into the loop with the starting-up pump. A special mixing device, located at the injection position, ensures that the injected water is equally distributed over the cross section. It has to be taken into account, that due to the considered pump start-up process the transfer behaviour changes. Therefore, the time position of the injection in the pump start-up ramp has been varied in the different experiments. The time dependent mixing scalar was measured at each fuel element position.

The impulses of three experimental series are shown on fig. 2a, the answers to these impulses measured at a certain fuel element position are shown in fig. 2b.

As can be seen from fig. 2a, the transfer functions of the above introduced systems were exposed to an input signal, nearly being a Dirac impulse.
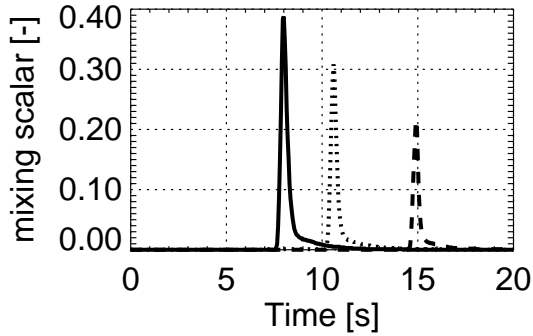
Fig. 2a: Examples for the experimental impulses
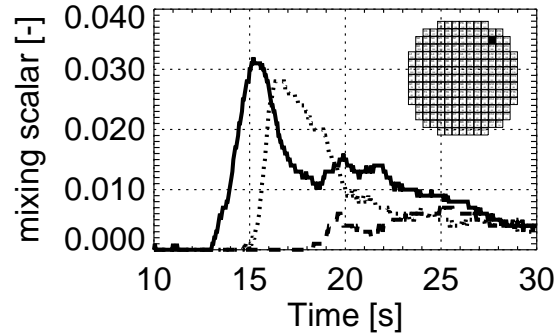
Fig. 2b: Mixing scalars (answer to 2a) at a certain fuel element position

For an adequate representation of a plug, the limited number of experimental impulses is not sufficient. Therefore, additional impulses were derived by interpolation between the experimental ones. This was performed to the input and the output signals of the systems in the same manner. An example for the combination of experimental and interpolated impulses is shown in fig. 3.

The time course $F(t)$ of the plug to be modeled at the reactor inlet can be reconstructed from n impulse functions by the following formulae:

$$F(t) = \sum_{j=1}^{n} a_j \cdot g_j(t) \tag{1}$$

where $g_j(t)$ is the time course of the jth impulse, a_j is a weight coefficient, determining the contribution of the jth impulse to the requested plug. The number n depends on the volume of the plug to be modeled. The coefficients a_j are obtained as solution of a least squares deviation problem between measured and approximated plug.

Supposing, that the linearity of the system is ensured, the transient course of the mixing scalar at each fuel element position can be derived in a similar manner using the same coefficients a_j. The time course of the mixing scalar $H_k(t)$ for each k of the 193 fuel element positions can be calculated by:

$$H_k(t) = \sum_{j=1}^{n} a_j \cdot h_j(t) \tag{2}$$

where $h_j(t)$ is the time course of the jth answer function at the corresponding fuel element position.

The described linear superposition technique is the main part of a calculation program, called Semi-Analytical Plug Reconstruction (SAPR) model.

3. Verification of the model

A numerical analysis of a hypothetical deboration event in a German PWR has been performed [2]. A plug of lower borated coolant, which goes through the reactor inlet nozzle from t = 7 s to t = 14 s during the start-up of the first main coolant pump was assumed in that work.

The same boundary conditions were used for generic experiments at the ROCOM test facility. The experimentally created plug is shown on fig. 3.

The pulse shape reconstructed by means of the model using equ. (1) (red) coincidences practically with the experimental one (green).

Due to the turbulent fluctuations of the mixing scalar observed earlier [1], the experiment was repeated several times to average over these fluctuations. The results of the single realisations were used to carry out a statistical analysis of the experimental data.
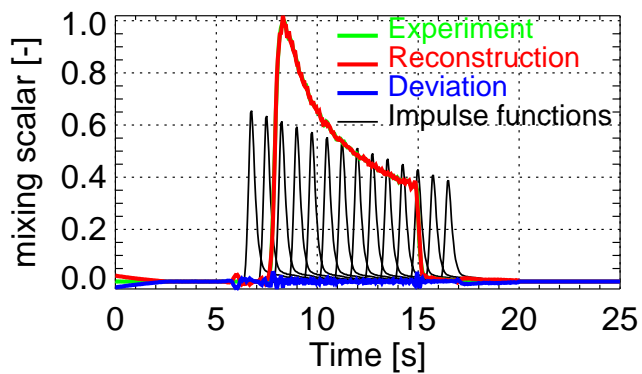
Fig. 3: Experimental plug and reconstruction using equ. (1)

Additionally, by means of the CFD code CFX-4 a calculation was carried out using the experimentally obtained plug shape as boundary condition. So, the semi-analytical model can be compared with the experimental data and the CFX-results.
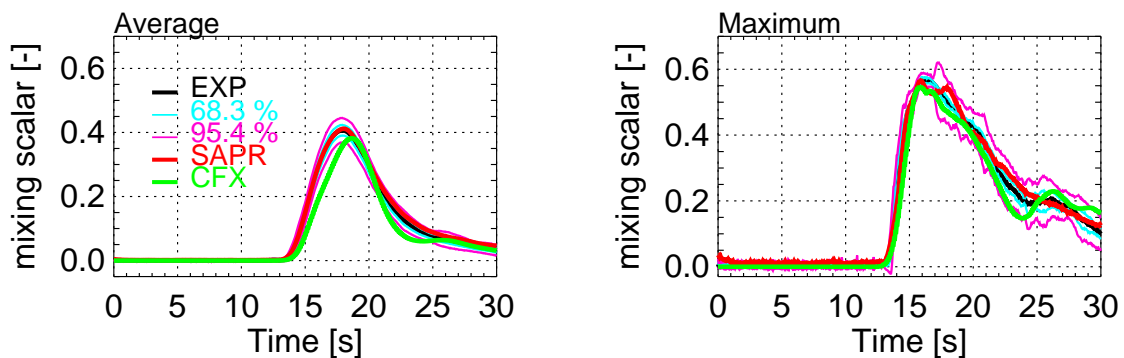
Fig. 4: Average and maximum value of the mixing scalar at the core entry in comparison between experiment, semi-analytical model (SAPR) and CFX-calculation (with confidence intervals)

Fig. 4 shows the transient course of the average value of the mixing scalar at the core entry. Two confidence-intervals (68.3 % and 95.4 %) are shown, too. The curve calculated by the SAPR-model shows practically the same behaviour like the experimental curve. The maximum is reached at the same time. In the later part of the transient, the calculated

concentration is slightly higher than the measured one, but always inside the 95.4 %-confidence interval. In the CFX-calculation, the concentration increases more slowly and the maximum is reached later. In the further course, the CFX-values are also in the 95.4 %-confidence interval (lower boundary).

The transient course of the maximum value is shown on fig. 4. In the experiment as well as in the calculations, the maximum value is determined at each time step over all fuel element positions. Therefore the position can vary, which has (in the experiment) also an influence on the width of the confidence intervals.

In both calculations, the course of the maximum concentration at the core inlet, is very close to the experimental data. After reaching the maximum in time, the value calculated by the SAPR-model belongs mostly to the upper part of the 68.3 %-confidence interval, the CFX-value to the lower edge of the 95.4 %-confidence interval.

Table 1 summarises a quantitative assessment of the calculated data in comparison to the experiment. The semi-analytical model is not only able to predict integral values (average or maximum over the core). The comparison of the maximum values reached at each fuel element position during the transient shows, that the values for 129 fuel elements (more than 60 % of all positions) belongs to the experimentally determined confidence interval of 95.4 %, 68 of them even to the very narrower interval of 68.3 %, what is better than for the CFX-calculation.

Tab. 1: Some key parameters of the comparison

	Experiment	SAPR-model	CFX-calculation
Number of fuel elements with a maximum mixing scalar of > 50 %	56	72	16
Number of fuel elements, which maximum belongs to the 68.3 %-confidence interval of the experiment	-	68	20
Number of fuel elements, which maximum belongs to the 95.4 %-confidence interval of the experiment	-	129	45

In addition to this table, the transient course of the mixing scalar at one fuel element position from the outer part and one from the middle of the core is shown on fig. 4. For both fuel element positions, the curves calculated by the SAPR-model are mostly inside the inner confidence interval. The maximum values are reached practically at the same time.

Both curves, calculated by CFX increase more slowly. The maximum values reached during the transient are smaller than the experimental data and the values calculated by the SAPR-model.
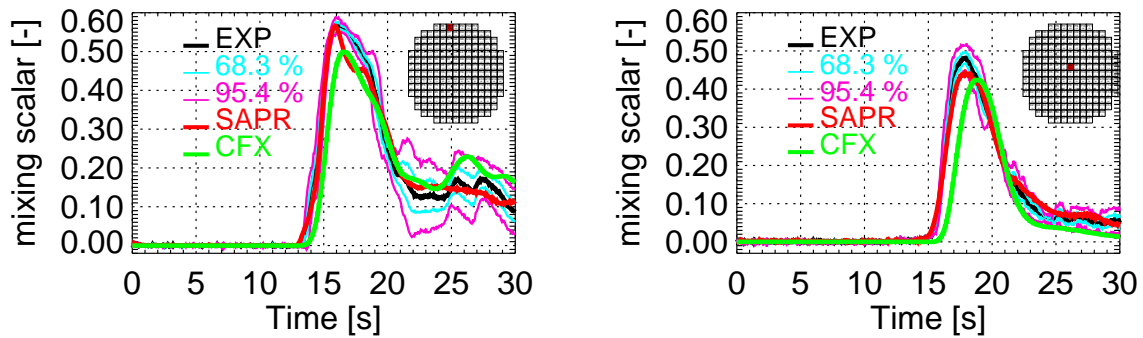
Fig. 5: Mixing scalar at different fuel element positions in comparison between experiment, SAPR-model and CFX-calculation

4. Outlook

The work on the semi-analytical model for the description of the coolant mixing in the downcomer and the lower plenum of KONVOI-type reactors will be continued including additional scenarios. In the near future, the model is to be implemented into the coupled code DYN3D/ATHLET, so that the influence of the coolant mixing on the neutron kinetics can be investigated. The capabilities of the model have to be assessed in a systematic manner: The influence of the number of basic impulse functions will be investigated. A further refinement is possible (for instance: enhancing the number of experimental basic functions included into the model). The possibility of creation of basic impulse functions for the model by means of the CFD- code CFX-4 should be taken into account, too. That would also allow to create models for the description of the coolant mixing in different geometry and under various conditions without performing additional experiments.

Acknowledgement

References

[1]   G. Grunwald, Th. Höhne, H.-M. Prasser, F.-P. Weiß (2000), Coolant mixing in PWR at constant coolant flow in the primary circuit, in Proc. Annual Meeting on Nuclear Technology '00 (pp. 109 – 114), INFORUM GmbH, Bonn

[2]   R. Reinders (1998), Dreidimensionale Berechnung der Borkonzentration im RDB nach einem DE-Heizrohrleck, in Proc. Annual Meeting on Nuclear Technology '98 (pp. 107 – 110), INFORUM GmbH, Bonn

TIME RESOLVING GAMMA-TOMOGRAPHY FOR PERIODICALLY CHANGING GAS FRACTION FIELDS

Dieter Baldauf, Jürgen Fietz, Uwe Hampel, Dietrich Hoppe, Horst-Michael Prasser, Cornelius Zippe, Jochen Zschau, Michael Christen[1] and Gotthard Will[1]

1. Introduction

During the last decade, there is a growing interest in pumping two-phase mixtures. A prominent example is the tendency to utilise the gas evolved at oil wells, which was usually burned on site in the past. Often the most economical way to transport the gas is to deliver the oil-gas mixture instead of separating it from the crude oil. Beside displacement pumps, which are determining the state of art in this field today, the use of turbo pumps may be of benefit, too.
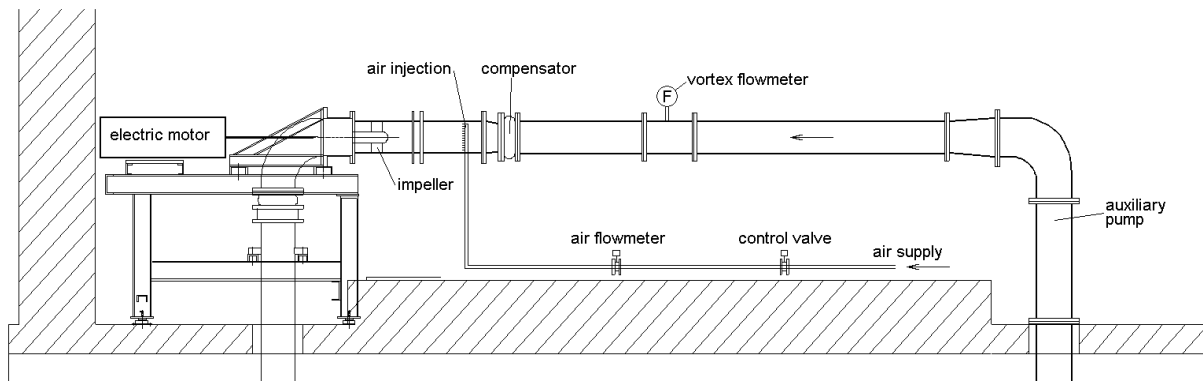
Fig. 1: Scheme of the axial pump test facility of the Technical University in Dresden

The present work aims at the development of a non-intrusive method to visualise the gas fraction distribution inside the rotating impeller of an axial pump delivering a two-phase flow. The pump test facility (Fig. 1) is located at the Technical University of Dresden. Its impeller (Fig. 2) has three helical blades, the diameter is 220 mm, the pump operates at approximately 1500 revolutions per minute (25 Hz). Air-water mixture is used as model fluid, created by a gas distributor upstream the pump inlet nozzle.
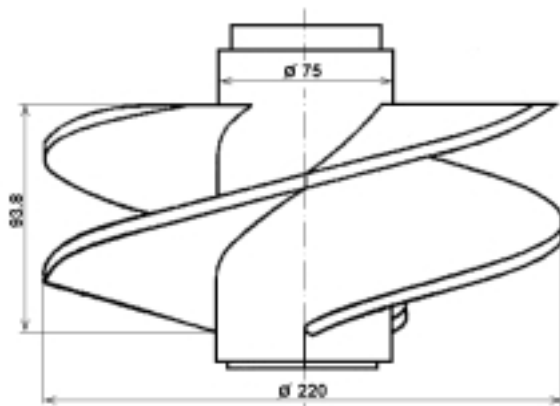
Fig. 2 Impeller of the axial pump

2. State of art in gamma-tomography

In case of the gamma-tomography, projections of the density distribution inside the object area are obtained by measuring the transmission of gamma-radiation. For this purpose, a gamma-source is placed on one side of the object, and the distribution of the radiation flux arriving at the other side is measured by one or more detectors. The flux of the emitted gamma quanta decreases exponentially with growing integral gamma absorption along the

---

[1] Technical University Dresden, Institute of Energy Machines and Machine Laboratory

chord between source and detector. Classical arrangements consist of a fan-beam source and a row or an arc of detectors to obtain a one-dimensional projection of the measuring cross section. A set of independent projections for different aspect angles is obtained by rotating source and detector array around the object. In some cases, the object is rotated instead of the tomography system [1]. The distribution inside the measuring cross section is calculated from the measured projections using tomographic image reconstruction methods.

Usually, the acquisition of the projections is a time consuming process. At first, the statistics of the gamma-decay has to be considered. Depending on the activity of the source, obtaining one projection with the necessary accuracy usually takes from several seconds to minutes. The acquisition of the number of independent projections necessary for the image reconstruction ($\approx 10^2$) leads to measuring periods in the range of minutes, which cannot be decreased without limitations, even if very strong gamma-sources are applied, because the mechanical rotation of the source around the object is the only way to change the aspect angle. This is the main problem of applying gamma-tomography to fast transient processes in two-phase flows.

For the visualisation of the instantaneous gas distribution in an axial pump, the framing rate must be in the range of the rotation frequency divided by the desired angular resolution. In case of 1500 revolutions per minute a complete set of projections must be obtained within time intervals of about 100 µs, if an angular resolution of 1 deg is required. A single projection must therefore be acquired within less than 1 µs. This has been not reached by any kind of gamma or X-ray tomography up to now, and it must me doubted whether it is feasible at all. The most advanced X-ray tomography systems worldwide allow to obtain an image within 500 µs [2]. The corresponding X-ray device consists of 66 pulsed X-ray tubes, placed around the object. These sources are flashing in a successive order to produce a complete set of projections within the imaging period. Beside the problem of further decreasing the measuring period, the use of comparatively weak X-ray radiation is limited in the case of technical machines like our axial pump due to the high absorption in constructional materials. The latter requires higher energies of the radiation which can be obtained with moderate efforts from gamma emitting nuclides only, so that pulsed source techniques cannot be used.

A possible way out is to refrain from the visualisation of instantaneous gas distributions and to restrain to obtain time-averaged void fraction distributions. In order to visualise the void distribution inside the rotating impeller we decided to develop a gamma tomograph with a time resolving radiation detection system and to take advantage from the periodicity of the gas fraction distribution inside the impeller in order to perform an ensemble-averaging.

3. Measuring principle

The measurement is based on counting the pulses delivered by the detectors synchronised to the rotation of the impeller. One revolution of the impeller is divided into a number of equal angular intervals $\Delta\gamma$. Each detector responsible for a given angular interval $\Delta\psi$ of the detector arc is connected to several counter units via signal switches (Fig. 3). The counters are grouped into counter banks, the number of which equals to the number of required angular intervals. Each counter bank corresponds to an angular interval i, which is defined as $(i-1)\cdot\Delta\gamma < \gamma < i\cdot\Delta\gamma$. Signal switches (S) perform the successive connection of the detectors to the currently activated counters. The successive closing of the switches is organised by a control unit. Each counter is activated for the period of 100 µs which is defined by the clock signal of 10 kHz. The synchronisation is carried out using a trigger pulse generated at each revolution of the impeller. The arrival of the trigger pulse defines the zero angular position $\gamma=0$ and forces the

control unit to terminate the successive activation of the counters and to restart the counting process in the counters of the first bank.
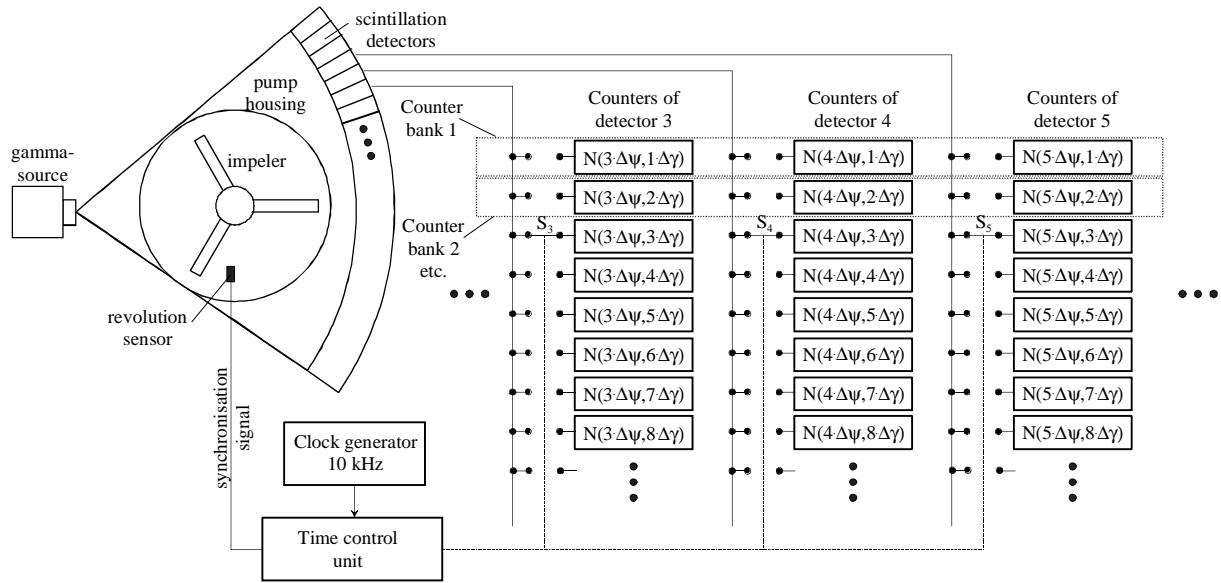
Fig. 3: Working principle of the time resolving tomography

To achieve a sufficient statistical accuracy of the counting results $N(i \cdot \Delta\psi, j \cdot \Delta\gamma)$ the measuring procedure is continued over a large number of pump revolutions. Due to the synchronisation it is guaranteed that each counter collects pulses originating from the detector for the corresponding aspect angle ψ, which arrive in the time interval corresponding to the impeller rotation angle γ defined for the bank the counter belongs to. Therefore, the device is able to obtain ensemble averaged projections of the gamma absorption density distribution, which are resolved according to the rotating angle of the impeller.

If a uniform or radially-symmetric distribution of the gas fraction at the inlet nozzle of the pump can be assumed, the gas fraction distribution inside the rotating parts of the pump is quasi-stationary related to the moving co-ordinate system due to symmetry. In this case the rotation of the gas fraction field itself can be used to obtain the necessary set of independent projections, while the tomography system can stand still. This situation is similar to the technique to rotate the object instead of the tomography system [1], but with a very high revolution speed.
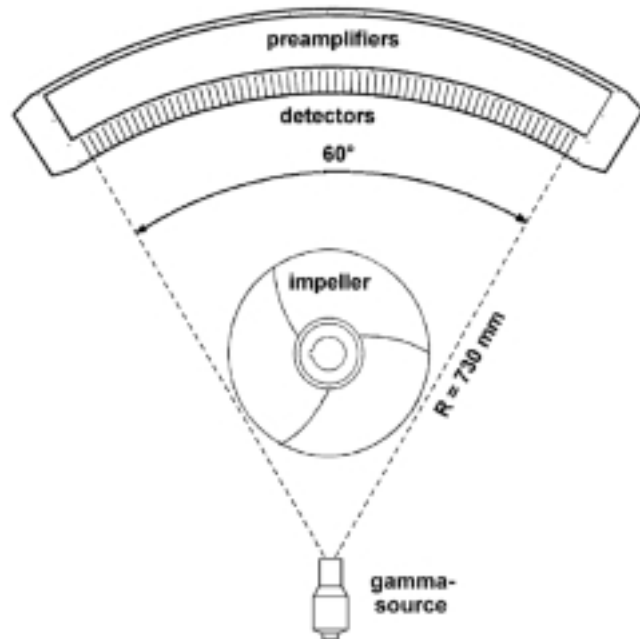
Fig. 4 Sketch of the gamma tomography system

11

The situation is different, if the gas fraction distribution at the inlet of the axial pump is depending from the azimuthal angle in the laboratory co-ordinate system. In this case the void fraction distribution cannot be regarded as quasi-stationary in the rotating co-ordinate system of the impeller. The only property which can be used is periodicity in time, i.e. it can be assumed that the void distributions found in identical intervals of the rotation angle of the impeller can be treated as quasi-stationary. To obtain the necessary projections for an imaging of this distribution, the tomography system must be rotated around the object, too. The image has to be reconstructed from a set of projections for one and the same interval of the impeller rotation angle obtained at the different angular orientations of the tomography system $\theta_k = k \cdot \Delta\theta$. In this way, for each interval of the impeller rotation angle $\gamma_j = j \cdot \Delta\gamma$ an individual image can be reconstructed. The resulting series of images can be used for an animation of the periodically changing void fraction distribution inside the impeller.

4. Technical realisation of the tomography system

The tomograph consists of a gamma source, a detector arc (Fig. 4), a mechanical structure allowing to rotate both source and detector array around the object, a mechanism to move the tomograph along the axis of the pump, power supply units for the high voltage needed for the photomultipliers and a signal acquisition unit connected with a personal computer. A total view of the device is shown in Fig. 5 Source and detector arc are fixed to a metallic double ring resting on four ball bearings. The rings can be rotated by a toothed wheel mechanism equipped with a handle. For the axial movement, the entire construction rests on ball bearings rolling on rails. A rack mechanism with a handle allows to perform the translation.

A Cs-137 source with an activity of 185 GBq ($E\gamma$ = 662 keV, 5 Ci) is used. The source container is equipped with a fan-beam collimator. The detector arc consists of 64 scintillation crystals of Bismuth-Germanate (BGO) with a front face of 10 x 10 mm² and a length of 30 mm.
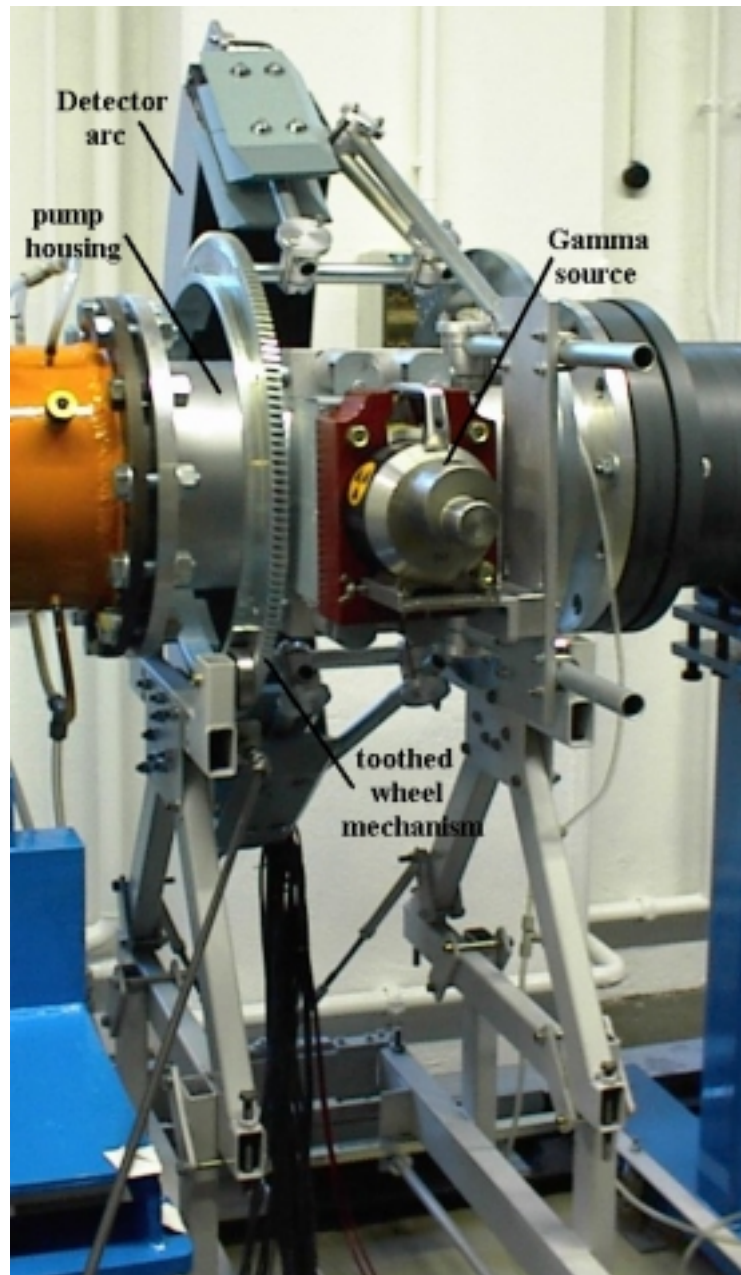
Fig. 5 View of the tomography system at the axial pump test facility

12

Photo-multipliers are coupled to the side planes of the crystals. The dimensions of the crystals allow to achieve a resolution of about 5 mm inside the measuring plane. The length of 30 mm is important for a high quantum efficiency at the comparatively high gamma energy.

Preamplifiers with energy discrimination cascades are connected to the photo-multipliers. The binary pulses are counted by two banks of 64 hardware counters with a width of 8 bit. The banks are swapped periodically each 100 µs. One bank is working in counter mode while the accumulated counts of the second one are transferred to the data acquisition PC. The counter banks shown schematically in Fig. 3 are represented by a two-dimensional data array of four byte long integer values. The counts from the instantaneously non-active hardware counter bank are added to the corresponding elements of this array, allocated in the RAM of the PC. After completing the data transfer the hardware counters are set to zero. A data acquisition during 10 000 revolutions of the impeller (i.e. during a measuring period of about 7 min) is sufficient to obtain total count results in the order of magnitude of 10^4 for each of about 400 rotation angle intervals and each of the 64 detector channels.

5. Results

Preliminary measurements were carried out at the operating pump in single phase mode (water) and in the two-phase mode, i.e. during symmetrical air supply. For calibration purposes, some measurements were taken for the case of the pump filled with air. The obtained tomographic data were processed under the assumption of a void fraction distribution, which is quasi-stationary in the co-ordinate system rotating together with the impeller. The measurement of effects caused by the unsymmetrical air supply due to stratification in front of the pump are planned for the future.

The image reconstruction was carried out by filtered back-projection, applying a modified Shepp-Logan filter [3]. When the data obtained during single-phase operation with plain water are used for the reconstruction, the impeller structure inside the measuring cross section as well as the Aluminium pipe serving as pump housing are clearly reproduced (Fig. 6). The axis of the impeller is hollow, which is also reflected by the reconstructed image.

Fig. 6 Tomographic image of the impeller structure (pump with plain water)

The void fraction distribution can be visualised only by means of differential tomography. For this purpose, the set of projections obtained for the case of two-phase operation is related to the case of plain liquid (Fig. 7). The test was carried out at a volumetric gas fraction at the pump inlet of about 10 %. The resulting tomographic image shows only those parts inside the measuring plane, where the gamma absorption density changed between the two working regimes, i.e. impeller and pump house structures disappear. The contours of these structures are overlaid to the tomographic images in Fig. 7.

The measurements were taken at different axial positions along the pump. In the measuring plane A areas with air concentration are observed close to the back surface of the impeller blades. There is some evolution of the distribution in axial direction. Regions of increased void fraction are still observed in the wakes of the impeller blades (cross section C).

6. Conclusions

A new kind of time-resolving gamma tomography was developed and applied to visualise the void fraction distribution inside the impeller of an axial pump operating in two-phase mode. The method of data acquisition synchronised to the rotation of the impeller was successfully tested in preliminary experiments. Next steps are calibration of the device to generate quantitative void fraction distributions, investigation of the degree of asymmetry of the void fraction profile at the pump inlet, measurements with void distributions non-stationary in the rotating co-ordinate systems and systematic investigation of the influence of changes of the working point of the pump to the void fraction distribution inside the impeller.
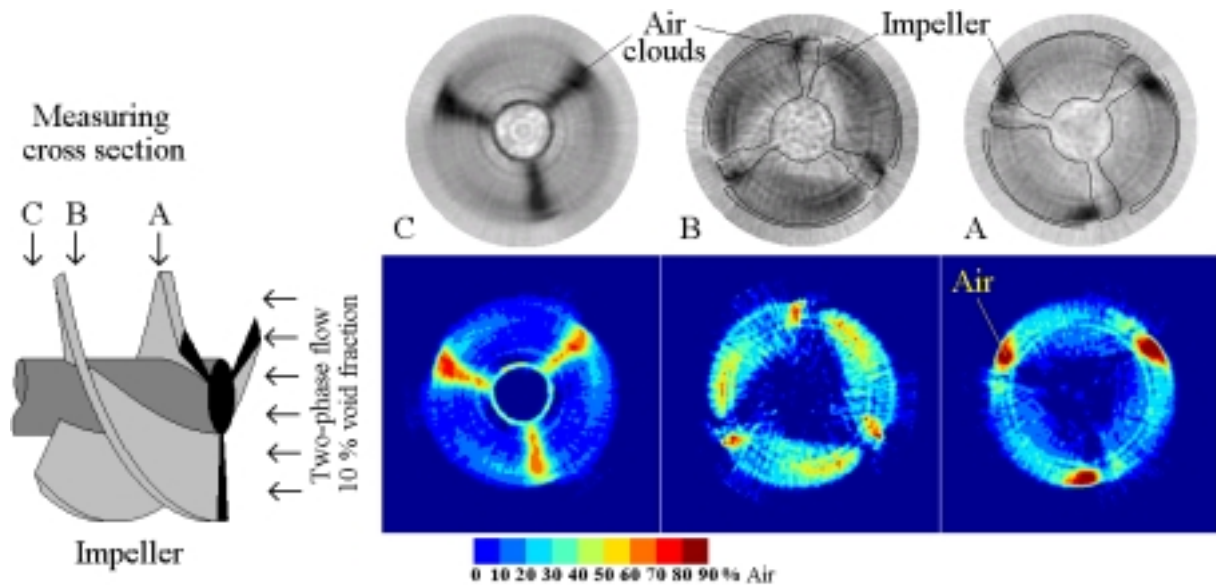
Fig. 7: Differential tomographic images of the void fraction distribution inside the impeller of the axial pump working in two-phase mode (average void fraction about 10 %)

References

[1] D.Schmitz, N.Reinecke, G.Petritsch, D.Mewes (1997), X-Ray Computed Tomography for Stationary Multiphase Flow in Random and Structured Packings, Frontiers in Industrial Process Tomography, Delft 9.-12.4.1997, proc. pp. 303-308.

[2] K. Hori, T. Fujimoto, K. Kawanishi, H.Nishikawa (1997), Advanced High Speed X-Ray CT Scanner for Measurement and Visualisation of Multi-Phase Flow, OECD/CSNI Specialist Meeting on Advanced Instrumentation and Measurement Techniques, Santa Barbara, USA, March 17-20, 1997.

[3] Kak, A. C.; Slaney, M. (1988), Principles of Computerised Tomographic Imaging. IEEE Press. New York.

TOPFLOW - A NEW MULTIPURPOSE THERMALHYDRAULIC TEST FACILITY FOR THE INVESTIGATION OF STEADY STATE AND TRANSIENT TWO PHASE FLOW PHENOMENA

Andreas Schaffrath, Anne-Kathrin Krüssenberg, Frank-Peter Weiß, Enno Frerich Hicken[1], Horst-Michael Prasser

1. Introduction

The Forschungszentrum Rossendorf (FZR) e.V. is building a new large-scale test facility for thermal hydraulic single effect tests, the TOPFLOW facility. The acronym stands for Transient Two Phase Flow Test Facility. It will mainly be used for the investigation of generic and applied steady state and transient two phase flow phenomena in power- and process industries. Main research activities are the investigation of:

- transient flow regimes in horizontal, vertical and inclined tubes,
- the dynamic behaviour of interphase areas in gas-liquid flows,
- critical mass flows and oscillations during depressurization of chemical reactors,
- natural convection in large pools with local heating,
- natural convection in parallel channels and feed pipes and
- condensation phenomena.

It is our strategy to use TOPFLOW as a central experimental basis for the nuclear competence centre, rejoining FZR, the Technical University of Dresden and the University of Applied Sciences Zittau-Görlitz (HTWS) and to offer it to working groups throughout Europe. They will be invited to come to Rossendorf with their ideas and to perform their experiments here making use of the parameters (power, water and steam mass flow, pressure range, measuring instrumentation) and the multipurpose character of the test facility.

2. Embedding of TOPFLOW in the matrix of thermal hydraulic test facilities in Western Europe

TOPFLOW stands in the tradition of single-effect tests in large-scale models of safety relevant components of nuclear plants performed at the NOKO test facility successfully operated at the Forschungszentrum Jülich for many years. The new test facility in Rossendorf will be constructed using parts of NOKO, which will be transferred to the new site. With a series of important new test sections, the profile of TOPFLOW will be shifted from previous investigations of passive safety systems for a new generation of nuclear power plants carried out on NOKO to more generic work for both nuclear safety and chemical plant safety and efficiency. Special attention is paid to the experimental support of the development of a new generation of best-estimate computer codes for safety analyses, based on three-dimensional CFD techniques.

Main components of NOKO, which are taken over, like the electrical heater and the condenser tank, are determining the power, pressure and mass flow ranges of the facility. TOPFLOW and

---

[1] Forschungszentrum Jülich, Institut für Sicherheitsforschung und Reaktortechnik

NOKO are therefore very close in respect to their scale, which is for many tests close to industrial scale.

The construction of the NOKO test facility was decided by the Ministry for Research and Technology, SIEMENS, the German Utilities and the Forschungszentrum Jülich in 1993. In the first time it was aimed at studying experimentally and analytically the effectiveness of the SWR 1000 emergency condenser. From 1996-1998 the facility was used for a project within the 4th FWP of the EU "European BWR R&D-Cluster for Innovative Passive Safety Systems"; 7 partners participated. In 1997, in addition, 7 partners of an Concerted Action "BWR-CA" took part in this project [1]. This was followed by studies of the behaviour of the building condenser, the passive pressure pulse transmitter of the SWR1000 designed by Siemens (see [1] and [2]).

In Fig. 1, the most important European test facilities capable to perform thermal-hydraulic tests of passive safety systems are shown. It is evident that the wide range of power and pressures will allow the test of the same component in several facilities of different size and thus increasing the confidence in the assessment of the effectiveness of this component. It has to be mentioned that the PANDA test facility has a higher volume than the other test facilities.
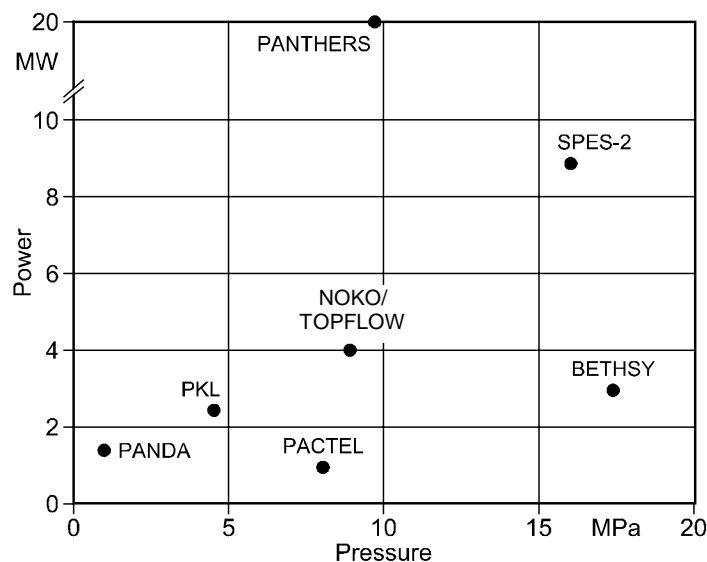
Fig. 1: European test facilities to perform thermal-hydraulic tests of passive safety systems [2].

In 2000, it was decided to decrease substantially the safety research at the Forschungszentrum Jülich. To maintain the experimental competence in two-phase flow main components of NOKO will be transferred to Forschungszentrum Rossendorf by the beginning of the 2001, where they shall be used to build the new TOPFLOW thermohydraulic test facility.

The main objectives of TOPFLOW will be oriented towards more generic research: investigation of steady state and transient two phase flow phenomena especially transient two phase flow patterns, the generation of a data basis for Computational Fluid Dynamic (CFD)-Code validation, testing of heat exchangers and the development of two-phase flow instrumentation.

3. TOPFLOW test facility

The TOPFLOW facility is designed for pressures up to 10 MPa and temperatures up to 300 °C. The max. steam mass flow is up to 2.6 kg/s, achieved with an electrical heater of 4 MW. The maximum water mass flow less than 50 kg/s.

The flow diagram of the TOPFLOW facility is given in fig. 2. Additionally, a front view is shown in fig. 3. The main test sections are:

- two vertical pipes (D = 50 and 200 mm, L = 9 m)

- the condenser (L = 6 m, D = 2 m, V = 20 m³, p < 1.5 MPa)

- the steam drum (L = 5 m, D = 1.5 m, V = 8 m³, p < 7 MPa)

In the vertical pipe with DN200 the following superficial phase velocities can be reached: steam < 2.2 m/s at 7 MPa and <15 m/s at 1 MPa, water < 2.2 m/s.

Further, several junctions are foreseen for the connection of additional test sections e.g. a PWR hot leg model.
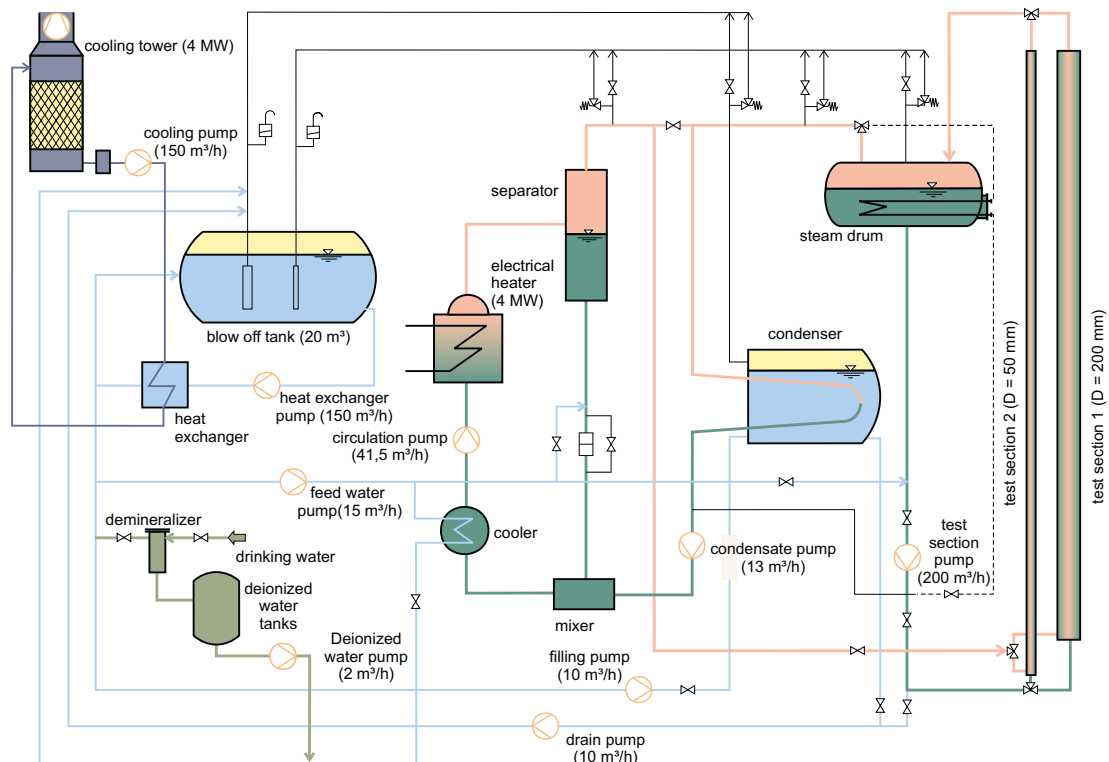
Fig. 2: Flow diagram of the TOPFLOW test facility.

TOPFLOW will be equipped with advanced two-phase instrumentation mainly adapted and developed at Rossendorf, such as wire-mesh sensors, needle-shaped conductivity probes with integrated thermocouple, gamma and X-ray tomography and passive ultrasonic droplet probes. Additionally, laser-doppler anemometry and a phase-doppler particle analyser will be available. The Rossendorf wire mesh sensors provide a quasi tomographic visualization of the two phase flow [3].

It is planned to apply this type of fast flow visualisation to different test sections of the TOP-FLOW facility. In the first experiments, the flow pattern in a vertical pipeline of 200 mm diameter will be studied. A specially developed sensor will allow a spatial resolution of 3 mm at a measuring rate of 2.5 kHz and consist of 64 transmitter and 64 receiver wires (64x64 measuring matrix).
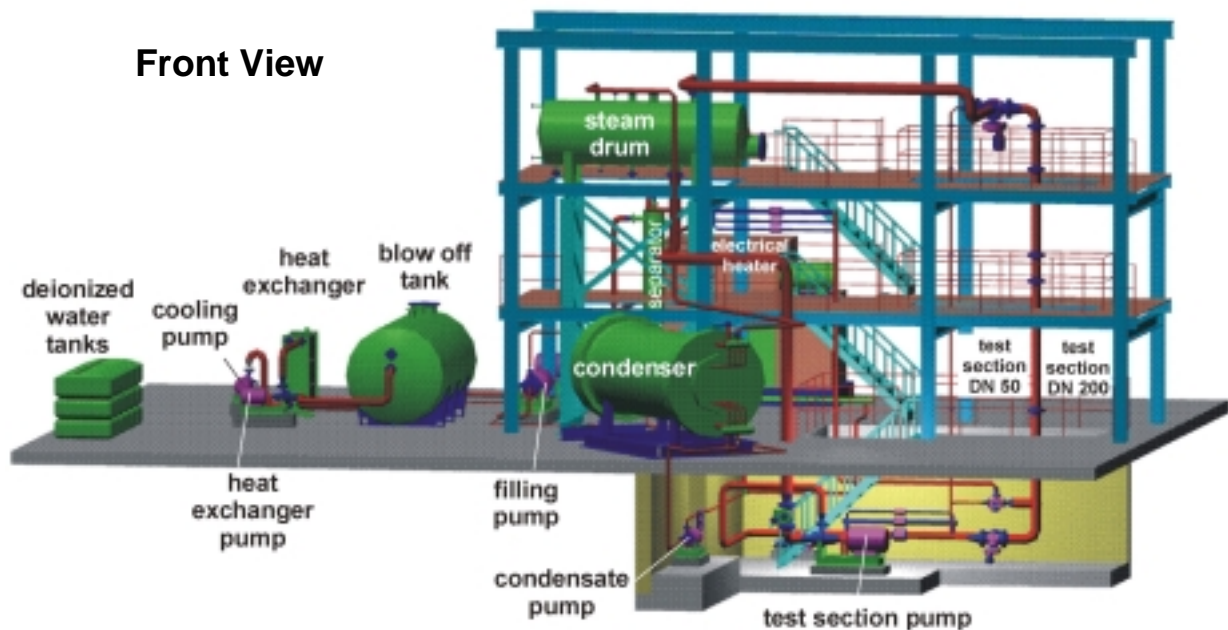
Fig. 3: Front view of the TOPFLOW test facility.

4. Planned experiments

The planned experiments have already roughly been listed in chapter 1. In the following the investigation of two phase flow pattern in vertical pipes is described in detail. The tests were prepared by small scale experiments at the MTLOOP at the Institute for Safety Research performed in the frame of the running research project BMWi 1501215 "Flow Pattern and Models for Transient Two Phase Flows".

4.1 Phase distribution and flow pattern in vertical tubes

The known models and flow diagrams for the prediction of the phase distribution and flow pattern in vertical tubes are not universally available, because most of them were developed from adiabatic water-air experiments in small tubes (< 50 mm) and atmospheric pressure. The experiments were performed in transparent tubes and the flow pattern classification is based on visual observations. Therefore an extrapolation outside the experimental conditions is not possible. Based on stability analysis it is assumed, that comparable flow patterns cannot exist in large tubes. This missing of reliable, universal criteria for prediction of phase distribution leads to numerous empirical and semi-empirical models for the determination of pressure losses, heat and mass transfer.

The flow experiments in TOPFLOW will be performed with water steam mixtures under high pressures (< 7 MPa) and in tubes with diameters up to 200 mm and length up to 9 m. The corresponding L/D-ratios are 45 for DN200 and 180 for DN50.

In the first step steady state flow conditions will be investigated for the verification of existing flow pattern maps. The evaluation of void fraction and velocity profiles as a function of the distance from the vapour injection shall be measured as well as two phase parameters, which characterize the structure of the two phase flow and allow to derive objective and reproducible criteria for flow pattern classification. The experiments are performed under steady state boundary conditions (pressure, phase mass flow). This kind of flow investigations shall be extended to bends, junctions, isthmuses and dilations.

4.2 Droplet entrainment and deposit in a PWR hot leg

A typical example for the above mentioned topic is the droplet entrainment and deposit during the end of the blown-down phase of a large break LOCA. After reaching a system pressure less then 2.6 MPa water is injected by the accumulators in both - hot and cold leg of the primary circuit.

The water injected into the hot leg flows through the upper plenum to the core. Due to the wetting of the fuel pins 100 - 150 kg/s steam is produced and flows through the hot legs to the steam generators. In the steam large amounts of liquid droplets (up to 500 - 750 kg/s) are entrained. Most of these droplets are deposited in the upper plenum, only 50 kg/s are deposited in each hot leg. The scenario described above take places at 0.4 - 2.6 MPa.

The deposit of the droplet in the hot leg mainly happens in the bend at the steam generator (Fig. 4.). Due to inertia the droplets are impacting against the bend wall. At the bottom of the bend the liquid collects and flows back to the pressure vessel. A stratified, counter current steam liquid flow establishes in the tube. From its surface liquid droplets can be entrained again.
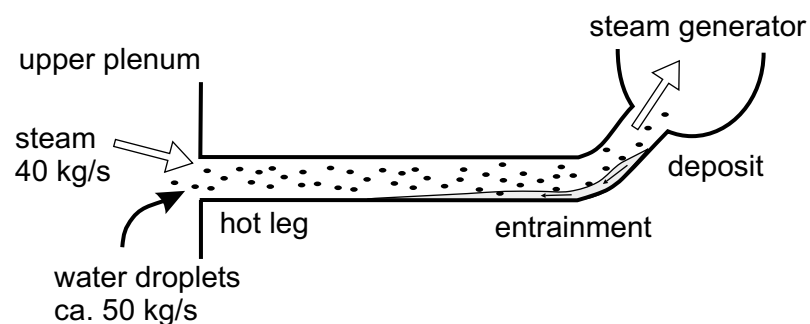
Fig. 4:   Entrainment and deposit of water droplet in a PWR hotleg [6].

The effective liquid transport from the upper plenum to the steam generator inlet chamber depends on these two strongly interacting phenomena entrainment and deposit. It is strongly safety relevant, because the cold emergency cooling water entrained into the steam generators is evaporated there. This evaporation leads to a pressure increase, which impedes the flooding of the reactor pressure vessel (so called steam binding). Therefore, the transport of the liquid from the pressure vessel to the steam generators characterises the effectiveness of the flooding of the primary circuit.

Entrainment and deposit in the hot leg shall be investigated in a 1:3.75 scaled model of a PWR hot leg. The hydraulic backlash of the steam generator inlet chamber is modelled by a second bend. The instrumentation of the hot leg model allows the determination

- of droplet velocities and size (approx. 0.01 - 0.1 mm)
- size and shape of the phase interface and

19

- local velocities in the liquid film.

For the visualization of the flow pattern and the liquid film in the bend, a wire-mesh sensor with 32 ×32 wires is arranged vertical in the center of the tube. Velocities in the liquid film can be measured by tracer injection. Additionally two further wire-mesh sensors will be arranged in front and behind the first bend. They will be used for the measurement of the void fraction distribution and the phase velocities.
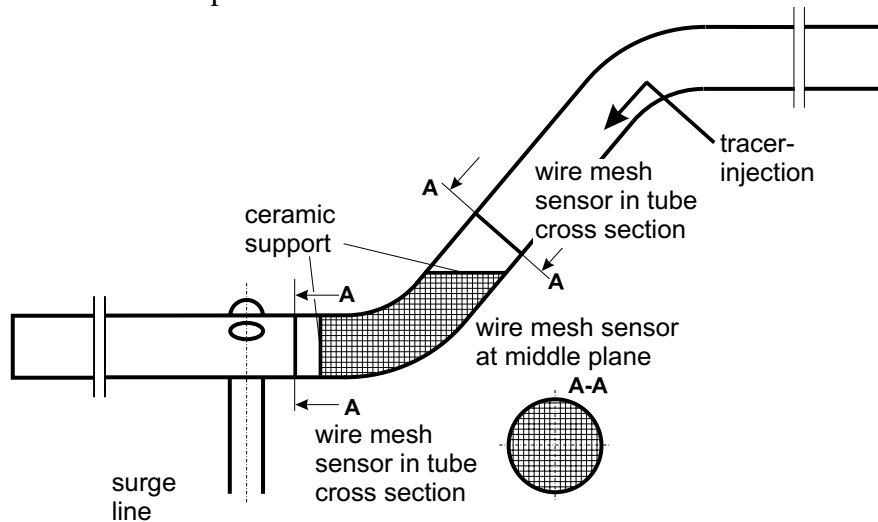
Fig. 5:   Arrangement of wire mesh sensors in the PWR hot leg model [6].

Droplet detection, shape and velocity measurement shall additionally be performed with LDA/PDPA-laser measurement via glasses in the tube wall. These laser measurements will be combined with passive droplet wave guides arrays at the hot leg inlet and outlet.

4.3 Condensation at high temperature differences

At the NOKO test facility series of experiments were started to study steam condensation in horizontal and slightly inclined tubes. These experiments were aimed at the test of the efficiency of the passive heat removal system for the boiling water reactor SWR1000. A special characteristic of the condensation process is the high temperature difference between steam and water in the geodetic flooding pool and the resulting high power density. In cooperation between FZ Jülich and FZR the scope of the experiments was extended to investigations of the transient flow pattern in the heat exchanger tubes. For this purpose, NOKO was equipped with an additional single-tube, which was instrumented with advanced void probes.

After a series of preliminary tests with standard void probes produced in FZR, a new type of probe was developed. In these special probes the sensitive electrode wire was replaced by a micro-thermocouple. Beside the phase detection through the conductivity measurement, a fast temperature measurement is possible. The shroud of the thermocouple is serving as probe electrode. Phase identification and temperature measurement is carried out in the same place. This allows to define whether the measured temperature has to be related to the gaseous or to the liquid phase. The depth of immersion of the probes can be changed during the experiments by stepping motors developed by FZ Jülich. By periodically moving the probes through the boundary layer, the condensate layer thickness and the temperature profiles were recorded. From these results, the distribution of the condensate layer thickness along the pipe perimeter can be deduced. The probes furthermore clearly indicate, when noncondensible gases are present. In this case, the temperature remains below saturation, while the conductivity measurement clearly identifies gas at the tip of the probe.

20

The positive results of a series of experiments performed with these probes have shown that further tests are very useful and necessary. Experiments of this kind are therefore included into the research programme for TOPFLOW.

5. Conclusions and outlook

The new multipurpose thermal hydraulic test facility TOPFLOW (Transient Two Phase Flow Test Facility) is under construction at Forschungszentrum Rossendorf (FZR) e.V. The reconstruction of the building has started in October 2000 and will be finished probably in July 2001. The disassembly of the NOKO test facility will take place from January up to February 2001. All components, which will be reused are moved to FZR. The construction of TOPFLOW starts in March 2001 and will be finished at the end of the year. After a 3 months commissioning phase, the experiments shall start in April 2002.

In the first configuration, TOPFLOW contains three test sections. These are a large pool with a volume of 20 m³ and a design pressure of 1.1 MPa, a steam drum with a volume of 8 m³ and a design pressure of 7 MPa and two vertical test sections with DN50 and DN200, each 9 m long. The first experiments aim at the determination of the phase distribution and flow pattern in large vertical tubes under high pressure conditions and the evaluation of the phase distribution as a function of the distance from the gas injection. Further experiments will include bends, junctions, isthmuses and dilations as well as condensation experiments. This kind of experiments requires new high resolution two phase flow measuring devices (e.g. needle shaped conductivity probes, wire mesh sensors or γ-ray tomography).

References

[1]   E.F. Hicken, K. Verfondern (2000), Investigation of the Effectiveness of Innovative Passive Safety Systems for Boiling Water Reactors, Schriften des Forschungszentrums Jülich, Reihe Energietechnik 11, ISSN 1433-5522.

[2]   E.F. Hicken, H. Jaegers, A. Schaffrath, F.-P. Weiss (2000), The NOKO/TOPFLOW Facility for Natural Convection Flow, TCM-Meeting, Vienna.

[2]   H.-M. Prasser, A. Böttger, J. Zschau (1997), A New Wire-Mesh Tomograph for Gas-Liquid Flows, Frontiers in Industrial Process Tomography II, Delft, The Netherlands, 109-112.

[3]   H.-M. Prasser, E. Krepper, D. Lucas (2000), Fast wire-mesh sensors for gas-liquid flows and decompositions of gas fraction profiles according to bubble size classes, Second Japanese-European Two-Phase Flow Group Meeting, Tsukuba, Japan, September 25-29, proceedings on CD-ROM: D-3.pdf

[4]   A.-K. Krüssenberg, H.-M. Prasser, A.Schaffrath (1999), A New Criterion for the Bubble Slug Transition in Vertical Tubes, Ninth International Topical Meeting on Nuclear Reactor Thermal Hydraulics (NURETH-9), San Francisco, California, USA, October 3-8, proceedings on CD-ROM.

[5]   V. Teschendorff, M. Scheurer, H.-G. Sonnenburg (1998), Konzertierte Aktion zur Integration von CFD-Codes bzw. deren Module in den Systemcode ATHLET zur physikalisch fundierten und sicher skalierbaren Simulation mehrdimensionaler Zweiphasenströmungen, 12. Sitzung des Projektkommittees "Transienten und Unfallabläufe", Köln.

[6]   A. Schaffrath, H.-M. Prasser, F.-P. Weiß (2001), TOPFLOW - Transient Two Phase Flow Test Facility - EFRE (European Fund for Reconstruction)-Projektantrag für die Errichtung einer Mehrzweck-Thermohydraulikversuchsanlage für generische Untersuchungen von Zweiphasenströmungen und die Validierung von CFD-Codes.

THE COLD WATER HAMMER TEST FACILITY (CWHTF)

Eberhard Altstadt, Thomas Mössner and Rainer Weiss

1. Introduction

The rules for pipeline systems of nuclear power plants [2] require the consideration of fluid-dynamic loads in the design phase. These loads will occur e.g. with water hammers. If water hammers happen the fluid mass is decelerated in a very short time, this leads to a strong increase of the pressure. The influence of the fluid-structure interaction on the magnitude of the loads on pipe walls and support structures is not yet completely understood. In case of a dynamic load caused by a pressure wave, the stresses in pipe walls, especially in bends, are different from the static case. The propagating pressure wave may cause additional non-symmetric deformations that increase the equivalent stresses in comparison to the symmetric load created by a static inner pressure. On the other hand, fluid-structure interaction causes the structure to deform, which leads to a decrease of the resulting stresses.

In the past the pipe design was based on analytical calculations and/or one-dimensional simulations [3, 4]. Newer investigations consider the influence of fluid-structure interaction (FSI) on the pressure amplitudes and on the local material stresses [5, 6]. These simulations are based on 3D finite element models for straight and curved pipes. The results of the 3D simulations were used develop advanced analytical equations for design considering the FSI effects.

The lack of experimental data obtained at well defined geometric boundary conditions is a significant obstacle for the validation of codes which consider fluid-structure interaction. Furthermore, up to now the feedback from structural deformations to the fluid mechanics is not fully implemented in existing calculation codes. There fore, at FZR a cold water hammer test facility (CWHTF) was designed and built up. The experimental work at CWHTF is done in the frame work of a project funded by the European Community.

2. Construction and working principle of the water hammer test facility

The CWHTF consists of a pressure vessel (tank), a pipe line with two straight sections (one horizontally and one vertically oriented), two 90° bends (curvature radius 306 mm) and a fast opening valve. The total length of the pipe line is about 3 metres, the outer pipe diameter is about 219 mm and the wall thickness 6 mm. The vertical pipe region is terminated by a lid flange which acts as a bouncing plate. Figure 1 shows the principal construction
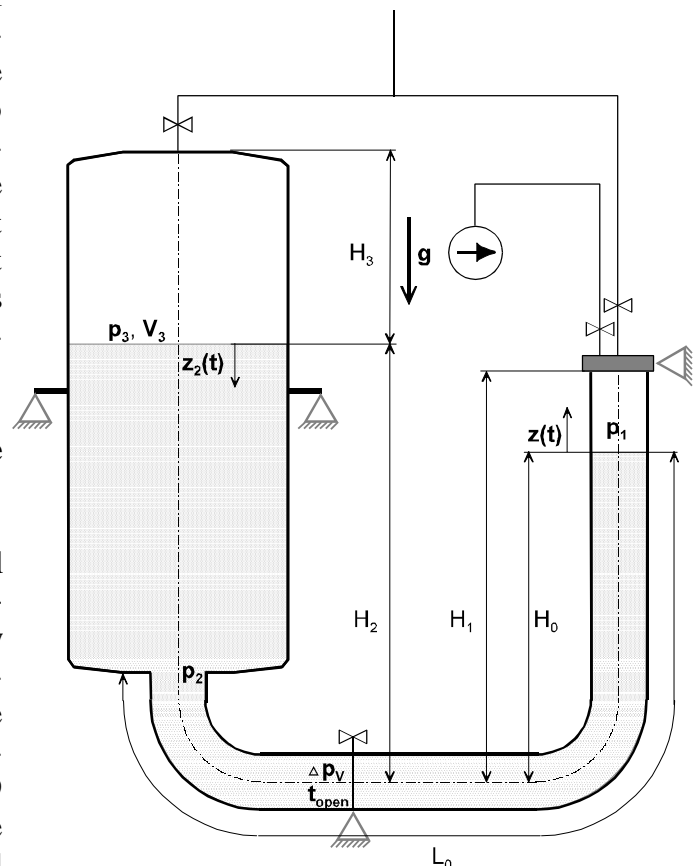
Fig. 1: Working principle of the CWHTF and quantities used for the simulation of the acceleration phase

of the facility.

The water level in the vertical part of the pipeline is adjusted in a certain distance from the lid flange. This free volume above this level is evacuated (p << 1 bar) through a hole in the bouncing plate. During this time the fast acting valve is closed. After the fast opening of the valve the fluid is accelerated until bouncing against the upper lid of vertical pipeline. At that time a water hammer is induced. The pressure in the tank may be increased by pressurised air (up to 6 bars) to increase the amplitude of the pressure waves generated. The generated pressure wave travels back through the bend, causing a strong structural response of the pipe system.

The valve is connected to a spring mechanism which allows the quick opening of the turning plate within a defined time. The opening time can be varied between 0.02s and 0.5s by changing the pre-stress of the springs. The opening mechanism is hydraulically initiated by loosening the arrest of the pre-stressed springs. This makes no counterthrust onto the pipe system, so the excitation of vibrations is rather low.

The frame is connected to foundation via bolts. The valve flange is also connected to the ground. At the lid flange (bouncing plate) the connections for vacuum pump and for the pressurised air can be seen. Table 1 contains the principal parameters of the pipe and of the tank:

Table1: Main parameters of the CWHTF

Pipe line	
Outer diameter	219 mm
Wall thickness	6.0 mm
Curvature radius of the bend	306 mm
Total pipe length	3.285 m
Internal volume	124 Litres
Design pressure	60 bar
Pressure of plastification	90 bar
Pressure of break	226 bar
Vessel	
Outer diameter	800 mm
Wall thickness	6.0 mm
Volume	ca. 750 Litres
Design pressure	10 bar

3. Instrumentation

The pipe line is instrumented with a number of sensors between the lid flange and the valve. Dynamic pressures, strains, void fractions and acceleration can be measured. Figure 2 shows the arrangement of the measurement positions. The needle probes measure the conductivity of the

medium at its tip. If there is high conductivity the measuring tip is surrounded by water; if there is low conductivity the surrounding medium is air or steam. Therefore, the needle probe signals give information about position and velocity of the water front during the acceleration phase (before the water hammer). The dynamic pressure sensors detect the pressure change at the inner side of the pipe wall. The acceleration sensors measure the motion of the pipe line at the bouncing plate in 3 spatial directions. Strain gauges are mounted at 7 axial locations of the outer surface of the pipe line. At each axial location there are at least two pairs of strain gauges (one axially and one tangentially oriented gauge per pair) at the circumferential positions $0°$ and $180°$. At some locations there is an additional pair at the $90°$ position (cf. Fig.3). The maximum sampling frequency is 10 kHz for all signals. The measurements are performed at room temperature.
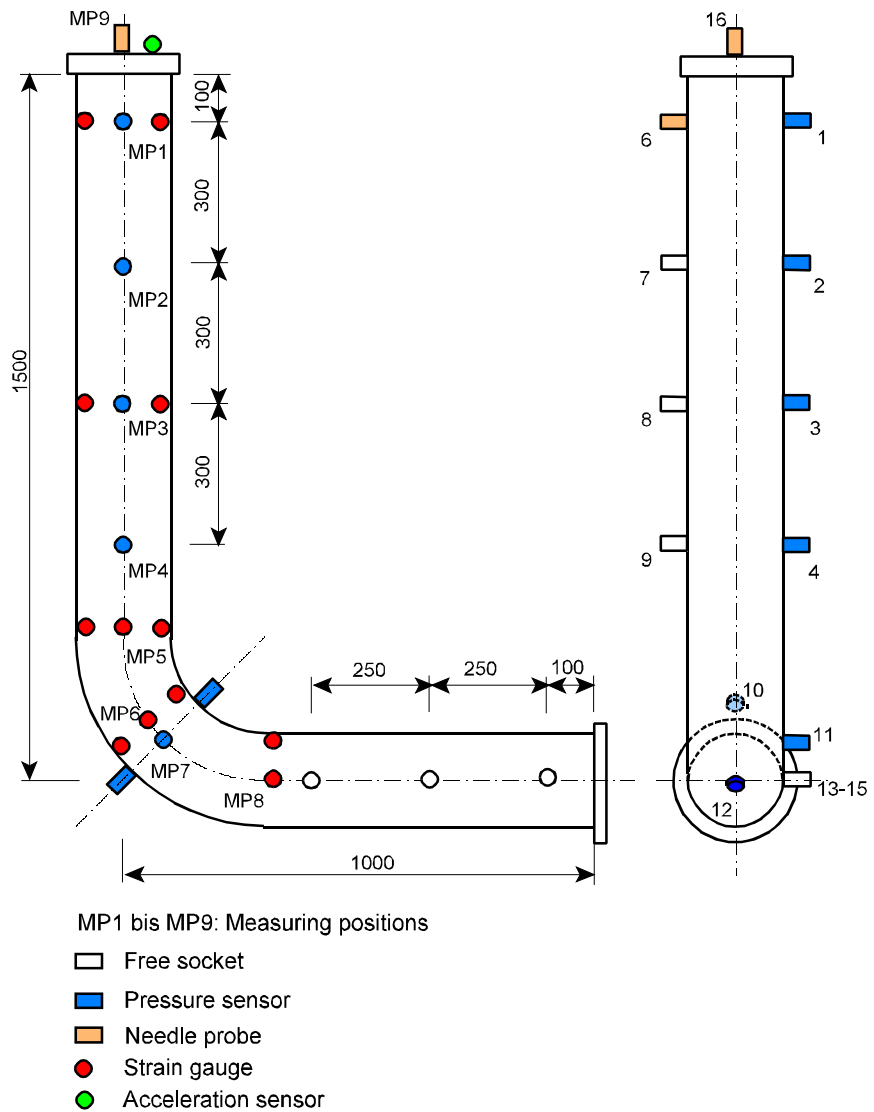
Fig. 2: Instrumentation and measuring positions.

MP1 bis MP9: Measuring positions
☐ Free socket
🟦 Pressure sensor
🟧 Needle probe
🔴 Strain gauge
🟢 Acceleration sensor

4. Estimation of the pressure amplitudes of the water hammer

The following test parameters can be varied to influence the pressure amplitude of the water hammer (shown in table 2).

Table 2: Variation of the test parameters

Evacuation pressure	20 mbar ...... 1 bar
Evacuation height	0.1 m ..... 1 m
Valve opening time	0.02 s .... 0.5 s
Pressure in the tank	1 bar ..... 6 bar

To estimate the bouncing velocity and the amplitude of the initiated pressure wave a 1D numeri-

cal model for the acceleration phase is developed which is based on the following assumptions:

- incompressible, frictionless fluid (density ρ = const)
- one dimensional velocity field (constant over cross section)
- evacuation pressure in the free volume remains constant until the impingement of the fluid front

Figure 1 shows the geometrical and physical quantities used in the model equations. The momentum balances for pipe and vessel are:

$$\frac{d}{dt}\left[\dot{z}\cdot(L_0 + z)\right] + g\cdot(H_0 + z) = \frac{p_2 - p_1 - \Delta p_V}{\rho}$$

$$\frac{d}{dt}\left[\dot{z}_2\cdot(H_2 - z_2)\right] - g\cdot(H_2 - z_2) = \frac{p_3 - p_2}{\rho} \tag{1}$$

The motion of the fluid level in the vessel z_B can be expressed by the motion of fluid level in the vertical pipe z (continuity):

$$z_2(t) = \frac{A_{Pipe}}{A_{Vessel}} z(t) = \alpha \cdot z(t) \tag{2}$$

where A and A_B are the cross section areas of the inner pipe volume and of the tank respectively. Combining equations (1) and (2) leads to the second order differential equation for the motion of the fluid front z:

$$\ddot{z}\cdot[L_0 + \alpha\cdot H_2 + (1-\alpha^2)\cdot z] + \dot{z}^2\cdot(1-\alpha^2)$$

$$+ g\cdot[H_0 - H_2 + (1+\alpha)\cdot z] = \frac{1}{\rho}\cdot[p_3(t) - p_1 - \Delta p_V(t)] \tag{3}$$

$$z(0) = 0 \qquad \dot{z}(0) = 0$$

The pressure loss at the valve is approximately:

$$\Delta p_V(t) = \frac{\rho}{2}\cdot\dot{z}^2\cdot\left[\frac{A_{Pipe}^2}{A_{Valve}^2(t)} - 1\right] = \frac{\rho}{2}\dot{z}^2\varsigma(t) \tag{4}$$

where A_V is cross section which corresponds to the opening degree of the valve. If the vessel is closed the pressure in its gas volume develops according to:

$$p_3(t) = p_{3,0}\cdot\frac{V_3}{V_3 + A_{Vessel}z_2} = p_{3,0}\cdot\frac{H_3}{H_3 + \alpha\cdot z(t)} \tag{5}$$

Equation (3) is solved with a 4th order Runge-Kutta algorithm after inserting equations (4) and (5) and transforming it into a system of two 1st order equations. As a result of this simulation the bouncing velocity v_{end} and the time t_{end} from valve opening till fluid impingement are calculated.

The pressure amplitude can then be estimated from the extended Joukowsky formula:

$$\hat{p} = \rho_F \cdot v_{end} \cdot c'_F \tag{6}$$

where c'_F is the reduced sound velocity of water (consideration of the elasticity of the pipe). Table 3 shows the values which in maximum can be expected with different test parameters.

Table 3: Bouncing velocity and pressure amplitude in dependence on evacuation height and vessel pressure (valve opening time 0.02 s)

Evacuation height $H_1 - H_0$	Vessel pressure $p_{3,0}$	Bouncing velocity v_{end}	Pressure amplitude (Joukowsky)
0.155 m	1 bar (open)	2.97 m/s	36.5 bar
1.19 m	6 bar	18.3 m/s	225 bar
1.30 m	8 bar	21.8 m/s	268 bar

The values for v_{end} and p are upper limits since the assumptions made in the beginning of this section are not fulfilled. Furthermore this simulation does not consider the global FSI effects resulting from the bending flexibility of the pipe line (junction coupling). Figure 3 shows the influence of the valve opening time t_{open}. For small values of t_{open} the bouncing velocity is cons-

tant, only if the opening time exceeds a critical value the bouncing velocity is reduced. The critical opening time depends on the other test parameters such as evacuation height and vessel pressure. At an opening time of 0.02s ... 0.03s there is only an insignificant reduction of the bouncing velocity even for short acceleration phases.
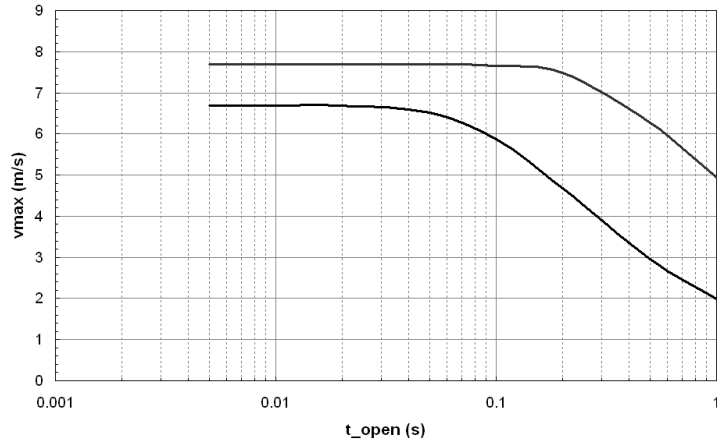
5. First experimental results

The first experiments were carried out with an open vessel (i.e. $p_3(t) = $ bar = const) at room temperature. The water level in the vertical pipe and in the vessel (before

Fig. 3: Bouncing velocity versus valve opening time; lower curve: short acceleration phase (small evacuation height); upper curve: long acceleration phase (large evacuation height).

evacuation) varied between 0.15 m and 0.35 m for the different test series. The valve opening time was some 0.0265 s. The free volume beneath the bouncing plate was evacuated to evaporation pressure ($p_1 = 0.023$ bar). A sampling frequency of at least 5 kHz is necessary to see the dynamic effects and to get reproducible results. With an evacuation height of 0.155 m a pressure amplitude of some 25 bars was obtained. Figures 4 and 5 show the pressure at measuring positions 1 and 7 (cf. Fig. 2). Figures 6 and 7 show the strains at measure positions 1 and 6. The time between trigger (start of valve opening) and bouncing (initiation of the water hammer) is about 110 ms. This fits very well to the pre-calculation using the model of section 4 ($t_{end} = 104$ ms). After the main pressure wave there are some additional smaller pressure peaks. This might hint to cavitation due to the sub-pressure in the reflection phase of the main pressure wave. The circumferential strains are in the linear-elastic range. As expected in the straight pipe they follow the pressure signal. In the pipe bend range an ovalization of the cross section occurs,

DMS_3004

Fig. 4:   Black: pressure (bar) at MP1-90° (right ordinate axis); orange: horizontal (in-plane) acceleration [m/s²] of bouncing plate; blue: needle probe signal at MP1; green: trigger (valve opening phase); test with $v_0 = 3$ m/s, $t_{open} = 26.5$ ms, T = 20 °C, H_1-H_0 = 0.155 m

25092000 - DMS_3001
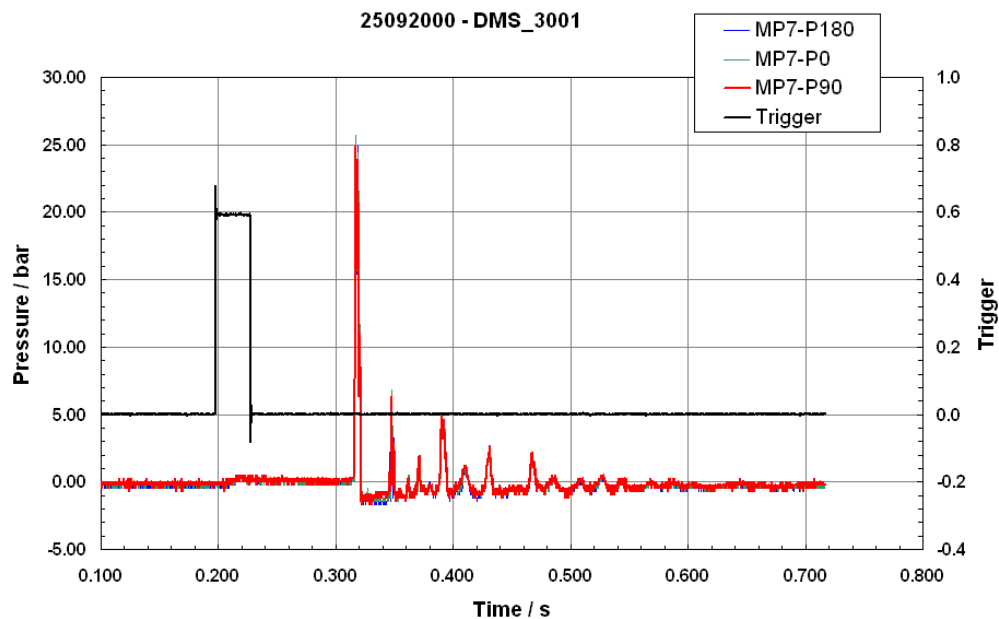
Fig. 5:   Black: trigger (valve opening phase - right ordinate axis); red: pressure (bar) at MP7-90° (pipe bend crown); green: pressure at MP7-0° (pipe bend intrados); blue: pressure (bar) at MP7-180° (pipe bend extrados); test with $v_0 = 3$ m/s, $t_{open} = 26.5$ ms, T = 20 °C, H_1-H_0 = 0.155 m

consequently at the intrados position (0°) and the extrados position (180°) circumferential tension is observed, whereas at the 270° position circumferential pressure strain is detected at the outer wall surface. Due to the junction coupling effect the pipe system is excited to vibrations by the

27

bouncing fluid what is also clearly visible in the strain signals of the pipe bend (MP6). In the pipe bend the strain amplitudes caused by junction coupling are higher than those caused by the pressure wave itself.
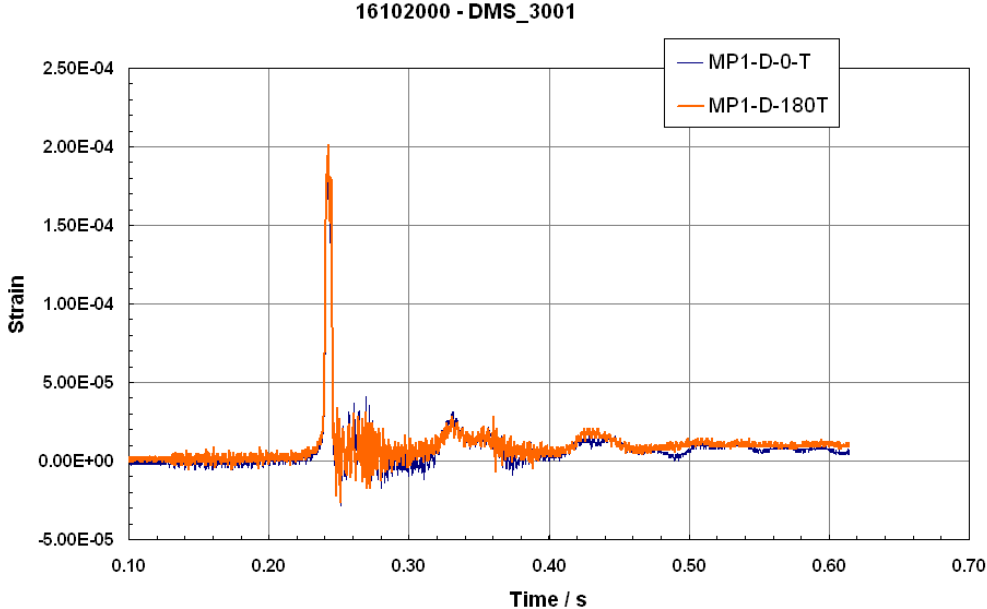
Fig. 6: Tangential strains at MP1-0° and MP1-180°; test with $v_0 = 3$ m/s, $t_{open} = 26.5$ ms, $T = 20$ $^{\circ}$C, H_1-$H_0 = 0.155$ m;
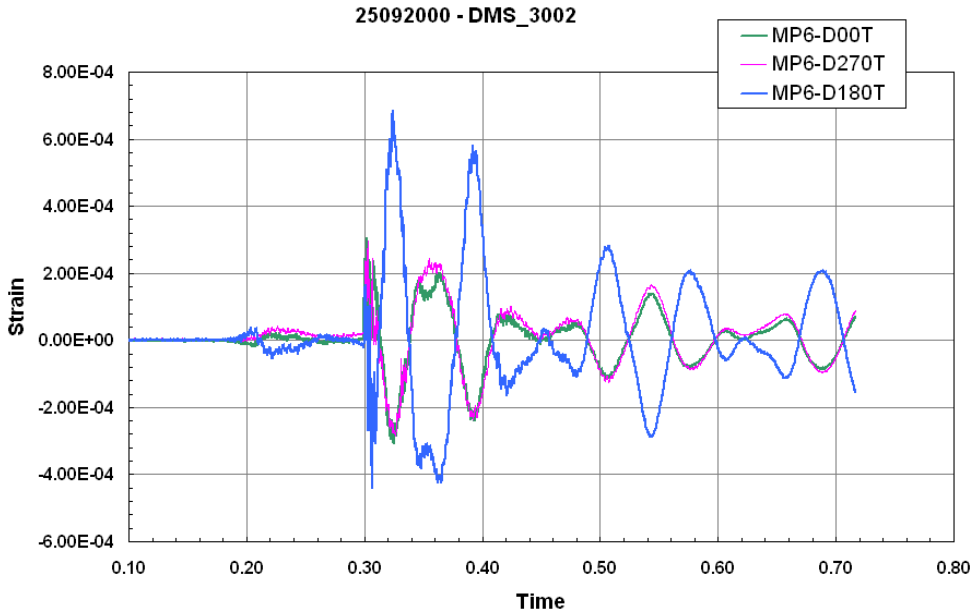
Fig. 7: Tangential strains; green MP6-0° (pipe bend intrados), red: MP6-270° (pipe bend crown), blue: MP6-180° (pipe bend extrados); test with $v_0 = 3$ m/s, $t_{open} = 26.5$ ms, $T = 20$ $^{\circ}$C, H_1-$H_0 = 0.155$ m

28

6. Conclusions

At the FZR a cold water hammer test facility has been installed. Pressure amplitudes of up to 200 bars can be generated. First test have shown that it works as expected. A one-dimensional model for the acceleration of the fluid was developed and validated with the results of the first experiments. The bouncing velocity is predicted quite well by this model, whereas the pressure amplitude is over-estimated by some 30-50% since the effect of the junction coupling is not included.

References

[1]   Sicherheitstechnische Regeln des Kerntechnischen Ausschusses (KTA) für den Primär- und Sekundärkreislauf, 3200 ff, aktuelle Version

[2]   Handbuch Reaktorsicherheit und Strahlenschutz, Abschnitt 4: Empfehlungen der Reaktorsicherheitskommission, Herausgeber: Der Bundesminister für Umwelt, Naturschutz und Reaktorsicherheit, aktuelle Version

[3]   F. Borchsenius, J.-Th. Bornemann (1998), Entwicklungen bei fluiddynamischen Berechnungen im atomrechtlichen Aufsichts- und Genehmigungsverfahren, Tagungsbericht der Jahrestagung Kerntechnik 1998, München, ISSN 0720-9207

[4]   A.S. Tijsseling (1993), Fluid-structure interaction in case of water hammer with cavitation, Ph. D. Thesis, Delft University of Technology, Faculty of Civil Engineering, Communications on Hydraulic and Geotechnical Engineering, Report No. 93-6, Delft, The Netherlands, 1993, ISSN 0169-6548

[5]   T. Repp (1999), Fluid dynamic water hammer simulations with consideration of fluid-structure interaction (FSI), Workshop of the initiative for competence maintenance in nuclear technology on the Jahrestagung Kerntechnik 1999, Karlsruhe

[6]   T. Repp (2000), Acoustic water hammer simulations with consideration of fluid-structure interaction (FSI), Workshop of the initiative for competence maintenance in nuclear technology on the Jahrestagung Kerntechnik 2000, Bonn

PRE- AND POST-TEST CALCULATIONS OF
SCALED CORE-MELTDOWN EXPERIMENTS

Eberhard Altstadt, Jürgen Böhmert, Gudrun Müller and Hans-Georg Willschütz

1. Introduction

Assuming the hypothetical scenario of a severe accident with subsequent core meltdown and formation of a melt pool in the reactor pressure vessel (RPV) lower plenum of a Light Water Reactor (LWR) leads to the question about the behaviour of the RPV. One accident management strategy could be to stabilize the in-vessel debris or melt pool configuration in the RPV as one major barrier against uncontrolled release of heat and radio nuclides.

To get an improved understanding and knowledge of the melt pool convection and the vessel creep and possible failure processes and modes occurring during the late phase of a core melt down accident the FOREVER-experiments (Failure Of REactor VEssel Retention) are currently underway at the Division of Nuclear Power Safety of the Royal Institute of Technology Stockholm [1]. These experiments are simulating the behaviour of the lower head of the RPV under the thermal loads of a convecting melt pool with decay heating, and under the pressure loads that the vessel experiences in a depressurization scenario. The geometrical scale of the experiments is 1:10 compared to a common LWR.

Due to the multi axial creep deformation of the vessel with a non-uniform temperature field these experiments are on the one hand an excellent source of data to validate numerical creep models which are developed on the basis of uniaxial creep tests. On the other hand the results of pre-test calculations can be used to optimize the experimental procedure and can help to make on-site decisions during the experiment.

Therefore an axisymmetric Finite Element (FE) model is developed based on the multi-purpose code ANSYS/Multiphysics®. Using the Computational Fluid Dynamics (CFD) module the temperature field within the melt pool and within the vessel wall is evaluated. The transient structural mechanical calculations are then performed applying a creep model which takes into account large temperature, stress and strain variations.

Additionally metallographic post test investigations of the experiments are conducted to improve the numerical damage model and to adjust the correlation between the metallographic observations and the calculated damage.

2. Experimental setup and issues related to the pre-test calculations

The hemispherical bottom head was made of the French RPV steel 16MND5 with an internal diameter of 188mm and a wall thickness of 15mm. The applied oxidic melt was a CaO-B_2O_3 mixture (30-70 wt.-%) which has a solidus temperature of T_s=1250K. To model the internal decay heat generation special designed heater rods fixed to an internal insulation-reflector-lid are immersed into the melt from the top (Fig .1). The latest heater design can provide a heat genera-tion of more than 45kW. After melt pouring the melt injection orifice in the vessel lid is closed and the vessel inside can be pressurized by Argon. Due to the thermal and the creep expansion of the vessel the volume of the hemisphere is increasing approximately to the third power of the increase of the radius. This causes a decreasing melt level and as a consequence in the experiment C2 the uppermost parts of the heater rods were no longer immersed in the pool. Therefore they burned out and the power supply was stopped. But with decreasing temperatures it was not

possible to fail the vessel. (For a detailed description of the experiment see [1]).

After performing successful post-test calculations of the experiment FOREVER-C2 [2], the model was applied to develop a promising heat generation and pressure load schedule for the experiment EC-FOREVER-2, which was conducted on 2nd of November 2000.

According to the experience gained in the 3 prior experiments the following issues were related to the pre-test calculations:

- Evaluation of the temperature field, for assessment of the thermocouple readings.
- Expected transient displacement at the positions where the displacement is measured.
- Evaluation of the risk of a prompt plastic failure, due to high temperatures in the welding between hemisphere and cylinder and the cylinder itself, especially at the beginning of pressurization.
- Calculation of the melt level drop due to the expansion of the vessel, so that the critical time of uncovering of the heater is known. And finally:
- Time and location of failure.
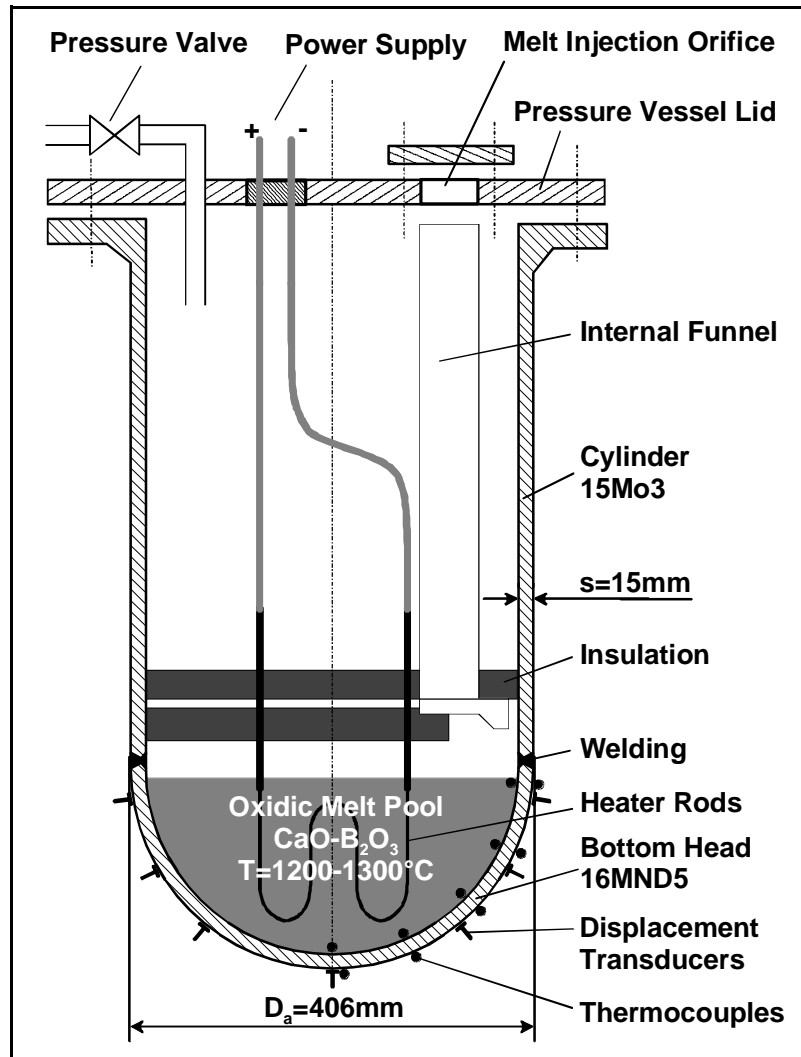
Fig. 1: Principal experimental setup - not to scale.

3. CFD analysis of convection and heat transfer

For the evaluation of the temperature field within the vessel wall the CFD-module FLOTRAN® of the FE-code ANSYS® is used. A 2D-axisymmetric model with appropriate boundary conditions and material properties is developed. A pure homogenous melt pool is assumed inside the vessel with the surface level set 10mm below the welding joint between hemisphere and cylinder, which compensates the melt drop due to the thermal expansion of the vessel. A homogenous volumetric heat source is assumed which is applied to the volume within which the heaters are installed. Especially at the very bottom the distance between the heater and the vessel wall has a significant influence to the crust formation.

Figure 2 shows the temperatures for the vessel inside and outside surfaces calculated at a heating power of Q=38kW compared to the measured outside temperatures after reaching thermal steady-state (t=260min). Due to the melt convection inside, the hottest region of the vessel wall
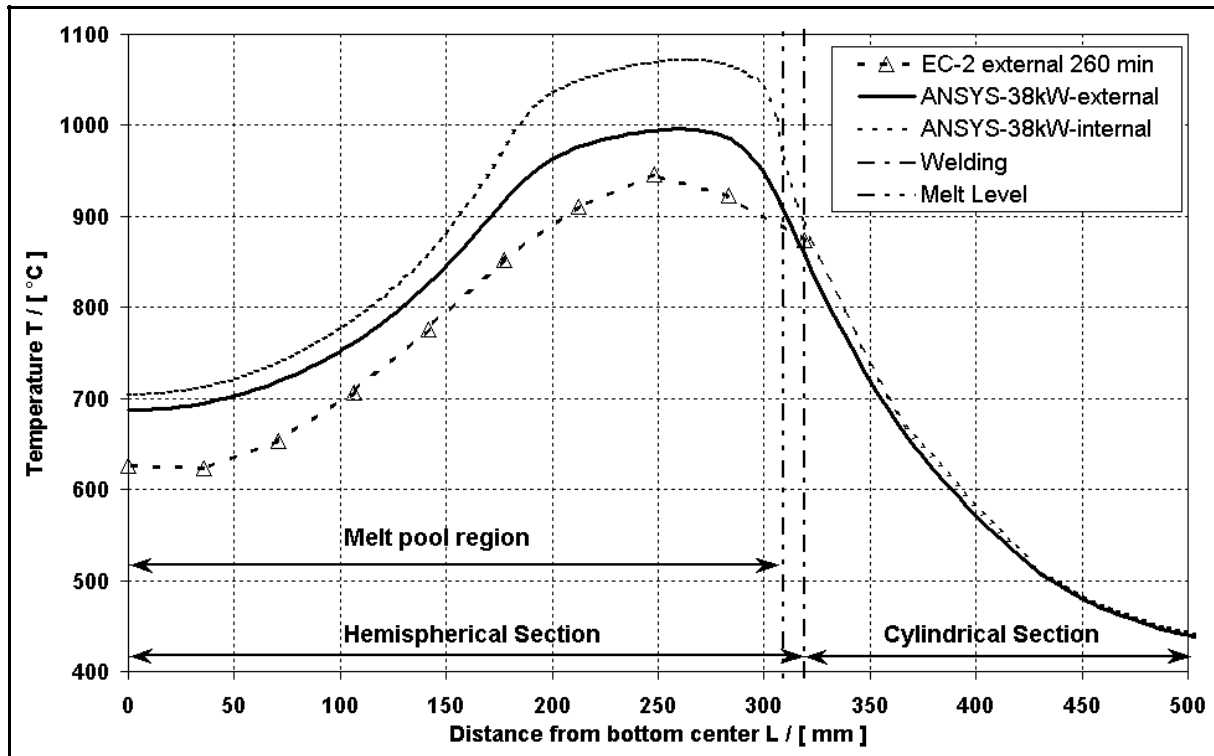
Fig. 2: Measured external and calculated external and internal wall temperatures for a power input of Q=38kW and a melt level 10mm below the welding. T in [°C], abscissa starts at very bottom centre and shows the chord length L in [mm] to the top of the cylinder. Triangles refer to measurement positions.

is the upper part of the hemisphere just below the surface of the melt. The local temperature difference over the vessel wall corresponds to the local heat flux. The calculated maximum temperature difference is around 80K, which corresponds to a heat flux of some 140kW/m^2. The measured temperatures at the outside show lower values than calculated because the thermocouples are mounted at the wall and cannot exactly measure at the surface, but qualitatively the agreement between experiment and calculation is very well.

The inside measurement is much more difficult. Because of the aggressive melt the thermocouples were protected by stainless steel tubes fixed to the wall. The measured temperatures at the inside were several hundred degrees higher than calculated. This can be due to the very thin boundary layer of the melt at the wall. Additionally some of the tubes lost their wall contact and may have been very close to the heater rods. It was decided not to use these measurements for comparison. But due to the integral character of the FOREVER-experiment the calculated temperature field is assessed again indirectly by the mechanical response of the vessel to the pressure load, which will be discussed later.

4. Damage modeling in the transient mechanical calculation

The material damage due to significant creep and plastic strains is modeled by a damage measure "D" which is incrementally accumulated at the end of a time step. D=0 means "no damage" and is the initial value for all elements. This damage also includes the prompt plastic deformation of the structure. The damage increment is:

$$\Delta D = \left[\frac{\Delta\varepsilon_{eqv}^{cr}}{\varepsilon_{frac}^{cr}(\sigma,T)} + \frac{\Delta\varepsilon_{eqv}^{pl}}{\varepsilon_{frac}^{pl}(T)} \right] \cdot R_v \qquad (1)$$

with ε_{frac}^{cr} being the creep fracture strain of the uniaxial creep test at constant stress and tempera-ture and ε_{frac}^{pl} being the plastic fracture strain at the corresponding temperature. R_v is a function which considers the damage behaviour in dependance on the triaxiality of the stress tensor [3] :

$$R_v = \frac{2}{3} \cdot (1+v) + 3 \cdot (1-2v) \cdot \left(\frac{\sigma_h}{\sigma_{eqv}} \right)^2 \qquad (2)$$

where v is the elastic Poisson´s ratio, σ_h is the hydrostatic stress and σ_{eqv} is the von-Mises equivalent stress. The damage increment is calculated for each element by averaging its nodal equivalent creep strains. The accumulated damage is:

$$D = \sum_{i=1}^{ldstep} \Delta D_i \qquad (3)$$

If the element damage reaches the value of D=1, the element is killed by setting its death flag to 1, i.e., this element does no longer contribute to the wall strength. The implementation of this model is described in [4].

5. Structural analysis model for the vessel creep

The FE-model has 8 elements over the wall in the high temperature region of the vessel. A sufficient number of elements over the wall thickness is necessary to model the changing material properties and the body load due to the temperature field which is taken from the CFD analysis. To save computational time, regions of lower temperatures were meshed with 4 element layers over the wall thickness.
Because of the large spatial and transient temperature and stress changes within the vessel wall an advanced approach for the numerical creep modelling has been developed. Usually creeping is described by analytical formulas (creep laws) with a number of free coefficients. The coeffi-cients are used to adapt the creep laws to creep test results performed at constant load and temperature. However, it is difficult to achieve a satisfying adjustment for a wide range of temperatures and stresses with only one set of coefficients. Therefore a supplementary tool for the ANSYS® code has been developed which allows to describe the creep behaviour of a material for different stress and temperature levels independently. Moreover, the damage is calculated as described above. The Digital® Fortran Compiler (Rev. 6.1A) was used for programming and for generating the customized ANSYS-executable on a Windows/NT® platform [4]. The creep data base has been generated using an experimental results analysis performed by Ikonen [5]. Due to the uncertainties of the creep fracture strains measured in the uniaxial tests the creep fracture strain ε_{frac}^{cr} was set to 60% for temperatures above 600°C. The plasticity of the material is modelled by using the multilinear isotropic hardening option of ANSYS®. The plastic fracture strain ε_{frac}^{pl} is taken from the upper end of the stress-strain curve. With these values the damage increment (cf. eq. (1), (3)) can be calculated.
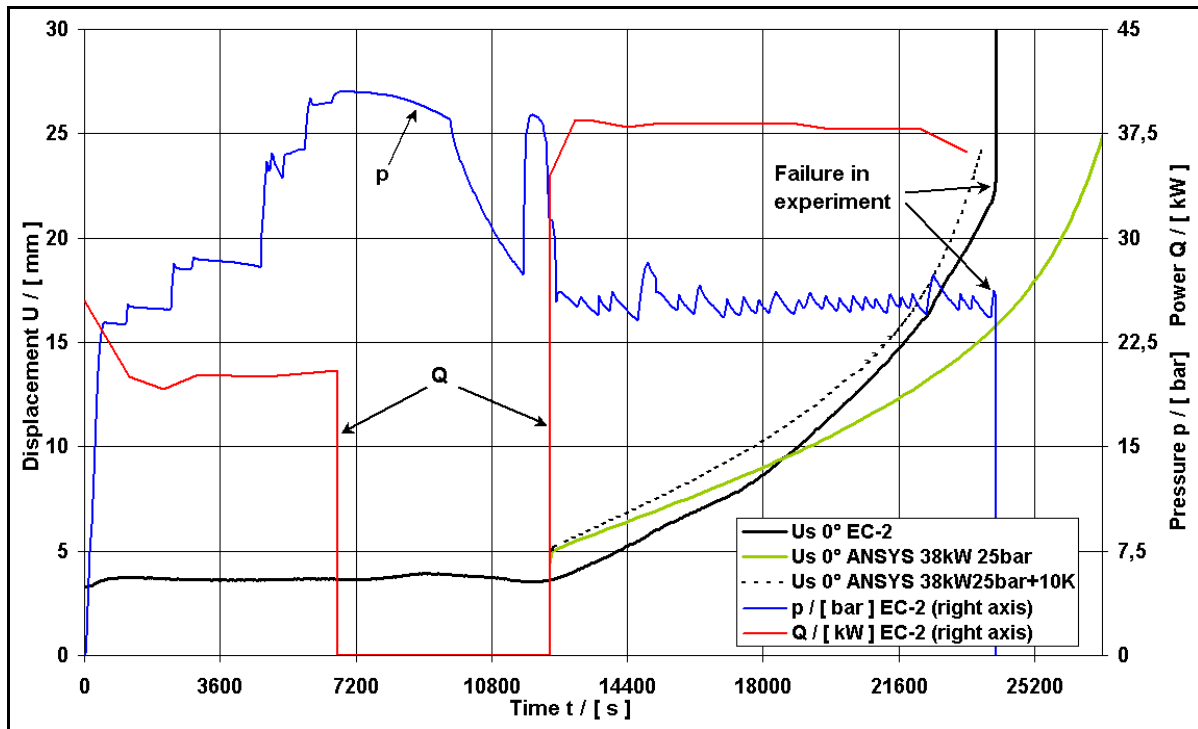
Fig. 3: Measured and calculated total displacement at the very bottom over time. Additionally the measured power input and pressure are shown.

6. Results of the pre-test calculation and comparison with the experiment

There was a power supply problem in the experiment, which limited the heat generation rate to some 20kW instead of the scheduled 38kW (cf. Fig. 3). To initiate the creep process despite of this, the pressure was increased from the designed 25bar to 40bar, but then the heat generation was stopped and after 1:30h the designed heat generation rate could be applied. From this time also the designed pressure was kept. In contrast to this experimental sequence with a lot of transients the pre-test calculation assumed a steady-state temperature field in the vessel wall generated by a power of 38kW, when the pressure is applied constantly at 25bar. Therefore the mechanical calculation is compared with the experiment over the time when the full power was regained. This is shown in Fig. 3: the thick curve represents the measured displacement of the bottom centre. At t=12,360s the power was regained and the pressure was decreased to p=25bar. The beginning of the ANSYS-calculations is referred to this point. The small difference between calculation and measurement is mainly caused by the cooler vessel wall in the experiment, i.e. less thermal expansion. Some 30min after power was regained a quasi steady-state temperature field was reached, i.e. the temperature distribution corresponded to that shown in Fig. 2. The first ANSYS-curve entitled "38kW 25bar" is a pre-test run, failure is predicted at 4:05h after initiation of the creep process, which corresponds to t=27,060s in the experiment. In fact, failure happened 48min earlier in the experiment, therefore the second ANSYS-curve shows the displacement progression, if the whole temperature field is increased by only +10K (post test run). Then the calculation predicts failure 6min earlier then it occurred in the experiment. This indicates that the mechanical response of the vessel is very sensitive to small temperature changes. This confirms also that the calculated temperature field is quite reasonable and that the thermocouples do not measure the temperature exactly at the wall surface (cf. Fig. 2). Another reason for the relatively fast failure of the vessel compared to the pre-test calculation is a possible "pre-damage" caused
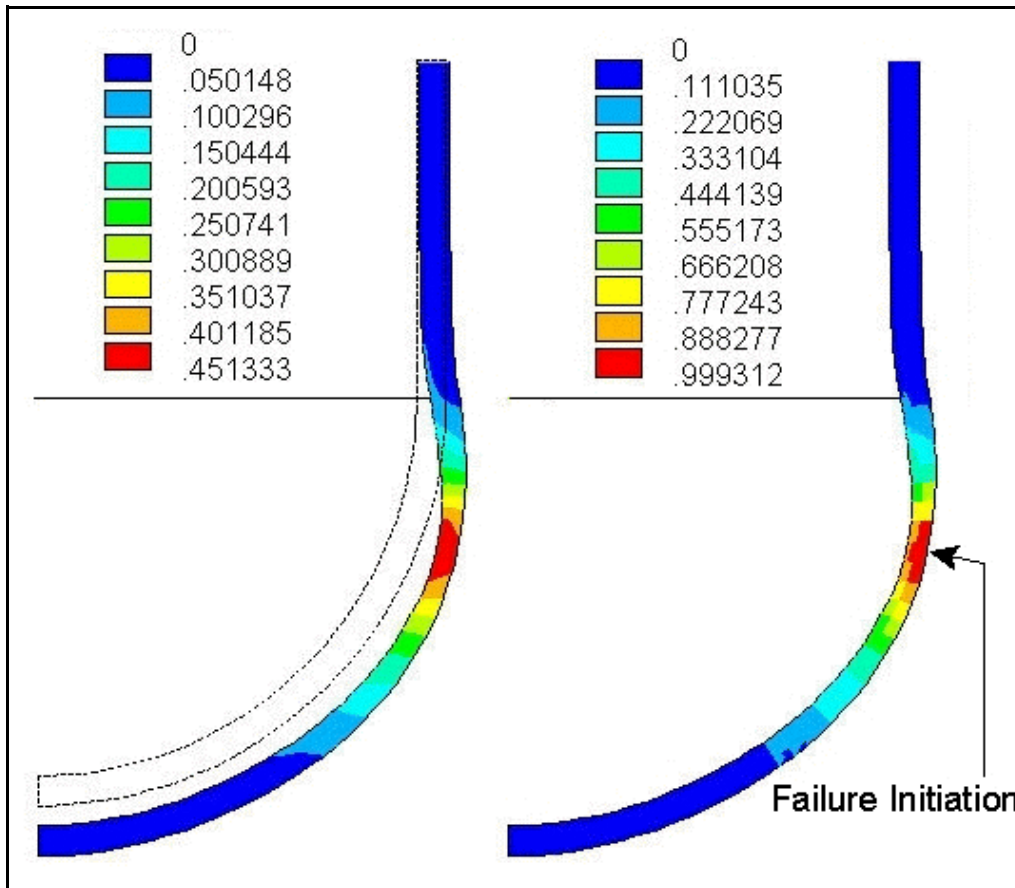
Fig. 4: Creep strain (left side, max. 45.13%) and damage (right side, max. 0.9993) at the calculated rupture begin after t=4:05h (38kW, 25bar). The black triangle indicates the expected failure initiation position.

by the transients, which were not considered in the calculations.

Figure 4 shows the creep strain and the accumulated damage at failure time. The horizontal lines indicate the initial welding line. The maximum creep strain is some 45%, i.e., the first element is killed before reaching the assumed uniaxial creep fracture strain of 60%. One reason is that there is a small contribution to the damage by plastic strain, but the main reason is the triaxiality factor (cf. eq (2)), which was around 1.3. The expected failure position is also shown in Figure 4. The most damaged element is some 60mm below the welding, on the vessel outside. On the outside the triaxiality factor was larger than on the inside. These results correspond very well to the failure position observed in the experiment, where a horizontal crack of some 150mm length occurred about 50mm below the welding.

According to the calculations the failure position is independent on the temperature shift (+10K), i.e. it is nearly independent on the time of failure.

7. Metallographic Observations

Complementing the working programme metallographic post test investigations have been added. Such investigations provide insights into the material processing during the experiment. Firstly, damage mechanism due to environmental effects, e.g. reactions between melt and vessel, are revealed. Secondly, the evaluation of creep damage can be identified.
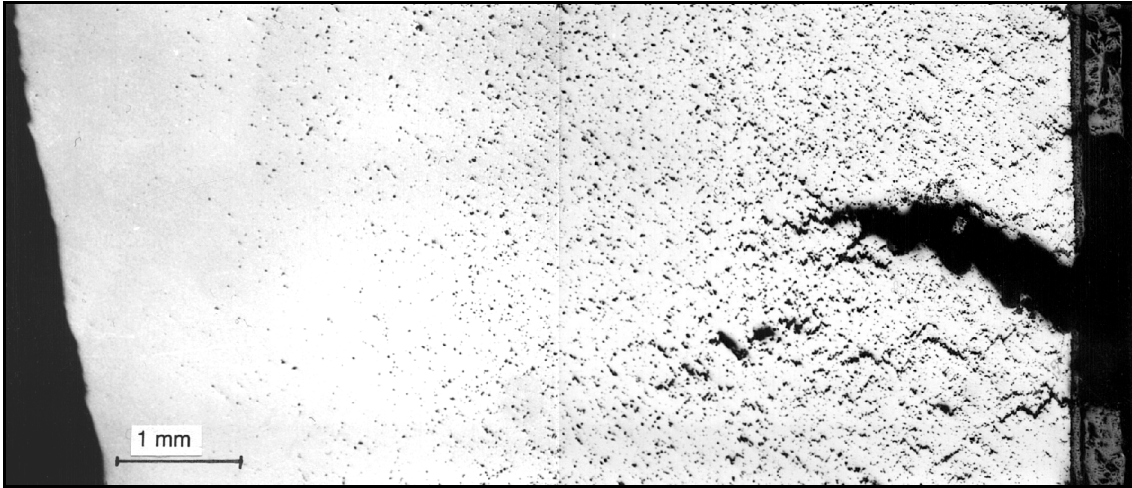
Fig. 5: Micrograph of a polished, non etched sample just above the final crack position (ca. 50mm below the welding). Dark areas indicate voids: creep pores and cracks.

Metallographic examinations of samples taken from different positions of the vessel wall were performed in order to detect experiment-induced microstructural changes. Additionally, annealing experiments with subsequent microstructural investigations, microhardness measurements, ion microprobe analysis and scanning electron microscopy with energy dispersive X-ray analysis of selected samples were also carried out (FOREVER C1 and C2, [6]). In this way the temperature regime and the temperature profile could be determined with an accuracy of +/- 20°C.

The result of the metallographic examination is a two-dimensional profile of the microstructure over the wall thickness and along the height position. Regions of microstructural appearances that are correlated to special transformation temperatures or environmental effects could be defined. In this way the region of highest thermal loads could be identified and the axial and radial thermal gradient could be proven. The investigations revealed that creep pores are formed at highly loaded positions. They indicate a remarkable creep damage.

Figure 5 shows a cross sectional view over the vessel wall just above the final crack position in EC-FOREVER-2. On the left side, i. e. vessel inside, nearly no creep pores are found. Towards the outside the number of pores increases significantly and finally the coalescence of the growing pores is clearly oriented horizontally and small cracks are formed. Figure 6 shows a detailed damage contour plot of the most damaged region (cf. Fig. 4) for comparison. Qualitatively, the agreement between the microscopically observed damage distribution and the calculated damage parameter "D" is quite well.
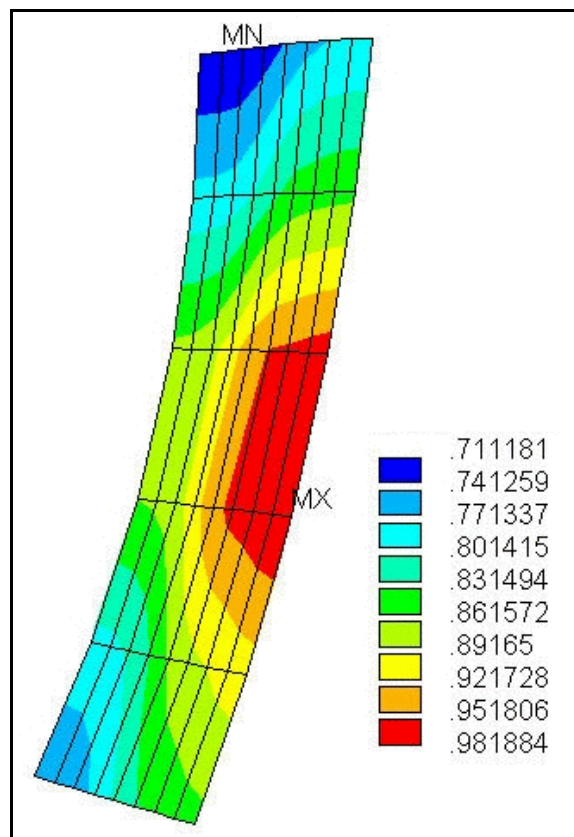
Fig. 6: Contour plot of the damage parameter D [-] just before calculated failure.

36

8. Conclusions

The on-line evaluation of the according pre-test calculation was a quite reasonable help during the experiment. Finally it can be stated that the developed Finite Element Model is roughly validated for this kind of scaled experiments. Additionally microscopic investigations were made to get insights into the complex structural behaviour within the vessel wall and the distribution of the creep pores. The microscopic examinations have proven to be a valuable tool for the analysis of the conditions and the sequence of the FOREVER experiments. Qualitatively, the agreement between the metallographic and the numerical results is quite well.

References

[1]   B. R. Sehgal, R. R. Nourgaliev, T.N. Dinh and A. Karbojian (1999), FOREVER experimental program on reactor pressure vessel creep behavior and core debris retention, Proceedings of the 15-th International Conference on Structural Mechanics in Reactor Technology (SMiRT-15), Seoul, Korea, August 15-20, 1999.

[2]   H.-G. Willschütz, E. Altstadt, B.R. Sehgal and F.-P Weiss (to be published), Coupled Thermal structural Analysis of LWR Vessel Creep Failure Experiments, Nuclear Engineering and Design, Elsevier Science, Amsterdam.

[3]   Lemaitre, J. (1996), A Course on Damage Mechanics, ISBN 3-540-60980-6, 2nd edition Springer-Verlag Berlin, Heidelberg, New York.

[4]   Altstadt, E., Moessner, Th. (2000), Extension of the ANSYS® creep and damage simulation capabilities, Rossendorf, Report, FZR-296.

[5]   Ikonen, K., 1999, "Creep Model Fitting Derived from REVISA Creep, Tensile and Relaxation Measurements", Report MOSES-4/99, VTT-Energy, Espoo, Finland.

[6]   G. Müller, J. Böhmert (2000), Metallographic Post-Test Investigations for the scaled Core-Meltdown-Experiments FOREVER-1 and -2, Rossendorf, Report, FZR-298.

RADIAL GAS FRACTION PROFILES IN VERTICAL PIPE FLOW

Eckhard Krepper, Dirk Lucas and Horst-Michael Prasser

1. Introduction

One-dimensional codes are frequently used for the simulation of two phase flow in the field of design, optimization and safety analysis of nuclear and chemical plants. Most of the correlations used by these codes e.g. for pressure drop or heat and mass transfer are valid only for a given flow regime. The definition of these flow regimes is based on steady state flow regime maps. Steady state flow maps, however are not able to predict the flow pattern in case of transient flows. Recently attempts were made to solve this problem by the introduction of additional equations for the bubble density or corresponding parameters like bubble diameter, bubble volume or interfacial area. Bubble coalescence and break-up rates, which form the source terms in these equations, are determined by local events. That means, they depend on local parameters of turbulence as well as on the local bubble size distribution.

Forces acting on bubbles in a gas-liquid flow strongly depend on the bubble diameter. This is well known for the drag force, which was investigated by many authors. In the field of the so-called non-drag forces, which act perpendicular to the flow direction, there are still open questions. Recently, it was found, that the lift force changes its sign at some critical bubble diameter [1], e.g. in a vertical upwards pipe flow, small bubbles are moved towards the wall, while bubbles with a diameter greater than the critical migrate towards the centre of the tube. Concerning the other non-drag forces, i.e. the lubrication force and the turbulent dispersion force, there are also still needs to complete the models.

The experimental input for the study of these forces comes mainly from the observation of single bubbles. In this paper a method is introduced, that allows to effectively analyse the motion of bubbles depending on their size in a multi-disperse flow. For this purpose, measurements applying a wire-mesh sensor developed in Forschungszentrum Rossendorf [2], [3] in a vertical upwards flow were carried out. A method to measure bubble size distributions by evaluating wire-mesh sensor data was presented [4]. The bubble identification algorithm can be used to decompose radial gas fraction profiles according to bubble size classes. Measurements taken at different distances from a gas injection show the evolution of the gas fraction profiles for different bubble size classes separately. This makes it possible to study the net motion of the bubbles in the direction perpendicular to the flow, and to check theoretical models of the non-drag forces in a realistic multi-disperse flow [5].

A one-dimensional model is presented, which predicts the radial volume fraction profiles from a given bubble size distribution [6]. It bases on the assumption of equilibrium of the non drag forces acting on a bubble perpendicularly to the flow path. This model together together with appropriate models for local bubble coalescence and break-up could be used for the prediction of the flow pattern.

2. The experiments

2.1. Processing of the wire-mesh sensor data

The tests were performed to study the evolution of the bubble size distribution in a vertical tube of 51.2 mm diameter. Air-water flow at a temperature of 30 °C was investigated. The superficial velocities were varied in the range of $0 < J_{gas} < 4$ m/s and $0 < J_{liquid} < 12$ m/s. The distance between sensor and air injection was varied from 0.03 m to 3.5 m. This corresponds to related inlet lengths of $0.6 = L/D = 70$.

The wire-mesh sensor delivers a sequence of two-dimensional distributions of the local instantaneous conductivity, measured in each mesh formed by two crossing wires (see [3], [4]). Local instantaneous gas fractions are calculated assuming a linear dependence between gas fraction and conductivity. The result is a three-dimensional data array (i,j,k where k is the number of the instantaneous gas fraction distribution in the time sequence. The indices correspond to co-ordinates x,y of the local measurement in the cross section and the time t. $t = k \cdot \Delta t$. Averaging the local gas fractions over the time, radial gas fraction profiles, i.e. average gas fractions in dependence on the distance from the tube centre may be determined. In the case of steady flow conditions, the time axis can be transformed into a virtual z*-axis by scaling it with the average phase velocity of the gaseous phase: $z^x = \overline{w_{gas}} t \cong t \cdot J_{gas} / \overline{\varepsilon}$.

At moderate flow velocities, the high time resolution allows to perform a bubble size measurement, because individual bubbles are mapped in several successive frames. Furthermore, gas fraction portions belonging to bubbles the dimensions of which exceed the electrode pitch are found in more than one mesh of the sensor. A detailed description of the method can be found in [4] or [5].

2.2. Decomposition of radial gas fraction profiles

The bubble identification algorithm allows to identify the elements [i,j,k] of the gas fraction distribution $\varepsilon_{i,j,k}$ that belong to a given bubble. Since the bubble diameter is known after the summation of all elements, it is possible to decompose the gas fraction distribution according to the belonging bubble diameter. Partial radial gas fraction profiles are obtained, which consider only bubbles from a given range of diameters [5].

The left column of Fig. 1 represents a virtual sectional side view of the sequence of gas fraction distributions measured by the sensor. The upper
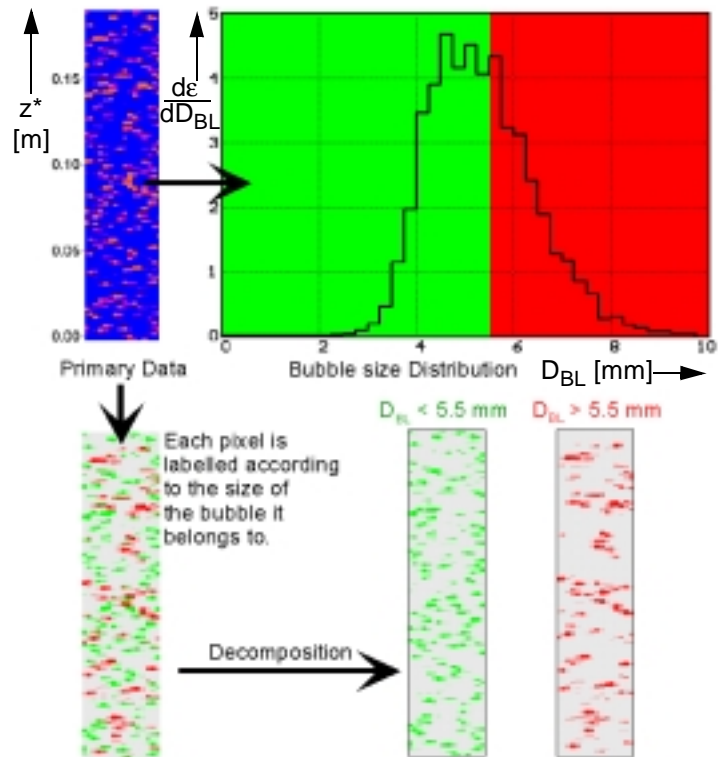
Fig. 1: Decomposition of radial gas fraction profiles according to the bubble size

39

right plot shows the bubble size distribution. In the lower left column the bubbles are labelled according to their diameter: If the diameter is less than 5.5 mm, they are painted green, in the opposite case red. Now, the initial sequence can be divided in sequences of gas fraction distributions considering only bubbles with $D_{bub} < 5.5$ mm (column with only green bubbles) and $D_{bub} > 5.5$ mm (column with only red bubbles). These decomposed data sets are taken to calculate time averaged gas fraction distributions.

2.3. Influence of primary gas fraction profile and primary bubble size distribution on the evolution of the two-phase flow

Three different types of air injecting devices were used (see Fig. 2): A - an array of 19 capillaries of 0.8 mm inner diameter, the ends of which were bent into the flow direction and equally distributed over the cross section, B - 36 orifices in the tube side wall with 1 mm inner diameter and C - 8 orifices in the side wall of 4 mm diameter.

The described decomposition of radial gas fraction profiles was applied to data obtained in experiments at superficial velocities of $J_{liquid} = 0.4$ m/s and $J_{gas} = 0.06$ m/s, which were carried out with all three air injection devices (see Fig. 3). The inlet length was varied from L/D = 0.6 (H = 30 mm) to L/D = 60 (H = 3133 mm).
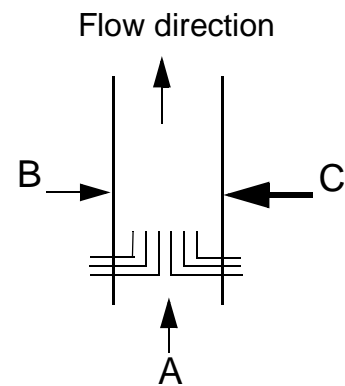
Fig. 2: Investigated injection devices

The measured bubble size distribution at L/D = 0.6 indicates, that in case of injection A all primary bubbles have an equivalent diameter smaller than 5.5 mm. The gas injection through the 1 mm orifices in the wall also produces small bubbles with a diameter mainly below 5.5 mm, while the 4 mm orifices generate larger primary bubbles of about 8 mm. Along the flow path, the bubble size distributions remain almost constant in case of injection A and B, while the larger bubbles produced by the 4 mm orifices (C) start to coalesce. The bubble size distribution is changed from the initial mono-modal one to a bimodal. Both large bubbles of about 30 mm diameter as well as small bubbles with a diameter significantly less than the initial bubble diameter are found at the end of the test section (L/D=60).

In case of the capillary injection (A), bubbles larger than the critical diameter of 5.5 mm are not present in the initial distribution. The decomposed radial gas fraction profiles in Fig. 4 clearly show the tendency of the small bubble fraction to move towards the wall. At H = 30 mm, the profile is still
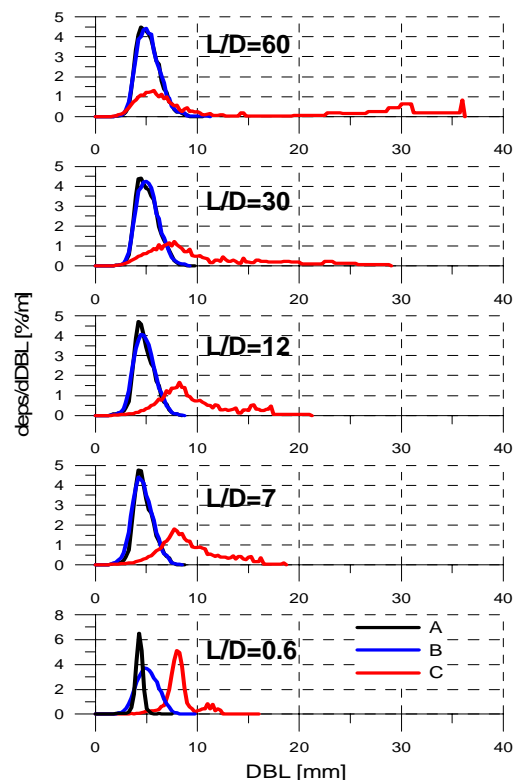
Fig. 3: Bubble size distribution (J_{liquid}=0.4m/s; J_{gas}=0.06m/s)

strongly determined by the gas fraction maxima found at the places where capillaries are located. With growing distance, the gas fraction represented by the small bubble fraction shifts towards the wall. The increase of gas fraction near the wall leads to an intensification of coalescence, which leads to a generation of bubbles with $D_{bub} > 5.5$ mm in this region. These bubbles experience an inverse lift force, pushing them towards the centre of the pipe. A pronounced wall peaking of the total gas fraction profile is observed, caused by the peak of the partial gas fraction of the small bubble class. The large bubbles ($D_{bub} > 5.5$ mm) tend to form a central maximum. Despite of the completely different initial gas fraction profile produced by the equally distributed capillaries (A) and the wall orifices of 1 mm diameter (B), the decomposed radial profiles converge with growing distance (Fig. 4). At a relative length of L/D 60, the profiles become identical.

The gas fraction profiles obtained for the injection device C (4 mm orifices) behave completely different. Here, the primary bubbles are larger than 5.5 mm. Closely above the injection they are still found at the periphery, since they have been generated at the wall. With growing height, a generation of bubbles smaller than 5.5 mm and larger that 12.5 mm is observed. Since bubbles with a diameter less than 5.5 mm are not generated at the gas injection orifices, they must be the result of fragmentation events. Bubbles larger than 12.5 mm are the result of coalescence. The bubbles of both classes of large bubbles (5.5 mm < D_{bub} < 12.5 mm and
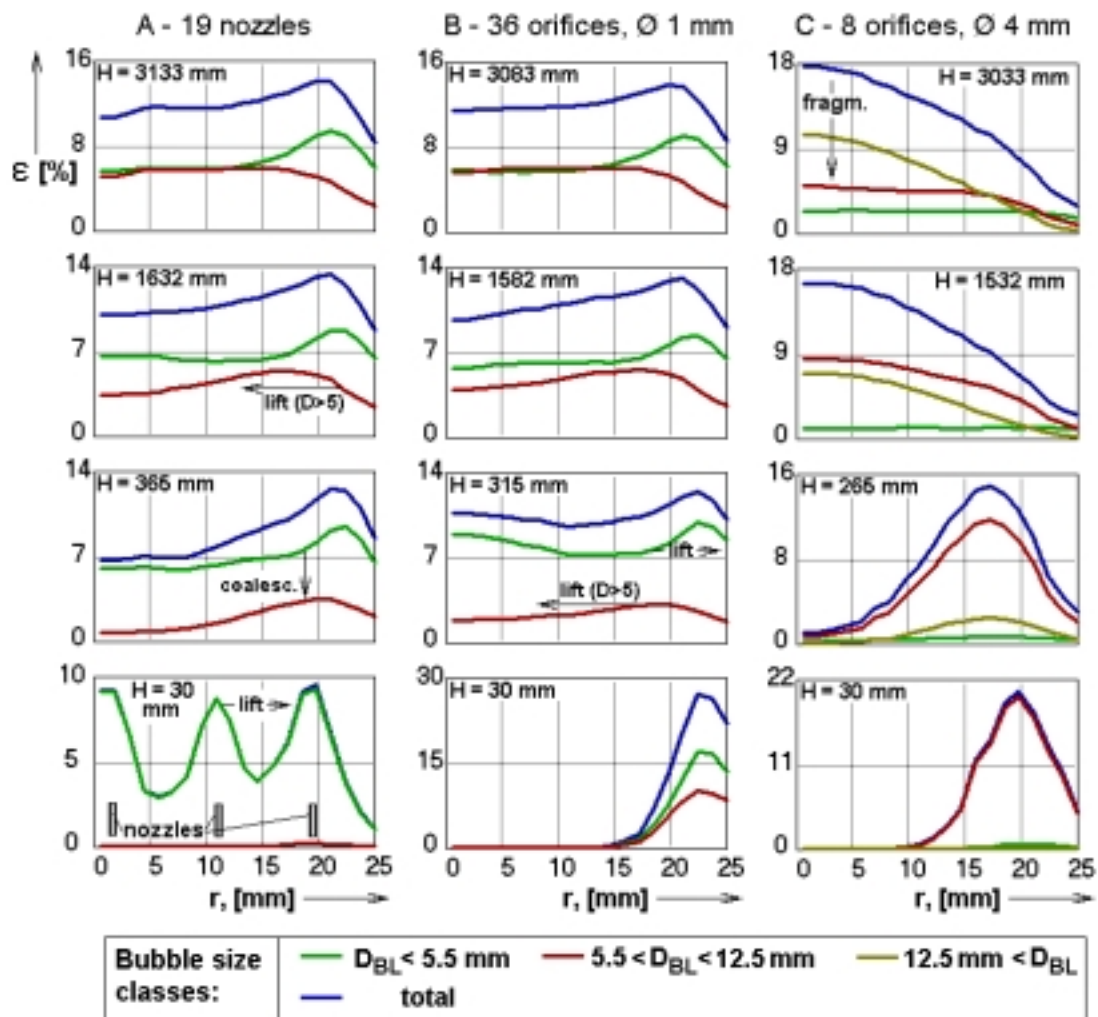
Fig. 4: Measured bubble radial gas fraction distribution

12.5 mm $< D_{bub}$) are quickly shifted to the centre of the pipe. Although the small bubbles are transported towards the wall, they are almost uniformly distributed at the end of the test section. This can be explained by a source of small bubbles due to fragmentation in the central region.

During the test presented in Fig. 4, injection device B and C represent the same primary gas fraction profile and device A and B the same primary bubble size distribution. In Fig. 4 the gas fraction profile at the end of the tube is almost the same for injection devices A and B. That means, that the primary bubble size distribution has a larger influence on the evolution of the two phase flow than the primary gas fraction profile.

3. The model

Forces acting perpendicular to the flow direction determine the formation of radial distributions of the bubbles. The classical lift force is shear-induced and acts toward the wall. Related on the unit volume it can be calculated as

$$\overrightarrow{F_L} = -C_L \rho_L (\overrightarrow{w_g} - \overrightarrow{w_l}) \times rot(\overrightarrow{w_l}) \tag{1}$$

with a positive lift force coefficient C_L. ρ_L is the liquid density, w_g and w_l the gas respective the liquid velocity. Tomiyama et al. [1] proposed another kind of transverse lift force, which is caused by the interaction between the wake and the shear field. It acts to the opposite direction, that means it is also calculated by equation (1), but has a negative coefficient C_L. Tomiyama expresses both forces summarized as a net transverse lift force with the experimentally determined coefficient C_T, which depends on the bubble Eötvös number. For the water-air system at normal conditions C_T changes its sign at the bubble diameter $D_{bub}=5.8$ mm, i.e. the net transverse lift force acts towards the wall for bubbles with a diameter less than 5.8 mm and it acts towards the pipe centre for larger bubbles.

The lubrication force, introduced by Antal et al. [7], drives bubbles away from the wall. Tomiyama [1] developed an modified equation for this force per unit volume:

$$\overrightarrow{F_W} = -C_W \frac{D_{bub}}{2} \left(\frac{1}{(R-r)^2} - \frac{1}{(R+r)^2} \right) \rho_l w_{rel}^2 \overrightarrow{n_r} \tag{2}$$

with w_{rel} as the velocity difference between liquid and gas, R the tube radius and r the distance of the bubble from the tube centre. $\overrightarrow{n_r}$ is the normal vector to the wall. The coefficient C_W also depends on the Eötvös number.

The model does not consider single bubbles, but the radial distributions of volume fractions for single bubble classes. The turbulent dispersion force considers the smoothing of these radial gas profiles caused by turbulence. Lahey et al. [8] derived an equation for the force per unit volume as

$$\overrightarrow{F_D} = -0.1 \rho_l k_l \nabla \alpha \tag{3}$$

with k_l as the turbulent kinetic energy of the liquid and $\nabla \alpha$ the gradient of the gas volume fraction. Following [1] there is a fluctuating motion of single bubbles, which increases with the

Eötvös number. It is caused by the deformation of the bubbles. These fluctuations cause an additional smoothing of the profiles, which is not taken into account by the dispersion force according to equation (3). For this reason a second dispersion force is introduced, which depends on the Eötvös number. As reported in [1] the fluctuations were observed at bubbles with Eötvös numbers larger than about 1. For this reason we stated

$$\overrightarrow{F_{D,Eo}} = -C_{D,Eo}\rho_l(Eo-1)\nabla\alpha \tag{4}$$

for the new Eötvös number dependent dispersion force.

The parameter $C_{D,Eo}$ is the only new model parameter. According to integral experimental data (see below) $C_{D,Eo} = 0.0015 \ m^2/s^2$ is assumed for Eo>1. For Eo<1 $C_{D,Eo}$ is set to zero.

The radial balance of forces applying equations (1)-(4) results in

$$(0.1k_l + C_{D,Eo}(Eo-1))\frac{d\alpha_i}{dr} + \left(C_T w_{rel}\frac{dw_l}{dr} + C_W \frac{D_{bub}}{2}\left(\frac{1}{(R-r)^2} - \frac{1}{(R+r)^2}\right)w_{rel}^2\right)\alpha_i = 0 \tag{5}$$

This equation is a first order differential equation with respect to the volume fraction of a bubble size class $\alpha_i(r)$. It is solved separately for each bubble class. The sum of these profiles is the radial gas fraction profile. The radial profiles of the turbulent kinetic energy of the liquid k_l and of the gradient of the liquid velocity dw_l/dr are still needed to solve the equation.

The radial profile of the liquid velocity is calculated for a given radial gas distribution using the model of Sato et al. [9]. They subdivided the eddy diffusivity into a component, which considers the inherent wall turbulence and a component, which considers the turbulence caused by the bubbles. This causes a feedback between the radial gas profile and the radial profile of liquid velocity. The complete model equations as well as a scheme for a numerical solution procedure can be found in [9].

For the calculation of the turbulent kinetic energy the equations of the k-ε model are used. A common non-linear differential equation of second order for the steady state turbulent kinetic energy k of the liquid can be derived using the following assumptions:

- The time averaged liquid velocity has only a component in axial direction.
- The time averaged liquid velocity is only a function of the radius and does not depend on the azimuthal position and the height.

There is a very sensitive feedback between the velocity profile and the gas fraction profile. For this reason they are calculated within an iteration procedure. An underrelaxation is necessary to guarantee the stability of the iteration. Calculations with an assumed velocity profile according to a 1/m-law typical for turbulent flow through a tube have shown, that this feedback is not negligible. In case of a flow with bubble sizes below 5.8 mm the feedback smoothe the radial gas profiles. The bubbles are located preferably at the wall. For this reason the liquid velocity near to the wall is increased. This smoothe the velocity profile apart from the wall and reduces the lift force in the core region of the flow, which acts towards the wall. Otherwise, if a considerable fraction of bubbles with a diameter larger than 5.8 mm occurs, there is a positive feedback between the gas and velocity profiles. The bubbles in the centre accelerate the liquid. For this reason the velocity gradient in the central region increases. This again causes an
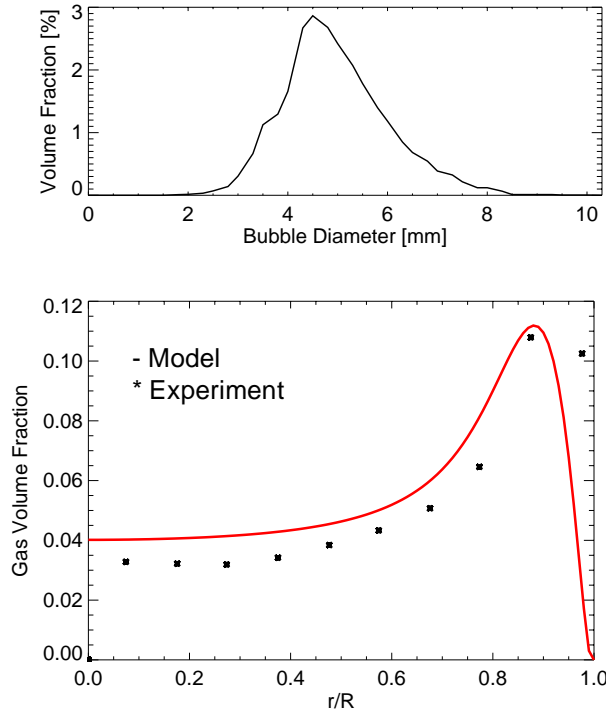
Fig. 5: Measured bubble size distribution and radial gas profiles $J_{liquid} = 1.0167$ m/s, $J_{gas} = 0.0574$ m/s
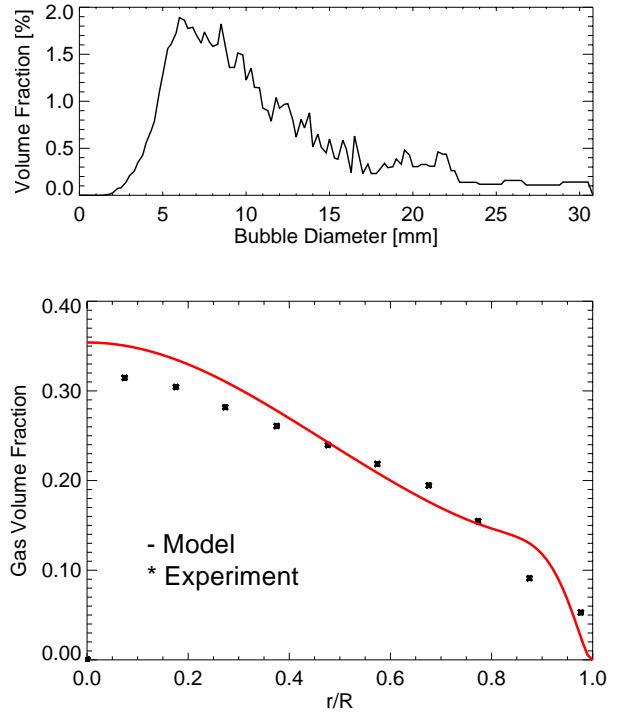
Fig. 6: Measured bubble size distribution and radial gas profiles $J_{liquid} = 1.0167$ m/s, $J_{gas} = 0.219$ m/s

increase of the lift force, which acts bubbles with a diameter larger than 5.8 mm towards the pipe centre in the calculation. The turbulent component of the dispersion force is not strong enough to distribute the large bubbles over the cross section of the pipe. Obviously, another mechanism is dispersing the bubbles. The fluctuating motion of the large bubbles, as observed by Tomiyama [1], may be such a mechanism. Therefore the additional dispersion force according to equation (4) was introduced. The parameter $C_{D,Eo}$ was tuned to achieve a good agreement between calculated and measured radial profiles for large bubbles.
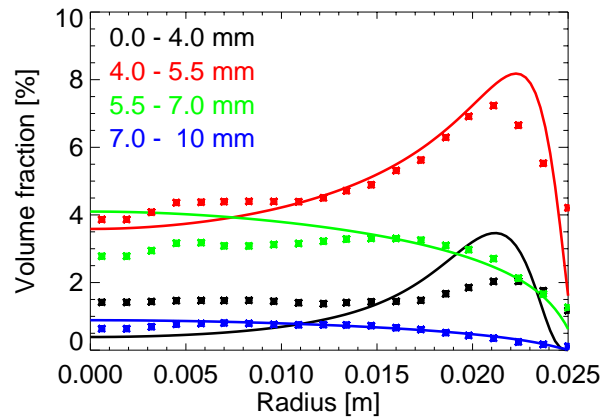
Fig. 7: Comparison of radial volume fraction profiles for bubbles of different size. stars: experiment, solid line: model, $J_{liquid} = 0.4$ m/s, $J_{gas} = 0.057$ m/s

The results of the model were compared with experimental data for a number of gas and liquid superficial velocities. Measured bubble size distributions were taken as an input for the model. There is a good agreement between experimental and calculated radial profiles. In particular the change from wall peaking to central peaking is well predicted. As an example Fig. 5 and Fig. 6 show a comparison of experimental and calculated data. Fig. 7 shows a comparison of radial volume fraction profiles for bubbles of different size. The good agreement confirms the

results from [1] concerning the bubble size dependency of the lift force and following the radial profiles.

4. Conclusions

The presented model allows the prediction of radial gas profiles in vertical pipe flows. In particular the model allows a prediction whether wall peaking or core peaking occurs in dependence of the gas and liquid superficial velocities and the bubble size distribution. The good agreement between experimental and calculated data confirms the dependency of the radial forces acting on a bubble on the bubble size as reported by Tomiyama [1]. The correlations for these forces as well as the model for the radial velocity profile were taken from literature without any change of the empirical parameters. The only extension was the introduction of a Eötvös number dependent dispersion force. The dependency of radial forces on bubble size is very important for the modelling of the transition between bubble flow and slug flow. It is supposed, that the attempts for a one-dimensional modelling of bubble coalescence and bubble break-up suffer from neglecting the radial profiles of the particle densities for the single bubble classes. This assumption will be proofed in a next step by including correlations for bubble coalescence and break-up into the presented model. Further it will be proofed, whether a few-zone model (e.g. core region - wall region) is sufficient to reflect the radial profiles. Such a model could be used in one-dimensional transport codes.

References

[1]   A. Tomiyama (1998), Struggle with computational bubble dynamics, Third International Conference on Multiphase Flow, ICMF'98, Lyon, France, June 8-12, 1998

[2]   H.-M. Prasser, A. Böttger, J. Zschau (1998), A new electrode-mesh tomograph for gas-liquid flows, Flow Measurement and Instrumentation 9, 111-119

[3]   H.-M. Prasser (1999), Wire-Mesh Sensors for Two-Phase Flow Investigations, in F.-P. Weiß, U. Rindelhardt (Ed.) Annual Report 1998 Institute of Safety Research, pp. 23-28

[4]   H.-M. Prasser, D. Scholz, C. Zippe (2001), Bubble Size Measurement using Wire-Mesh Sensors, Flow Measurement and Instrumentation (submitted).

[5]   H.-M. Prasser, E. Krepper, D. Lucas (2000), Fast wire-mesh sensors for gas-liquid flows and decomposition of gas fraction profiles according to bubble size classes, 2nd Japanese-European Two-Phase Flow Group Meeting Tsukuba, Japan, September 25-29, 2000

[6]   Lucas, D.; Krepper, E.; Prasser, H.-M. (2000), Influence of the bubble size distribution on radial gas fraction profiles in vertical pipe flow, 2nd Japanese-European Two-Phase Flow Group Meeting Tsukuba, Japan, September 25-29, 2000

[7]   S.P. Antal, R.T. Lahey, J.E. Flaherty (1991), Analysis of phase distribution in fully developed laminar bubbly two-phase flow, International Journal of Multiphase Flow 17, 635-652

[8]   R.T. Lahey, M. Lopez de Bertodano, O.C. Jones (1993), Phase distribution in complex geometry conduits, Nuclear Engineering and Design 141, 177-201

[9]   Y. Sato, M. Sadatomi, K. Sekoguchi (1981), Momentum and heat transfer in two-phase bubble flow-I, International Journal of Multiphase Flow 7, 167-177

VERIFICATION OF THE CODE ATHLET BY POST-TEST ANALYSIS OF TWO EXPERIMENTS PERFORMED AT THE INTEGRAL TEST FACILITY CCTF

Eckhard Krepper and Frank Schäfer

1. Introduction

In the framework of the external validation of the thermo-hydraulic code ATHLET, which has been developed by GRS (Gesellschaft für Anlagen- und Reaktorsicherheit mbH), post test analyses of two experiments were done, which were performed at the Japanese test facility CCTF. The experiments C2-04 and C2-19 simulate a double ended break in the cold leg of a PWR with emergency core cooling (ECC) injection into the cold leg and with combined ECC injection into the hot and cold legs. The main phenomena are the quenching of the hot fuel rods and the condensation of steam by cold ECC water under strongly thermodynamic non-equilibrium conditions. The movement of the quenchfront and the core cooling are calculated very well.

2. The CCTF test facility

The CCTF test facility (Fig. 1) is a 1:25 volume-scaled model of a 1000 MW pressurized water reactor, [1-2]. The test facility is designed to investigate the refill-reflood phenomena after a large break loss of coolant accident. All four loops of the reference reactor are modelled in the test facility. The broken cold leg is connected to two containment tanks. The reactor core consists of 1824 electrically heated rods. In the core a radial and axial power profile is simulated.
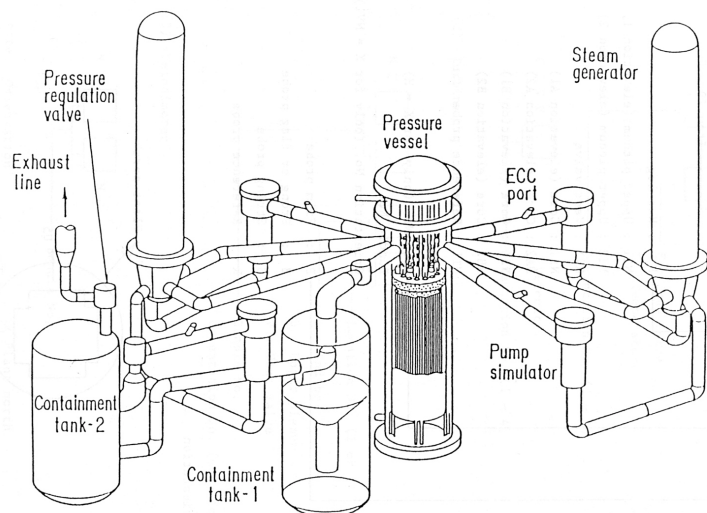
Fig. 1: Sketch of the CCTF test facility

3. Thermohydraulic model

The presented calculations were performed with ATHLET Mod 1.2 Cycle C, [3]. The input deck (see Fig. 2) models the four loops of the test facility by a two-loop representation, one loop for the broken loop and one loop for the three intact loops. The reactor core is modelled by two channels. 62% of the specified power are related to the central channel C1, 38% to the periphery channel C2. Using this nodalization, radial effects caused by the radial power profile can be simulated. In both channels the axial power profile of the test facility is modelled. In all control volumes the 6-equation two-phase flow model and the flow regime pattern dependent condensation model were used. For calculation of the rewetting process, in the reactor model the quenchfront model was applied. The containment tanks were simulated by time dependent volumes.
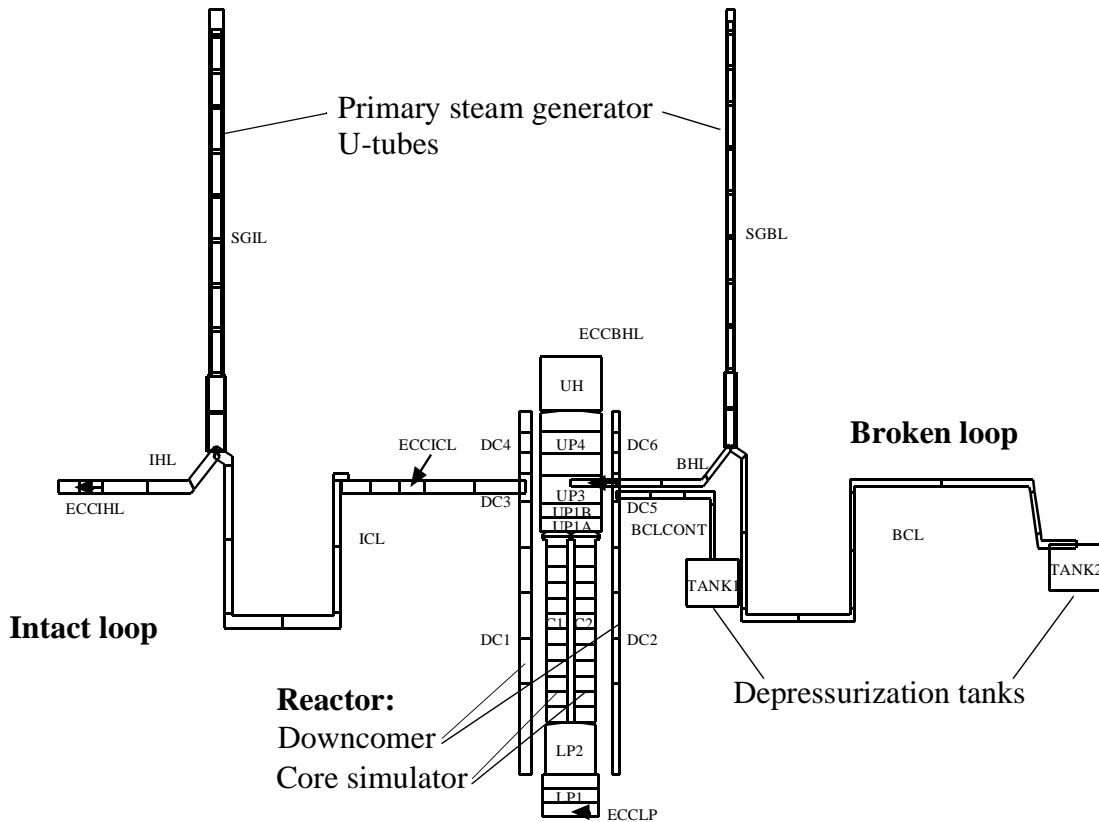
Fig. 2: Nodalization scheme of the CCTF test facility
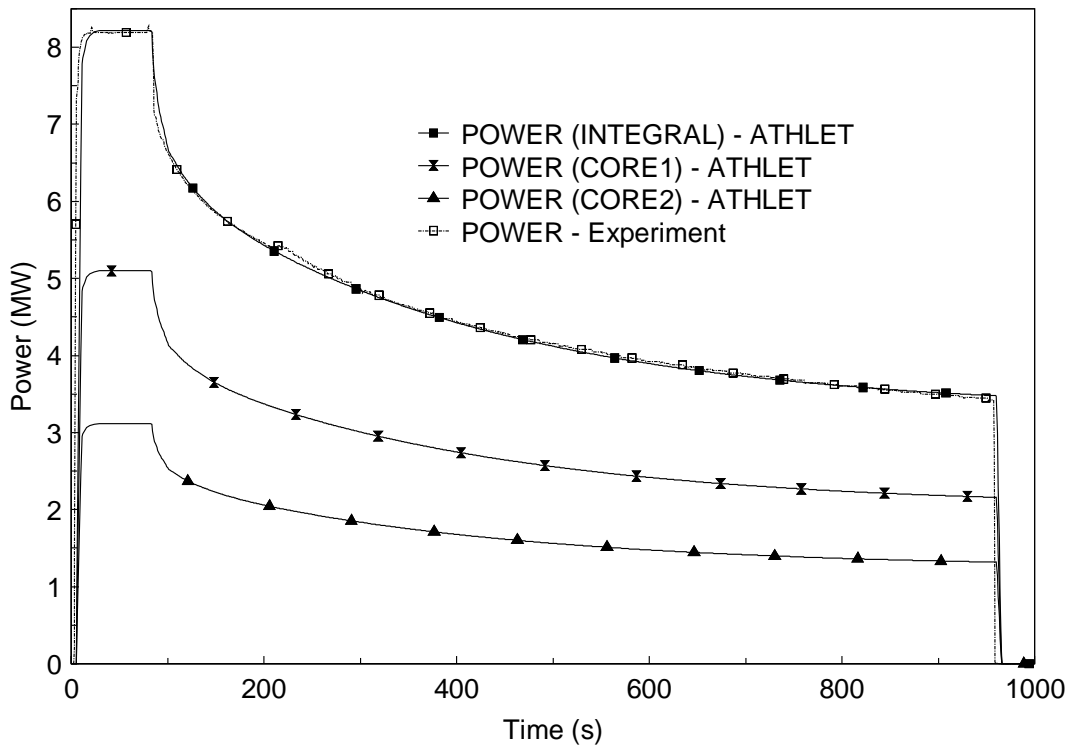
Fig. 3: Reactor power - experiment and calculation

4. Results of the ATHLET calculations

4.1 Experiment C2-19

The experiment C2-19 simulates a double ended break in the cold leg of a PWR with combined ECC injection into the hot and cold legs. With the start of the transient the reactor power is increased from zero to a specified decay heat level (Fig. 3). The initial pressure in the primary loops and in the containment tanks was 0.6 MPa and 0.3 MPa respectively. The lower plenum excepted, the test facility is filled with steam. The break valves between cold leg and containment are opened at t=83 s, simulating the end of the blowdown-phase of a large break loss of coolant accident. At the same time the power decay of the reactor is initiated. The ECC injection into the hot and cold legs is started at t=83 s and t=85 s respectively. The low pressure injection (LPIS) is initiated at t=174 s.

Fig. 4 shows the measured and calculated pressure in the lower and upper plenum of the reactor. The rising reactor power leads to a pressure increase up to t=83 s. After opening the break valves a fast depressurization of the primary system can be observed. Due to the high condensation rates at the ECC injection points, the pressure decrease is overestimated by ATHLET. In the calculation, the containment tanks are modelled with given pressure and enthalpy. Apart from the first 200 s the calculated primary pressure corresponds to the experimental results.

An important aspect is the behaviour of the quench front. In the case of a combined ECC injection, the development of the upper quench front will be delayed by the steam flow produced in the reactor core. The formation of the quench front can be observed by the course of the pressure difference in the reactor model. Fig. 5 shows the pressure difference between the lower plenum and the upper part of the reactor core. In comparison to the experiment, the calculated quench front formation is started with a delay of about 50 s. Due to the higher power in the central channel of the core (C1) the development of the upper quench front is delayed. In the periphery of the core (C2) the level rises faster. In the experiment and also in the calculation, the reactor level decreases after t=600 s. Up to the end of the transient the reactor level rises again. Due to the quench front formation, the rise of the cladding temperatures will be stopped (Fig. 6 and 7). Both measured and calculated cladding temperatures indicate, that the quench front develops faster in the lower part than in the upper part of the core. The core cooling from the upper plenum is impeded by the steam flow from the core towards the upper plenum. The measured and calculated temperatures show also the faster quench front formation in the periphery of the core. The calculated cladding temperatures show a good agreement with the experimental data.

4.2 Experiment C2-04

The experiment C2-04 simulates a double ended break in the cold leg of a PWR with ECC injection only into the cold leg. The initial pressure was 0.26 MPa in the primary system and 0.2 MPa in the containment. As in the previous experiment, at the start of the transient the reactor power is increased from zero to the specified level. The depressurization of the primary system starts at t=85 s by opening of the valves between broken cold leg and containment. At the same time the accumulator injection into the lower plenum is initiated. The power decrease starts at t=94 s and the accumulator injection into the cold legs is initiated at t=100 s. The LPIS is activated at t=120 s.
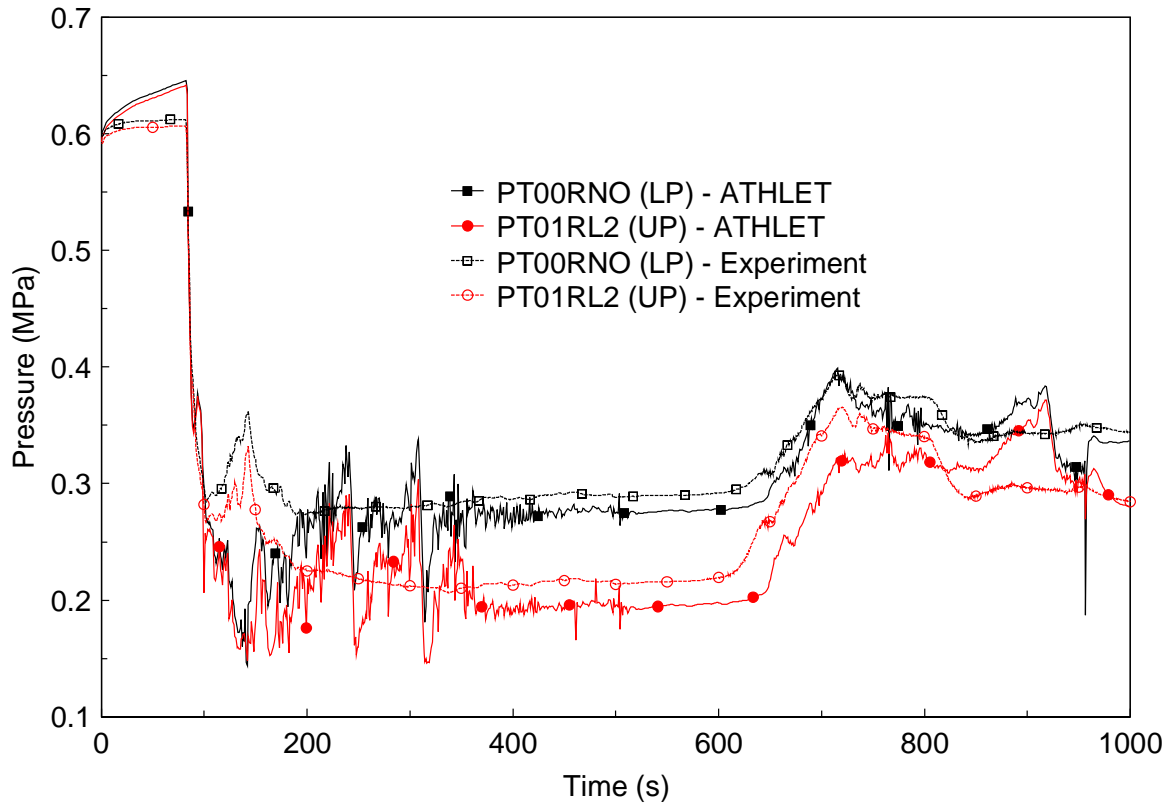
Fig. 4: Pressure in the reactor model (LP and UP)
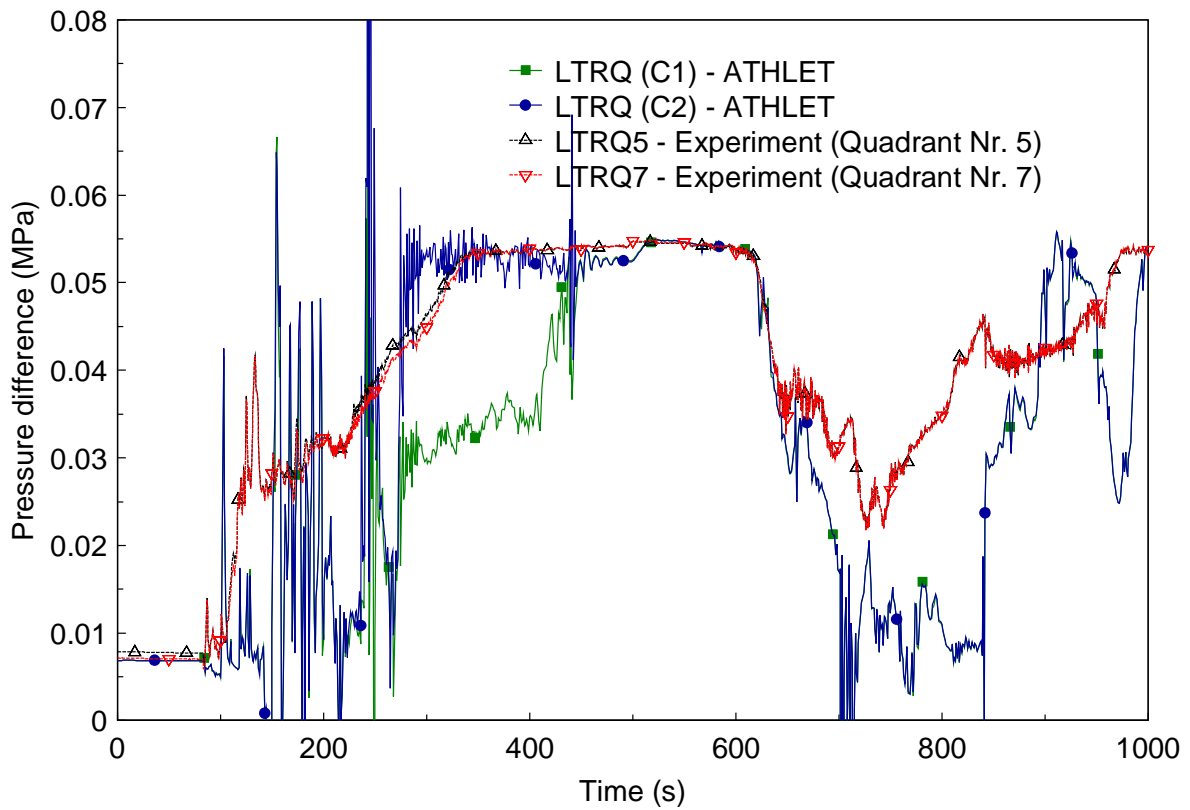
Fig. 5: Pressure difference between LP and UP (ATHLET - core channel C1 and C2)
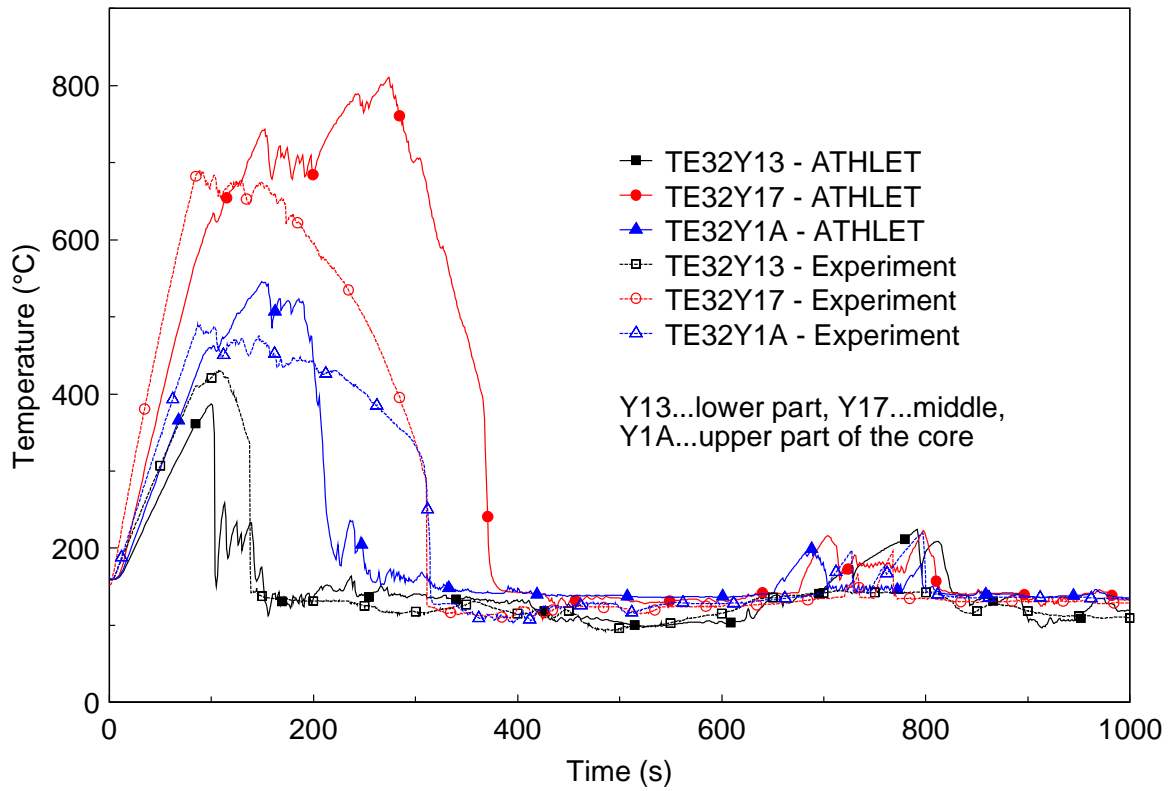
Fig. 6: Cladding temperatures in the reactor core (ATHLET - core channel C1)
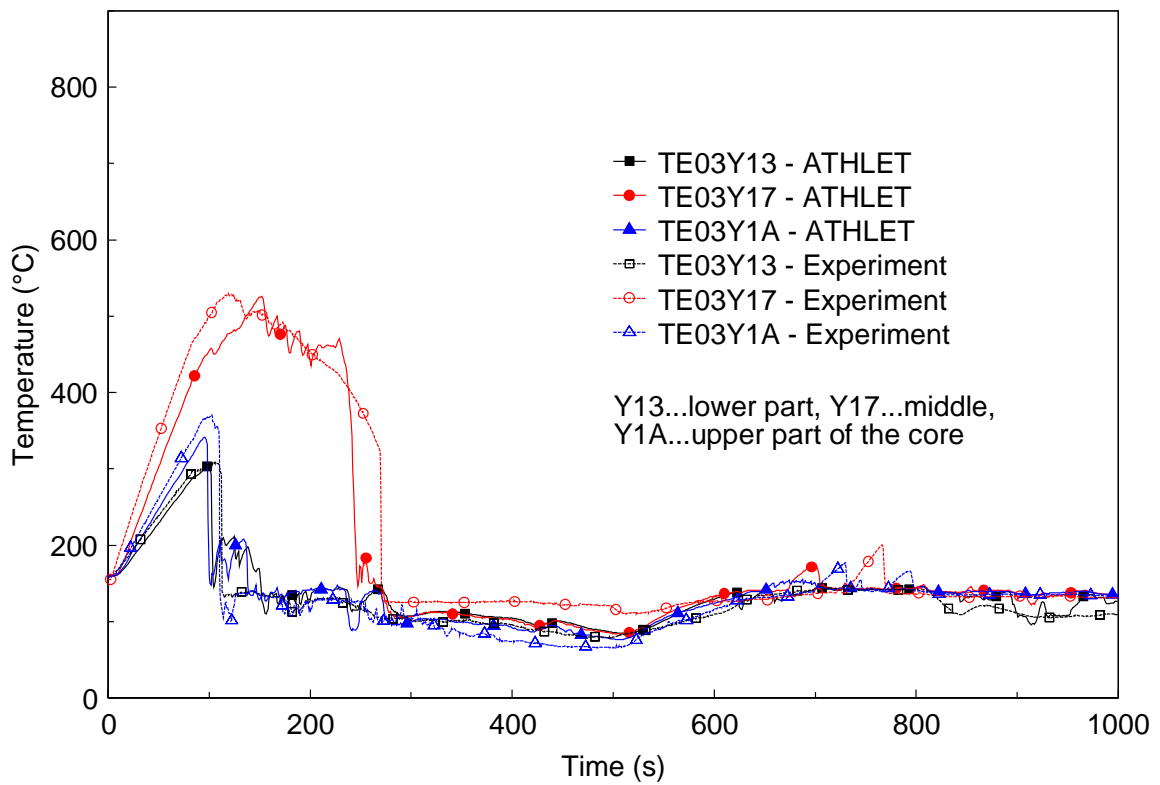
Fig. 7: Cladding temperatures in the reactor core (ATHLET - core channel C2)
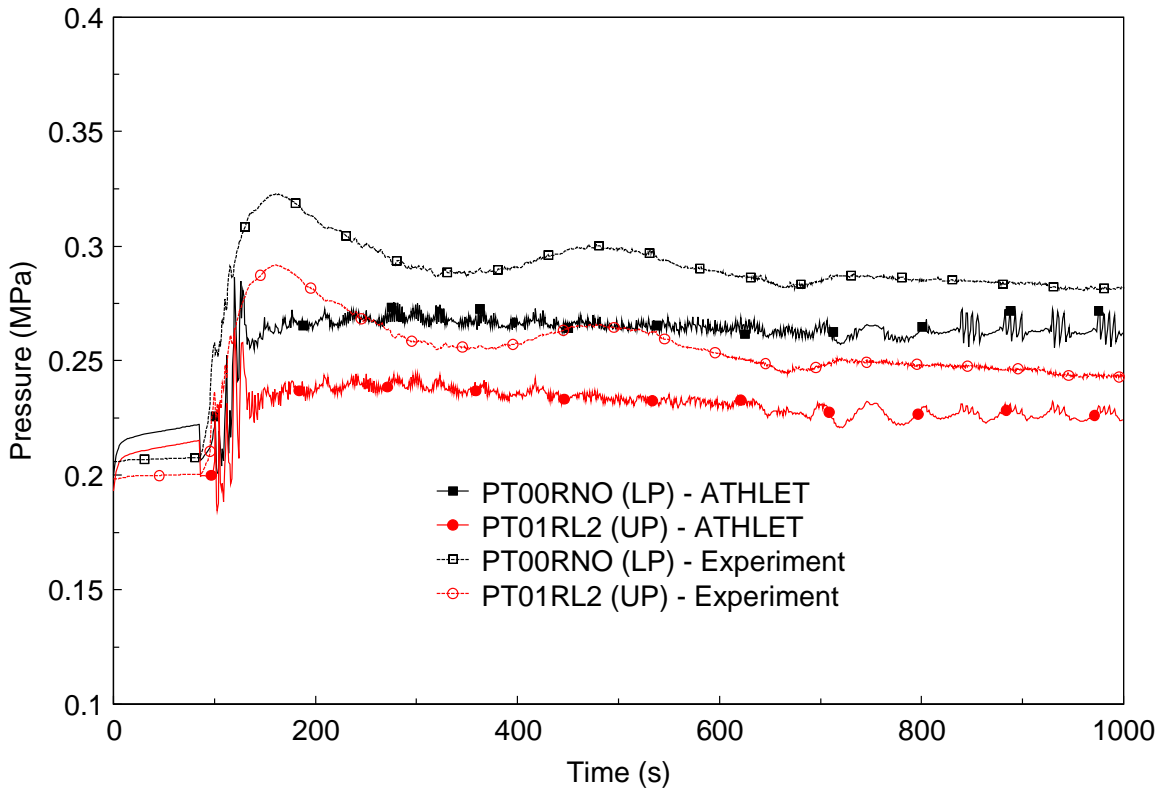
Fig. 8: Pressure in the reactor model (LP and UP)
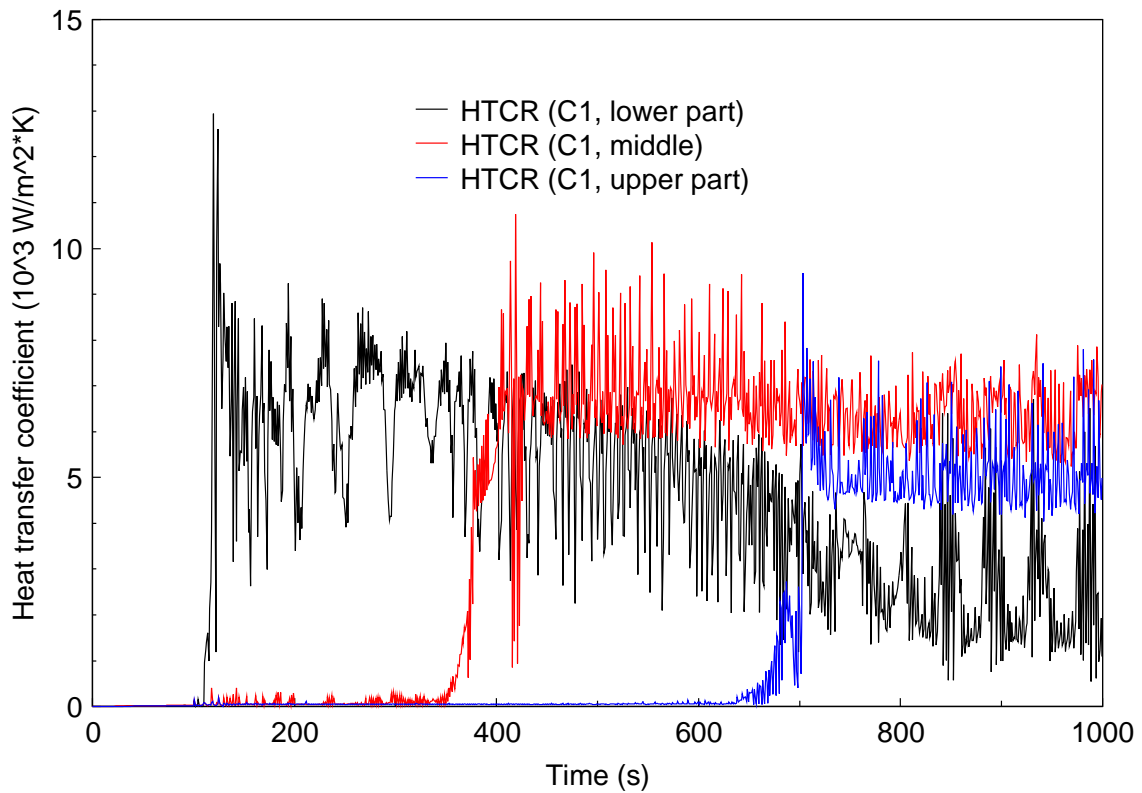
Fig. 9: Calculated heat transfer coefficients for the heater rods in the central channel (C1)

51
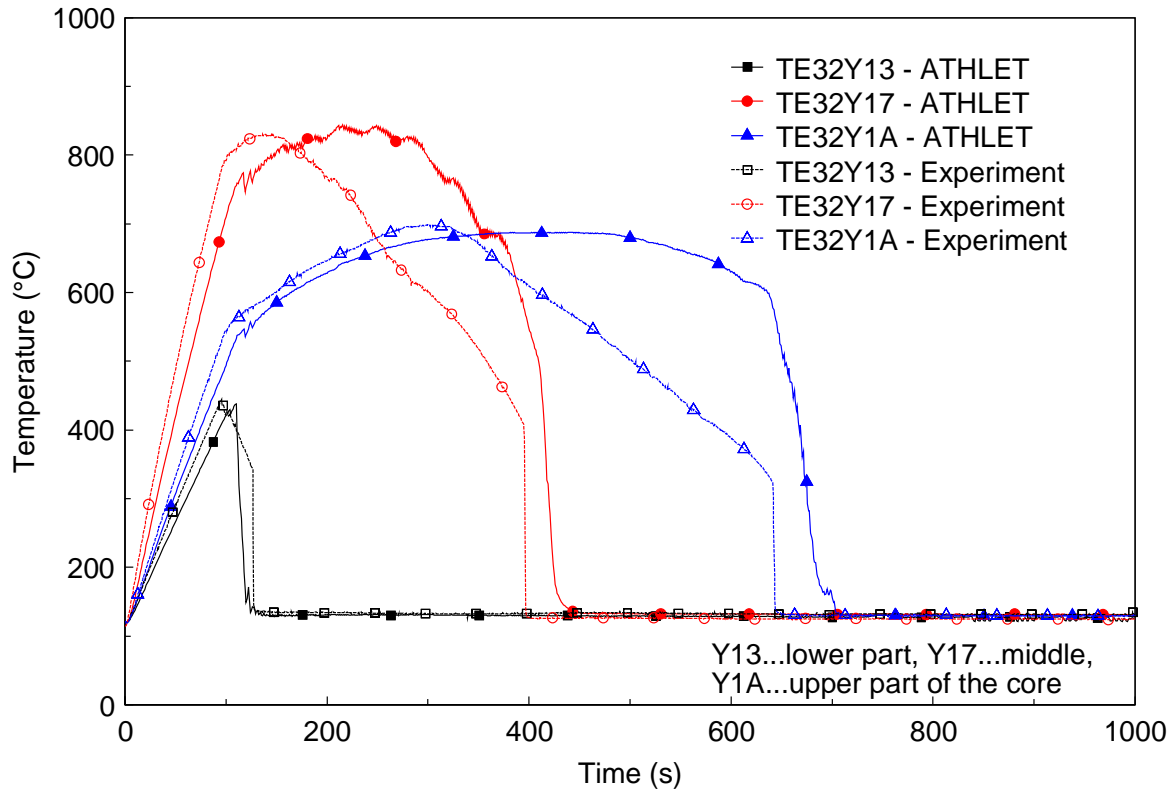
Fig. 10: Cladding temperatures in the reactor core (ATHLET - core channel C1)
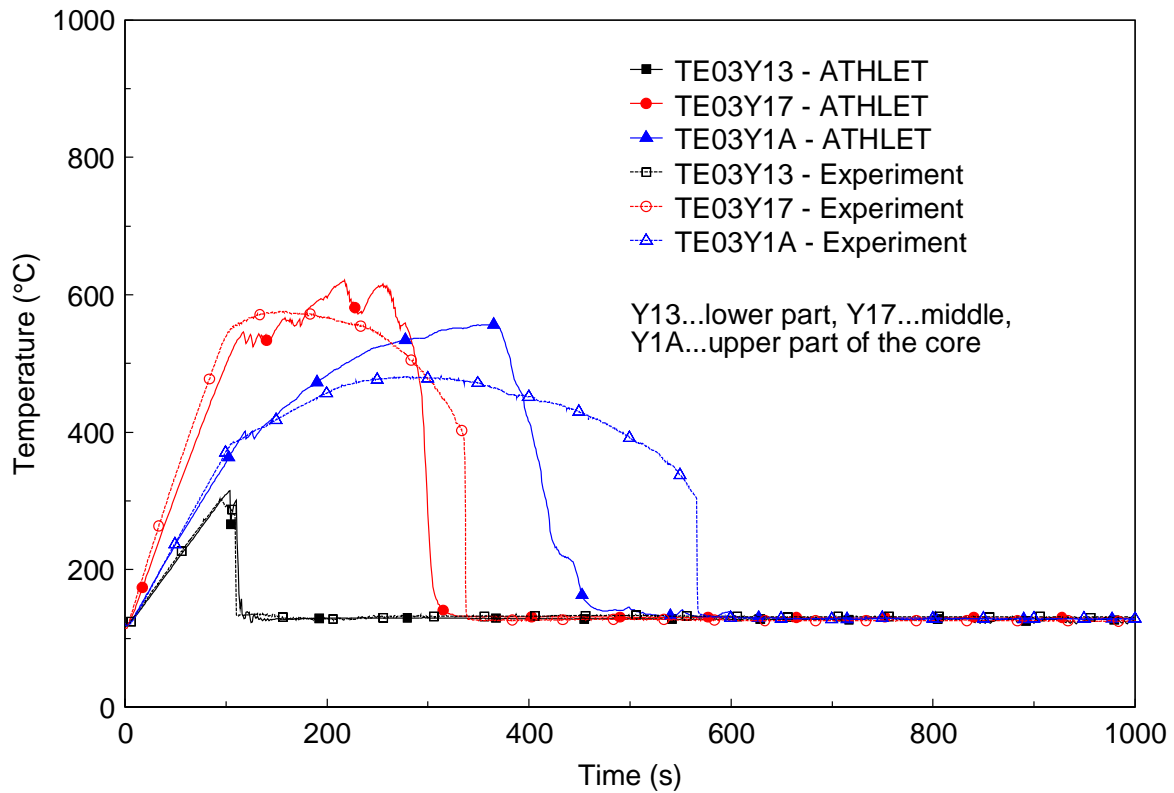
Fig. 11: Cladding temperatures in the reactor core (ATHLET - core channel C2)

Fig. 8 shows the measured and calculated pressure in the lower plenum and the upper plenum of the reactor. The calculated rise of the primary pressure up to t=85 s is caused by the power increase in the reactor core. After opening the break valves the primary pressure decreases and a pressure balance between primary system and containment is achieved. Afterwards the primary pressure rises very fast in the experiment. In comparison with the first experiment, where a pressure decrease was observed, the pressure increase is caused by the dominance of evaporation over the condensation. In the calculation, the primary pressure temporarily decreases. This deviation between calculation and experiment is caused by the overestimation of condensation rates in the cold legs in the calculation. In the further course of the transient, the calculated pressure is lower than in the experiment.

Due to the quench front development, the rise of the cladding temperatures will be stopped. In the case of the cold leg ECC injection, the quench front starts only from the lower plenum. The cladding temperatures for the central channel and the periphery are shown in Figs. 10 and 11. The measured and calculated temperatures for the lower part, the middle and the upper part of the core shows a good agreement with the experimental results. The quench front formation can be also observed from the behaviour of the heat transfer coefficients for the heater rods. The calculated heat transfer coefficients for the lower part, middle and upper part of the central core channel (C1) are presented in Fig. 9. The calculated results show that the core is filled from the bottom to the top.

5. Conclusions

The evaluation of the calculated results shows, that the main phenomena connected with strong thermodynamic non-equilibrium can be calculated in a good agreement with the experimental data. Especially the behaviour of the quench front and the core cooling are calculated very well.

The experimental results show, that the thermohydraulic behaviour in the core region is influenced by radial effects. An axial and also a radial power profile is simulated at the CCTF test facility. Radial effects can be observed especially in the experiment with combined ECC injection into the hot and cold legs. In this case the core cooling from the upper plenum is impeded by the steam flow from the core towards the upper plenum being higher in the centre of the core. The different behaviour of the quench front formation for the central region and the periphery of the core can be successful modelled with the applied two-channel representation.

Deviations from the experiment can be observed in the beginning of the transients. The injection of cold water into the hot and cold legs filled with pure steam leads to high condensation rates. The pressure decrease in this phase of the transients is overestimated by ATHLET.

References

[1] Data Report on Large Scale Reflood Test-82, CCTF CORE-II Test C2-4 (Run 62), JAERI - memo - 59 - 450, Februar 1985
[2] Data Report on Large Scale Reflood Test-128, CCTF CORE-II Test C2-19 (Run 79) JAERI - memo - 63 - 081, March 1988
[3] G. Lerchl, H. Austregesilo, ATHLET Mod 1.2 Cycle C: User's Manual, Gesellschaft für Anlagen und Reaktorsicherheit (GRS) mbH, November 2000

COMPARATIVE ASSESSMENT OF CONDENSATION MODELS FOR HORIZONTAL TUBES

Andreas Schaffrath, Anne-Kathrin Krüssenberg, Ulrike Gocht[1] and Andrej Fjodorow[1]

1. Introduction

The condensation in horizontal tubes plays an important role for the prediction of the operation mode of horizontal steam generators of VVER reactors or passive safety systems for the next generation of nuclear power plants. Two approaches (KONWAR and HOTKON) for modeling this process have been applied by Forschungszentrum Jülich (FZJ) and University for Applied Sciences Zittau/Görlitz (HTWS) and were implemented into the 1D-thermohydraulic code ATHLET, which is developed by the Gesellschaft für Anlagen- und Reaktorsicherheit (GRS) mbH for the analysis of LOCA and transients in light water reactors [1].

Although the improvements of the condensation models are developed for different applications (VVER steam generators, SWR1000 emergency condenser) with strongly different operation conditions (HORUS: max. temperature difference 30 K, max. mass flow 0.025 kg/s, max. steam velocity 5 m/s, stratified counter-current gas-liquid flow, NOKO: max. temperature difference 260 K, max. mass flow 0.75 kg/s, max. steam velocity 35 m/s, annular, stratified, bubble, slug and plug counter-current gas-liquid flow) both models are now compared and assessed by Forschungszentrum Rossendorf FZR e.V. For that, post test calculations of four selected HORUS (<u>hor</u>izontal <u>u</u>-tube <u>s</u>team generator) experiments were performed with ATHLET/KONWAR and compared with existing ATHLET and ATHLET/HOTKON calculations of HTWS.

2. Horus test facility

The HORUS II test facility was designed for the investigation of small break loss of coolant accidents (SBLOCA) in VVER reactors [2]. The crucial component of the separate effect test facility is the single steam generator tube (length L = 9.2 m, outer diameter D = 16 mm, wall thickness s = 1.5 mm) which is arranged in a tank (length L = 4.62 m, outer diameter D = 219.1 mm, wall thickness s = 8.2 mm). The tube is fabricated of the original stainless steel material (X8 CrNiTi 18 10). The design of the test facility allows to adjust the same initial and boundary conditions as during a SBLOCA (primary side pressure up to 8 MPa, secondary side pressure up to 6.4 MPa and primary and secondary side temperatures up to 300 °C). The tube is coupled with collectors at the beginning and the end. These collectors are used for the connection to the necessary support systems (e.g. the steam supply, the venting or the non-condensable injection system) and are volumetrically scaled in 1:1400. They agree in principle with the original collectors, but they serve essentially as separators. The HORUS II facility is densly equipped with measuring transducers for the acquisition of the thermohydraulic process parameters such as pressure, temperatures, water level at the primary and secondary side.

---

[1] University of Applied Science Zittau/Görlitz

3. Comparison of the condensation model improvements

The condensation model of the original version of ATHLET was developed for the calculation of heat transfer coefficients (HTC) in vertical tubes. The condensation process is characterized by symmetrical condensate films with an equal layer thickness over the cross section area. The HTC are calculated by the correlations of Chen [3], Nusselt [4], or Carpenter and Colburn [5], or a minimum of 20 W/(m²K). The maximum of these values is used in the further calculation.

Inlet Collector

Test Tube
(L = 9.2 m; D = 16 mm;
s = 1.5 mm)

Outlet
Collector

Pressure Vessel
(L = 4.62 m; D = 219.1 mm;
s = 8.2 mm)

Throttle Valve

Condensate Outlet

Reactor Simulator
(h = 3 m; D = 0.32 m)

Electrical Heater
(max. 150 kW)
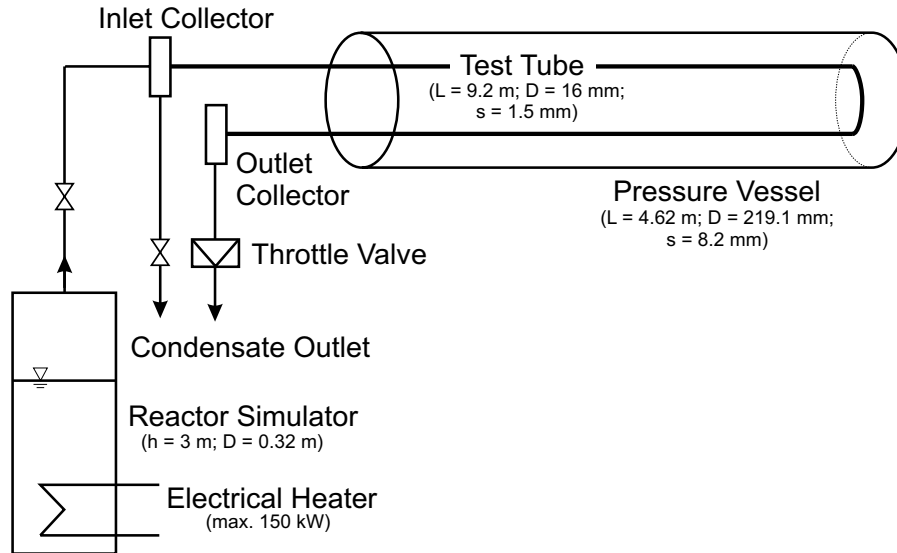
Fig. 1: Flow diagram of the HORUS test facility.

The condensation process in horizontal tubes is much more complicated than in vertical tubes. Over the tube length different flow regimes (e.g. spray, plug, slug, bubble and stratified flow) may occur (see fig. 2). Vapor enters the tube with a relatively high velocity and annular flow establishes with nearly equal condensate layer thickness in the cross section area. During the condensation the steam velocity decreases down to the liquid velocity. At moderate steam velocities the condensate collects at the bottom. It is assumed that film condensation takes place at the upper part of the tube cross section area. The condensate film is very thin and drains down driven by gravity forces. The stratified condensate layer in the tube sump flows along the bottom of the tube, often ripples or waves are generated at the phase surface [6]. To describe these complicated processes the condensation model in ATHLET had to be improved. Two different approaches, HOTKON and KONWAR, have been developed. In the four HORUS tests which are selected by HTWS for post test calculations, stratified flow is expected to occur along the whole tube. Therefore, in the following the attention is focussed on the calculation of the HTC during the stratified flow regime.

HOTKON [6] is based on Huhn's general film flow theory [7] with respect to filmwise condensation. Here the field equations governing the mass, energy and momentum transfer between the liquid and the vapor phases are simplified using the thin film approximation by taking into account

- the effects of frictional shear stresses (as a result of friction between the vapor bulk and the condensate film as well as between the vapor bulk and the droplets entrained from the condensate film),

- the gravity forces acting upon the condensate,

- the development of the stratified angle β (see Fig. 2) associated with the accumulated condensate layer at the bottom of the tube,

- the liquid volume fraction existing as droplets in the vapor region of the two-phase flow.

The influence of these parameters is evaluated with respect to the heat transfer at the condensate film inside horizontal tubes for both laminar and turbulent water and vapor flow. A solution for condensation may be obtained solving the momentum and energy equation using the similarity concept.
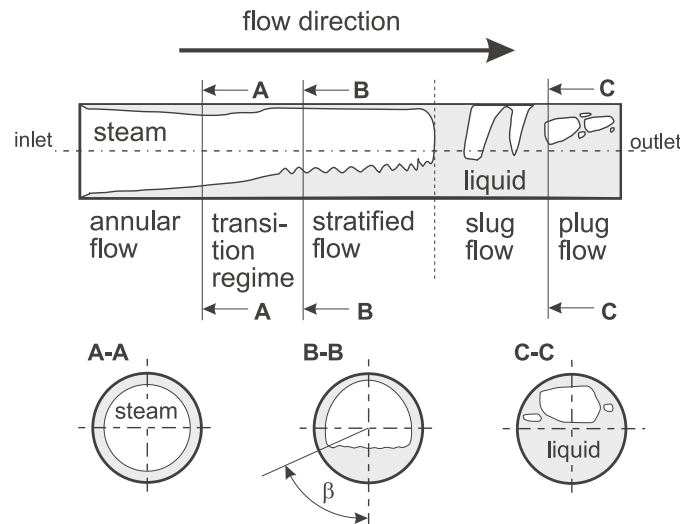
Fig. 2: Flow regimes during condensation in horizontal tubes [6]

The heat transfer coefficient for laminar stratified flow is determined by the modified Nusselt model [7], which takes into account the decrease of the heat transfer surface due to the collection of condensate in the tube sump. The heat transfer coefficient for this case is calculated by

$$\alpha_{ls} = C \left(\frac{\rho_L (\rho_L - \rho_V)\, g\ r\ \lambda}{\eta\ D\, (T_S - T_W)} \right)^{0.25}$$

with respect to the peripheral angle β of the condensate layer in the tube (Fig. 2), which can be determined from the local void fraction ε. In HOTKON the value for C = 0.296 is taken over from Russian reactor safety experiments in original VVER steam generators [8], which means C is averaged over the tube length.

KONWAR [9] was developed by FZJ for the investigation of the operation mode of the emergency condenser of the SWR1000. KONWAR uses the flow regime map of Tandon for the determination of the actual flow regime and switches to flow regime dependent semi-empirical correlations for the calculation of the HTC (spray flow: Soliman, laminar annular flow: Nusselt, turbulent annular flow: Kosky and Staub, stratified flow: Rufer and Kezios, bubble, slug and plug flow: Breber - all models were described in detail in [9]).

Both improvements HOTKON and KONWAR use the same (modified Nusselt) model, for the calculation of the HTC. They differ in the choice of the sump coefficient. A review of sump coefficients is e.g. presented by Shah [10]. The author shows that the condensation rate decreases with increasing L/D ratio and upward inclination of the tube, in tubes with downward inclination the heat transfer coefficient increases.

The different geometry parameters and flow conditions in the HORUS and the NOKO tubes are considered by choosing different sump coefficients in HOTKON and KONWAR. In HORUS, the steam generator tube is arranged exactly horizontal: the L/D ratio is about 700 and condensate and steam are flowing first in co-current and after the filling of the outlet collector in counter current direction. In this second phase the thickness of the condensate film is maximum at the end of the tube. In NOKO, the tubes are arranged with an inclination of 1.6° in the upper and 3.2° in the lower leg and includes a 180° bend in the middle. The L/D ratio is about 250 and the condensate sump thickness increases along the tube length. Both, steam and condensate flow into the same direction.

Because the sump coefficient in HOTKON describes exactly the conditions inside the VVER steam generator tubes and was derived from experiments in original geometries and with typical initial and boundary conditions [8], this coefficient was taken over to KONWAR for this case, too. Therefore, the results of the post test calculations with ATHLET/HOTKON and ATHLET/KONWAR are expected to be very similar.

4. Post test calculations

Four HORUS tests (PCHS23, PCHS25, PCHS30, PCHS36) were selected by HTWS for post test calculation with ATHLET/KONWAR. The results of these calculations are compared to the experimental data and calculations with the original version of ATHLET, and ATHLET/HOTKON [6]. To avoid user-influence the same input decks were used for all calculations.

In the following, the results of the calculations of the test PCHS30 are presented and discussed in detail. The test run PCHS30 simulates the fourth phase of a small break loss of coolant accident with a cold leg loop seal, which is characterized by the following conditions:

- the water level in the reactor pressure vessel lies under the hot leg connection,
- at least one hot leg loop seal is cleared

and

- the heat removal out of the core is realized by steam condensation in one or more steam generators.
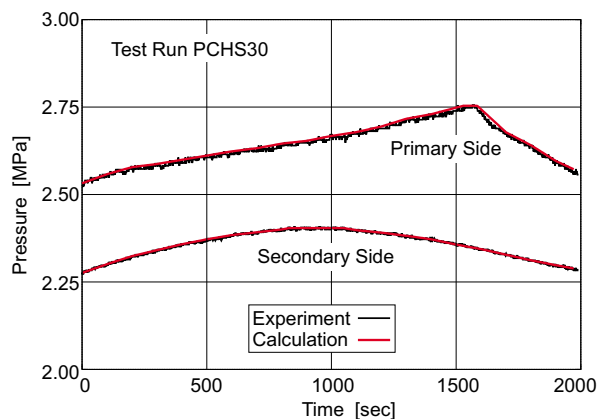
Fig. 3: Primary and secondary side pressure boundary condition
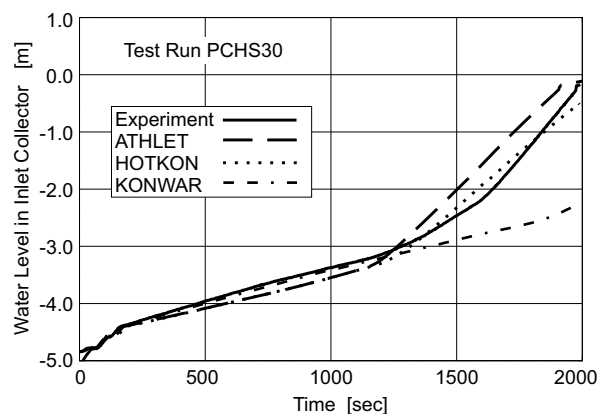
Fig. 4: Water level in the inlet collector

Therefore the experiment is performed with a closed throttle valve at the outlet collector (see fig. 1). The adjusting steam flow conditions are only caused by the condensation rate, which depends on the driving temperature differences between the primary and secondary side of the tube. The following initial conditions are adjusted: primary side pressure 2.53 MPa, primary side temperature 224.8 °C, secondary side pressure 2.28 MPa.
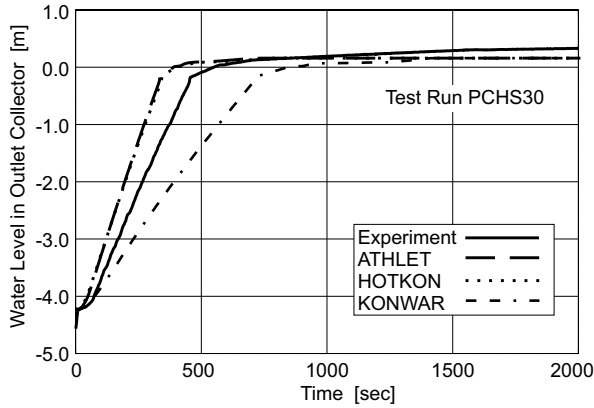
Fig. 5: Water level in the outlet collector.
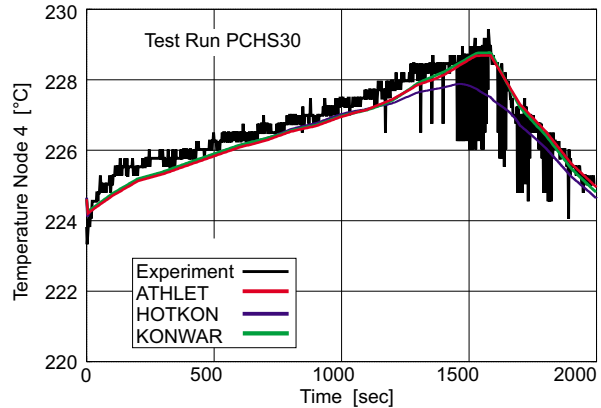
Fig. 6: Fluid temperature in node 4

The records of the primary and secondary side pressure are shown in fig. 3. The power in the reactor simulator is constant during the first 1590 seconds. Because the steam generation dominates over the condensation the pressure increases. After switching off the electrical heater the pressure decreases. For a better condensation model comparison it was decided to adjust the pressure boundary conditions via time dependent volumes.

Fig. 4 and 5 show the water levels inside the inlet and outlet collector. It can be seen that the calculations with the improved versions of the condensation model agree significantly better with the experimental data than the calculation with the original condensation model. The condensate flows forward and accumulates in the outlet collector in the first time period. After approx. 500 seconds the outlet collector is totally filled with water and the condensate collects in the tube. The tube is filled from the outlet to the inlet collector. The condensate reaches the inlet collector at 1300 seconds.
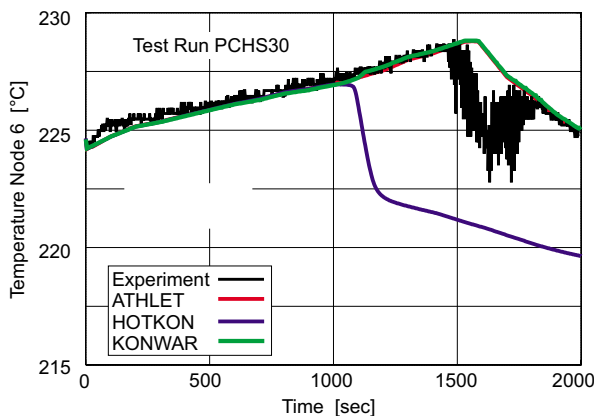
Fig. 7: Fluid temperature in node 6
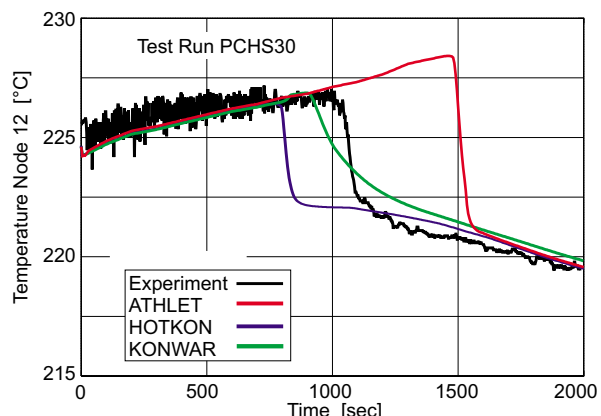
Fig. 8: Fluid temperature in node 12

This is indicated by a significant increase of the inlet collector water level. The slow increase of the water level in the inlet collector during the first 1300 seconds can be explained with the collection of condensate from the steam feed line, which connects the reactor simulator and the

inlet collector. The water level of both collectors shows a better agreement with the experimental data than the calculation with the original ATHLET version, although the improved ATHLET versions overestimate the condensate accumulation in the outlet collector moderately.

Figure 6 - 9 show the fluid temperatures inside the HORUS tube. As discussed above, the tube is filled with condensate from the end to the outlet to the inlet collector. The HORUS tube is divided into 19 control volumes, each about 0.5 m long. At the beginning and the end two control volumes with half length are located. The indices of the control volumes increase from the inlet to the outlet collector. This nodalization is adapted to the arrangement of the thermocouples. At the beginning, the HORUS tube is totally filled with steam and the readings of the thermocouples show saturation temperature. After the nodes are filled with water, the temperatures decrease. The figures confirm, that both improved versions of ATHLET meet - with exception of node 6 - the time points, when a temperature decrease indicates the filling with condensate, better than the original version of ATHLET. It can be seen that the nodes with higher indices, that means the nodes at the end of the tube, are filled earlier. The comparison of the calculated data of the two improved versions of ATHLET show a slight overestimation of the condensate temperatures (reading of the thermocouples after temperature decrease). This is an effect of the modified Nusselt model. During stratified flow, film condensation takes place in the upper part of the tube, while in the sump the condensate flows along the bottom. The water in the sump is slowly cooled down by convective heat transfer. The efficiency of the condensation heat transfer is much higher than the efficiency of the convection heat transfer. Therefore, this convective heat transfer is neglected in HOTKON and KONWAR.
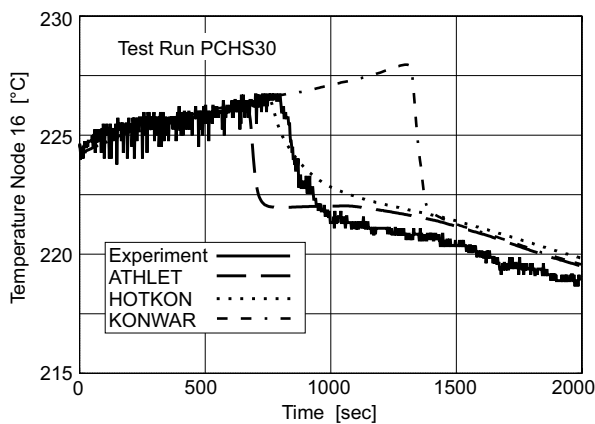
Fig. 9: Fluid temperature in node 16   Fig. 10: Removable Power
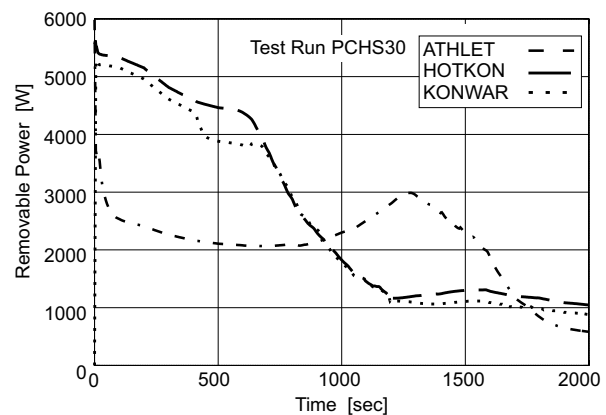
At last in fig. 10 the resulting calculated removable power of the condenser tube is compared. As expected the calculations with the improved condensation models agree very well and are almost two times higher than the calculation with the original condensation model. Therefore both collectors are filled earlier. After filling of the HORUS tube with condensate the tube surface is covered with water and the removable power of the tube decreases strongly.

5. Conclusion and outlook

Two different approaches for modeling the condensation in horizontal tubes - HOTKON by University for Applied Sciences Zittau (HTWS) and KONWAR by Forschungszentrum Jülich (FZJ) - have been implemented into the 1D-thermohydraulic code ATHLET. These models

were originally developed for post test calculations of the HORUS and NOKO experiments, which differ extremely concerning the operation conditions. The aim of the performed investigation was to broaden the scope of the condensation model improvement KONWAR and to check the applicability to post test calculations of HORUS experiments. Therefore, four HORUS experiments were calculated with ATHLET/KONWAR, and the results were compared with the experiments and the calculations with the original version of ATHLET and ATHLET/HOTKON, respectively. To avoid a user-influence exactly the same input decks were used for all calculations.

The post test calculations of the selected HORUS experiments show that the calculations with the improved condensation models are capable of performing proper calculations. The results of the calculations with the improved condensation models are very similar. During these experiments stratified flow occurs inside the tubes and both condensation model improvements use the same (modified Nusselt) model for the determination of the HTC in this flow regime. This model takes into account the decrease of the heat transfer surface, due to the collection of condensate in the tube sump. The HTC calculated by the Nusselt model has to be multiplied with an empirical sump coefficient. The value of this coefficient depends on several geometric values (inclination of the tube, length/diameter ratio) and flow conditions (co- or counter-cur-rent flow of steam and condensate). Therefore, it has to be fitted to the concrete application. A further generalization, that means a model without any empirical coefficients which allows calculations of arbitrary geometrical configuration, requires a mechanistic model for the modeling of the sump influence. That's why new and well equipped condensation experiments with high time and spatial resolution measurements of local parameters are needed.

References

[1]   G. Lerchl, H. Austregesilo (1995), ATHLET Mod. 1.1 Cycle C - User's Manual, Gesellschaft für Anlagen- und Reaktorsicherheit (GRS) mbH, GRS-P-1, Vol. 1, Oktober 1995

[2]   S. Alt, W. Lischke (1997), Experiments with the HORUS-II Facility, Proceedings of the Fourth International Seminar on Horizontal Steam Generators, 11-13 March, Lappeenranta, Finnland.

[3]   J.C. Chen (1966), Correlation for Boiling Heat Transfer to Satured Fluids in Convective Flow, Ind. Eng. Chem. Proc. Des. Dev. 5, 322

[4]   W. Nusselt (1916), Oberflächenkondensation des Wasserdampfes, Zeitschrift des Vereins Deutscher Ingenieure 27, 541 and 569

[5]   E. F. Carpenter, A. P. Colburn, (1951), The Effect of Vapor Velocity on Condensation Inside Tubes, Proceedings of the General Discussion of Heat Transfer, Inst. Mech. Eng., 20

[6]   A. Fjodorow, W. Lischke (1998), Modell zur Berechnung von Wärmeübergangskoeffizienten bei der Kondensation in horizontalen Rohren für den ATHLET-Code, Zittau, IPM-610205-04

[7]   J. Huhn (1983), Eine allgemeine Theorie der Filmströmung und ihre Anwendung, Dissertation Technische Universität Dresden

[8]   J. N. Kusnezow (1989), Teploobmen i Probleme Besopasnosti Jadernych Reaktorow, Energoatomisdat, Moskau

[9]   A. Schaffrath (1997), KONWAR - eine Erweiterung von ATHLET zur Berechnung der Kondensation in waagerechten Rohren, Jülich, Jül-3343

[10]   M. M. Shah (1979), A General Correlation for Heat Transfer during Film Condensation Inside Pipes, Int. J. Heat Mass Transfer 22, 547

VALIDATION OF COUPLED NEUTRON-KINETIC / THERMAL-HYDRAULIC CODES FOR VVER-TYPE REACTORS

Siegfried Mittag, Sören Kliem, Frank-Peter Weiss, Riitta Kyrki-Rajamäki [1], Anitta Hämäläinen [1], Siegfried Langenbuch [2], Serge Danilin [3], Jan Hadek [4], György Hegyi [5], Alexander Kuchin [6] and Dobromir Panayotov [7]

1. Introduction

Three-dimensional neutron-kinetic core models have been coupled to advanced thermal-hydraulic system codes. These coupled codes can be used for the analysis of the whole reactor system, since they are capable of estimating the feedback effects in a consistent manner. Such code systems have been developed also for modelling transients in Russian VVER-type reactors. The stand-alone neutronic codes, including their nuclear databases, have already been validated e. g. by using data from experiments in critical facilities and zero-power reactors, in which thermal-hydraulic feedback on neutron kinetics cannot be observed. The thermal-hydraulic system codes have also been separately validated against a lot of experiments in thermal-hydraulic test facilities. The interaction between the neutronic effects of the reactor core and the thermal-hydraulic behaviour of the plant cannot be measured in these experimental facilities, but only in nuclear power plants. Hence in a project within the European Commission's Phare programme (SRR1/95), five well-documented VVER transients were made available; two of them have been chosen for the code validation [1,2]. The measured VVER data as well as the validation of the burn-up and steady-state versions of the neutronic codes involved have been described in the Annual Report 1998 [3].

2. Codes

The coupled neutron-kinetic / thermal-hydraulic codes listed below have been validated against measured VVER-440 and VVER-1000 transients. The nuclear data libraries applied in the calculations have been generated by the codes given in parentheses.

- VTT $\Rightarrow$ HEXTRAN/SMABRE [4,5] (VVER-1000: CASMO-4)
  (VVER-440: CASMO-HEX)
- KI $\Rightarrow$ BIPR8/ATHLET [6,7] (KASSETA)
- FZR $\Rightarrow$ DYN3D/ATHLET [8] (VVER-1000: NESSEL)
  (VVER-440: KASSETA)
- INRNE $\Rightarrow$ DYN3D/ATHLET (NESSEL)
- STCNRS $\Rightarrow$ DYN3D/ATHLET (NESSEL)
- NRI $\Rightarrow$ DYN3D/ATHLET (KASSETA)
- AEKI $\Rightarrow$ KIKO3D/ATHLET [9] (KARATE)

[1] VTT Energy/Nuclear Energy, Finland
[2] GRS, Gesellschaft für Anlagen- und Reaktorsicherheit mbH
[3] KI - Russian Research Center "Kurchatov Institute"
[4] NRI Nuclear Research Institute Rez, Czech Republic
[5] AEKI - KFKI Atomic Energy Research Institute, Hungary
[6] STCNRS - Scientific & Technical Centre on Nuclear and Radiation Safety, Ukraine
[7] INRNE - Institute of Nuclear Research and Nuclear Energy, Bulgaria

3. Analysis of a VVER-1000 transient measured in Balakovo-4 (Russia)

The initiating event for the transient was the switching-off of one of the two working steam generator feed water pumps at full power. Two seconds after the pump failure, the power control system responded by inserting the first control rod group from core top to bottom within four seconds. As a result, the neutron power decreased to about 63% of the nominal value within 10 seconds. After that, group No. 10 started moving in at the rate of 2 cm/s. The slow insertion of this group resulted in an additional power decrease to about 45%. The differences between the temperatures of the hot legs and the corresponding cold legs of the four primary circuit loops decreased proportionally to the thermal power reduction, as all four pumps continued working. In the secondary circuit, where the transient had been initiated, the flow rate through the second feed water pump that was still in operation, was increased by some 50% within 16 seconds after the failure of the first pump, in order to partly compensate the deficient feed water flow. In the following, the flow rate of the second pump was reduced again to match the decreasing thermal power of the primary circuit. During the whole transient, the water level in the steam generators was kept well above the heat exchanger tubes.

In the transient analysis, the control rod group positions as functions of time were provided as input to all calculations. Fig. 1 (upper part) depicts the positions of the control rod group 10. The measured pressure in the main steam header (MSH), shown in the lower part of Fig. 1 was also applied as a boundary condition, except for the VTT calculations (SMABRE), where the secondary circuit was modelled in more detail. The average cold leg temperature as well as the calculated and measured reactor power are shown in Fig. 2. The power is controlled for the most part by the control rod movements, but there is also an effect of fuel and coolant temperature on reactivity and power. The coolant temperature decreases with falling power, but it is influenced by the pressure in the secondary circuit, too. A rising steam header pressure means an increasing saturation temperature, which leads to a decreasing heat transfer in the steam generator. The result is a rising cold leg temperature, and vice versa.

In the first seconds of the transient, the power decreases very fast as a result of dropping the first control rod group. The minimum is reached at t = 6 s, when the group is fully inserted. The power rise observed in the next few seconds, is mainly caused by the fuel temperature which continues falling after the end of the rod drop (Doppler effect). The respective measured power growth is about 200 MW. The calculated values are between 190 and 300 MW. The deviations between the calculations are caused by different temperature dependencies of the nuclear cross sections and different assumptions on the thermal properties of the fuel rods. Detailed investigations have shown that the change of the heat transfer coefficient (HTC) in the gas gap between fuel pellets and rod cladding during the transient is relevant. With dropping fuel temperatures, the gap width increases, which leads to a decreasing HTC. This reduces the fuel temperature decrease. Comparing the results of DYN3D/ATHLET calculations with constant and changing HTC in the gap [10], performed by FZR, has shown that the difference in the power level of the final state (caused by this effect) is about 150 MW.

In the time interval between t = 10 s and t = 60 s, the power is mainly controlled by constantly inserting control rod group No. 10. However, the cold leg temperature decrease between 10 s and 20 s (FZR, INRNE, KI, STCNRS) causes a reactivity increase (moderator density feedback), which for the most part compensates the reactivity effect of group 10, so that the power does not drop much in this short interval. The different modelling of the
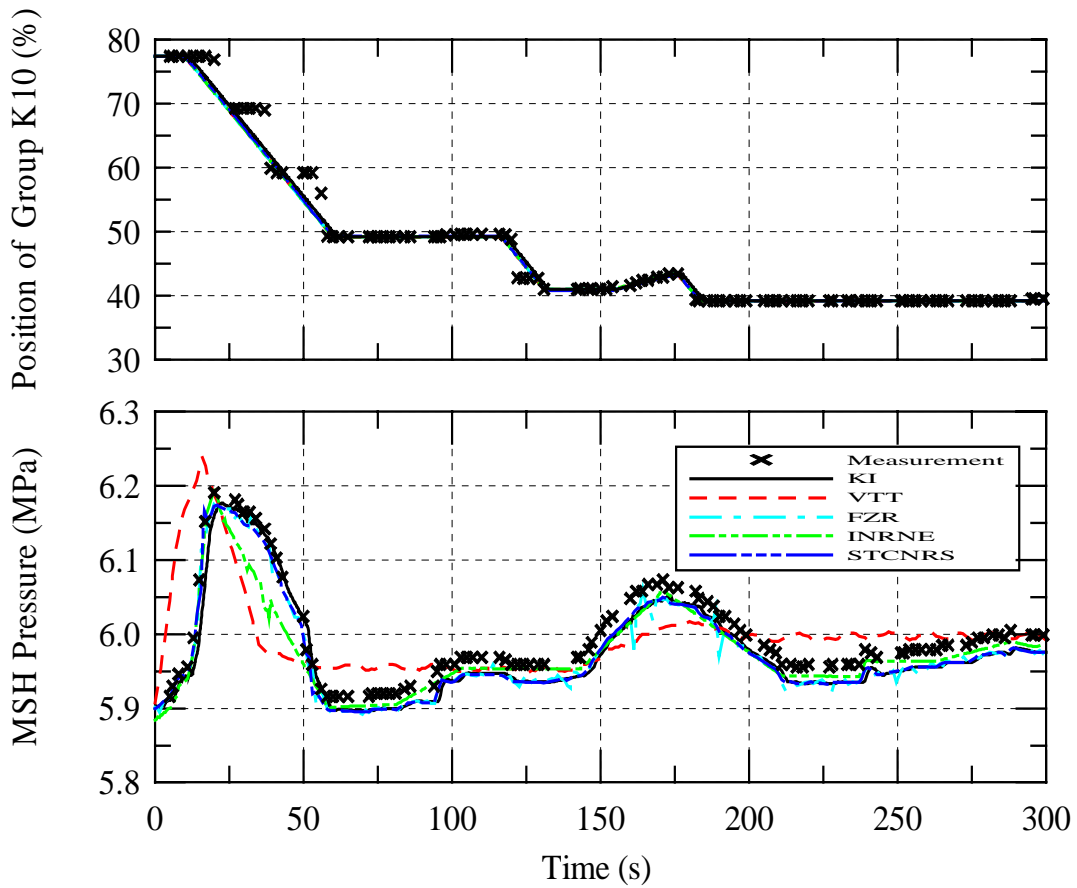
Fig. 1: Position of control rod group 10 and main steam header pressure
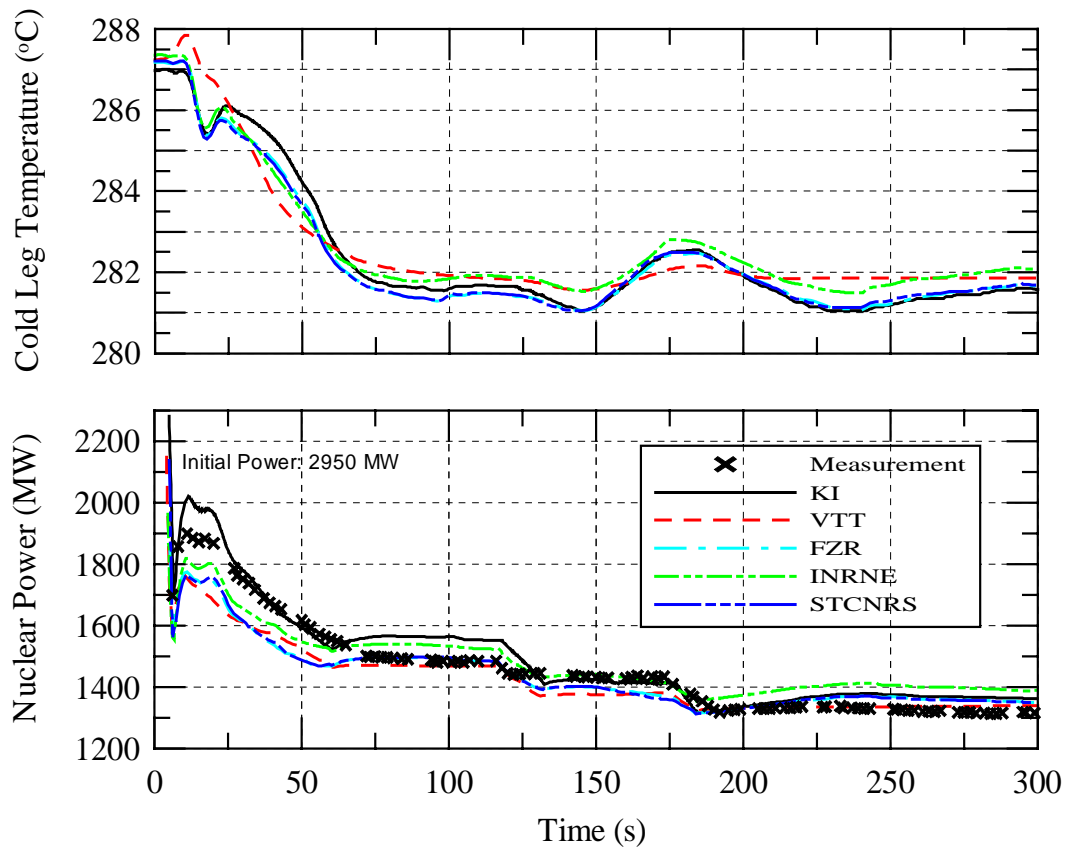
Fig. 2: Cold leg temperature and nuclear power

secondary circuit by VTT leads to some deviation from the cold leg temperature and power curves calculated by the other participants.

After stopping the insertion of group 10 at t = 60 s, power and temperatures are stabilised. Due to the much slower rod motion, the power increase resulting from the reduced fuel temperatures is significantly lower than that observed after dropping group 1. At t = 100 s, the calculated power values are between 1470 MW and 1550 MW. The measured value amounts to 1480 MW.

In the time between t = 115 s and t = 130 s the control rod group No. 10 is further inserted at working speed, which leads to a further power reduction. The coolant temperature rise between t = 150 s and t = 175 s does not decrease the power, because the reactivity loss is compensated by withdrawing group No. 10 by some 5%. In the following 10 seconds, the reinsertion of group No. 10 further reduces the power. This behaviour is well described by all calculations. When approaching a new stationary state (t > 250 s), the differences between calculated and measured power are within the accuracy of the neutron power measurement of ± 2%.

Other relevant plant parameters, such as hot leg temperatures, upper plenum pressure, and pressurizer water level are also well described by the codes.

4. Analysis of a VVER-440 transient (Loviisa-1, Finland)

The transient was initiated by a load drop down to house load level in one of the two working turbo-generators, i.e. the electric power output of the plant was suddenly reduced by half. As the turbine valves were closed, the secondary-circuit pressure started increasing sharply, but was quickly brought back to its nominal value by opening the turbine bypass valves. At the moment of generator load drop, the nuclear power production in the reactor core was still at 100%. Shortly after the load drop, the reactor control system started to reduce reactor power
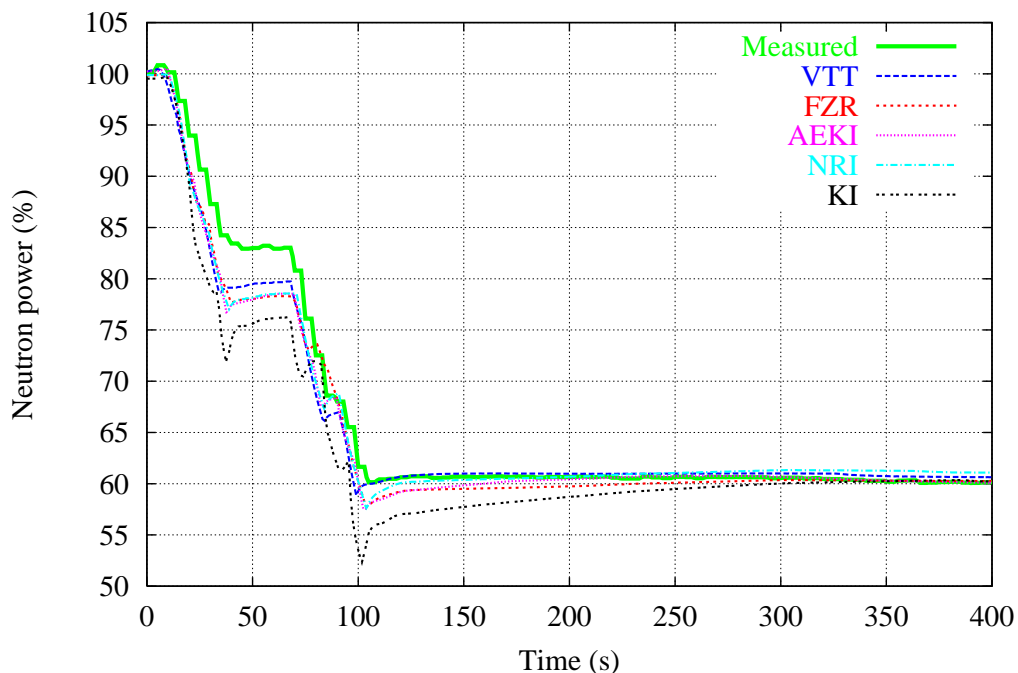
Fig. 3: Neutron Power
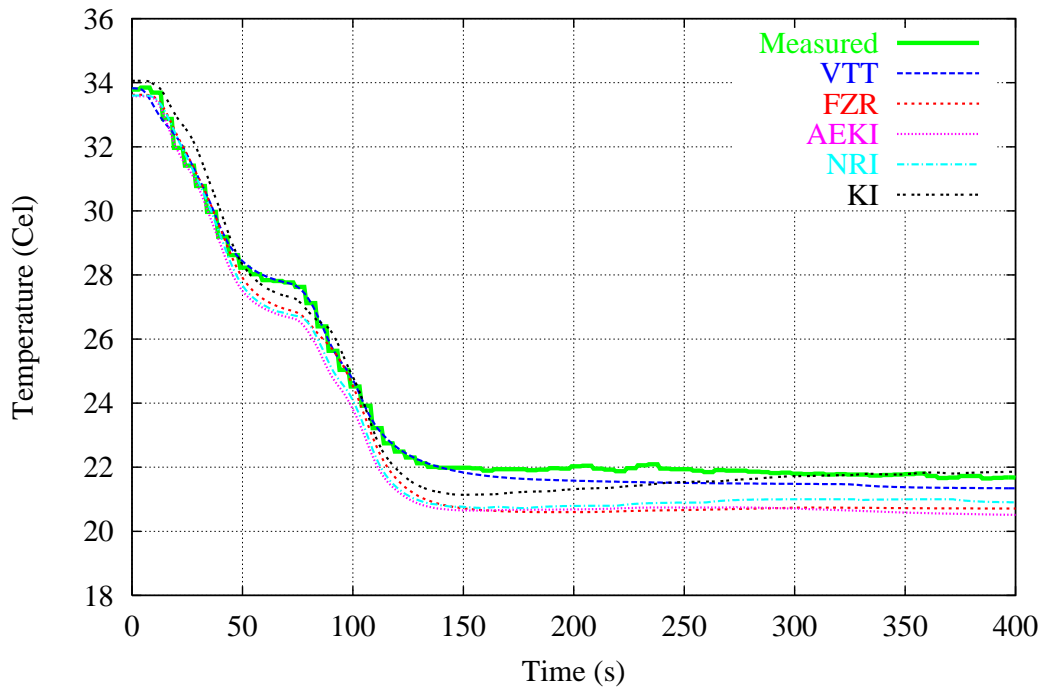
Fig. 4:   Average temperature difference between hot and cold legs
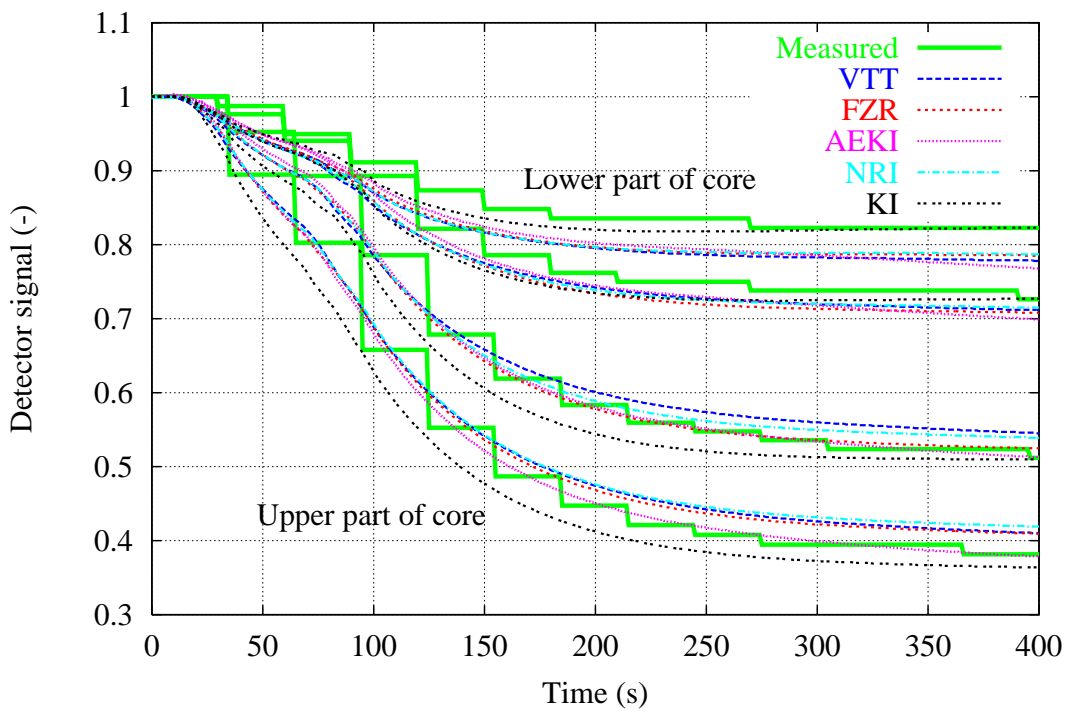
Fig. 5:   Relative SPND signals (neutron flux) at different heights in a fuel assemby

by inserting the control-assembly group No. 6. Thus neutron power was reduced down to 60% within some 100 seconds (Fig. 3). As a result of power reduction, the hot leg temperatures of the primary circuit decreased. At the start of the transient, the cooling of the primary circuit through the steam generators was reduced because of the increasing steam pressure at the secondary side. Therefore, the cold leg temperatures first increased significantly. Some 20 seconds later these temperatures also started decreasing. The primary pressure first increased with the temperature, but was quickly reduced by spraying into the pressurizer. Later on, when the reducing nuclear power decreased temperature and pressure, the pressurizer heaters were switched on to stabilize pressure at its nominal level.

The measured pressure as a function of time is well reproduced by all coupled codes involved. As the reactor power decreases due to the control-assembly group insertion, the average temperature difference between hot and cold legs, i.e. the coolant heat-up in the core (Fig. 4), is also reduced. However, the thermocouples measuring the coolant temperatures are encapsulated in tubes, so that there is some delay in the measured temperature signals. Taking into account these low-pass filter properties of the temperature sensors leads to a good agreement (Fig. 4) between the calculated and measured coolant heat-up. The signals of the rhodium-emitter self-powered neutron detectors (SPND), measuring the local neutron fluxes inside the VVER-440 core, are also delayed. As the different half-life components of the delayed responses are known, the low-pass filter behaviour of the detectors was simulated and applied to the neutron fluxes that had been calculated by the coupled codes. A constant SPND sensitivity during the transient was assumed. Four fuel assemblies in the 60-degree core symmetry sector are equipped with SPND lances, each lance carrying SPND at the distances of 50 cm, 100 cm, 150 cm and 200 cm from the active core bottom. In Fig. 5, the time behaviour of the signals from the SPND at these four height positions are shown for a fuel element being next neighbour but one to a control assembly of group No. 6. The measured signals and the respective calculated fluxes were normalized to the initial state. The different courses of the neutron fluxes at different axial levels, due to the control-assembly group No. 6 moving in, is clearly to be seen. As group No. 6 is moved from its uppermost position down to the middle of the core, the upper detectors see much more flux reduction than the lower ones. There is a satisfying agreement between the calculations and the measurements. A similar degree of agreement has been reached for the other assemblies equipped with SPND. In all, the simulation for the upper core region is better than that of the lower part.

5. Conclusions

Generally, the physical behaviour of the NPP, especially of the core and the primary circuit is well described by the coupled codes involved. A good agreement between calculated and measured safety-relevant parameters has been achieved for both the VVER-440 and the VVER-1000 reactor transient. In the neutronic part of the calculations, the achieved accuracy was somewhat better for the VVER-440 core. The VVER-1000 core is more difficult to model, due to its larger fuel assemblies. It is important to take into account the systematic errors of the measurements, whenever possible. For example, the time delay properties of measuring chains, like thermocouples and SPND, must be considered.

In both transients, a main effect was the fission power decrease due to control-assembly group insertion. Differences in the nuclear data used in the calculations cause different control rod efficiencies leading to differences in power levels. The fuel temperature feedback

on reactivity also influences power. Both effects can hardly be separated. For separately studying the control rod efficiencies, the neutronic codes including the applied nuclear databases should additionally be validated against measurements in zero-power research reactors. As for the calculated fuel temperature, the present investigations have revealed that it is very sensitive to the modelling of the gas gap between fuel pellets and rod cladding. A detailed dynamic modelling of the gap width is recommended.

Altogether, it was shown that the coupled neutron-kinetic / thermal-hydraulic codes under consideration are capable of simulating typical VVER plant transients. Hence the work contributes to increase the confidence in the results of the code systems. In future, some more details of the automatic control systems should be included in the thermal-hydraulic system models. The remaining transients, measured in VVER-1000 and VVER-440 plants, that were documented for the SRR1/95 project but not yet calculated by the coupled codes, can be used for further validation work.

References

[1]   S. Mittag, S. Kliem, F. P. Weiss, R. Kyrki-Rajamäki, A. Hämäläinen, S. Langenbuch, S. Danilin, J. Hadek, G. Hegyi, A. Kuchin, and D. Panayotov (2001), Validation of coupled neutron kinetic / thermal-hydraulic codes, Part 1: Analysis of a VVER-1000 transient (Balakovo-4), Annals of Nuclear Energy 28/9, pp. 857-873

[2]   A. Hämäläinen, R. Kyrki-Rajamäki, S. Mittag, S. Kliem, F. P. Weiss, S. Langenbuch, S. Danilin, J. Hadek, and G. Hegyi (2001), Validation of coupled neutron kinetic / thermal-hydraulic codes, Part 2: Analysis of a VVER-440 transient (Loviisa-1), Annals of Nuclear Energy, accepted for publication

[3]   S. Kliem, S. Mittag, U. Rohde, A. Seidel, and F.-P. Weiß (1999), Improvement of the verification of coupled thermal-hydraulic /neutron kinetic codes: DYN3D burn-up and steady-state calculations, in: F.-P.Weiß and U. Rindelhardt (Ed.) , Annual Report 1998 of the Institute of Safety Research, FZR-268 (Juli 1999), pp. 17-22

[4]   R. Kyrki-Rajamäki (1995), Three-dimensional reactor dynamics code for VVER type nuclear reactors, Espoo (Finland), VTT Publications 246

[5]   J. Miettinen (1998), SMABRE Code Manual, Volume 1: SMABRE System Models and Numerical Methods, Espoo (Finland), Interim report

[6]   M. P. Lizorkin, V. N. Semenov, V. S. Ionov, and V. I. Lebedev (1992), Time dependent spatial neutron kinetic algorithm for BIPR8 and its verification, Proceedings of the Second Symposium of AER (pp. 389-407), Paks, Hungary

[7]   V. Teschendorff, H. Austregesilo, and G. Lerchl (1996), Methodology, status and plans for development and assessment of the code ATHLET, Proceedings of the OECD/CSNI Workshop on Transient Thermal-Hydraulic and Neutronic Codes Requirements (pp.112-128), Annapolis, USA

[8]   U. Grundmann, D. Lucas, S. Mittag, and U.Rohde (1995), Weiterentwicklung und Verifikation eines dreidimensionalen Kernmodells für Reaktoren vom Typ WWER und seine Ankopplung an den Sörfallanalysecode ATHLET, Rossendorf, Report FZR-84

[9]   G. Hegyi, A. Kereszturi, I. Trosztel, S. Langenbuch, W. Horche, and K. Velkov (1998), Improvement of Plant Transient Analysis for VVER by Coupling KIKO3D with ATHLET, Proceedings of ICONE-6, San Diego CA USA

[10]   U. Rohde (2001), The Modelling of Fuel Rod Behaviour under RIA Conditions in the Code DYN3D, Annals of Nuclear Energy, accepted for publication

THE MODELING OF FUEL ROD BEHAVIOUR UNDER RIA CONDITIONS IN THE CODE DYN3D

Ulrich Rohde

1. Introduction

The code DYN3D has been developed in the Research Centre Rossendorf for the analysis of reactivity initiated accidents (RIA) in light water reactors [1]. It comprises 3D neutron kinetics based on a nodal expansion approach both for hexagonal and square fuel element geometry and a thermo-hydraulic model of the reactor core. In RIA analysis, the heat transfer from fuel to coolant plays an important role. This heat transfer is significantly affected by the behaviour of the gas gap between fuel and cladding, but also by the heat transfer conditions at the cladding surface. Therefore, a transient fuel rod behaviour model is implemented into DYN3D [2,3]. This model is coupled with a heat transfer regime map for cladding surface - coolant heat transfer ranging from subcooled liquid convection conditions to dispersed flow with superheated steam. For the validation of the model, experiments on fuel rod behaviour during RIAs carried out in Russian and Japanese pulsed research reactors are calculated. Because the experiments were carried out at atmospheric pressure and stagnant flow conditions, additional calculational studies on the fuel rod behaviour during RIAs in power reactors at high pressure and high mass flow rate conditions were performed.

2. Fuel rod model

For the estimation of fuel and cladding temperatures the heat conduction equation in one–dimensional radial geometry is solved numerically taking into account temperature–dependent heat conductivity. However, the main problem of fuel rod behaviour modelling is the determination of heat transfer coefficients α_{gap} in the gas gap between fuel and cladding and α_c from cladding to coolant.

The general assumption of the gas gap behaviour modeling in DYN3D is that the parameters for the stationary reference state (e.g. geometrical gap width, gas pressure and composition) are known from detailed fuel rod behaviour codes. The changes of the gas gap parameters during the transient process due to variation of gap width, gas temperature and pressure, coolant and fuel - cladding contact pressure are estimated by the DYN3D model.

In the gas gap between fuel and cladding the heat transfer components due to conduction in the gas, radiation and fuel–cladding contact are considered. The heat transfer coefficient due to conduction in the gas is determined by

$$\alpha_{cond} = \frac{\lambda_{g,mix}}{\delta_{gap} + \delta_{roug} + \delta_{ext}} \tag{1}$$

where $\lambda_{g,mix}$ is the thermal conductivity of the filling gas mixture. The composition of the filling gas mixture is a function of the actual depletion state and must be obtained from detailed fuel rod behaviour codes. δ_{gap} is the geometrical gap width and is determined by using a thermo-mechanical model. δ_{roug} is related to the surface roughness values of fuel and cladding. δ_{ext} is a gas kinetics extrapolation length. The radiation component α_{rad} is given by the Stefan–Boltzmann law. In the case of closed gap, heat transfer due to contact conductance is considered:

$$\alpha_{cont} = \frac{C\lambda_{f,c}}{\delta_{sr}^{n}}\left(\frac{p_{cont}}{H}\right)^{m}$$

(2)

where C, m and n are constants, δ_{sr} is the square averaged surface roughness, p_{cont} the contact pressure, H the Meyer hardness of the softer material (fuel or cladding), and $\lambda_{f,c}$ is the effective thermal conductivity at the fuel-cladding interface.

The contact pressure is estimated based on the following assumptions:

- one–dimensional modeling of mechanics in radial direction,
- linear superposition of radial thermal, elastic and plastic deformations without axial coupling,
- elastic deformation of the fuel is taken into account only in the case of fuel–cladding contact, plastic deformations of the fuel are not considered,
- cladding is described in the thin shell approximation.

The cladding stress is determined by the gas pressure inside the cladding, the outer coolant pressure and, possibly, the contact pressure. The gas pressure p_{gas} is obtained from the ideal gas law for the filling gas and taking into account the change of gas temperature as well as the change of free volume by changing gas gap width.

The plastic deformation of the cladding is considered in accordance with the creeping law:

$$\varepsilon = \frac{\delta R}{R} = \left(\frac{\sigma}{K\dot{\varepsilon}^{q}}\right)^{1/p}$$

(3)

where the coefficients K, p and q are material properties. $\dot{\varepsilon}$ is the strain rate, that means, the time-derivative of the cladding strain $\varepsilon = \delta R/R$. Plastic deformation is considered, when the stress exceeds the yield strength $\sigma_{yield,}$ which is a material property and a function of temperature and strain rate.

If the pressure outside the cladding is larger than the inner pressure, prompt creeping of the cladding on the fuel is assumed so that the gap vanishes and the cladding stress is zero. If the inner pressure exceeds outer pressure, two different situations are considered. If the gap is closed and the contact pressure is non-zero, it is assumed that prompt creeping will take place reducing the stress until it becomes equal to the yield strength. If there is no fuel - cladding contact and the gas pressure exceeds the coolant pressure, time-dependent creeping will be considered according to equation (3). The last situation is typical for low coolant pressures like in RIA experiments at pulsed research reactors or in LOCA cases and leads to cladding ballooning, while the first one is typical for RIA conditions in power reactors.

A mechanistic model of fuel rod failure during accidents is not included in DYN3D, but some parameters needed for the assessment of fuel rod integrity are provided:

- fuel enthalpy for each axial node of the rod,
- cladding oxide thickness,
- signalization of possible cladding rupture, when the cladding stress is positive (inner pressure is larger than outer pressure) and exceeds the yield strength.

The cladding oxidation due to metal-water reaction (MWR) at high temperatures is described

by the equation:

$$D\frac{dD}{dt} = \frac{A}{C^2}\exp\left(\frac{-B}{T}\right)$$ (4)

where D is the oxide layer thickness , T the cladding surface temperature, C the mass density of oxygen in ZrO_2 , A and B are constants. The MWR is considered as an additional heat source in the cladding, but the additional heat transfer resistance at the cladding surface and the change of mechanical properties of the cladding caused by the oxide layer are not taken into account (restriction to thin oxide layers).

3. Heat transfer regime map

The heat transfer from fuel to coolant is affected not only by the behaviour of the gas gap, but also by heat transfer conditions at the cladding surface. In DYN3D, a heat transfer regime map is used which covers all flow regimes from one-phase liquid convection over different boiling heat transfer mechanisms to superheated steam convection.

Appropriate correlations for single phase convection and the region of boiling heat transfer are chosen from [4]. The occurence of heat transfer crisis is determined from various critical heat flux correlations. For low mass flow densities (G << 200 kg/m^{2}s) the Kutateladse correlation for q"$_{crit}$ with a non-equilibrium correction is used [4]. An additional criterion for the detection of dryout is considered. After reaching the critical heat flux or critical dryout quality, the heat transfer is decreasing, which leads to an increasing temperature difference between the heated wall and the fluid. In this unstable transition boiling region the heat flux is interpolated between the critical heat flux value and the value at the minimum stable film boiling point. In the stable post-crisis region heat transfer correlations for inverted annular or dispersed flow are used. Additionally, the heat transfer from wall to coolant by radiation is taken into account. After full evaporation of coolant, heat transfer to superheated steam is estimated by a single phase forced convection correlation .

The following additional non-equilibrium corrections due to subcooled liquid are applied to the Leidenfrost or minimum stable film boiling point T_{MSFB} and the heat transfer coefficients in the post crisis region α_{pc}:

$$T_{MSFB} = T_{sat} + 350 + 5.1\ (T_{sat} - T_{liq})$$ (5)

$$\alpha_{pc}(T=T_{liq}) = \alpha_{pc}(T=T_{sat})[1 + 0.025\ (T_{sat} - T_{liq})]$$ (6)

The formulaes (5) and (6) are based on correlations proposed by Ohnishi et al. [8].

4. Calculations for RIA experiments

For the validation of the fuel rod and heat transfer model in the code DYN3D several experiments known from literature were selected. Experiments on the fuel behaviour during large power pulses were carried out e. g. in the Japanese Nuclear Safety Research Reactor (NSRR) [6], in the Russian research reactors IGR and GIDRA [7] and in the framework of the French CABRI experimental program [5]. The NSRR is a modified TRIGA reactor whith a power pulse half width of a few milliseconds. The Russian GIDRA reactor contains an aqueous solution of enriched fuel producing narrow power pulses, while the IGR reactor is a graphite moderated one

with higher pulse half - width between 0,5s and a few seconds. In the experiments shortened probes of fresh fuel rods were inserted into a water or air filled capsule [8], [9], [10]. In all tests, the water was at atmospheric pressure. An overview of the experiments calculated by use of the DYN3D fuel rod model is given in Table 1.

Table 1: Overview on RIA experiments calculated with the DYN3D fuel rod model - experimental and calculated results

		NSRR Experiments			IGR Experiments				
Exp. Nr.		1	2	3	4	5	6	7	8
ΔE [cal/g]		190	190	190	207	284	326	360	93
τ [ms]		7	7	7	1050	650	500	800	4300
ΔT [K]		10	40	80	80	80	80	80	Air
$h_{f,max}$ [cal/g]		187	185.5	183.5	123	179	216	200	-
T_{clad}	meas.	1500	1330	1000	141	177	967	940	1200
[^{o}C]	calc.	1447	1278	1177	153	167	891	1040	1320
t_{rewet}	meas.	38	15	10	-	-	6.3	11.0	-
[s]	calc.	41	20	7.2	-	-	6.6	12.5	-
δ_{OX}	meas.	12	8	5	-	-	-	-	-
[μm]	calc.	29	13	7	-	-	-	-	-

ΔE is the energy release in the fuel probe, τ - the power pulse half-width, ΔT - the coolant sub-cooling, $h_{f,max}$ - the energy deposition in the fuel (calculated), T_{clad} - the maximum cladding temperature, t_{rewet} - the time until rewetting after heat transfer crisis, δ_{OX} - the oxide layer thickness due to cladding oxidation.

In general, a good agreement is achieved between the calculations and the experiments, which were performed in very different conditions (pulse half width, coolant subcooling, energy re-
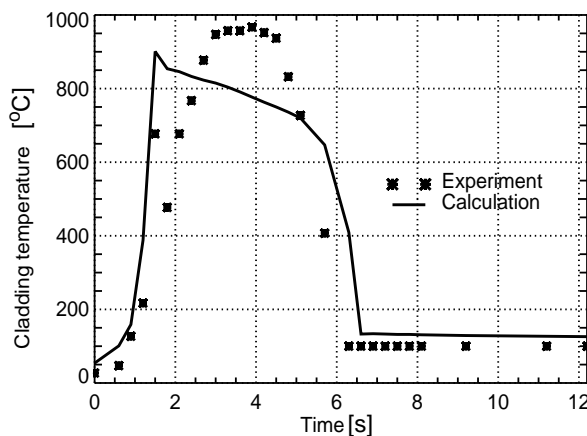
Fig. 1: Comparison for IGR RIA experiment Nr.6
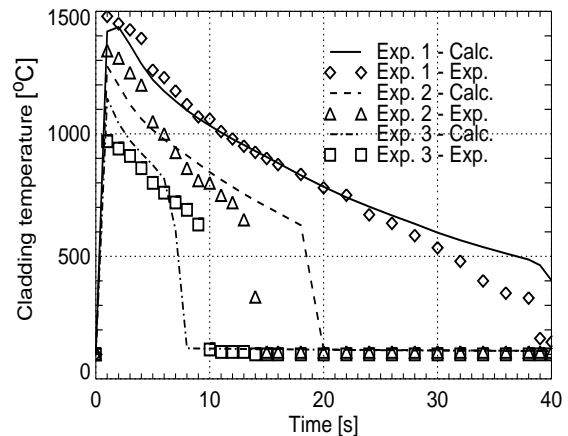
Fig. 2: Measurement and calculation for the NSRR RIA experiments
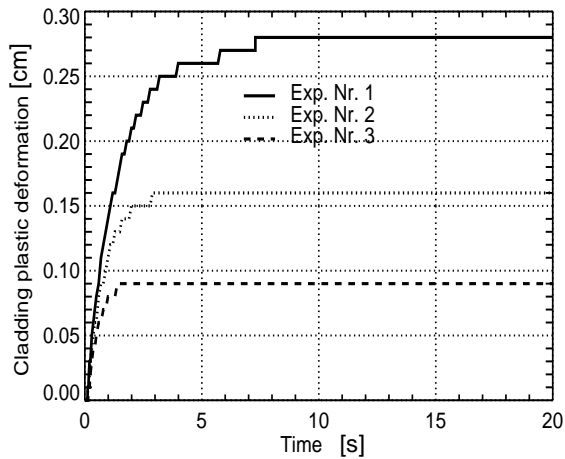
Fig. 3: Calculated cladding plastic deformation

lease).The comparison between calculated and measured cladding temperatures for the IGR experiment No. 6 (see the table) is shown in fig. 1, for the NSRR experiments (number 1, 2 and 3) in fig. 2. The behaviour of the cladding and fuel temperature strongly depends from the gas gap propoerties. In the first milliseconds, the gap is closed due to thermal expansion of the fuel. This increases the heat transfer from fuel to cladding and leads to very fast cladding heating. The cladding material becomes plastic and the cladding starts to expand. The calculated plastic deformation of the cladding (increase of cladding radius) for the NSRR experiments is shown in fig. 3. Experimental data on the cladding ballooning in these experiments are not available. Fig. 4 shows the cladding stress and yield strength of the cladding material. Within the first tenth of second, the yield strength is decreasing very rapidly due to the rising cladding temperature. When the stress becomes equal to the yield strenght, the plastic deformation of the cladding starts (see left part of fig. 4). After decrease of the cladding temperature due to the decreased heat transfer from fuel to cladding, the yield strength is increasing and the plastic deformation stops (see fig. 3 and right part of fig. 4). Disregarding the plastic deformation results in much higher cladding temperatures.
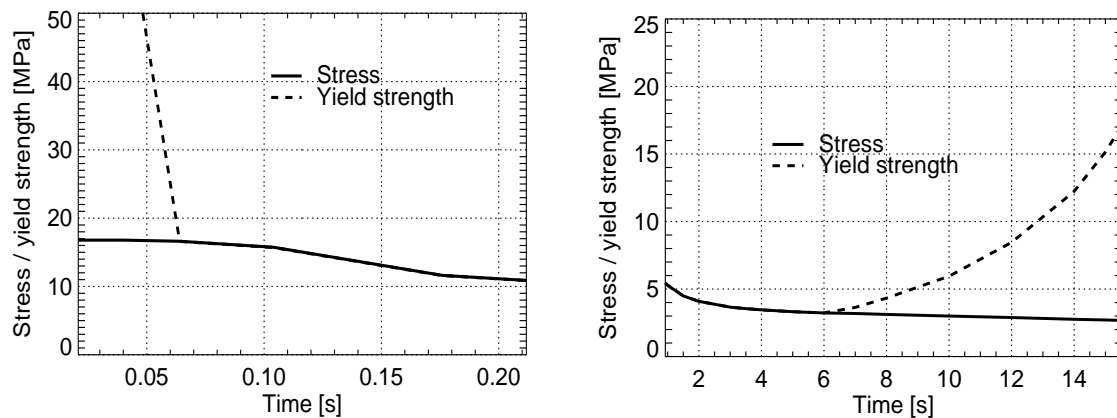
Fig. 4: Calculated stress and yield strength of the cladding for Exp. No. 1

Remarkable differences can be seen between the NSRR and the IGR experiments. In the NSRR experiments, the energy release in the burst was lower than in the IGR experiments with water cooling, but much higher cladding temperatures are reached. This is due to the very small pulse width which leads to an almost adiabatic heating of the fuel rod during the burst. In the NSRR experiments considered, the effect of coolant subcooling was investigated while the other conditions (energy release, pulse width) were fixed. This allows to adjust the heat transfer model.

However, the experiments were carried out under atmospheric pressure and stagnant flow conditions, while for RIAs in power reactors high pressure and high flow rate conditions are typical. Additional calculational studies on the fuel rod behaviour under power reactor conditions were performed, where reactor power peak curves with a half-width of 0.4 s and different energy release values were given as input to the fuel rod model calculations. Burn-up dependent data for

the nominal state of the gas gap were obtained from calculations with the code STOFFEL [11]. In comparison with the experimental data from the research reactors, for the same energy deposition in the fuel and about the same pulse half-width, higher cladding temperatures are reached under power reactor conditions. This is due to the different gap behaviour. While at low coolant pressure the ballooning effect is observed, at higher pressures the cladding creepes on the fuel. The gap is closed and the heat transfer from fuel to cladding is enhanced.

The calculations have shown that the relevant mechanism of fresh fuel failure is melting, the fuel enthalpy at failure is about 230 cal/g. For burned-up fuel, cladding failure is possible due to high mechanical stress at much lower fuel enthalpy values (about 125 cal/g for a burn-up of 25 MWd/kg). This corresponds to results reported about in [12].

5. Conclusions

For the validation of the transient fuel rod model used in DYN3D, experiments on fuel rod behaviour during RIAs carried out in Russian and Japanese pulsed research reactors with shortened probes of fresh fuel rods are calculated. A good agreement between calculated and measured results was achieved.

Numerical studies concerning the fuel rod behaviour under RIA conditions in power reactors demonstrated, that the fuel rod behaviour at high pressures and flow rates in power reactors is different from the behaviour under atmospheric pressure and stagnant flow conditions in the experiments. The mechanisms of fuel rod failure for fresh and burned fuel reported from the literature can be qualitatively reproduced by the DYN3D model. However, the model must be extended and improved for proper description of burned fuel behaviour.

References
[1]   U. Grundmann and U. Rohde (1996), DYN3D - a 3-dimensional Core Model for Steady-state and Transient Analyses of Thermal Reactors, Proc. Int. Conf. on the Physics of Reactors PHYSOR 96, Mito (Japan), pp. J-70 - J-79
[2]   U. Rohde (1992), Modeling of Fuel Rod Behaviour and Heat Transfer in the Code FLO-CAL for Reactivity Accident Analysis of Reactor Cores, in: Recent Advances in Heat Transfer, Elsevier Publ., Amsterdam, 1992
[3]   U. Rohde: The Modeling of Fuel Rod Behaviour under RIA Conditions in the Code DYN3D, Annals of Nuclear Energy, to be published
[4]   L.N. Poljanin, M. Ch. Ibragimov, G. P. Sabeljev (1982), Teploobmen v jadernykh reatorakh, Moscow, Ehnergoatomizdat
[5]   Papin, J. et al. (1996), Nuclear Safety 37, 289 - 327
[6]   T. Fuketa et al. (1996), Nuclear Safety **37**, 328 - 342
[7]   V. Asmolov and L. Yegorova (1996), Nuclear Safety **37**, 343 - 352
[8]   N. Ohnishi, K. Ishijima and S. Tanzawa (1984), Nucl. Sc. and Engineering **88**, 331-341
[9]   V. Asmolov et al. (1987), Kernenergie **30**, 299-304
[10]   E. Burmistrov, S. Bashkirzev, U. Rohde (1993), Validation Experience for FLOCAL, ESCES, MAIVA, SCDAP/RELAP Codes on the Basis of Post-Test Calculations for Russian and Japanese RIA Experiments", Internal Report, Research Centre Rossendorf
[11]   D. Reinfried (1985), Zur mathematischen Modellierung des Bestrahlungsverhaltens von Druckwasserreaktorbrennstäben, PhD Thesis, Rossendorf
[12]   E. L. Courtright (1979), A Survey of Potential Light Water Reactor Fuel Rod Failure Mechanisms and Damage Limits, NUREG/CR - 1132 (PNL - 2787), 1979

MONITORING SYSTEM FOR BATCH REACTORS USING ADAPTIVE HEAT BALANCES

Günther Hessel, Holger Kryk, Wilfried Schmitt, Torsten Seiler and Frank-Peter Weiss

1. Introduction

The operation of batch reactors is characterized by nonsteady-state conditions due to the discontinuous process control so that even experienced operators have difficulties to distinguish allowable from forbidden process deviations or to identify the cause of process trends. To support the personnel in decision making, a monitoring system for batch reactors is being developed within the framework of a BMBF project with the Faunhofer Institute UMSICHT and the Degussa AG as an industrial partner and user in the future.

In this report the working principle of the <u>Mo</u>nitoring <u>Sy</u>stem (MoSys) is described. Since dangerous and undesired faults cannot be generated in production plants, the scale-up plays a crucial role when a monitoring system has to be adapted to an industrial chemical plant. To solve the scale-up problem, adaptive heat balances are used to derive scaleable or scale-invariant characteristic values for monitoring process-relevant faults. Results are presented from experimental studies in laboratory reactors (1- and 10 litre-scale) and from online-testing in a pilot plant. As a reference process, the strongly exothermic, homogeneous catalytic esterification between acetic anhydride and methanol was chosen.

2. Description of the monitoring system

The monitoring system MoSys has a structure as shown in Fig. 1. MoSys is connected with the process control system (WinCC) or with data bases in dependence on the requirements. This coupling is the prerequisite for real time processing.
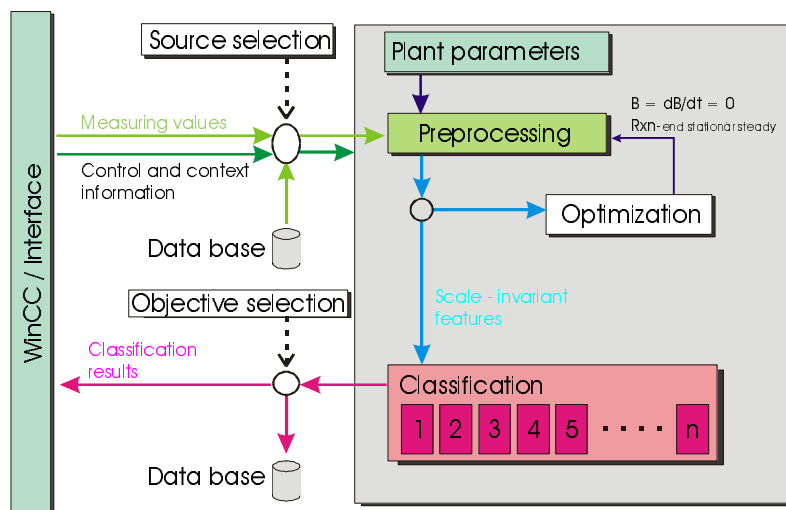
Fig. 1: Structure of the monitoring system MoSys

The MoSys kernel consists of a specialized data preprocessing module with the following functions:

- signal conditioning
- determination of derived parameters and
- calculation of the feature vectors by means of adaptive heat balance models

For calculating the heat balances, the parameters of the substances and their thermochemistry, as well as of the plant have to be available in a special data base represented as the module "plant parameters" in Fig. 1. The heat balance has to be fitted to the target plant by using process data from complete batches under normal reaction conditions. This fitting is carried out offline by the module "optimization" (Fig. 1). The process monitoring and fault classification based on the generated features are realized by the module "classification". MoSys supports an arbitrary set of fault monitors. That means that there are special monitors for different faults. The results of the outputs of the monitors are transferred to the process control system. However, the operator has to decide which counter-measures must be initiated to avoid dangerous and undesired process states when any fault is recognized.

3. Heat Balance Model

By solving a set of dynamic mass / heat balances in real time (every 10 seconds), the heat release of the chemical reaction can be monitored. In Fig. 2 the heat balance model is schematically depicted for a semibatch reaction where the expected heat production rate $\dot{Q}_{R,e}$ is characterized by the molar reaction enthalpy ΔH_R of the spontaneous reaction of the fed-batch reactant:

$$\dot{Q}_{R,e} = \left(-\Delta H_R\right)\frac{\dot{m}_{DOS}}{M_{DOS}} \tag{1}$$
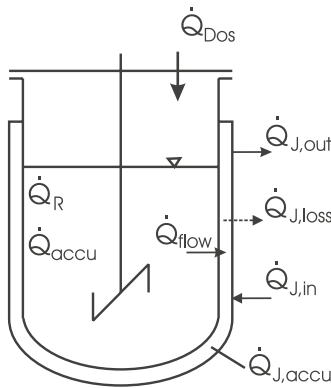
$$\dot{Q}_{flow} = k_{RW} \cdot A_{RW}\left(\overline{T_R - T_j}\right)$$

$$\dot{Q}_{accu} = \left(m_R \cdot c_{p_R} + m_{App} \cdot c_{p_{App}}\right)\frac{dT_R}{dt}$$

$$\dot{Q}_{Dos} = \dot{m}_{Dos} \cdot c_{p_{Dos}}\left(T_{Dos} - T_R\right)$$

Fig. 2: Heat fluxes in a semibatch reactor

The heat balance around the reactor is given by:

$$\dot{Q}_{R,c} = \underbrace{\Delta\dot{Q}_j + \dot{Q}_{j,accu} + \dot{Q}_{j,loss}}_{=\dot{Q}_{flow}} + \dot{Q}_{accu} - \dot{Q}_{Dos} \tag{2}$$

while the heat balance around the jacket is defined by:

$$\dot{Q}_{flow} = \Delta\dot{Q}_j + \dot{Q}_{j,accu} + \dot{Q}_{j,loss} \tag{3}$$

where the notation of the used terms are given in Chap. 8 and in Fig. 2, respectively.

Since thermal hazards have their origin in a perturbation of the heat balance, different faults can be recognized by online calculation of the respective heat balance. This will exemplarly be discussed on the reactant accumulation that can lead to a runaway in a homogeneous, strongly exothermic esterification due to a self-acceleration of the reaction. When a reactant accumulation occurs, a difference between the expected heat production rate $\dot{Q}_{R,e}$ and the measured current heat flux $\dot{Q}_{R,c}$ is given by:

$$\Delta Q_{R,accu} = \int_{t_b}^{t_c} \left(\dot{Q}_{R,e} - \dot{Q}_{R,c} \right) dt \qquad (4)$$

The current accumulated reactant mass $m_{R,accu}$ can be determined by:

$$m_{R,accu} = \frac{\Delta Q_{R,accu}}{\left(-\Delta H_R \right)} M_{Dos} \qquad (5)$$

By using the current adiabatic temperature rise ΔT_{ad}, defined by Eq. 6,

$$\Delta T_{ad} = \frac{\Delta Q_{R,accu}}{m_R c_{pR}} \qquad (6)$$

a dynamic thermal reaction characteristic B can be calculated by:

$$B = \frac{E_A \Delta T_{ad}}{R T_R^2} \qquad (7)$$

To compensate errors in calculating the heat balance due to a model approximations and/or unknown heat losses, the correction term $\dot{Q}_{cor}$ was introduced:

$$\dot{Q}_{R,cor} = \dot{Q}_{R,c} + \dot{Q}_{cor} \qquad (8)$$

with

$$\dot{Q}_{cor} = \alpha_0 + \alpha_1 \left(T_R - T_{Amb} \right) + \alpha_2 \left(\overline{T_j} - T_{Amb} \right) \qquad (9)$$

The coefficients α_i of this function (Eq. 9) are adapted to the respective target plant by means of reaction courses under normal process conditions.

4. Adaptation of the heat balance

To determine the correction term $\dot{Q}_{cor}$ in the heat balance, a neural network is used. The coefficients α_i correspond to the weights calculated by a gradient descent procedure to minimize the following error function E:

$$E = \sum_l \left(\left(\frac{d\Delta Q_{R,accu}}{dt} \right)^2 + \left(\Delta Q_{R,accu} \right)^2 + \sum_i \alpha_i^2 \right) \qquad (10)$$

Due to B ~ $\Delta Q_{R,accu}$ the optimization is carried out using . $\Delta Q_{R,accu}$ E is determined from all l records of training data. This error function minimizes the influence of the adaptive term on the heat balance at the same time. The following adaptation rule e results from the partial derivative of E to the coefficients α_i:

$$e = \eta \left(\frac{d\Delta Q_{R,accu}}{dt} + \frac{\Delta Q_{R,accu}}{\tau \cdot n} \right) \tag{11}$$

where n is the number of summation steps, η is the learning rate and τ is the sampling period. The coefficients α_i are adapted using the formula:

$$\Delta \alpha_i^{k+1} = e \cdot S_{\alpha_i}^n + \mu \cdot \Delta \alpha_i^k \tag{12}$$

where k is the number of learning steps (iteration over k data records), μ is the momentum and S is the sum of α_i since the begin of charging of a batch.

5. Results

In two laboratory reactors (ALR1 and ALR10) and a pilot plant (T70) the monitoring system MoSys was tested for three safety-relevant faults – reactant accumulation, lack of mixing and loss of cooling. For each fault a special monitor was implemented. The monitor "reactant accumulation" is based on the dynamic thermal characteristic B (Eq. 9), while the monitor "runaway" uses the OLIWA-criterion [1]:

$$K_R^0 : \left(\frac{d^2 T_R}{dt^2} > 0 \right) \wedge \left(\frac{dT_R}{dt} > 0 \right) \wedge \left(\frac{d\overline{(T_R - T_j)}}{dt} > 0 \right) \tag{13}$$

For monitoring the mixing of reactants, two temperature sensors in different heights in the reaction mixture are used. Lack of mixing is given if the temperature deviation exceeds the limit value:

$$K_{mix} : \left(T_{R,0} - T_{R,1} \right)^2 > \Delta T_{D,max}^2 \tag{14}$$

where $\Delta T_{D,max}$ is the maximum permissible temperature deviation under good mixing conditions. As an alternative monitor for reactant accumulation, the monitor "adiabatic temperature" was also tested. The adiabatic reactor temperature $T_{R,ad}$ would be reached when the current accumulated reactant mass (Eq. 7) reacts after a loss of cooling where the charging of the reactant was stopped:

$$T_{R,ad} = T_R + \Delta T_{ad} \tag{15}$$

When $T_{R,ad}$ crosses a permissible design temperature $T_{R,perm}$, there is a hazardous potential. The criterion for this monitor is:

$$K_T : T_R + \Delta T_{ad} > T_{R,perm} \tag{16}$$

A similar criterion is used for the monitor "reactant accumulation":

$$K_B : B > B_{perm} \tag{17}$$

Based on the principle definition of the above monitoring criterions the monitor outputs $Z_i(x)$ are defined as follows:

$$Z_i(x) = 1 - \frac{1}{1 + x^2} \qquad i = accu, mix, run \tag{18}$$

with the monitor variables $x(t)$

$$x(t) = \alpha_{accu} \cdot \max(0, B) \tag{19}$$

$$x(t) = \begin{cases} \alpha_{mix} \cdot (T_{R,0} - T_{R,1}) & \text{for } V_R > V_{R,min} \\ 0 & \text{otherwise} \end{cases} \tag{20}$$

or

$$x(t) = \begin{cases} \alpha_{run} \cdot r(t) + (1 - \alpha_{run}) \cdot x(t - \tau) & \text{for } dk_{load} / dt \le 0 \\ (1 - \alpha_{run}) \cdot x(t - \tau) & \text{otherwise} \end{cases} \tag{21}$$

5.1 Validation of the scale-up model

Before applying the monitoring system for fault detection, the scale-up model based on mass/heat balances has to be validated by experiments under normal conditions in the chemical reactor to be monitored. In particular, these experiments were used for the adaptation of the heat balance model regarding to the non-considered heat losses due to thermal bridges and leakages by the ambient air as mentioned above in chapter 3. In Figure 3 the profiles of the process variables for the esterification under normal conditions in the ALR10 are depicted. As shown by the profiles of the constant dosing rate dV_{Dos}/dt and the reactor temperature T_R, the isoperibolic esterification course is controlled by dosing. This means that T_R follows the course of the dosing rate and remains relatively constant. After dosing of acetic anhydride, the time constant of the decreasing reactor temperature is essentially determined by the heat capacitie of the reaction mixture and the reactor vessel.
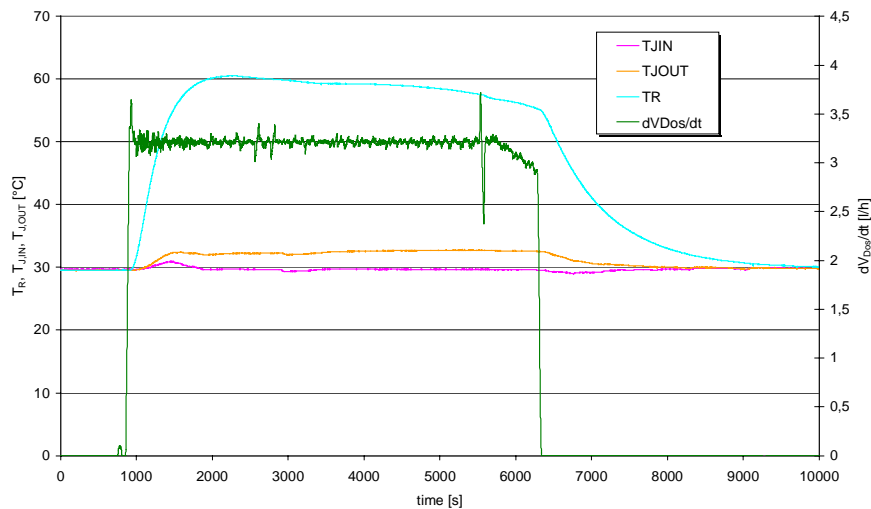
Fig. 3: Profiles of process variables for the esterification under normal conditions in ALR10

5.2 Fault monitoring

First, the efficiency of MoSys for fault monitoring was investigated using different faulty conditions in the laboratory scale and then, tested in the pilot scale. Since a non-recognized reactant accumulation contains a high hazardous potential, this fault shall be discussed in detail. The accumulation can be caused by a high dosing rate, low concentration of catalyst or low reactor temperature. Figure 4 shows the influence of reduced nominal catalyst concentrations on the thermal characteristics B. When the reduced catalyst concentration leads to a considerable decreasing of the reaction rate, then the dosing rate does not control the reaction rate and there is an accumulation of the fed-batch reactant. As can be seen in Fig. 4, the thermal characteristic B represents a significant feature for reactant accumulation due to the reduction of the catalyst concentration.
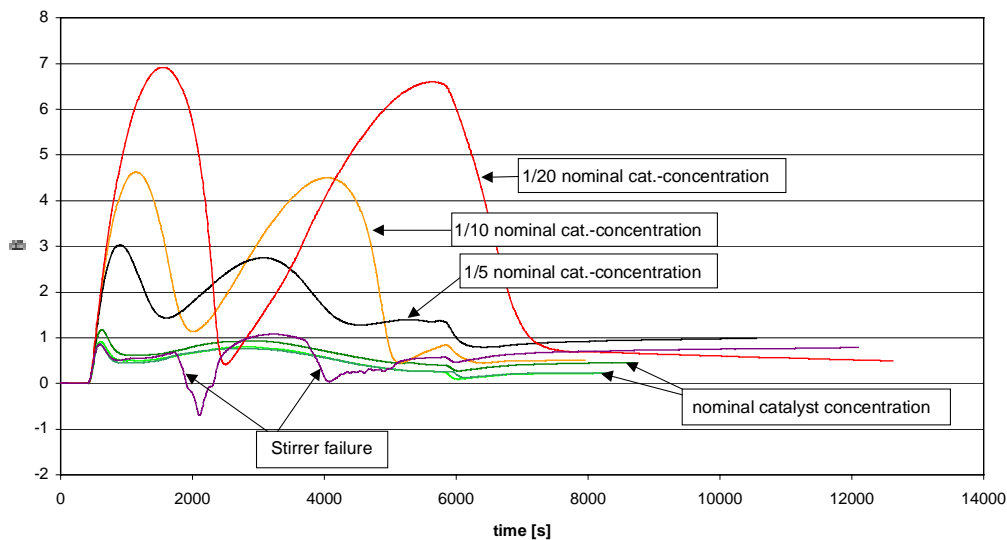
Fig. 4: Thermal characteristic B in dependence on different catalyst concentrations in ALR10

Furthermore, the oscillation of B shows that a self-acceleration of reaction rate (self-ignition) can occur under low catalyst concentrations where the reactant accumulation decreases temporarly. That is a very dangerous operation mode as represented in Fig. 5.
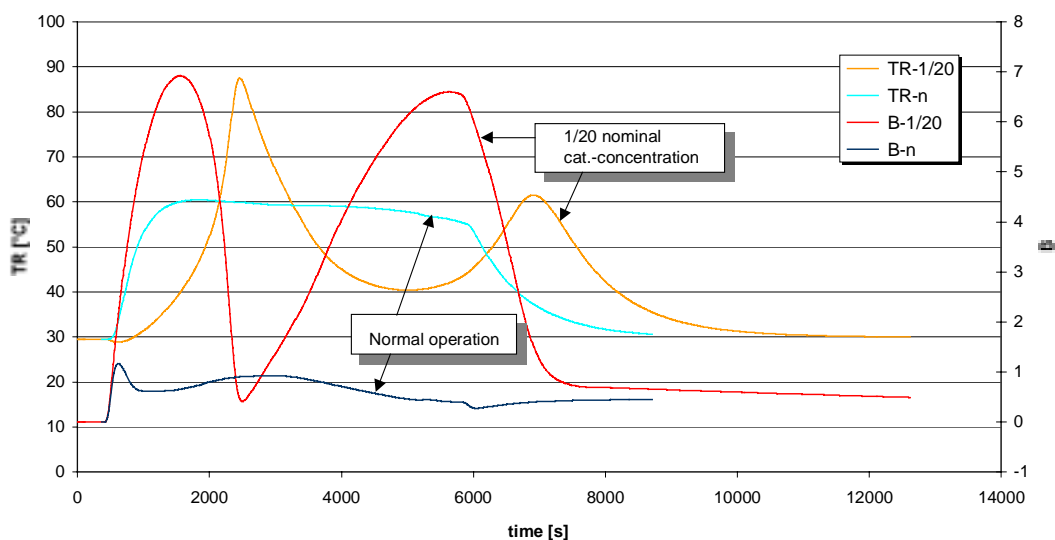
Fig. 5: Profiles of the reactant accumulation B and the reactor temperature T_R under nominal and 1/20 reduced catalyst concentration in ALR10

79

This figure also shows that the thermal characteristics B can be used for the early detection of critical reactant accumulations. The steep increase of the reactor temperature can be detected only some minutes later as the comparison between the profiles of TR-1/20 and B-1/20 (Fig. 5) shows. In Fig. 6 the results of MoSys are presented during a reaction course with a strongly reduced catalyst concentration in the pilot plant. MoSys recognizes the reactant accumulation by means of B, $T_{R,ad}$ and Z (accumulation) much earlier than it is possible by monitoring of the reactor temperature T_R.
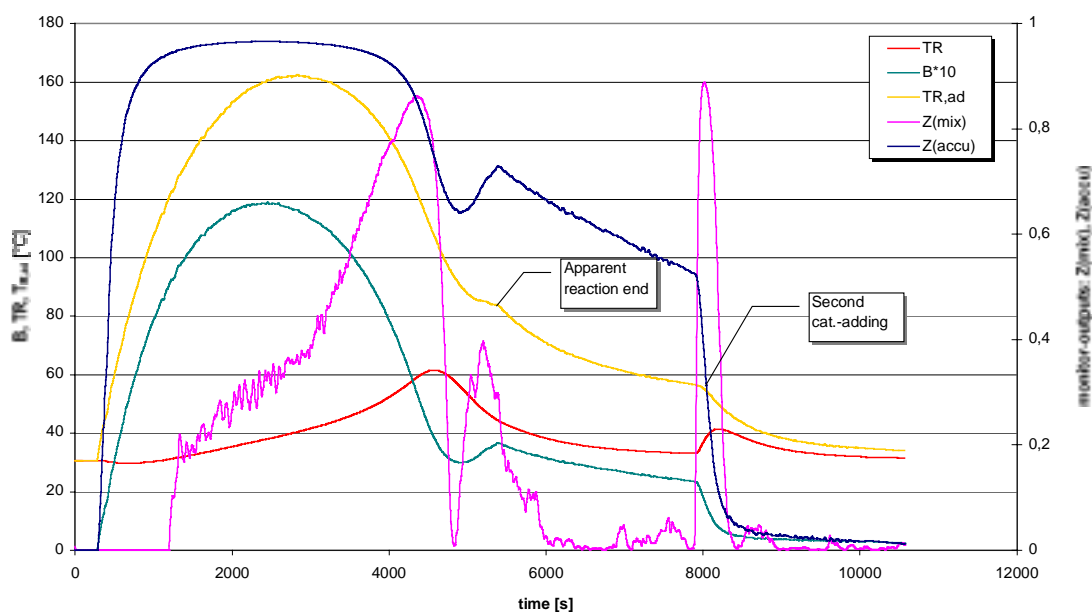
Fig. 6: Reaction course with strongly reduced catalyst concentration in the pilot plant

Further, after the delay of reactor temperature, the accumulation monitor indicates that the esterification seems to be not finished. It was found that by adding of the catalyst the reaction was initiated once more. Afterwards, the accumulation monitor showed a value near zero (Fig. 6). By extensively online-testing in the pilot plant, the efficiency of MoSys for fault monitoring could be proven. Figure 7 shows the profiles of process variables and the corresponding MoSys results during several fault scenarios.

Besides the fault "high dosing rate", one cooling fault and two stirrer faults (low speed of stirrer and stirrer failure) were experimentally simulated. All faults were correctly detected by MoSys. A comparison between the outputs "runaway-criterion" Z(run) and "thermal characteristic B" shows that B responds more sensible and much earlier to the fault "high dosing rate" and the "cooling fault" than the runaway criterion based on progressive temperature decreases (Fig. 7). The monitor "mixing fault" Z(mix) based on two temperature sensors can recognizes all four faults very well.

A)
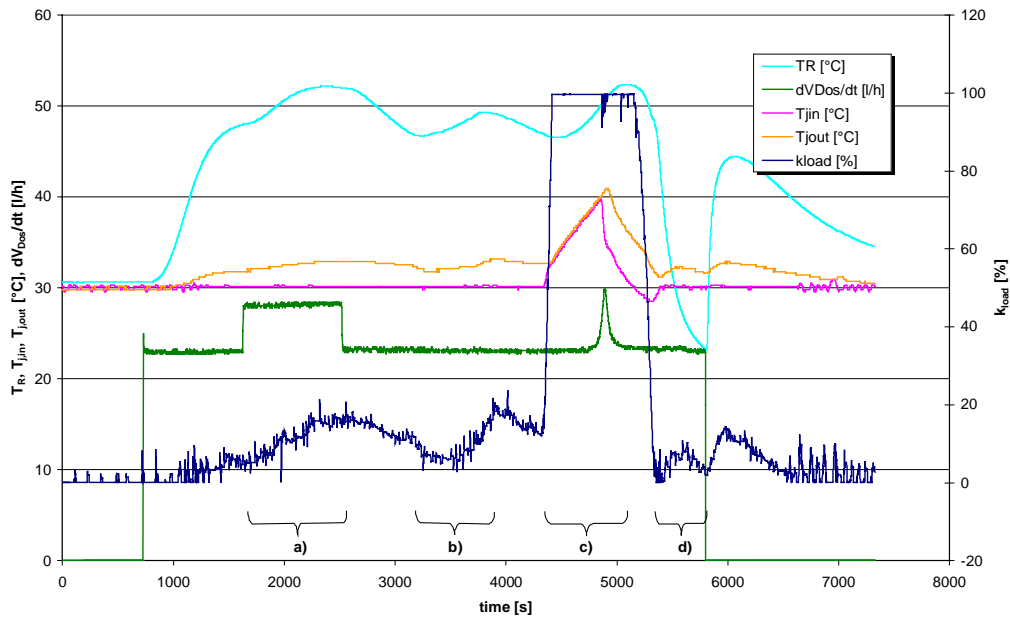
B)
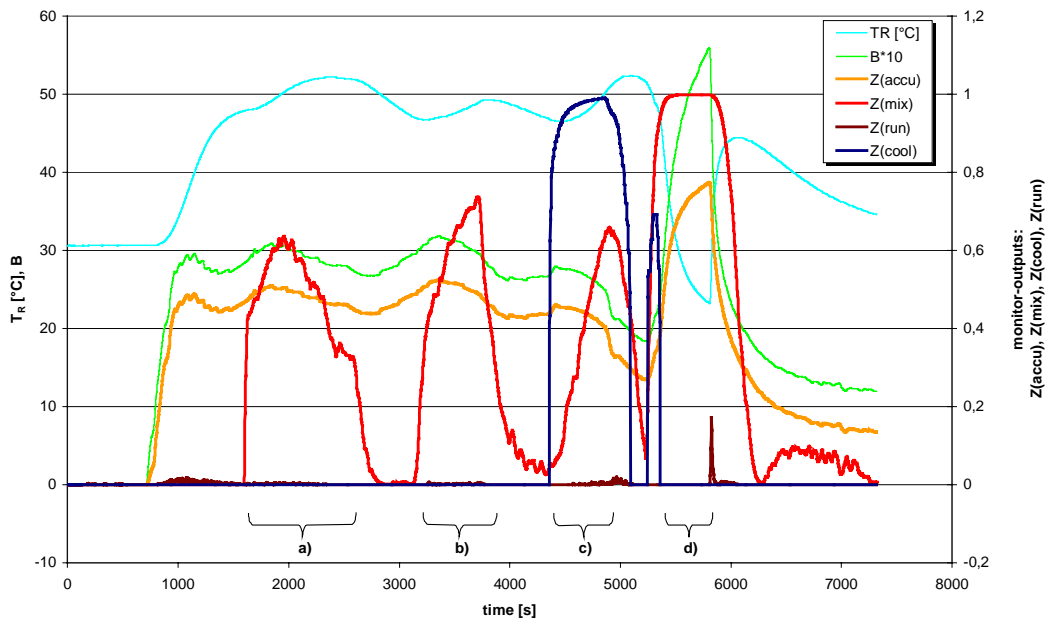
Fig. 7: Different fault scenarios carried out in the pilot plant
a) high dosing rate, b) low speed of stirrer, c) cooling fault caused by switching off the
secondary cooling loop, d) loss of agitation (stirrer failure)
A) Profiles of process variables and k_{load} (=load signal of the cooling)
B) Profiles of MoSys-outputs (B = thermal caracteristic, Z(accu) accumulation factor,
Z(run) = runaway-criterion, Z(cool) = cooling fault factor, Z(mix) = mixing factor,
T_R = reactor temperature)

6. Conclusion

A monitoring system (MoSys) based on adaptive heat balances has been developed for early fault detection in strongly exothermic reactions. Its efficiency could experimentally be proven for a homogeneous esterification model-reaction in the laboratory reactor and pilot plant scale. Experiments under normal and several faulty conditions were carried out in different reactor scales to prove the adaptation of the monitoring technique to various scales of chemical batch reactors. For the adaptation of the heat balance model to the respective reactor, a neural network was used to determine the corrective term in the heat balance. Results of the online testing of MoSys showed that it was able to recognize undesired faults correctly. In particular, the hazardous reactant accumulation could be detected much earlier than by a monitor based on the OLIWA-criterion for a runaway reaction. Further work is planned to develop an equivalent monitoring system for the heterogeneous hydrogenation of nitro-aromatic compounds in an industrial chemical plant.

7. References

[1]   A. Benuzzi and J. M. Zaldivar, Safety of Chemical Batch Reactors and Storage Tanks, Kluwer Academic Press, 1991, pp. 201-226

8. Notation

Notation:

A	heat transfer area
B	dynamic thermal characteristic
c_p	specific heat capacity
e	adaptation rule
E_A	activation energy
ΔH_R	molar reaction enthalpy
k	heat transfer coefficient or
k_{load}	load signal of the cooling
M	molar mass
m	mass
$\dot{m}$	mass flux
P	pressure
Q	amount of heat
$\dot{Q}$	heat rate or heat flux
r	runaway variable
R	universal gas constant
T	temperature
t	time
x	monitor variable
Z	monitor output
α_i	coefficients
Δ	difference or rise
μ	momentum
η	learning rate
τ	sampling period or time base

Index list:

accu	accumulation
App	apparatus
ad	adiabatic
Amb	ambient
c	current
cor	corrected
b	begin
D	difference
Dos	dosing
e	expected
ESA	acetic anhydride
flow	flow
in	inlet
j	jacket
i,l,k,n	variable index
loss	loss
max	maximum
mix	mixing
n	number of summation steps
out	outlet
perm	permissible
R	reaction
Rw	reactor jacket

THE SATURATION REGIME OF THE RIGA DYNAMO EXPERIMENT

Frank Stefani, Gunter Gerbeth, Thomas Gundrum,
Agris Gailitis[1], Olgerts Lielausis[1] and Ernests Platacis[1]

1. Introduction

Homogeneous dynamo action is responsible for the occurrence of planetary, stellar, and galactic magnetic fields. During the last decades, enormous analytical and numerical work had been devoted to the study of fluid dynamos. At the same time, dynamo science was suffering from the lack of any experimental possibility to verify the outcomes of numerical simulations. This situation changed on 11 November 1999 when at the Riga dynamo facility magnetic field self-excitation in a liquid metal flow was observed for the very first time. On the back-ground of an amplified external signal, a slowly growing eigenmode of the dynamo was detected for a period of 15 seconds. Growth rate and frequency of this mode were in surprisingly good correspondence with the numerical predictions. The publication [1] of this break-through has found remarkable scientific and public response [2]. For some technical reason, it was not possible to reach the saturation regime which follows the initial kinematic regime characterised by exponential growth of the magnetic field. This saturation regime was studied in a second series of experiments during 20-25 July 2000.

What is saturation, and why is its experimental investigation so important? Saturation has to do with Lenz's rule meaning that the generated field inhibits the cause of its own generation. Saturation is a very general feature of all dynamos, whether technical or cosmic ones. Typically it leads to an increase in the power which is necessary to keep the dynamo running. The interesting thing with fluid dynamos is now that it is not only the overall intensity of the fluid velocity but also its geometrical distribution which can be changed by the back-reaction of the magnetic field. Hence, the interplay between fluid dynamics and electromagnetic becomes extremely complex, and numerical simulations are still far from realistic in the descriptions of cosmic dynamos. In the Riga experiment (Fig. 1), the sodium flow is free enough to allow for interesting deformation effects. This is a remarkable advantage in comparison with the Karlsruhe dynamo facility [3] where the flow structure is extremely rigid due to the experimental design comprising 52 wall-separated spin-generators. Thus, the Riga facility provides a unique possibility to study paradigmatically the dynamo behaviour in the non-linear regime.

2. A typical run

In the July 2000 experiment, it was possible to work at considerably lower sodium temperatures and hence at higher electrical conductivities. In the following we choose one from a total of four experimental runs in order to illustrate the behaviour of the dynamo.

Fig. 2a shows the magnetic field signal which was recorded at one of the external Hall sensors (the fourth H from above in Fig. 1) during the whole run, whereas Fig. 2b depicts the signal at the internal fluxgate sensor (F in Fig. 1) only for the very beginning of the self-excitation. This

---

[1] Institute of Physics, Latvian University, Salaspils, Latvia

sensor was the most sensitive one, and the record shows clearly how an exponentially growing dynamo eigenmode emerges spontaneously out of the noise when the rotation rate crosses a critical value of about 1900 rpm (close to 130 seconds in the Fig. 2b). Whereas this fluxgate sensor was overloaded when the internal magnetic field reached 2 mT, the signal was still recorded by an internal induction coil (also at position F in Fig. 1) and by the eight external Hall sensors. Fig. 2a shows how the initial exponential growth passes into saturation with a visible amplitude dependence on the rotation rate and how the magnetic field disappears again when, at the end of the run, the rotation rate falls below the critical value.
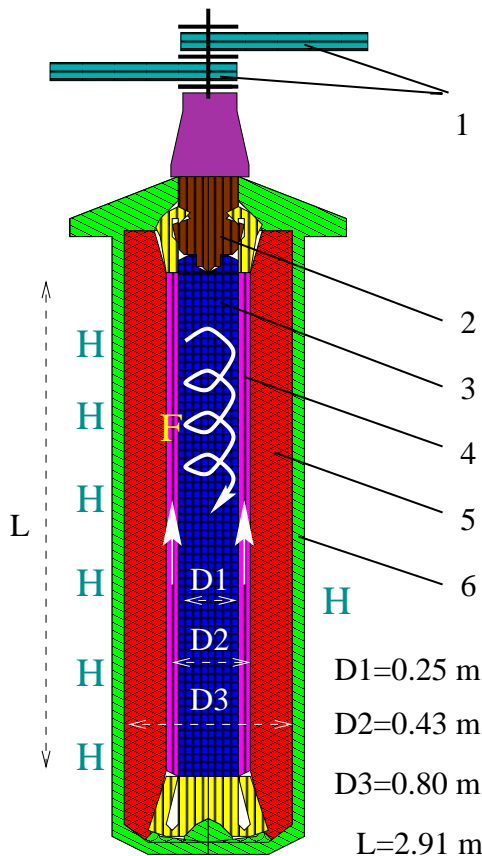
Fig.1: The central module of the Riga dynamo facility: 1-Belts to the motors; 2-Propeller; 3-Helical flow; 4-Back flow; 5-Sodium at rest; 6-Thermal insulation; 7-Hall sensors; 8-Fluxgate sensor and induction coil
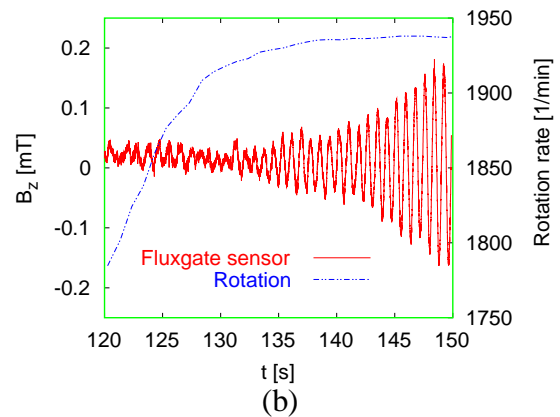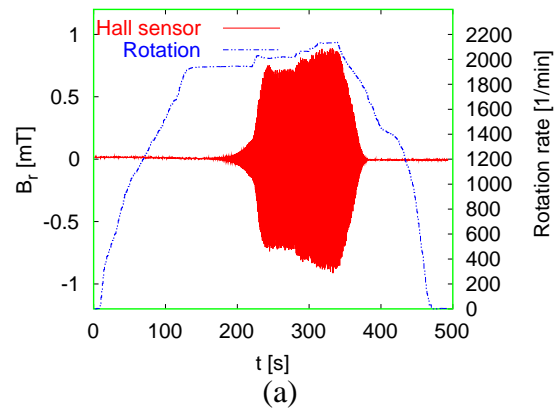
Fig. 2: One experimental run in July 2000. Radial magnetic field recorded at one of the external Hall sensors during the whole run (a), and axial magnetic field recorded at the internal fluxgate sensor during the starting phase (b).

For a period of 15 seconds within the saturation regime, Fig. 3 shows in more detail the signal recorded by the external Hall sensor. Basically it consists of an oscillation with the eigenfrequency of the dynamo, superposed by some turbulence induced noise. In the signal measured by the internal induction coil this turbulence is of course stronger expressed. Fig. 4 shows the power spectrum of the magnetic field deduced from the induction coil data. The sampling rate for the induction coil was 25 Hz so that the highest frequency shown in Fig. 4 is 12. 5 Hz. Besides the dominant peak at the eigenfrequency (1.47 Hz) there is another significant peak at the

triple frequency (4.41 Hz). The appearance of this triple mode can be attributed to the back-reaction of the Lorentz forces on the flow.
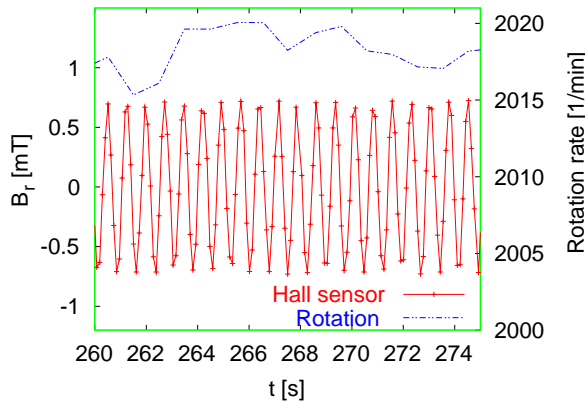
Fig. 3: External Hall sensor signal within the saturation regime.
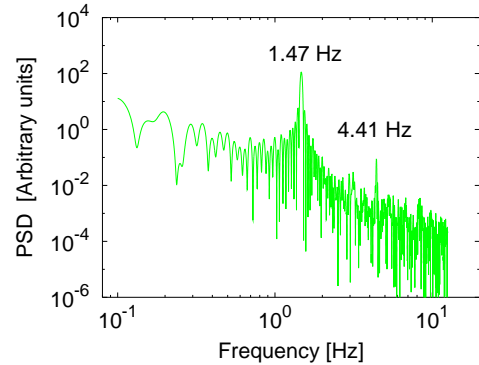
Fig.4: Power spectrum of the internally measured signal. Besides the large peak at the main frequency, the triple frequency is also shown.

3. Results

From a total of four experimental runs in July 2000, together with one run in November 1999, we have compiled the data for the growth rates and the frequencies in dependence on the rotation rate which are shown in Fig. 5. For the sake of clarity, we have rescaled all data which were recorded at different temperatures between 150°C and 215°C (and thus at different electrical conductivities) to one common reference temperature T_{ref} =157°C, for which our numerical prediction is also depicted.

(a)

(b)
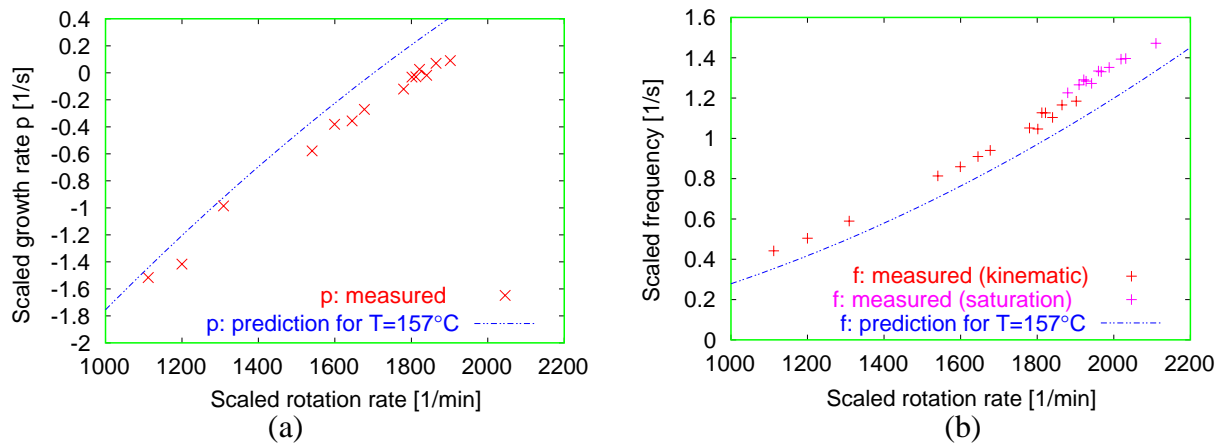
Fig. 5: Measured growth rates (a) and frequencies (b) in comparison with the numerical prediction. The red crosses are for the kinematic phase, the pink crosses are for the saturation phase (only b).

At first consider the red crosses in both figures which belong to the kinematic regime. We see that for both data, growth rates and frequencies, there is a convincing correspondence with the prediction. Relative to the prediction curve, the growth rate data are shifted by about 5 per cent to the right, the frequency data by about 5 per cent to the left.

85

As for the saturation regime, there is an interesting observation to be made in Fig. 5b. Note at first, that we have taken into account only those time intervals with a length of at least 10 seconds where a quasi-stationary behaviour is observed. Hence, the growth rate in the saturation regime is zero, and the continuation of the kinematic curve in Fig. 5a to the saturation regime should be considered as being sharply bend into a zero curve. Imagine for a moment that the only saturation effect were a homogeneous breaking of the flow so that the geometric velocity distribution would be unaffected. Then a similar sharp bend as for the growth rate should also occur for the frequency. But this is not the case. By contrast, the frequency continues to grow with the rotation rate. This must be explained by a deformation of the velocity field.

This picture becomes clearer if we consider the measured power increase and the axial deformation of the externally measured magnetic field, which are documented in [4]. It turns out that the motor power increase can be explained (even quantitatively) by the axial component of the Lorentz forces, whereas the azimuthal component of this force causes a downward accumulating decay of the flow rotation. Even without any numerical code for the non-linear regime, we can explain the observed features of the magnetic field (continuing frequency increase and axial deformation) by simply applying the kinematic code to velocity profiles deformed in the described way [4].

4. Conclusion and prospects

Considering a number of uncertainties and the complete novelty of an experiment of that sort, we were surprised that the kinematic phase of the Riga dynamo experiment turned out to be so well predictable. Actually, this can be explained by the thought-out concept and design of the whole facility and the effort spent in its optimization. The non-linear regime has already revealed a non-trivial saturation mechanism which will be studied in more depth in further experiments. Applications in the framework of various European research programs will hopefully give the necessary financial back-ground for the continuation and the broadening of these investigations.

References

[1]   A. Gailitis, O. Lielausis, S. Dement'ev, E. Platacis, A. Civersons, G. Gerbeth, Th. Gundrum, F. Stefani, M. Christen, H. Hänel, G. Will (2000), Detection of a flow induced magnetic field eigenmode in the Riga dynamo facility, Phys. Rev. Lett, 84, 4365

[2]   M. Schrope (2000), Stirring stuff, New Scientist, 20 May 2000, 7; Anon. (2000), Modeling Earth's dynamo, Science, 288, 1301; A. Jackson (2000), Critical time for fluid dynamos, Nature, 405, 1003

[3]   R. Stieglitz, U. Müller (2001), Experimental demonstration of a homogeneous two-scale dynamo, Physics of Fluids, 13, 561

[4]   A. Gailitis, O. Lielausis, E. Platacis, S. Dement'ev, A. Civersons, G. Gerbeth, Th. Gundrum, F. Stefani, M. Christen, G. Will (2001), Magnetic field saturation in the Riga dynamo experiment, Phys. Rev. Lett, 86, 3024

INSTABILITIES
OF ELECTROMAGNETICALLY LEVITATED BODIES

Janis Priede, Gunter Gerbeth and Yurii Gelfgat[1]

1. Introduction

Electromagnetic levitation is a well-known technique for container-less processing of metals and alloys both in the solid and in the molten state. The technique typically consists of one or two coils with a few windings (see Fig.1) fed by an alternating current with a frequency in the order of some 100 kHz. The alternating magnetic field interacts with eddy currents induced in the electrically conducting body and, thus, causes a repulsion between the coil and the levitated sample. In addition, the eddy currents provide a contact-less heating. In such a way metallic samples can be levitated and melted without a contacting crucible. This technique allows to avoid contamination of the melt with container material and so to achieve a considerable super-cooling of the melt before it solidifies. Nowadays electromagnetic levitation is widely used in material research for measuring of thermophysical properties of molten metals. Especially under micro-gravity conditions in space it has become a powerful technique for precise measurements of material properties like surface tension, viscosity or electrical conductivity [1]. In a kind of semi-levitation it is also in industrial use for the processing of special alloys like TiAl: the crucible contact is avoided at the side-walls without lifting up the whole melt at all.
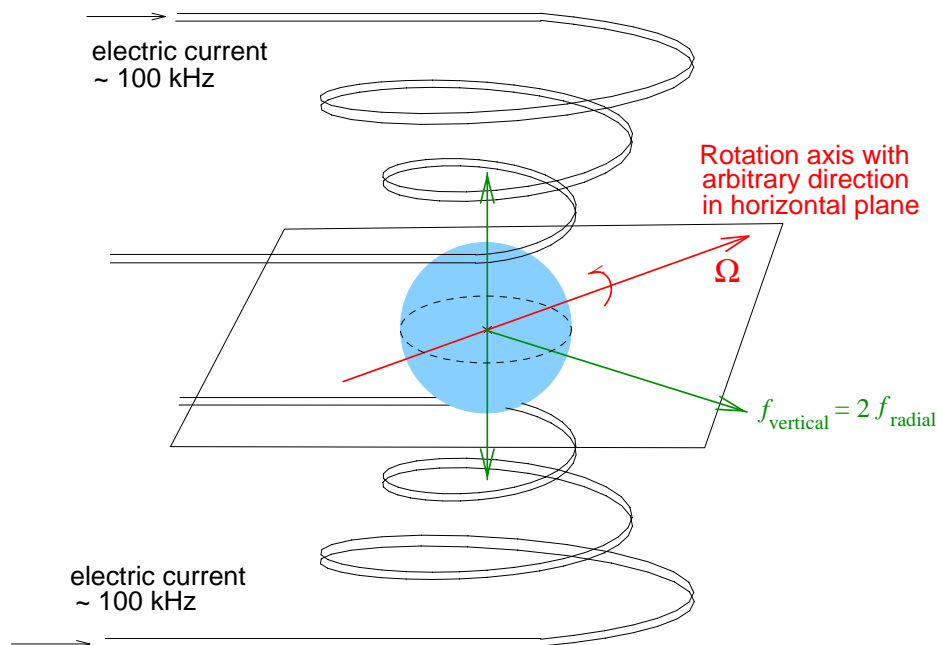
Fig. 1: Scheme of the levitation process with levitated sample (blue) and sketched instabilities: Rotations (red) and oscillations (green).

There is one essential drawback of this technique: The sample is often not at rest, it performs rotations and/or oscillations as sketched in Fig.1. These instabilities may become so strong that the overall levitation process is stopped simply due to the fact that the sample escapes from the

---

[1] Institute of Physics Riga, Latvia

coil volume. Obviously, such instabilities are undesirable. Even if they are less pronounced, they seriously disturb the intended property measurements which typically work with an induced surface oscillation of the molten sample. Therefore, there was a serious interest in analysing the reasons for those instabilities and to conclude on suitable counter measures.

We have theoretically analysed various physical mechanisms responsible for the occurrence of such instabilities [2,3,4]. Here we summarise these results and compare the predictions with model experiments performed with solid Al or Mg spheres. Finally we conclude on an active stabilisation method by means of suitable DC magnetic fields.

2. Theoretical characterisation of instabilities

Let us first briefly consider a type of instability due to the possible coupling between the electric current passing through the magnetic system and the variation of the position of the levitated body. In the regime of a fixed-voltage power supply alternating currents passing through heating and positioning coils depend on the inductance of these coils which, in turn, is influenced by the position and the geometry of the levitated body. So there is a coupling between the position of the body and the electric currents passing through the coils. Besides, each circuit operating the coil possesses its own electric relaxation time determined by the active resistance. Therefore the current is expected to depend not only on the position of the body, but also on its velocity. Such a force depending also on the velocity is evidently non-potential that implies exchange of the mechanical energy between the moving levitated body and the magnetic system. As a result, an oscillatory motion of the body may be either damped or amplified by the magnetic system depending on the characteristics of both.
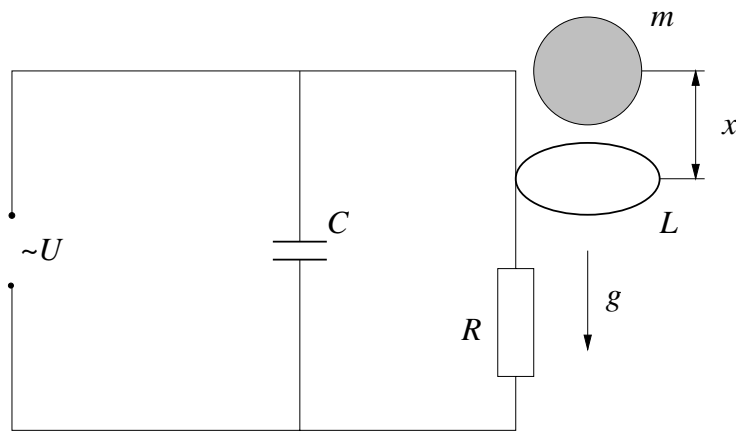
Fig. 2: Principal scheme of the electro-mechanical circuit

A sketch of the problem is shown in Figure 2. It incorporates three basic elements: an active resistance R, a coil of inductance L and a capacity C. The inductance of the magnetic system is assumed to be variable depending on the position of the levitated body denoted here by x. The possibility of such electrodynamically induced oscillations of the sample depends mainly on the relation between field frequency and the inverse of the characteristic relaxation time of the electrical circuit $\tau_0 = L_0/R$ where L_0 denotes the inductance for the static equilibrium position x = x_0. The analysis in [2] showed that in principle this type of coupling leads to oscillations of the sample, but the corresponding growth rates of that instability are usually so high that it may not be of relevance in typical levitation experiments. However, this general statement should be checked in each specific case taking into account the actual values of R, L, C and the exact type of power supply control.

Let us now consider the possibility of spontaneous rotations or oscillations of a levitated sample. Such type of instabilities may occur because of the coupling between the motion of the body and the electric currents induced in the body itself. Spontaneous means that it is of a typical linear instability character: Below some instability threshold any infinitesimal disturbance results in a force or torque on the sample driving it back to its rest state. Above this threshold this force or torque leads to a further increase of the sample motion eventually resulting in a macroscopic motion of the levitated body.

To illustrate the instability mechanism in more detail we consider the case of a rotational instability in an alternating magnetic field which far away from the spherical sample is uniform. Basically there is no torque acting on the sphere. However, this rest state might be unstable with respect to infinitesimal rotational disturbances. To describe this type of instability it is advantageous to consider the uniform alternating magnetic field as a superposition of two oppositely rotating fields. It is evident that a single rotating magnetic field creates a torque M on the body which for a spherical body could analytically be given by

$$M = \frac{18\pi}{\sqrt{2\varpi}}\left[\frac{1}{2}\frac{\sinh\left(\sqrt{2\varpi}\right)+\sin\left(\sqrt{2\varpi}\right)}{\cosh\left(\sqrt{2\varpi}\right)-\cos\left(\sqrt{2\varpi}\right)}-\frac{1}{\sqrt{2\varpi}}\right] \tag{1}$$

which for low and high frequencies reduces to

$$M \approx \frac{\pi}{5}\varpi \qquad \text{for} \qquad \varpi \ll 1,$$

$$M \approx \frac{9}{\sqrt{2\pi}}\varpi^{-1/2} \qquad \text{for} \qquad \varpi \gg 1,$$

respectively. Here $\varpi = R_0^2\mu_0\sigma\omega$ is the dimensionless frequency of the magnetic field involving the radius of the spherical sample R_0, the magnetic permeability of vacuum μ_0, the electrical conductivity σ of the sphere and the frequency of the alternating magnetic field ω. It is important to note that the torque first increases with increasing frequency whereas at higher frequencies it again decreases with further increasing ϖ.

The total torque on the sphere in an alternating field is just a superposition of two torques due to two oppositely rotating magnetic fields. For a sphere at rest the relative frequency of rotation of both fields is the same. In this case both torques acting in opposite directions are equal and, therefore, cancel each other. When the sphere rotates, the relative frequency of the co-rotating field reduces, whereas that of the counter-rotating one increases. As a result, a torque about the axis of rotation appears. Whether this torque leads to a braking or enhancing of some initial rotation of the sphere can be analysed by considering the relevant equation of motion written in a non-dimensional form as

$$\frac{d\Omega}{dt} = \frac{N}{2}(M(\varpi-\Omega)-M(\varpi+\Omega)) \approx -N\frac{dM}{d\varpi}\Omega \tag{2}$$

where Ω stands for the rotation frequency of the sphere non-dimensionalized with respect to the characteristic magnetic diffusion time $\tau_m = R_0^2\mu_0\sigma$ which is chosen as time scale for the given problem; $N = \mu_0 R_0^7 B_0^2\sigma^2/I$ is a dimensionless interaction parameter defining the characteristic ratio of electromagnetic and inertial force; $I = 2/5R_0^2 m$ is the moment of inertia of the sphere. The general solution of this equation is $\Omega = \Omega_0\exp(N\gamma t)$ where $\gamma = -dM/d\varpi$. At

negative growth rates corresponding to $dM/d\varpi > 0$ an initial perturbation will decay with time, whereas in the opposite case, it will grow leading to a spontaneous spin-up of the sphere. The threshold of instability is thus defined by $\gamma = 0$ corresponding to the frequency at which the torque due to a single rotating magnetic field attains a maximum for a fixed field strength.

The resulting curves $\gamma(\varpi)$ are given in Figure 3 both for the uniform and the linear magnetic field. The latter represents a typical positioning field, sometimes called quadrupole field. Figure 4 presents the rotation speed of the sphere as function of ϖ resulting from the balance between the clockwise- and counter-clockwise torques $M(\varpi-\Omega) - M(\varpi+\Omega) = 0$.
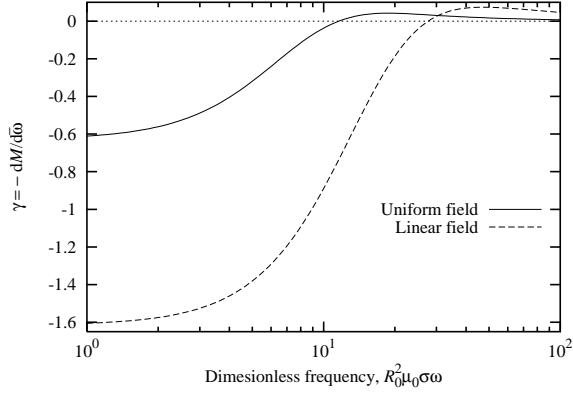
Fig. 3: Growth rate factor versus frequency for both uniform and linear magnetic fields.
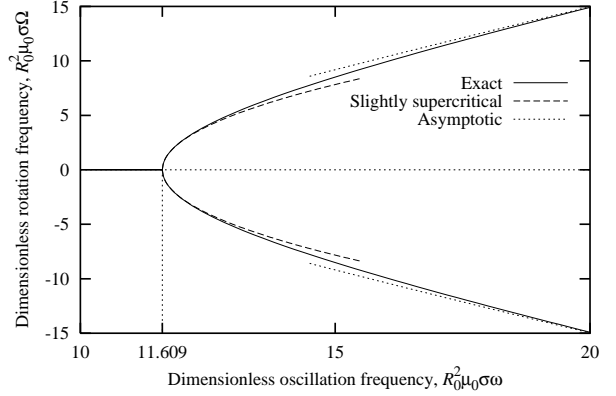
Fig. 4: Rotation rate of the sphere depending on the uniform magnetic field fre-quency.

The characteristic feature of figure 3 is that the growth rates γ exceed zero at some critical frequency ϖ_c, reach some maximum at ϖ_m and approach zero once again at higher frequencies. This shape of the curve is of principle significance when some braking mechanism is taken into account. Braking may be due to some friction with the ambient gas, or might be additionally supplied by a steady magnetic field. Upon adding a linear damping, equ. (2) takes the form

$$\frac{d\Omega}{dt} + N(\beta - \gamma)\Omega = 0 \tag{3}$$

where the dimensionless parameter $\beta > 0$ accounts for the damping. For the spin-up instability to occur, now it is necessary that $\gamma > \beta$. First, this constraint implies that with increase of damping the instability threshold is shifted to higher frequencies. Second, more important effect is that at sufficiently high frequency the growth rate factor will become smaller than any non-zero β. It means that due to an arbitrary small damping there has to be an upper frequency, above which the rest state becomes stable again.

The last and most important consequence results from the fact that γ becoming positive with increase of the frequency remains, however, bounded from above by γ_m. Consequently, any braking with $\beta > \gamma_m = 0.04209$ is sufficient to suppress the spin-up instability at all. For instance, if a steady magnetic field is used for stabilisation, it follows that for small disturbances of the angular velocity the braking due to the DC field is $\beta = \pi/5\alpha^2$, where $\alpha = B_s/B_0$ is a dimensionless parameter denoting the strength of the steady magnetic field B_s relative to that of the alternating field B_0. Now it follows that for suppression of the spin-up instability it is sufficient to impose a steady magnetic field with a relative strength of $\alpha_m \approx 0.26$. For a detailed theoretical description, including the analysis of finite amplitude disturbances, we refer to [3].

The main theoretical results might be summarised as follows: A levitated sphere may show spontaneous rotations or oscillations if the non-dimensional field frequency exceeds a critical value ϖ_c. The values are $\varpi_c = 11.609$ both for the rotational instability in a uniform field and the oscillatory instability in a linear magnetic field, but $\varpi_c = 27.682$ for a rotational instability in a linear field. There is a frequency ϖ_m at which the instability growth rate has a maximum. Those values are $\varpi_m = 18.073$ both for the rotational instability in a uniform field and the oscillatory instability in a linear magnetic field, but $\varpi_m = 47.196$ for a rotational instability in a linear field. There is no oscillatory instability in a uniform alternating magnetic field. In axially symmetric levitating fields, the rotation axis is perpendicular to the symmetry axis of the levitating field which is usually vertical. The spontaneous oscillations occur in vertical and radial directions, where the frequency of vertical oscillations is twice that of the radial ones.

The simplest way to avoid such instabilities would be to keep the non-dimensional frequency below the threshold ϖ_c. If this is not possible DC magnetic fields represent a powerful tool for an efficient active damping of all those instabilities. The DC fields must not be very strong, a strength in the order of the levitation field amplitude is sufficient. However, attention must be paid to the DC field direction. A DC field in direction of the levitating field damps rotations but not oscillations. A DC field perpendicular to the levitating field direction damps oscillations, but not rotations: the rotation axis adapts to the given DC field direction and no damping of rotation occurs anymore. Hence, sophisticated DC field geometries are necessary for an overall stabilisation of the sample.

3. Experimental results

A set of model experiments has been performed in order to verify the theoretical predictions as given above. The main goal of the experiment design was to study the stability behaviour of the levitated solid spheres just around the critical values of the non-dimensional frequency ϖ. Solid aluminium or magnesium spheres have been used, and their diameter was chosen according to the available generator frequencies and the desirable values of ϖ.

The levitating system consists of a bottom supporting coil and a top orienting (stabilising) coil with the levitated sphere between them. The coils are connected in series in such a way that the direction of currents in these coils is opposite. The interplay of an AC magnetic field with the electric currents induced by this field in the conducting sphere causes electromagnetic forces in the sphere. The sphere starts levitating if the upwards directed electromagnetic force component compensates the gravity forces on the sphere. The solid Al spheres had diameters of 10, 15, 29, 39, 50 and 59 mm, respectively. The stability behaviour was measured by visual observation of the sample, a point light source and a photodiode to measure rotational disturbances, and a set of special capacitance probes to analyse oscillatory disturbances.

For more details of the experiments and the stability results we refer to [5]. The main results can be summarised as follows:

- The levitation of the sphere is very stable for $\varpi < 8$. In that parameter range any external disturbances to the sphere are quickly damped out, the sample always goes back to its rest state within a few seconds.
- At approximately $\varpi \approx 8$ the sphere starts to oscillate.
- If ϖ exceeds about 10 the sphere starts to rotate, and the rotation rate increases with increasing frequency. High rotation rates in the order of several 100s^{-1} have been observed. At higher ϖ the sphere performs more and more complex superpositions of rotation and oscillation, destroying for $\varpi > 60$ the levitation process at all.

- In order to separate between rotations and oscillations a special pear-shaped body was levitated. For all ϖ considered this body showed no rotations due to its shape. However, oscillations developed for $\varpi > 8$ in the same way as with the spherical body.

In a second set of experiments possibilities for an active damping of the instabilities by means of additional steady magnetic fields have been investigated. Based on the theoretical investigations it was clear that application of any DC field with some pronounced direction would not lead to a full stabilisation. This was confirmed by the experiments. For instance, application of a vertical DC field reduced rotations but not the vertical oscillations. Hence, the main aspect of the solution was to look for realisations providing a DC field of high non-uniformity. This has been realised by two different approaches:

First a DC current has been superimposed to the alternating current in the levitation coil, thus providing a cusp-type DC magnetic field over the sample volume. However, this field type alone failed to deliver a total stabilisation since the rotation axis of the sphere turned around to the vertical symmetry axis, and the axisymmetric cusp field is not able to damp rotations around this axis. In order to reach a complete suppression of rotations two additional coils with ferrite cores have been applied in the horizontal mid-plane, i.e. a DC field perpendicular to the vertical axis was added. In that way a complete suppression of sample motions was achieved.

The second approach consists in the use of permanent magnets. Again, a strongly non-uniform field distribution turned out to be most efficient for an overall stabilisation. The obtained optimal configuration consists of a six-pole system of permanent magnets fastened on a common non-magnetic jacket and surrounded from outside by a common magnetic ring (see Fig. 5). Ferrite material was used to focus the field into the sample volume. This solution turned out to be very efficient for an overall stabilisation.

Fig. 5: Foto of the permanent magnet stabilization ring.

The experimental results might be summarised as follows:

- Steady magnetic fields can effectively be used to stabilise levitated samples. Full stabilisation has been obtained up to $\varpi \approx 100$. The necessary DC field strength in the sample volume is in the range of 50-80mT.
- The DC field could be provided by an electrotechnical solution, i.e. the superposition of a DC current to the levitating coil current, or by a suitable arrangement of permanent magnets. The first approach must be accompanied by an additional horizontal DC field component since otherwise rotations around the vertical axis are not damped.
- The spatial non-uniformity of the DC field is crucial for a complete damping of all sample instabilities.

4. Conclusions

We have considered various physical mechanisms which may give rise to spontaneous rotations or oscillations of levitated spherical bodies. These instabilities are characterised by a frequency threshold above which they set in spontaneously, and a frequency ϖ_m at which the growth rates attain a maximum. An active damping by means of suitable DC magnetic fields is developed. Whereas a strength of the DC field in the order of the levitating field strength is sufficient, attention must be paid to the DC field geometry. The results are verified by experiments. The possibility of an almost total stabilisation of the levitated sample has been demonstrated experimentally by two different approaches: first a DC field produced by external permanent magnets, second a DC field due to the superposition of a DC current to the alternating current in the levitating coil.

Acknowledgement

References

[1]   I. Egry, J. Szekely (1991), The measurement of thermophysical properties in microgravity using electromagnetic levitation. Adv. Space Res., 11(7), 263

[2]   J.Priede, G.Gerbeth (1999), Oscillatory and rotational instabilities in electromagnetic levitation. N.El-Kaddah, D.G.C.Robertson, S.T.Johansen, V.R.Voller (Eds.): Fluid Flow Phenomena in Metals Processing, 593, TMS, San Diego, USA

[3]   J.Priede, G.Gerbeth (2000), Spin-up instability of electromagnetically levitated spherical bodies. IEEE Transactions on Magnetics, Vol.36, No.1, 349

[4]   J.Priede, G.Gerbeth (2000), Oscillatory instability of electromagnetically levitated solid bodies. IEEE Transactions on Magnetics, Vol. 36, No.1, 354

[5]   Yu.M.Gelfgat, A.Mikelsons, A.Romancuks, G.Gerbeth (2000), Stability of levitation of solid and liquid conducting spheres in high frequency electromagnetic field. Magnetohydrodynamics, Vol.36, No.2, 167

COMPARISON OF THE IRRADIATION EFFECTS ON MICROSTRUCTURE AND MECHANICAL PROPERTIES

Jürgen Böhmert, Hans-Werner Viehrig and Andreas Ulbricht

1. Introduction

VVER-type reactor pressure vessel (RPV) steels were irradiated within an extensive irradiation programme at the VVER-2 of the Rheinsberg nuclear power plant. Subsequently they were tested by Charpy impact tests and 3-point bend tests. The results of theses investigations were already published [1-3]. The different heats of the RPV steels have proved to be differently sensible against radiation embrittlement. Whereas for some heats the ductile brittle transition temperature was hardly shifted to higher temperature, clear effects were indicated in other cases. The finding was not in correspondence to the content of copper and phosphorus known as promoting radiation embrittlement. In addition to the original working programme small angle neutron scattering (SANS) experiments have been applied to study the correlation between the effects of the irradiation on the mechanical behaviour and the microstructural evolution. The investigation is expected to provide to better understanding from the physical point of view.

The results of the SANS study and the comparison with the results of the toughness properties are presented in this paper.

2. Experimental

The material investigated comprises 7 heats:

- 4 heats of VVER 440-type RPV steel 15Kh2MFA (code: R1-R3, D25)
- 2 heats of VVER 1000-type RPV steel 15Kh2NMFAA (code: R16, R17)
- 1 heats of VVER 1000-type weld metal 10KhGNMAA (code: R19).

Most of the heats have a relatively low content of Cu and P. For every heat one set of Charpy V-notch specimens and one set of fatigue pre-cracked specimens of the same type were available in unirradiated, irradiated and, partly, annealed state. With these specimen sets the transition temperature TT related to a Charpy energy of 48 J and the reference temperature T_o according to ASTM E 1921-97 were determined. Furthermore the radiation embrittlement coefficients A_F were calculated using the Russian standard PNAE G 7-002-86 (quoted in [4]) for evaluating the effect of irradiation

$$\Delta TT = A_F \sqrt[3]{\phi} \tag{1}$$

$$\Delta TT = TT_F - TT_o \tag{2}$$

ϕ is the neutron fluence in 10^{18} n/cm², TT_F, TT_o is the transition temperature after irradiation or in the initial state, respectively. The same procedure was used for the evaluation of the reference temperature shift ΔT_o.

In Table 1 data of the material composition, the mean fluence and the results of the radiation embrittlement are summarized. More details are presented in [1-3].

Table 1: Material and radiation embrittlement parameters

Material	Code	Composition in weight-%			ϕ_{mean} [1]	ΔTT_{48J} [2] [K]	A_F	ΔT_o [K]	$A_F{}^{To}$ [3]
		Cu	P	Ni					
15kh2MFA	R1	0.10	0.011	0.27	43.6	13	3.7	-	-
	R2	0.12	0.014	0.12	80.7	32	7.4	38	8.7
	R3	0.12	0.024	0.12	45.7	47	15.1	95	25.6
	D25	0.11	0.017	0.10	127.6	76	13.1	-	-
15Kh2NMFAA	R16	0.07	0.012	1.11	46.0	65	18.1	57	16.5
	R17	0.13	0.013	1.30	72.7	124	29.7	109	26.2
10KhNGMAA	R19	0.04	0.012	1.71	65.1	191	47.5	150	37.9

[1] mean fluence, in 10^{18} n/cm² [E > 0.5 MeV] for Charpy test specimens

[2] related to Charpy energy of 48 J

[3] radiation embrittlement coefficient related to shift of T_o

SANS experiments were carried out at the SANS facilities of BENSC HMI Berlin, LLB Saclay (France) and ILL Grenoble (France). Some data of the experimental conditions are given in Table 2. Samples of the size of 10 mm x 10 mm x 1 mm cut from tested Charpy specimens were used. The SANS intensity was calibrated and processed by the software routines of each SANS facility. As the result of the data processing the nuclear and magnetic macroscopic scattering cross section $d\Sigma/d\Omega$ were determined. Under the assumption that the scattering structural defects are non-ferromagnetic, the volume fraction and the size distribution of the scatter can be estimated. For this the indirect Fourier transformation method according to Glatter [5] was used.

Table 2: SANS experimental conditions

Equipment	BENSC V4	D11	PAXE
Wave length / nm	0.6	0.5	0.5 / 0.6
Sample detector distance / m	1.1 / 4.0	1.1 / 4.0 / 16.0	1.5 / 5.0
Collimation length / m	2.0 / 4.0	2.5 / 4.0 / 16.5	2.0 / 5.0
Detector	2 d position-sensitive detector		
Magnetic field	1.4 T		

3. Results

For every heat the SANS intensity within the range of scattering vector Q of 0.8 – 3 nm⁻¹ is higher in the irradiated condition than in the unirradiated condition. Annealing reduces the intensity to a level near the level of the unirradiated state. Fig. 1 (left) shows the scattering curves of heat R19, which exhibits the highest radiation embrittlement coefficient, in the different conditions as an example. In Fig. 1 (right) the concerned volume fraction size distributions are depicted. Irradiation produces a high volume fraction of scattering microstructural defects in the range of a radius between 0 and 2 nm with a sharp maximum near approx. 1 nm. The volume fraction of these defects is clearly different for the heats investigated whereas the shape of the distribution and the position of the maximum is independent of the material. In principle, the highest volume fractions are measured for the VVER 1000-type base and weld metals. A general trend is observed: the higher the fluence the higher the volume frac-

tion (Fig. 2). Finally, the heats are distinguished by the A-ratio. The A-ratio is calculated as the ratio between the total SANS cross section to the nuclear contribution of the SANS cross section and contains information about structure and composition of the scattering defects. The results of the SANS experiments are given in Table 3.
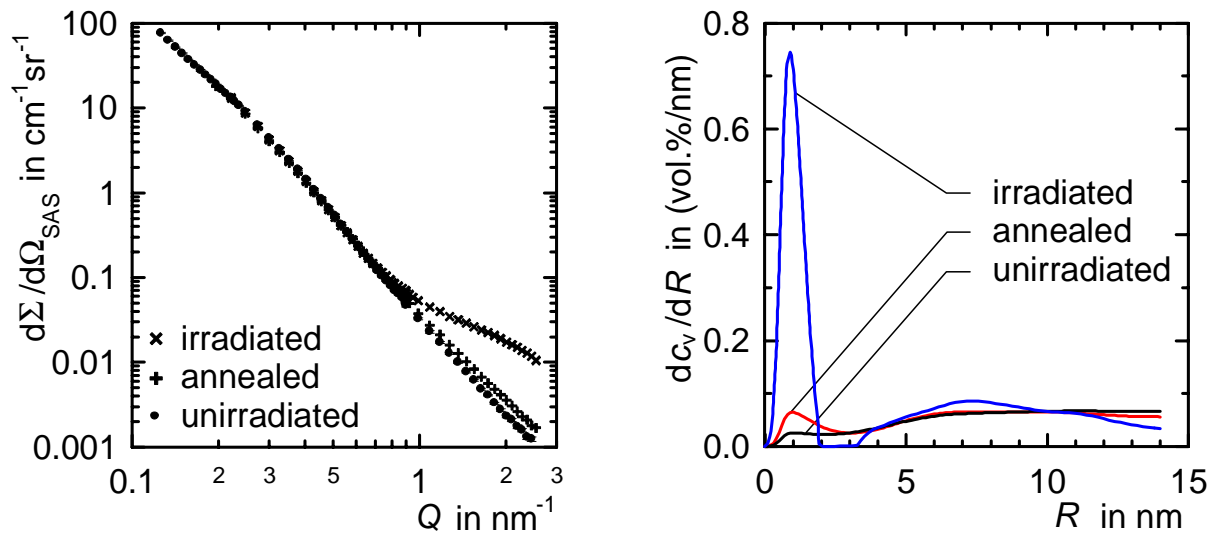
Fig. 1: Macroscopic SANS cross section (left) and volume-fraction-related size distribution of the scattering defects (right) for VVER 1000-type weld metal 10KhNGMAA (code R19) in different conditions
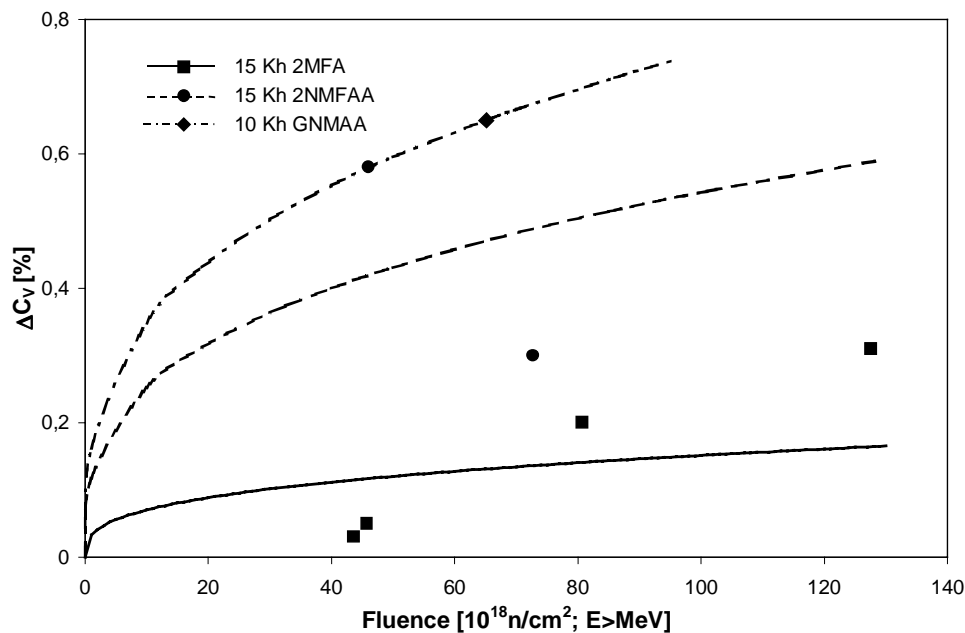
Fig. 2: Fluence dependence of the volume fraction of the irradiation-induced microstructural defects for the different heats
(The line is the average curve according to equ. 1 for each RPV steel class.)

Assuming the difference between the volume fraction of nano-scaled microstructural defects as an microstructural indicator for the radiation sensitivity of the steels, the microstructure-related radiation coefficient A_F^{MS} can be defined, in analogy to the radiation embrittlement coefficient A_F according to equ. 1. The value is also given in Table 3.

Table 3: Analysis results of SANS experiments

Material	Fluence [10^{18} n/cm²]	R_{max} [1] [nm]	C_v [%]	ΔC_v [2] [%]	A-ratio	A_F^{MS} [3] [10^{-2}]
R1 U		1.1	0.29		2.5	
I	43.6	1.0	0.32	0.03	2.2	0.85
R2 U		> 4	0.05		2.2	
I	80.7	1.0	0.25	0.20	2.1	4.63
R3 U		1.2	0.23		2.2	
I	45.7	1.2	0.28	0.05	2.4	1.40
D25 U		> 4	0.04		2.1	
I	127.6	1.0	0.35	0.31	1.7	6.16
R16 U		> 4	0.08		2.6	
I	46.0	1.0	0.66	0.58	2.5	16.19
R17 U		> 4	0.09		2.4	
I	72.7	0.9	0.39	0.30	2.8	7.19
R19 U		> 4	0.03		2.8	
I	65.1	0.9	0.68	0.65	2.8	16.16

U – unirradiated, I – irradiated
[1] radius at maximum of size distribution
[2] difference between irradiated condition and the unirradiated state
[3] ratio between total and magnetic scattering cross section
[4] A_F related to Δc_v according to equ. (1)

Fig. 3 compares the radiation embrittlement coefficient A_F related to the Charpy energy 41 J or T_o with the microstructure-related coefficient. Obviously, there is a correlation between these parameters. However, some heats deviate remarkably. In particular the VVER 1000-type RPV steel of the heat R16 shows a strong microstructural effect but low shift of the transition temperature due to radiation.
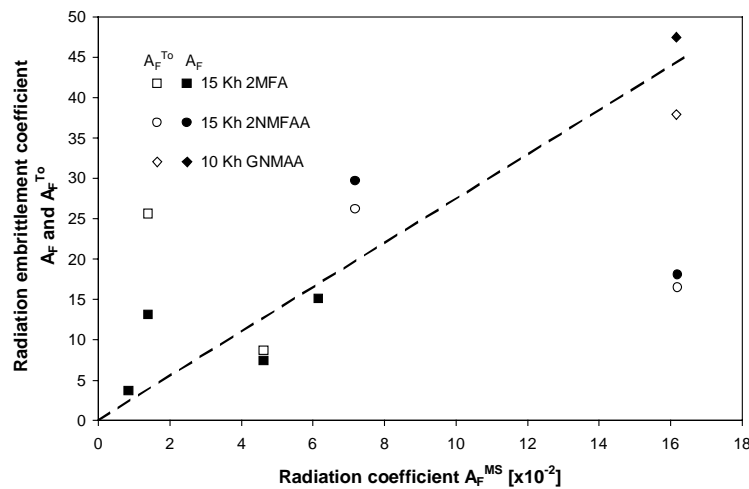
Fig. 3: Comparison of the radiation embrittlement coefficients A_F and A_F^{To} with the microstructure-related radiation coefficient A_F^{MS}

The transition temperature is a very complex parameter which is influenced by complicated microstructural mechanisms. A more direct relation to the microstructure can be presumed for the radiation hardening as represented by the hardness. The correlation to this parameter is given in Fig. 4. Regarding the irradiation-induced changes of the hardness, heat R16 fits the general trend. For the heats of VVER 440-type RPV steel the hardening effect seems to be larger. This is evident particularly for the heats 1 and 3 which already have a high volume fraction of small defects in the unirradiated initial state. As the A-ratio of these heats is lower than the A-ratio of the other heats, it is obvious that the radiation-induced microstructural features of the Ni-poor VVER 440-type RPV steels are not identical with the ones of the Ni-rich VVER 1000-type RPV steels.
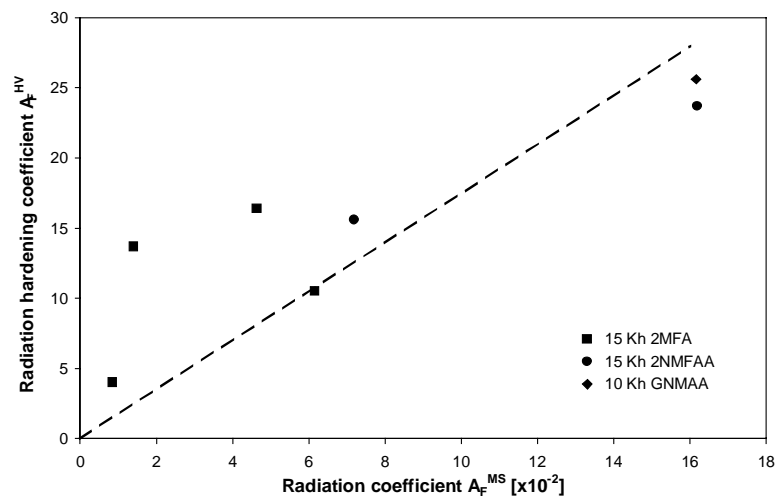
Fig. 4: Comparison of the radiation hardening coefficient H_F^{HV} and the microstructure-related radiation coefficient A_F^{MS}

In summary, the study proves that the volume fraction of small microstructural features with a radius near 1 nm induced by neutron irradiation correlates with the radiation effect on the shift of the transition temperatures or the changes of the hardness. The volume fraction, however, is not the only parameter that governs irradiation embrittlement and hardening.

References

[1]   J. Böhmert, H.-W. Viehrig, H. Richter (2000): Bestrahlungsverhalten von WWER-Druckbehälterstählen - Erste Ergebnisse aus dem Bestrahlungsprogramm Rheinsberg, Jahrestagung Kerntechnik 2000, Bonn, Tagungsbericht, S. 591

[2]   H.-W. Viehrig, J. Böhmert, J. Dzugan (2000): Bewertung des Bestrahlungsverhaltens russischer WWER-Reaktordruckbehälterstähle, 26. MPA-Seminar, Stuttgart, Okt. 2000, Proc. 20.1-20.20

[3]   J. Föhl, T. Weißenberg (1999): Einfluss der Neutronenbestrahlung auf die Werkstoffeigenschaften sowjetischer RDB-Stähle, Abschlussbericht, Staatliche Materialprüfanstalt (MPA) Universität Stuttgart, Bericht-Nr. 872701005, März

[4]   R. Gerard (1995): Survey of National Regulatory Requirements, AMES Report No. 4, Brussels, EUR 16305 EN

[5]   O. Glatter (1980): Determination of particle-size distribution functions from small-angle scattering data by means of the indirect transformation methods, J. Appl. Cryst. 13, 7

VERIFICATION OF NEUTRON TRANSPORT CALCULATIONS FOR NONSTANDARD PRESSURE VESSEL SURVEILLANCE POSITIONS IN THE VVER-1000 NOVOVORONEZH-5

Bertram Böhmer, Ernst Brodkin[1], Alexei Egorov[1], Jörg Konheiser, Eckhard Polke[2], Victor Vikhrov[1] and Sergei Zaritsky[1]

1. Introduction

To survey the embrittlement of the reactor pressure vessel, capsules with Charpy specimens made of pressure vessel steel are irradiated during reactor operation. In the present experiment assemblies of specimens were irradiated during the 17th fuel cycle in five baffle channels of the Novovoronesh VVER-1000. These positions are somewhat below the VVER-1000 standard surveillance positions. This is a region of strong radial and vertical flux gradients where the exact calculation of fluences for the irradiated specimens is much more difficult than for the pressure vessel. Therefore, an investigation program was performed aimed at testing the ability to determine reliably the neutron fluences of the specimens. Three independent fluence and activity calculations were performed by the Russian Research Center "Kurchatov Institute" Moscow (KI), by the Forschungszentrum Rossendorf (FZR) and by the Siemens Nuclear Power GmbH, Erlangen (SIE). Each institution used another calculation methodology. The calculation results were compared with each other and with neutron induced activities of detectors in special monitors as well as with the ^{55}Mn-activities of the irradiated specimens itself. First results of the intercomparisons are presented in the following. The work was supported by a TACIS project of the European Union.

2. Experiment and Calculation Methods

The location of the assemblies with irradiation capsules at three height levels is illustrated in Fig. 1. As example, Fig. 2 shows the arrangement of specimens and neutron monitors for assembly 3, level 2. Each monitor contained Fe, Cu and Nb activation detectors, from wich up-to-now only the ^{54}Fe(n,p) and ^{63}Cu(n,α) detectors had been evaluated. Contrary to expectations, the activities measured in assembly 3 were not symmetric relative to the core center direction. The asymmetry was obviously caused by a turn of the assembly around the channel axis by some degrees. In the following comparisons the experimental activities of the outer monitors and specimens had been corrected for that effect assuming a linear dependence of the fluence from the angle. So, for instance, the corrected activities for monitor 1 at Fig. 2 are obtained by $A(1)^{corr} = (A(1)+A(3)) / 2$.

The fluence and activity calculations for the five irradiated assemblies were performed independently by the three institutions using the same pin by pin source distributions, geometry data and material compositions, delivered by KI. KI obtained three-dimensional fluence distributions by synthesis of (r-θ), (r-z) and r calculation results from the S_N-codes DORT [1] and ANISN with the 47-group neutron data library BUGLE-96 [2]. For different levels and assemblies six (r-θ)- and two (r-z)-models have been used. The calculations of SIE were performed by the three-dimensional S_N-code TORT [3] with BUGLE-96. FZR used an improved version of the Monte Carlo Code TRAMO [4] and 123 group data generated on the basis of

---

ENDF/B-VI. Different to the S_N calculations, the region above the core was modelled more exactly on the base of detailed drawings also received from KI. For the following intercomparison results for assembly 3 were selected because only for that assembly experimental monitor data were available.
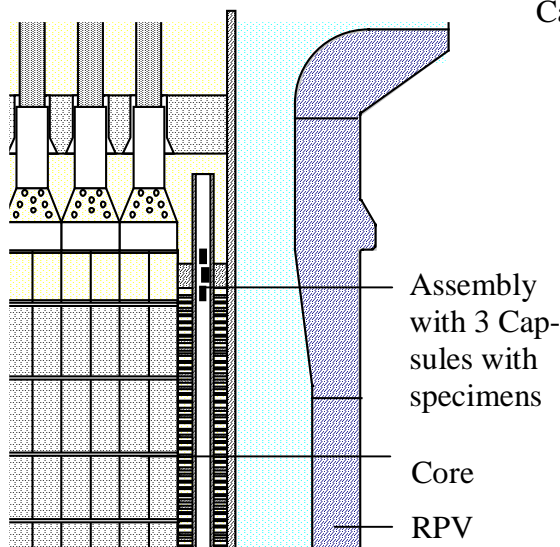
Fig. 1: Location of irradiated assemblies
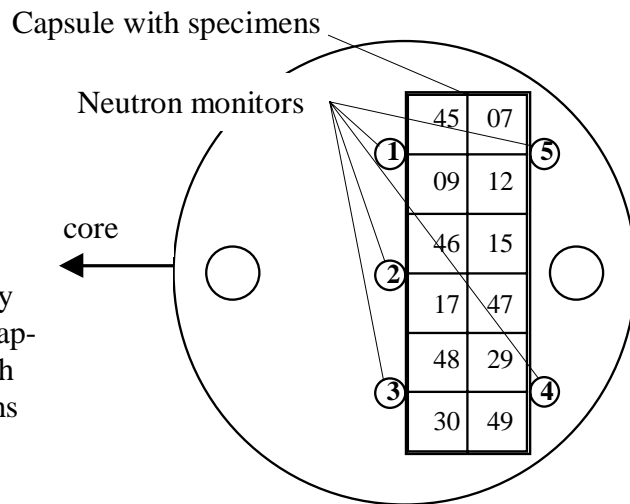
Fig. 2: Cross section of assembly 3 at level 2

3. Comparison of Calculated Fluence Integrals

The calculated fluence integrals above 0.5 MeV, the most important fluence characteristics for the neutron embrittlement of VVER pressure vessels, are given in Table 1 for the monitor positions and in Table 2 for the middle regions of the specimens. The agreement between the results of the three calculations is very close, considering the complexity of the problem, the different methodologies and partly different data bases. The maximum relative deviations of results for single points from the mean values of the three calculations is 6% for the monitors and 8% for the specimens. For the mean values of all monitors the corresponding maximum relative deviations are 4% for the monitors and 6% for the specimens.

4. Comparison of Calculations and Experiments

The results of the comparisons between calculated (C) and corrected measured (E) End Of Irradiation (EOI) activities are given in Tables 3 and 4 for the ^{54}Fe(n,p)^{54}Mn and ^{63}Cu(n,α)^{60}Co detectors, respectively, and in Table 5 for the ^{54}Mn EOI-activities of the specimens. The relative standard deviations of the measured activities are 4%.

The agreement between the three calculations and between the calculations and experiments is rather close for the ^{54}Fe(n,p)^{54}Mn detectors (Table 3). For the ^{63}Cu(n,α)^{60}Co reaction (Table 4) the agreement is worse. The calculated activities are on the average 20% less than the experimental ones, whereby these differences amount to 24% and 22% for the FZR and KI results, but only 14% for the SIE results. The largest deviations of C/E from 1 (up to 38%) are

Table 1: Calculation results for fluence integrals $\Phi_{E>0.5\ \text{MeV}}$ for the monitor positions

Monitor name	$\Phi_{E>0.5\ \text{MeV}}$ in units of 10^{19} n/cm^2				FZR/Mean	SIE/Mean	KI/Mean
	FZR	SIE	KI	Mean of FZR,SIE,KI			
7p	1.94	2.07	2.08	2.03	0.96	1.02	1.02
6p	1.44	1.45	1.48	1.46	0.99	1.00	1.02
1	2.81	3.03	3.04	2.96	0.95	1.02	1.03
2	2.8	3.04	3.03	2.96	0.95	1.03	1.02
3	2.79	3.03	3.04	2.95	0.94	1.03	1.03
5	2.03	2.1	2.18	2.10	0.97	1.00	1.04
4	2.01	2.1	2.18	2.10	0.96	1.00	1.04
0	5.24	5.68	5.14	5.35	0.98	1.06	0.96
8	5.17	5.63	5.11	5.30	0.97	1.06	0.96
6	5.22	5.68	5.14	5.35	0.98	1.06	0.96
p0p	3.7	3.79	3.5	3.66	1.01	1.03	0.96
8p	3.65	3.77	3.44	3.62	1.01	1.04	0.95
7	3.65	3.79	3.5	3.65	1.00	1.04	0.96
Mean of monitor positions:					**0.97**	**1.03**	**1.00**

Table 2: Calculation results for fluence integrals $\Phi_{E>0.5\ \text{MeV}}$ for the Charpy specimens

Level	Charpy Specimen No	$\Phi_{E>0.5\ \text{MeV}}$ in units of 10^{19} n/cm^2 Mean of FZR,SIE,KI	FZR / Mean	SIE / Mean	KI / Mean
3	54	1.95	0.93	1.00	1.07
	53	1.97	0.94	1.02	1.04
	52	1.97	0.94	1.02	1.04
	51	1.95	0.94	1.00	1.06
	27	1.72	0.95	0.99	1.05
	55	1.73	0.95	1.01	1.04
	28	1.73	0.95	1.01	1.04
	31	1.71	0.95	1.00	1.06
	Mean of Level 3:		**0.94**	**1.01**	**1.05**
2	09	2.87	0.94	1.02	1.04
	45	2.83	0.93	1.03	1.04
	07	2.47	0.93	1.03	1.04
	12	2.49	0.94	1.02	1.03
	17	2.88	0.94	1.03	1.03
	46	2.88	0.94	1.03	1.03
	15	2.50	0.94	1.02	1.03
	47	2.50	0.94	1.03	1.03
	30	2.82	0.92	1.03	1.04
	48	2.86	0.94	1.03	1.04
	29	2.49	0.94	1.03	1.04
	49	2.47	0.92	1.03	1.04
	Mean of Level 2:		**0.94**	**1.03**	**1.04**
2 + 3	Mean of Levels 2 and 3:		**0.94**	**1.02**	**1.04**

found at the first level most closely to the core. However, the contribution of neutrons to the interesting fluence integral above 0.5 MeV is very small, as the ^{63}Cu(n,α)^{60}Co reaction is sensitive only for neutron energies above 6 MeV. Partly, these discrepancies could be caused by a ^{59}Co impurity in the copper used as activation detector. The reason for the differences between the calculation results could be the use of different fission spectra.

Table 3: C/E-comparison of EOI-activities for the ^{54}Fe(n,p)^{54}Mn detectors

Level/ Monitor name		EOI-activity in 10^8 Bq/g ^{54}Fe		C/E		
		Experiment	Experiment corrected (E)	FZR	SIE	KI
3	7p	2.26	2.26	1.12	1.13	1.10
	6p	1.54	1.54	1.09	1.16	1.06
2	1	3.16	3.48	1.13	1.07	1.11
	2	3.66	3.66	1.07	1.02	1.06
	3	3.8	3.48	1.12	1.07	1.11
	5	2.1	2.32	1.07	1.12	1.05
	4	2.53	2.32	1.06	1.12	1.05
1	0	5.9	6.64	1.06	1.05	1.01
	8	6.67	6.67	1.04	1.04	1.00
	6	7.37	6.64	1.06	1.05	1.01
	p0p	4.53	4.81	0.93	0.97	0.88
	8p	4.08	4.08	1.07	1.14	1.01
	7	5.09	4.81	0.92	0.97	0.88
Mean C/E:				**1.057**	**1.070**	**1.026**
Mean absolute deviation from 1.0:				**0.081**	**0.080**	**0.063**

Table 4: C/E-comparison of EOI-activities for the ^{63}Cu(n,α)^{60}Co detectors

Level/ Monitor name		EOI-activity in 10^5 Bq/g ^{63}Cu		C/E		
		Experiment	Experiment corrected (E)	FZR	SIE	KI
3	7p	3.8	3.8	0.88	0.96	0.90
	6p	2.93	2.93	0.74	0.87	0.77
2	1	5.9	6.37	0.81	0.84	0.83
	2	6.12	6.12	0.87	0.87	0.87
	3	6.83	6.37	0.82	0.84	0.83
	5	3.71	4.05	0.80	0.91	0.82
	4	4.38	4.05	0.81	0.91	0.82
1	0	10.9	12.45	0.69	0.80	0.71
	8	13.5	13.5	0.62	0.74	0.66
	6	14	12.45	0.70	0.80	0.71
	p0p	7.06	7.36	0.74	0.91	0.76
	8p	7.79	7.79	0.70	0.85	0.70
	7	7.66	7.36	0.74	0.91	0.76
Mean C/E:				**0.763**	**0.864**	**0.779**
Mean absolute deviation from 1.0:				**0.237**	**0.136**	**0.221**

For the ^{55}Mn-activities of the specimens (Table 5) the mean deviations of C/E from 1 are similar to these of the monitors with the exception of the SIE results being on the average 10% higher than the FZR and KI results. To demonstrate the effect of the correction of the experimental activities, for the case of the FZR results the values of C/E$_{uncorrected}$ are given too. In Tables 6 and 7 the experimental and calculated attenuation coefficients, i.e. relations between activities of monitors at the core side of the specimens (M_{co}) to the monitors located at the other side of the specimens (M_{ot}), are given together with the corresponding C/E-values. The agreement between the calculated attenuation coefficients is better than 10%, the maximum discrepancy to the experiment is 21%.

Table 5: C/E-comparison of EOI-activities of ^{54}Mn of specimens of assembly 3

| Level | Charpy Specimen No | EOI-activities in 10^8 Bq/g ^{54}Fe | | C / UE | C/E | | |
		Experiment uncorr. (UE)	Experiment corrected (E)	FZR	FZR	SIE	KI
3	54	2.16	2.015	1.02	1.10	1.19	1.10
	53	1.98	1.980	1.13	1.14	1.25	1.13
	52	1.96	1.960	1.15	1.15	1.26	1.14
	51	1.87	2.015	1.19	1.11	1.19	1.10
	27	1.70	1.785	1.11	1.06	1.18	1.04
	55	1.72	1.720	1.08	1.08	1.25	1.06
	28	1.84	1.840	1.01	1.01	1.17	0.99
	31	1.87	1.785	1.01	1.06	1.18	1.04
	Mean			**1.09**	**1.09**	**1.21**	**1.07**
	Mean absolute deviation from 1.0:			**0.09**	**0.09**	**0.21**	**0.07**
2	09	3.08	3.325	1.13	1.04	1.09	1.04
	45	2.85	3.345	1.21	1.03	1.07	1.03
	07	2.43	2.785	1.17	1.02	1.13	1.01
	12	2.58	2.820	1.08	0.99	1.11	1.00
	17	3.33	3.330	1.03	1.03	1.09	1.04
	46	3.30	3.300	1.04	1.04	1.10	1.05
	15	2.67	2.670	1.03	1.03	1.18	1.05
	47	2.76	2.760	0.99	0.99	1.14	1.02
	30	3.84	3.345	0.88	1.01	1.07	1.03
	48	3.57	3.325	0.97	1.04	1.09	1.04
	29	3.06	2.820	0.91	0.99	1.11	1.00
	49	3.14	2.785	0.89	1.00	1.13	1.01
	Mean			**1.03**	**1.02**	**1.11**	**1.03**
	Mean absolute deviation from 1.0:			**0.03**	**0.02**	**0.11**	**1.04**
2 + 3	Mean			**1.05**	**1.05**	**1.15**	**1.04**
	Mean absolute deviation from 1.0:			**0.09**	**0.05**	**0.15**	**0.05**

Table 6: Calculated (C) and experimental (E) attenuation for ^{54}Fe(n,p)^{54}Mn

Level	M_{co} / M_{ot}	Attenuation coefficients A_{Mc}/A_{Mo}				C/E of attenuation coeff.		
		Exper.	FZR	SIE	KI	FZR	SIE	KI
3	7p / 6p	1.47	1.50	1.42	1.51	1.02	0.97	1.03
2	3 / 4	1.50	1.59	1.44	1.59	1.06	0.96	1.06
	1 / 5	1.50	1.59	1.44	1.59	1.05	0.96	1.05
1	6 / 7	1.45	1.59	1.50	1.58	1.10	1.04	1.09
	8 / 8p	1.63	1.58	1.49	1.62	0.97	0.91	0.99
	0 / p0p	1.30	1.58	1.50	1.58	1.21	1.15	1.21
1+2+3	Mean C/E:					**1.07**	**1.00**	**1.07**
	Mean absolute deviation from 1.0:					**0.08**	**0.06**	**0.08**

Table 7: Calculated (C) and experimental (E) attenuation for ^{63}Cu(n,p)^{60}Co

Level	M_{co} / M_{ot}	Attenuation coefficients A_{Mco}/A_{Mot}				C/E of attenuation coeff.		
		Exper.	FZR	SIE	KI	FZR	SIE	KI
3	7p / 6p	1.30	1.53	1.43	1.50	1.18	1.10	1.16
2	3 / 4	1.56	1.58	1.44	1.59	1.02	0.93	1.02
	1 / 5	1.59	1.59	1.44	1.59	1.00	0.91	1.00
1	6 / 7	1.83	1.59	1.50	1.58	0.87	0.82	0.87
	8 / 8p	1.73	1.52	1.49	1.63	0.88	0.86	0.94
	0 / p0p	1.54	1.58	1.50	1.58	1.03	0.97	1.02
1+2+3	Mean C/E:					**1.00**	**0.93**	**1.00**
	Mean absolute deviation from 1.0:					**0.08**	**0.06**	**0.08**

5. Conclusions

Considering the positions of monitors and specimens in a region of high flux gradients all three calculation methodologies agreed surprisingly well among each other and with ^{54}Fe(n,p)^{54}Mn activation data. Existing discrepancies, especially for the ^{63}Cu(n,p)^{60}Co detectors, can be explained by experimental errors, the not very detailed model input and uncertainties of the nuclear data.

References

[1]   DOORS 3.2 (1993), One-, Two- and Three-Dimensional Discrete Ordinates Neutron/Photon Transport Code System, RSIC Code Package CCC-650, Oak Ridge, Tennessy

[2]   J.E. White et al., BUGLE-96 (1996), Coupled 47 Neutron, 20 Gamma-Ray Group Cross Section Library Derived from ENDF/B-VI for LWR Shielding and Pressure Vessel Dosimetry Applications," RSIC Data Library Collection, DLC-185

[3]   Rhoades, Childs (1993), TORT/DORT: Two- and Three-Dimensional Discrete Ordinates Transport, Version 2.7.3., RSIC Code Package CCC-543, ORNL, Oak Ridge, Tennessy

[4]   H.-U. Barz, J. Konheiser (1998), Monte-Carlo Programm TRAMO - Möglichkeiten und Anleitung zur Nutzung , FZR-245, Rossendorf

INVESTIGATION OF CALCITE DISSOLUTION UNDER SATURATED AND UNSATURATED WATER CONDITIONS

Roland Küchler, Klaus Noack and Torsten Zorn

1. Introduction

In recent years a system of numerical codes was developed that calculates the water and radio-nuclide transport through unsaturated soil. The main application will be the calculation of the radio-nuclide transport through the dumps left behind by the former uranium mining in Saxony and Thuringia. The water of the rainfall penetrating into the dump on its flow path dissolves various minerals among them also those containing radio-nuclides and transports the reacting species through the dump possibly down to the ground water. The developed code system is based on a number of appropriate models describing the complex physical and chemical processes in a mathematical way. These models and the parameters required by them have to be verified by experiments. Although not resembling the full complexity of a natural system batch and column experiments play an important role regarding the research in this field in general and especially with respect to the code verification. By suitable modelling the experiments may be focussed on certain single effects. Therefore, last year a laboratory was built which allows to carry out batch and modelled column experiments.
This contribution reports on the first experiments performed, presents and discusses the most important experimental results and compares them with results of computations.

2. Goal and description of batch and column experiments

The goal of the present experimental investigations of the dissolution of several minerals consists in:
- the partial verification of dissolution rate laws given in the literature for water saturated conditions by batch experiments,
- the verification of the applicability of the known dissolution rate laws in the source terms of the radio-nuclide transport through the unsaturated zone.

For both types of experiments the mineral is crushed and sized by dry sieving to a typical grain size. For the batch experiments a certain mass (a few grams) of the mineral powder is mixed with sufficient MilliQ-water in a flask. It is permanently shaken to keep the mineral particles in suspension. The electrolytic conductivity of the solution is measured by a conductivity meter in a predefined time sequence. This quantity is a measure of the ion concentration produced by the mineral dissolution. So, it gives the possibility to check the dissolution rate laws for saturated conditions.

In column experiments sea sand is used as an inert matrix which has to hold the mineral grains and to form the water flow. Its chemical inertness must be checked for the mineral-water system which is to be investigated. The grain size of the sand has been chosen from the "fine sand" class. Two types of columns are presently in use: the "1 m – column" and the "0,5 m - column" which are schematically depicted in Fig. 1. They are filled with a homogeneous mixture of sand and mineral. Peristaltic pumps control the feeding of distilled water at the heads of the columns. Fraction collectors at the column feet take samples from the solution leaking the columns. Both columns are equipped with in-situ conductivity electrodes which

are equally distributed over the height. The 1 m – column has additionally pH-electrodes in the same height positions. These in-situ measurements give information on the chemical composition of the solution which results from the mineral dissolution and from the interactions of the various species appearing in the water phase. The foot of the 1 m – column is kept under saturated conditions. The water saturation s in the volume above it covers the range $0 \leq s \leq 1$. By contrast the 0,5 m – column is to form a saturation profile which is nearly constant over the height. For that a vacuum pump at the foot produces the necessary subpressure [1].

The results of the in-situ measurements and of the chemical analysis of the leaking solution are compared with the numerical solutions of the radio-nuclide transport through the column. This comparison allows to judge about the applicability of the source terms used in further calculations.
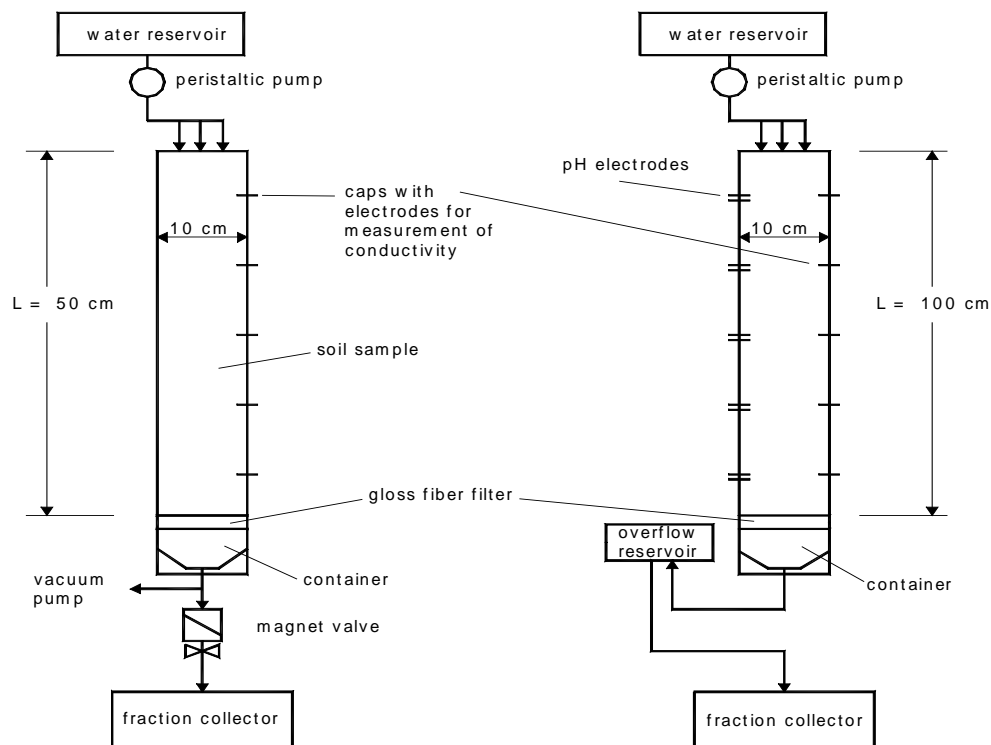
Fig. 1: Principal schemes of the column tests for the investigation of weathering processes

3. Batch and column experiments with calcite

The calcite used in the experiments is a natural double spar from Mexico Creel. Before the experiments were started, the calcite powder was investigated with Scanning Electron Microscopy/Energy Dispersive Spectrometry (SEM/EDS) and X-ray Powder Diffraction (XRD) and the calcite solution with Inductively Coupled Plasma-Mass Spectrometry (ICP/MS) to check the purity of the mineral. No essential impurities were observed. The calcite was prepared in the following way. After crushing and dry sieving the grain size was in the range between 63 and 200 µm. Then the powder was washed with MilliQ-water and dried to remove small particles. To clean up the minerals of possible impurities and to remove strong adhesive

micro-particles, the samples mixed with MilliQ-water were additionally heated up to 65 °C and the suspension was bubbled by 100 % CO_2 [2]. The calcite powder prepared in this way was used in batch and column experiments.

In the first series of column experiments sea sand with a Gaussian grain size distribution with the mean of 196 µm and a variance of 48 µm is used as inert matrix. To achieve inertness of the sand against the calcite-water solution it was washed with NaOH and after that with MilliQ-water because the reaction of the calcite solution will be basic. The calcite powder and the sand were mixed in the ratio of 5 g per 1 kg.

To observe the dissolution of calcite in batch experiments a defined mass of several grams of this powder was mixed with 400 ml MilliQ-water and the electrolytic conductivity κ was recorded. Fig. 2 illustrates the influence of the powder preparation. The equilibrium values
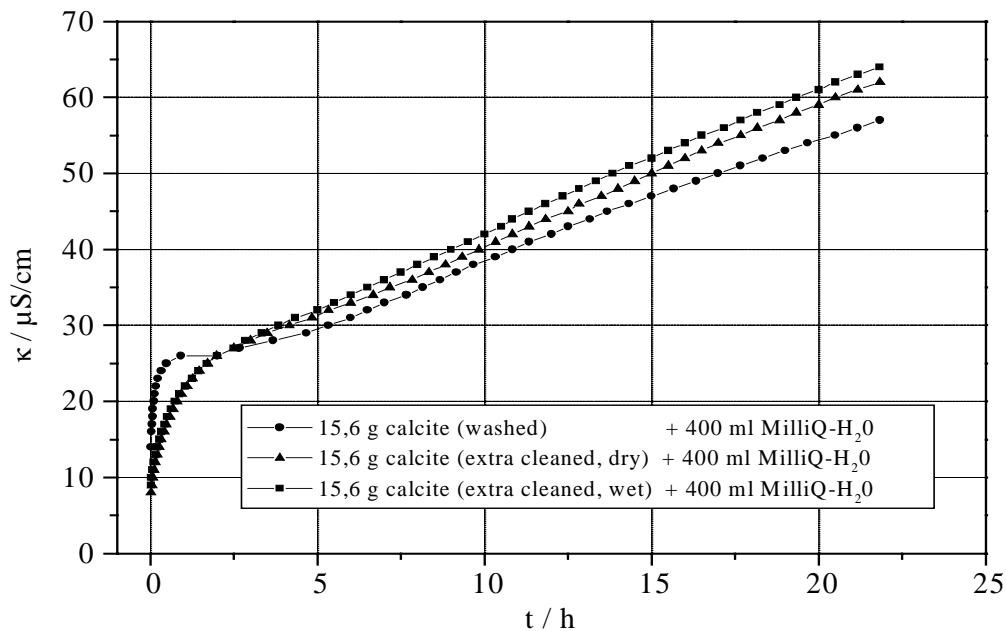
Fig. 2: Electrolytic conductivity κ of the calcite-water solution in dependence on time measured in batches with differently prepared calcite powders

are relatively close to each other: 110, 105, 107 µS/cm for calcite washed, extra cleaned dry and wet, respectively. They well compare with the calculated value of $\kappa=109,5$ µS/cm. But in the start phase the powder which was not extra cleaned, in contrast to the others, shows a steep rise followed by a relatively flat transition to the steady approach to equilibrium. In [2] this fact was explained as consequence of a surface contamination of the powder by organic inhibitors. By contrast, in section 4 this effect will be interpreted as result of calcite micro-particles which are just present only in the starting phase. This interpretation is supported by modelling results.

With the prospect of the column experiments several batch measurements were carried out to study the chemical activity of the sea sand which should be an inert matrix. Two batch pH-measurements were performed, one without and the other with sand, both under the CO_2-

partial pressure of air $3.037^{.}10^{-4}$ bar. The equilibrium pH-values were 8,28 and 8,30 without and with sand, respectively, whereas the value calculated for the calcite-water system was 8,34 (see section 4.). Additionally, the conductivity was measured in a batch which was a suspension of 200 g sand and 1 g of extra cleaned calcite powder in 400 ml MilliQ-water. In difference to the measurement without sand a higher equilibrium value of $\kappa=150$ µS/cm was obtained. So, one has to conclude that the especially prepared sea sand is not perfectly inert for the calcite-water solution. It has a negligible effect on the pH-value, but remarkably increases the electrolytic conductivity.

Fig. 3 shows the results of conductivity and pH-measurements of the solution leaking the 0,5m – column over a time period of 74 days after the start of the water injection. The asymptotic pH-value agrees well with that measured in the batch. Also, the higher conductivity appeared as it was in the batch with sea sand. The analysis by ICP/MS for the cations and by Ion Chromatography (IC) for the anions confirmed this fact. So, from these measurements one can conclude that both the pH-value and the electrolytic conductivity of the solution produced in the column under unsaturated conditions and those values measured in the batches under saturated conditions agree well.
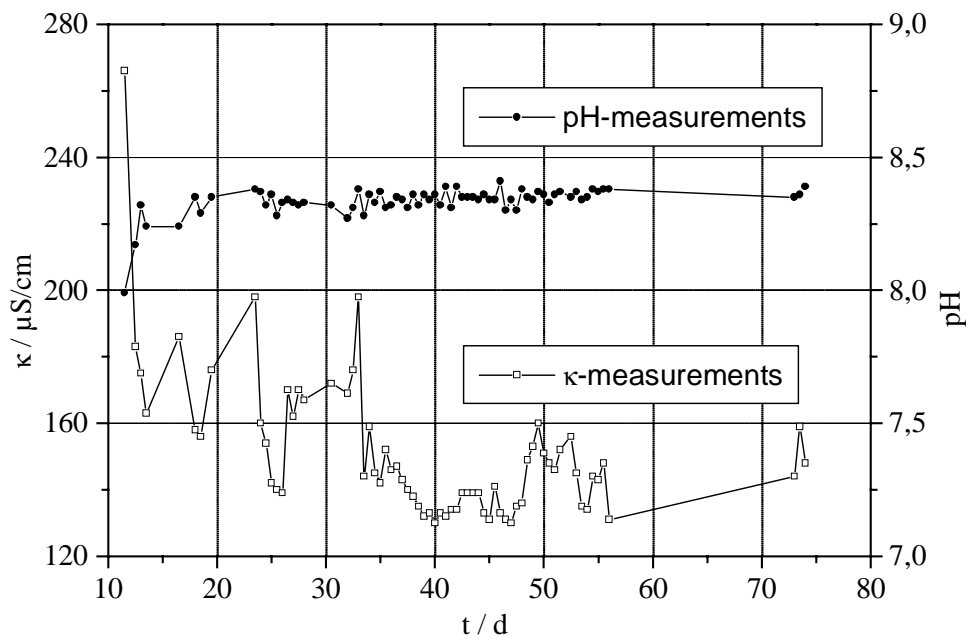
Fig. 3: pH-value and electrolytic conductivity of the solution leaking the 0,5 m - column in dependence on time after the start of the water injection

4. Modelling of batch and column experiments with calcite

In a part of the batch experiments described in section 3 the time course of the electrolytic conductivity of the calcite-water solution was monitored by a conductivity measuring cell. The conductivity is a linear combination of the different ion concentrations. Under the experimental conditions described in section 2 the following system of coupled differential equations describes the dynamics of the chemical system in the solution [3]:

$$\frac{\partial C_i}{\partial t} = \frac{O_p}{V_s} r_{ip}(solution) + \sum_{j=1}^{m} W_{i,j}(C_1,...,C_m) \qquad i = 1,...,m \qquad (1)$$

where C_i is the concentration of the ion species i, O_p is the total surface area of the mineral particles p, V_s is the volume of the solution and r_{ip} is the dissolution rate of the chemical component i from the surface of mineral p. m is the number of components and species which are involved in the reactions. In general, the dissolution rate depends on the chemical composition of the solution surrounding the mineral, especially, on its pH-value. $\sum W_{i,j}$ can be considered as the interaction rate which maintains the fast reactions in the water phase in equilibrium. This term determines the composition of the chemical solution on the basis of the mass action laws.

In column tests, transport, storage, exchange, and dissolution/precipitation processes will be investigated. The evaluation of column test data is based on the complete one-dimensional migration model. Assuming a constant flow rate v of the solution through the column the system of transport equations for the species is [4]:

$$n \cdot s(x) \frac{\partial C_i}{\partial t} = -v \frac{\partial C_i}{\partial x} + \alpha_L v \frac{\partial^2 C_i}{\partial x^2} + \frac{O_p}{V} r_{ip}(solution) + \sum_{j=1}^{m} W_{i,j}(C_1,...,C_m) \qquad i = 1,...,m. \qquad (2)$$

Here $n \cdot s(x)$ means the soil water content, n is the porosity and s the water saturation of the pores, v the water flow per unit area, α_L the longitudinal dispersion length (dispersivity) of the medium, and V the matrix volume. The free outflow at the end of the column is described by the boundary condition:

$$\frac{\partial C_i(L)}{\partial x} = 0.$$

This boundary condition is a good approximation for the outlet to a non-dispersive porous medium. At the column input a third-type boundary condition is usually applied:

$$v C_i^0 = (v C_i - \alpha_L v \frac{\partial C_i}{\partial x})_{|x=0}.$$

In the experiments this boundary condition is realised with peristaltic pumps leading to a homogeneous constant flow rate after a few centimetres.

The mixed kinetic-equilibrium system (1) for the calcite dissolution with the rate law according to Plummer et al. [5] has the form:

$$\frac{dC_{Ca^{2+}}}{dt} = \frac{O_{Calcit}}{V_s}(k_0 + k_1 \cdot \gamma_1 \cdot c_{H^+} + k_2 \cdot c_{H_2CO_3})(1 - \frac{\gamma_2 \cdot K_1}{K_{sp}} \cdot \frac{c_{Ca^{2+}} \cdot c_{HCO_3^-}}{\gamma_s c_{H^+}}) + \sum_j W_{Ca^{2+},j}$$

$$\frac{dC_{CO_3^{2-}}}{dt} = \frac{O_{Calcit}}{V_s}(k_0 + k_1 \cdot \gamma_1 \cdot c_{H^+} + k_2 \cdot c_{H_2CO_3})(1 - \frac{\gamma_2 \cdot K_1}{K_{sp}} \cdot \frac{c_{Ca^{2+}} \cdot c_{HCO_3^-}}{\gamma_s c_{H^+}}) + \sum_j W_{CO_3^{2-},j}. \qquad (3)$$

where the interaction term $\sum_j W_{i,j}$ will be replaced by the equilibrium approximation:

$$C_{H_2CO_3} = K_{CO_2} \cdot p_{CO_2}$$

$$\gamma_1^2 C_{H^+} \cdot C_{OH^-} = K_W$$

$$\gamma_2 C_{H^+} \cdot C_{CO_3^{2-}} = K_1 \cdot C_{HCO_3^-}$$

$$\gamma_1^2 C_{H^+} \cdot C_{HCO_3^-} = K_2 \cdot C_{H_2CO_3}.$$

In equ. (3) k_0, k_1 and k_2 are temperature dependent constants. γ_s is an activity coefficient of the H^+ ion at the calcite surface, K_{CO_2} is Henry's law constant for the solubility of CO_2 in water,

K_1 and K_2 are the first and second dissociation constants of carbonic acid in water, K_{sp} is the solubility product for calcite, and K_W is the dissociation constant of water. The activity coefficients γ_1, γ_2 were calculated using the Davies-Equation [6]. Solving equs. (3) one gets the conductivity as a linear combination function of the ion concentrations. To solve the set of equations (2) and (3), computer programs have been written in FORTRAN. These codes have been used to analyse the experiments.

Fig. 4 shows the time courses of the electrolytic conductivity calculated and measured in batch tests with calcite powder which was washed only but not especially cleaned (see section 3). The solid lines depict the fits to the experimental curves which are additionally marked by the measuring points. As mentioned in section 3 the unexpected steep inclines just after the start followed by slow approaches towards equilibrium can be explained by the dissolution of very small micro-particles which were deposited on the surface of the grains during crushing the calcite mineral. This statement may be supported by the following modelling. Because of their high specific surface the micro-particles solve very fast, i.e. their lifetime t_{life} which is
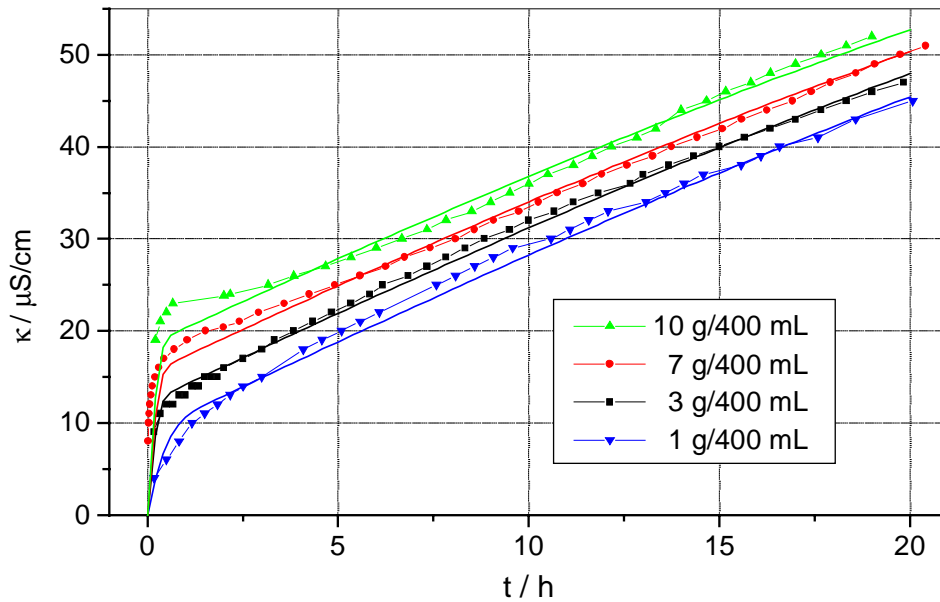
Fig. 4: Time courses of the conductivity in batch experiments with calcite

proportional to their radius is very small compared to that of the normal grains. It is assumed that the size of the small particles is Gauss-distributed. Furthermore, the steep rise of the curves is used to estimate the average lifetime of the particles what gives t_{life}=0,2 h. Therefore, the reacting surface is separated into two proportions:
- into the surface of small particles (index: *sp*) which vanishes according to the time law

$$f(t) = \frac{1}{2} erfc\left(\frac{t - t_{life}}{\sqrt{2} \cdot \Delta t}\right),$$ where *erfc(x)* is the error function and Δt=0,28 h is the estimated

mean variation, and
- into the surface of the large particles (index: *lp*) which determines the solution behaviour till the equilibrium is reached.

In this way, the model leads to the decomposition of the specific reactive surface of calcite:

$$\frac{O_{calcite}}{V_s} = \frac{O_{sp}}{V_s} f(t) + \frac{O_{lp}}{V_s} .$$

110

Table 1: Reactive surfaces of calcite derived from batch measurements ($\chi_S=1$)

Batch test	O_{sp} / cm^2/L	O_{lp} / cm^2/L	O_{sm} / cm^2/L
1 g	500	7600	681
3 g	7000	7900	2040
7 g	21000	8100	4770
10 g	31000	8300	6810

Using equ. (3) and the parameters in Table 1 the theoretical curves in Fig. 4 were calculated. The larger deviations at the beginning of the measurements are due to the imperfect description of the dissolution of the micro-particles. However, these errors could be further reduced by variation of the time distribution parameters t_{life} and Δt.

Surprisingly, the increase of the surface of the large particles does not significantly influence the solution process. A reason might be the surface roughness. A rough surface of a grain may be much larger than the surface corresponding to its geometrical dimensions. As a result, the surface controlled rate switches probably to a diffusion controlled rate, which should be independent on the surface. This speculation is confirmed by the "sphere model" (index: *sm*) that assumes all particles to be spheres. In the 1 g – batch test the surface is less than a tenth of the experimentally determined value. Just as in the case of the sphere model the surface of the small particles is proportional to the sample mass. In any geological relevant situation of dissolution the grain surfaces may be assumed to be smooth and its surface is then close to the geometric surface area. In such a case the above separation is not necessary.
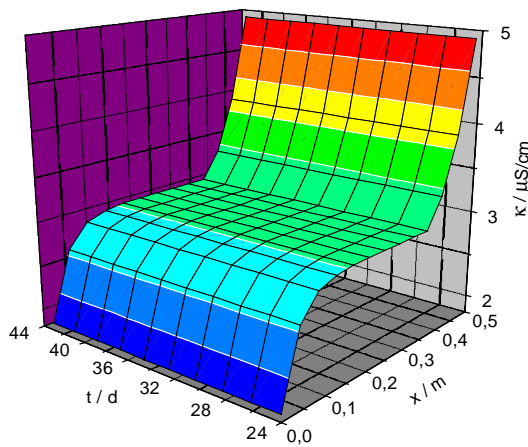
Fig. 5: Calculated conductivity for the 0,5 m - column
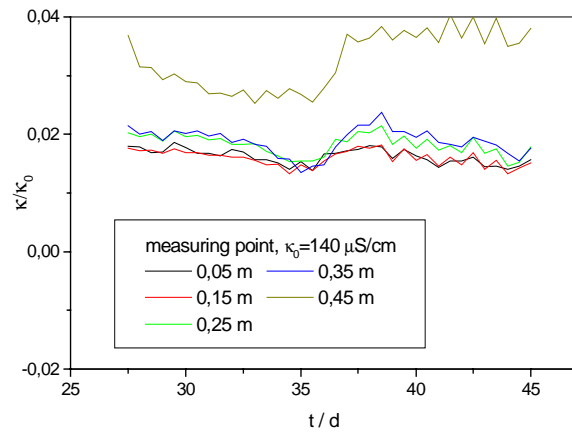
Fig. 6: Conductivity in-situ measured in the 0,5 m - column

For the 0,5 m - column Fig. 5 shows the calculated conductivity as function of space and of time after the equilibrium has been reached. 3 g calcite were mixed per 1 litre sand. The surface parameters of calcite were taken from the batch tests. The calculation shows that a fast saturation arises. Also, the in-situ values of the conductivity in Fig. 6 are caused by a saturated solution. This is confirmed by the curves measured at the points 0.05 m $\leq$ x $\leq$ 0.35 m which are nearly independent on the position. The larger values at the foot of the column (*x=0.45 m*) are caused by an increase in saturation. With the present low air pressure arrangement it is not possible to adjust a saturation profile which is constant over a wider range of the height of the column. The peaks in the measurement curves are due to temperature differences between day and night. The larger changes are caused by air pressure, temperature

and humidity variations. These influences also make the water distribution unstable. A control to hold the system in a less varying state seems to be not possible because of the slow-acting water movement.

6. Conclusions

The following conclusions may be drawn from the first experiments:
- Batch tests have shown that the sea sand though especially prepared is not perfectly inert for the basic calcite-water system: the pH-value is practically not affected whereas the electrolytic conductivity is increased by almost 50%. The increase of the conductivity has to be considered in the results of computations for column experiments. Generally, it became clear that the effect of the sea sand on the measuring quantities has to be checked in batch tests.
- Batch tests have also shown, that the reactive surface of the mineral grains which were produced by crushing does not correspond to their geometrical sizes. In spite of washing the calcite powder micro-particles may be attached to the grains and the surface itself may be of considerable roughness. This fact has to be considered in computations. The necessary information for this correction has to be taken from batch tests.
- The analysis of the solution leaking the 0,5 m – column has shown that both the pH-value and the electrolytic conductivity correspond to those values observed in the batch tests under saturated conditions.
- The experiment with the 0,5 m – column has shown that it is very difficult in practice to produce a constant saturation profile over the total height of the column.

References

[1]   D. Klotz (1991), Erfahrung mit Säulenversuchen zur Bestimmung der Schadstoffmigration, GSF-Bericht Nr. 7/91
[2]   Susan Stipp (2000), University Copenhagen, information FZR, 8/6/00
[3]   Peter C. Lichtner (1996), Continuum Formulation of Multicomponent – Multiphase Reactive Transport, in P. C. Lichtner, C. I. Steefel and E. H. Oelkers (Eds.), Reactive Transport in Porous Media, Reviews in Mineralogy, Vol. 34
[4]   L. Luckner und W. M. Schestakow (1991), Migration Processes in the Soil and Groundwater Zone, Leipzig, Verlag für Grundstoffindustrie
[5]   L. N. Plummer, T. M. L. Wigley and D. L. Parkhurst (1978), The kinetics of calcite dissolution in CO_2 water systems at 5°C to 60°C and 0.0 to 1.0 atm CO_2 , Am. J. Sci 278, 179
[6]   S. Pfeiffer, K. Pecher (1997), Experimentelle aquatische Chemie, Heidelberg, Berlin, Oxford, Spektrum Akademischer Verlag

Summaries of research activities

Thermo-fluiddynamics

H. Carl
A. Schaffrath
P. Schütz
W. Zimmermann

Thermal hydraulic test facility TOPFLOW
TOPFLOW is a large-scale high-temperature and high-pressure test facility for generic research in the field of transient two-phase flow and for studies of safety relevant fluid-dynamic problems in components of nuclear power plants and chemical installations. The design project of the facility is completed. The new facility will be built utilising components of the former NOKO test facility of the Research Centre Jülich, which helped to reduce costs to 9 - 10 million DM. The parameters allow experiments with steam-water mixture at saturation pressures of up to 7 MPa. The facility disposes of an electrical heating power of 4 MW. The construction work of the building was started.

A. Böttger
G. Grunwald
T. Höhne
S. Kliem
H.-M. Prasser
K.-H. Richter ☦
M. Tamme
J. Zschau

Coolant mixing in pressurised water reactors
The work aims at the determination of temperature and boron concentration distributions at the core entrance during main steam-line breaks and boron dilution transients. Experiments were carried out at the mixing test facility ROCOM modelling the German KONVOI type pressurised water reactor in the scale of 1:5. The disturbance is modelled by injecting salt water as a tracer into the affected loop. A new quality of tests is achieved by using mesh-sensors with numerous measuring positions in the downcomer and at the core entrance, the high measuring frequency (up to 200 Hz), the variability of the four-loop test facility and the direct comparison to CFD calculations. By variation of throttle orifices at the fuel element inlet positions the influence of the hydraulic resistance of the core was studied. Experiments were carried out for different lengths of the deborated plug for different scenarios of start-up of the coolant circulation. For these experiments, the test facility was equipped with a new fast-acting valve system to create short plugs. Furthermore, the velocity field in the downcomer was investigated using a Laser Doppler Anemometer. A repeated start-up combined with a special ensemble averaging technique allowed to obtain transient velocity distributions with a time resolution of 0.5 s. From the results the time constant of the development of large vortices in the downcomer can be deduced.

funded by BMWi
and VGB

A. Böttger
J. Fietz
F. Hensel
D. Hoppe
H.-M. Prasser
J. Zschau
C. Zippe
W. Zippe

Development and calibration of two-phase flow measurement techniques
The qualification of the diversified level indication system for boiling water reactors developed by FZR was continued according to the German reactor safety regulations. The qualification procedure and the series production will be accomplished by an industrial supplier of measurement instrumentation. FZR contributes as a scientific consultant and performed some finalising development tasks.

The new generation of signal acquisition units for the wire-mesh sensors for high-speed visualisation of two-phase flows at 10,000 frames per second for a 16 x 16 measuring points sensor was extended to 64 x 64

measuring points for the application in a pipe of 200 mm diameter. The framing rate for this sensor is 2,500 Hz. The sensor will be used for flow pattern studies at the test facility TOPFLOW.

In co-operation with the Technical University of Nishny Novgorod (Russia) a new ultrasonic mesh sensor was developed. The sensor is based on a system of crossing ultrasonic wave-guides. It is complementary to the electrical wire-mesh sensors of FZR, because it can be applied to non-conducting fluids. The dimensions of the wave guides were decreased to minimise the disturbance of the flow. The project was completed by the test of the new sensor design in a steam-water flow at up to 2.5 MPa.

For the investigation of transport processes in bubble columns and foam layers, a PET detector is under construction. The scanner will allow to measure the distribution of a tracer marked by a positron emitting nuclide with a time resolution of better than 1 s. It consists of 8 axial layers with 16 BGO detectors each. The spatial resolution will be in the range of a centimetre. The mechanical construction of the detector arrays and the development of the signal acquisition circuitry was finished. First tests with NaF labelled with F-18 are planned for the near future.

In co-operation with the Technical University Dresden, a quasi-stroboscopic gamma-tomograph for an axial turbo pump delivering an air-water mixture was developed and constructed. The device was put into operation. The first imaging of the gas fraction distribution inside the rotating impeller of the pump were successfully recorded.

A. Grahn

Thermoconvection and instabilities at the boundary layer of two non-miscible liquid reacting components
Flow instability at the inter-phase surface between two non-miscible liquids were investigated for the cases of non-reactive mass transfer (extraction) and exothermal reactions at the phase boundary. The work was concentrated at the continuation of the development of the numerical model for the two-dimensional flow in the gap. It considers the chemical reaction, the thermal and concentration effects on the fluid density and the surface tension. The model is capable of predicting all types of experimentally observed instabilities (density driven circulation cells, double-diffusive fingering regimes, Marangony type instabilities). The quantitative agreement concerning wave lengths and growth rates must be further increased.

D. Baldauf
D. Lucas
E. Krepper
H.-M. Prasser
C. Zippe
W. Zippe

Transient two-phase flows in pipelines
In the frame of a project sponsored by BMWi flow patterns and their evolution in a vertical tube are investigated. In the last year, experiments were concentrated on transient flows induced by pulsed air injection. The evaluation of previous measurements with the wire-mesh sensor was continued. Most important result is the method to decompose radial gas fraction profiles according to bubble-size classes. It was shown that

changes of the bubble size lead to qualitatively different profiles. Measurements taken by varying the inlet lengths allow to assess the non-drag forces acting on the bubbles and to estimate coalescence and fragmentation rates in dependence from the bubble diameter. Based on these experimental results, a theoretical method was developed that describes the evolution of the gas fraction profiles decomposed according to bubble size classes. The model is able to predict flow pattern transitions.

funded by BMWi

In the field of diabatic flows, a new type of local void probes was developed and used for condensation tests at the NOKO test facility in Jülich. The probes are equipped with a micro-thermocouple substituting the traditional electrode wire. In this way it is possible to detect the phase state and to measure the temperature at accurately the same location. This allows to detect non-condensibles in the gas phase and to characterise the boundary layer in the liquid phase. Four probes were mounted into a cross section of the single tube of NOKO. They are driven by step motors, developed by FZ Jülich, which translate the probes through the boundary layer. The probes were placed at different

cooperation with angular positions (0, 60, 120, 180 deg) of the horizontal pipe cross
Prof. E. Hicken section. The measured data show both thickness and structure of the
FZ Jülich condensation layer.

Safety and effectiveness of chemical processes

G. Hessel **Early detection of dangerous and undesired operating states in**
H. Kryk **chemical plants**
W. Schmitt Studies on the early detection of dangerous and undesired operating
T. Seiler states are accomplished in cooperation with Fraunhofer UMSICHT and
F.-P. Weiß an industrial partner. During the reporting period the Arzneimittelwerk Dresden left the project due to structural changes within the company. In the meantime the Degussa-Huels AG has taken over this part.
The development of a monitoring system based on adaptive heat balances for batch reactors is the most important contribution of FZR. The adaptation of the heat balance model to the respective plant is done by a neural network. For each relevant process fault there is a specially adaptive monitor. The validation of the heat balance model and fault monitors was conducted in batch reactors with different volumes (1–10–70-litres) for an exothermically homogeneous esterification reaction.
Results of the online testing in the pilot plant (UMSICHT) showed that the monitoring system was able to recognize undesired faults correctly. In particular, the hazardous reactant accumulation could be detected much earlier than by a monitor based on increasing rates of the reactor temperature.
supported by It is planned to develop an equivalent monitoring system for the
BMBF heterogeneous hydrogenation reaction in an industrial plant.

G. Hessel
H. Kryk
B. Noll
W. Schmitt
T. Seiler
F.-P. Weiß
T. Willms

Safe and ecofriendly process control

The knowledge of the thermochemistry during the normal and faulty operation of batch reactors is a prerequisite for a safe and ecofriendly process control of exothermal reactions in industrial chemical plants. The investigation was focussed on the hydrogenation process carried out by the Degussa-Huels AG. Preliminary tests conducted in an RC1 reaction calorimeter under conditions of the industrial plant showed that the hydrogen transport from the gas phase to the liquid phase is the rate determining step of this hydrogenation. Therfore, first this volumetric mass transfer coefficient had to be measured using an additional instrumentation in the industrial plant due to be able to realize similar conditions for process studies in laboratory reactors. Moreover, the thermodynamic parameters of the industrial plant, e.g. the heat transfer coefficient and the heat capacities of the reaction mixture and the reactor, were determined by specific experiments.

Besides this, two production samples were taken from all 16 conducted batches at the end of hydrogenation and analysed by HPLC (high performance liquid chromatography) in the FZR (cooperation with the Institute of Bioinorganic and Radio-Pharmaceutical Chemistry of FZR) to assess the process courses regarding to the extent of hydrogenation and the formation of side products as well as to obtain process data from the normal operation for the development of a monitoring system. It was

found that the products were completely hydrogenated and free from side products to a great extent.

Accident analysis

U. Grundmann
S. Kliem
S. Mittag
U. Rohde
A. Seidel

Development, validation and application of the code complex DYN3D – ATHLET

In the framework of an EU PHARE project under the leadership of FZR with participants from 8 European countries, different coupled 3D-neutronics/thermohydraulics code systems have been validated against measurement data on real plant transients from VVER type reactors. Two transients, the power drop of one generator down to house load level at the NPP Loviisa (VVER-440) and turning off one of two working feedwater pumps at the NPP Balakovo (VVER-1000), have been analysed. For the key parameters, a good agreement between measurements and calculations was achieved. It was found, that the correct modelling of the heat transfer in the gas gap between fuel and cladding is significant for the estimation of the fuel temperature Doppler feedback, which influences the change of power level during the transient. As a result of the project, the confidence of the results of the different codes has been improved.

The solution of an OECD benchmark exercise comprising the analysis of a main steam line break scenario for a Pressurized Water Reactor has been completed. Due to the overcooling of the reactor connected with positive reactivity insertion, re-criticality and return to power of the shut down reactor can occur. More than 14 organisations from 7 countries participated in the benchmark. The results obtained with DYN3D are in good agreement with the other codes.

A new version of the code DYN3D was elaborated combining the two versions for quadratic and hexagonal geometry of fuel assemblies. A new nodal method for hexagonal fuel assemblies with enhanced accuracy of the neutronic calculation has been integrated. Assembly discontinuity factors (ADF) can be taken into account. The flux reconstruction method for hexagonal geometry was integrated in the new version in co-operation with NRI Rez (Czech Republic). A nuclear data library, generated for a KWU Konvoi reactor by TSO Bavaria using the code CASMO, has been coupled to DYN3D.

A scientific conference on the development, validation and application of coupled 3D-neutronics/thermohydraulic codes has been organised in Rossendorf under the auspices of the German Nuclear Society. The participation of about 100 experts from research institutes, nuclear power plants and technical support organisations of the nuclear authorities proved the scientific authority, which Rossendorf has gained in this field.

E. Krepper
F. Schäfer

Validation of thermohydraulic system codes

The analysis of an experiment performed at the Japanese test facility CCTF simulating a large break loss-of-coolant accident (design basic accident) with cold leg respective combined cold and hot leg ECC injection by the help of the thermoydraulic code ATHLET (developed by Gesellschaft für Anlagen- und Reaktorsicherheit) has been completed. In this experiment, large counter current flows of water and steam with condensation occur. The analysis aimed at the validation of the six equation code version and of a new condensation model in ATHLET. Space-dependent effects in the flooding of the heated-up reactor core simulator had to be taken into account. In general, the course of the transient was calculated in good agreement with the experiment.

E. Krepper
T. Höhne
S. Kliem
M. Kliem

Computational fluid dynamics simulations of one and two-phase flow

The experiments on coolant mixing in PWRs in the ROCOM test facility have been accompanied with CFD simulations. Experiments with the injection of plugs of a tracer fluid (salt water) into a steady state flow field or during the start-up of circulation have been analysed. A good agreement between calculation and measurement was achieved even for the transport of the tracer in the complex instationary flow field during the start-up of the circulation. Based on measured response functions for quasi Dirac impulse shaped injections, time-dependent mixing curves are obtained for each fuel element position by applying linear super-position techniques. This Semi-Analytical Plug Reconstruction model SAPR is going to be implemented into the code DYN3D.

The simulation of experiments performed at the Rossendorf two-phase flow test loop by using the CFD code CFX has been continued. It becomes clear, that for a realistic modelling of the radial gas profile in a flow with higher gas fractions multi-bubble class models considering bubble forces dependent on the bubble diameter and simulating coalescence and break-up of the bubbles have to be applied.

CFD simulations of the natural convection in tanks with local heat sources have been performed. For the validation of the CFD models, international benchmark problems have been solved. Calculations were performed for experiments at the NOKO test facility modelling an emergency condenser of a BWR power plant, and for side wall heated tanks. Modelling the sub-cooled boiling near the heated walls, the flow phenomena in the heated tank have been simulated in qualitatively good agreement with the experiments. The formation of sharp layers with different temperature has been observed, which break up suddenly if boiling becomes more intensive.

The porous body model developed for 3D flow simulations for the reactor core has been improved by implementing an an-isotropic drag force model. An experimental set-up will be constructed to validate the model against flow measurements in rod bundles.

Liquid metal magnetohydrodynamics

I. Grants
V. Galindo
V. Shatrov
G. Gerbeth

Basics of MHD flows

A spectral code has been developed to simulate the flow in a cylindrical cavity driven by a rotating magnetic field. The high-precision spectral approach delivered a number of important insights into the instability details of that flow. First, the linear oscillatory instability is not of the Taylor-Görtler type as it has been concluded in all foregoing publications. Second, there is a high sensitivity of the flow to small but finite disturbances already about 30% below the linear instability threshold. This sensitivity indicates a non-linear route to turbulence in such flows.

Numerical simulations have been performed for the flow inside a magnetically levitated drop and in an inductively heated crucible. The basically axisymmetric flow in a levitated drop becomes oscillatory unstable in a 3d form with an azimuthal wavenumber of m=3. The flow in an inductively heated melt is strongly 3d. The numerical results differ from the experimental values due to the significant influence of free surface flow phenomena not taken into account in the simulation up to now.

A.Cramer
I. Grants
J. Priede
S. Eckert
G. Gerbeth

Crystal growth and metallurgy

The global heat modelling has been performed for the growth of GaAs in the new Vertical Gradient Freeze facility of Bergakademie Freiberg. The action of an external rotating magnetic field on the melt flow was especially designed in order to obtain an almost flat phase boundary during the growth process. For that, analytical as well as numerical solutions for the Stefan problem of the unknown phase boundary between melt and crystal have been developed. A significant influence on the phase boundary geometry is possible which shall now be verified in a set of growth experiments. The possibilities for flow control in the Floating-Zone growth process has been analysed with the conclusion that an influence on the phase boundary geometry is only possible if the double vortex structure could be changed. For that a novel magnetic

pump principle has been developed working with an additional magnetic winding without own power supply. These theoretical-numerical investigations lead to an experimental realization proposal which will be installed at a Floating-Zone facility of Institut für Festkörper- und Werkstoffforschung Dresden.

Systematic experiments at the melt extraction model facility gave quantitative results on the influence of the meniscus oscillations on the fibre diameter distribution. The counter measure based on a magnetic ring on the rotating wheel lead to a significant reduction of the diameter distribution and smaller mean diameters.

F. Stefani
Th. Gundrum
G. Gerbeth

Dynamo effect
A second measuring campaign was performed at the Riga dynamo facility in July 2000. During three different runs of the facility fully reproducable results were obtained for the magnetic field generation process consisting of the exponential field growth slightly above the instability threshold, the magnetic field saturation at higher liquid metal velocities and the exponential decrease of the field if the flow rate finally decreases below its critical value. The results for the magnetic field frequencies and growth rates agree very well with the numerical simulations and, in addition, with the first experiments from November 1999. A non-trivial backreaction of the magnetic field on the flow has been observed. It consists in an axial shift of the magnetic field maximum due to the breaking Lorentz forces in azimuthal direction which result in a decreasing swirl flow axially downwards from the driving propeller.

T. Weier
U. Fey
G. Mutschke
J. Hüller
G. Gerbeth

Boundary layer control in electrolytes
The electromagnetically controlled flow around two different airfoils have been experimentally studied in a salt water flow basin of HSVA Hamburg. Two leading effects have been identified: Production of lift due to the electromagnetically induced circulation, and suppression of vortex separation at inclined positions. The latter gives a serious lift increase of up to 80% compared to the uncontrolled case. Numerical simulations accompany these investigations. They reproduce the main tendencies of the experiments, but are still limited with respect to the Reynolds number due to the unknown type of turbulence modelling being appropriate for this type of flow control.

Small scale model experiments were performed in order to demonstrate the influence of an external magnetic field on the limiting current and the flow distribution in electrochemical cells. Just by simple adding of an external permanent magnet a strong influence on the limiting current density as well as on the flow field has been found resulting, e.g., in a change of flow direction close to the electrode surface in a bubble producing electrochemical process.

V. Shatrov,
J. Priede
G. Gerbeth

Levitation

Two different ways of active stabilization of electromagnetically levitated samples were developed. One works with a ring of permanent magnets, the other with an electrotechnical superposition of a direct current to the high-frequency levitating coil. Both give a full stabilization of the levitated sample. Both methods have been proposed to the company Astrium GmbH for an installation into the hardware of the levitation experiments on the International Space Station.

S. Eckert
W. Witke
Th. Gundrum
J. Hüller
G. Gerbeth
F. Stefani

Measuring techniques

The ultrasonic Doppler velocimetry (UDV) has been tested at higher temperatures for flows of sodium and lead-bismuth. The commercially available transducers are limited to about 100 °C. Systematic measurements have been performed with direct melt contact, through a solid wall of the melt or with an additional wave-guide for temperatures up to 250°C. Special care and design is needed for the channel wall thickness, the coupling conditions at interfaces and the wetting of the liquid metal to the contacting wall. If this is fulfilled UDV gives instantaneously a complete velocity profile over the flow cross section as demonstrated in the sodium and lead-bismuth experiments. An industry oriented European project has been started in order to develop UDV up to liquid steel temperatures for applications in metallurgical industries.

The idea of a magnetic tomography, i.e. reconstruction of the flow field out of external magnetic field measurements, has been developed. A demonstration experiment based on external magnetic field Hall measurements was designed which is currently being installed.

Materials and components safety

H.-W. Viehrig
S. Schneider

Radioisotope laboratory for machining of specimens for mechanical testing

In order to extent the potential to investigate radioactive materials a second part of the radioisotope laboratory for mechanical testing is built. It includes the hot cells with equipment for machining of specimens and for additional mechanical tests. The construction of the hot cells is finished and the machines have been installed. A CNC-controlled electric discharge machine allows to produce testing specimens according to the standards from pieces taken from components of current or decommissioned nuclear installations like power plants, research reactors or accelerators. Because the commercial machine was not suitable for operation under hot cell conditions, the design and some operational functions must be changed in a substantial extent. Essential steps have already been taken, some new assemblies and techniques were developed and successfully tested.

H.-W. Viehrig *G. Müller* *J. Böhmert*	**Evaluation of the neutron embrittlement of Russian reactor pressure vessel steels** Basing on the results of the irradiation programme Rheinsberg the shift of the ductile brittle transition temperature determined by the Charpy impact test and the shift of the reference temperature T_O using the code ASTM E 1921-97 were compared with the prediction according to the Russian guidelines. For the VVER 440-type reactor pressure vessel steels the results are in accordance to the Russian guidelines. The VVER 1000-type vessel steels show a higher neutron embrittlement. In particular the investigated 10KhNGMAA VVER 1000 weld metal exhibits a very large shift of the transition temperature that is not understandable on the base of the recent prediction formula. The detrimental effect of nickel that can be derived from the results of the Rheinsberg programme is not confirmed by recent investigations of VVER 1000 weld metal with different content of nickel irradiated at surveillance position of a VVER 1000. In this study the heat with the highest nickel content shows the lowest embrittlement. Furthermore for a better understanding of the embrittlement mechanism, the method of thermal activation analysis was used. The study shows that the irradiation effect is athermal regarding the interrelation between the radiation-induced microstructural features and gliding dislocations. The effect does not depend on the nickel content. The shift of the reference temperature T_O and the Charpy transition temperature shift correlate but the scattering is large. Thus T_O data cannot be substituted by the Charpy transition temperature in the frame of safety assessments for the reactor pressure vessel.
supported by *BMWi and EU*	
H.-W. Viehrig *J. Dzugan* *J. Böhmert*	**Methodical studies for the determination of fracture mechanics parameters** The determination of fracture mechanics parameters from small specimens to characterize irradiated materials is still an open issue. Appropriate approaches are the Wallin's master curve concept or the determination of crack resistance curves by single-specimen techniques like the unloading compliance method. Wallin`s master curve concept was used to determine a dynamic master curve. For this purpose fracture mechanics impact tests were performed and compared with the static master curve. Shape and scattering of the dynamic master curve are not identical with the static one. Thus the concept cannot be transferred without modifying the approach. This needs further work. The unloading compliance technique fails for materials of high toughness. Under this condition the compliance is not only dependent on the crack length but also on the displacement. Correction formula consider this influence only insufficiently. On the base of a comprehensive data bank suitable approaches were developed for a better correction. In order to generalize the correction obtained sensitivity studies by means of FEM modelling are planned. A new method was developed for the determination of crack resistance curves at 3-point bend specimens of Charpy geometry. The methods bases on ultrasound flight time measurements of a transverse wave diffracted at the crack tip. The method meets the demands according to

the standards for a single specimen technique of crack growth measurement.

A. Ulbricht
J. Böhmert

Modelling of the neutron embrittlement mechanism

Small angle neutron scattering experiments were carried out accompanying the mechanical test of the materials from the Rheinsberg irradiation programme. Heats of base and weld material were investigated in as-received, irradiated and post-irradiation annealed conditions. The small angle neutron scattering intensity increases in the scattering vector range between 0.8 and 3 nm^{-1} for all compositions in the irradiated state. The size distribution function of the irradiation induced defects has a pronounced maximum at a radius of 1 nm. Their volume contents vary between 0.1 and 0.7 vol.% depending on material composition and increases with increasing neutron fluence. The comparison between nuclear and magnetic scattering indicates that the microstructural features differ in their composition. Thermal annealing reduces the volume fraction of the irradiation defects. The effects of irradiation on the microstructure reflect the irradiation-caused shift of the transition temperature (irradiation embrittlement) or the changes of hardness (irradiation hardening). Further, the recovery of the mechanical properties by annealing corresponds to the restoration of the small angle neutron scattering curve of the as-received state. This is valid as a trend but there are some irregularities in these relations. Thus neither irradiation embrittlement nor irradiation hardening can be attributed to a simple microstructural parameter like the volume fraction of nanoscale defects.

H.-G. Willschütz
E. Altstadt

In-vessel retention in LWRs

Considering the hypothetical core melt down scenario for a light water reactor (LWR) the failure mode of the reactor pressure vessel (RPV) has to be investigated to determine the possible loads on the containment. The FOREVER-experiments, currently underway at the KTH Stockholm (Sweden), are simulating the thermal and pressure loads on the lower head for a corium melt pool with internal heat sources. Due to the multi-axial creep deformation of the vessel with a non-uniform temperature field these experiments are an excellent source of data for the validation of numerical creep models. Therefore, a Finite Element model has been developed based on a commercial multi-purpose code. Using the CFD module the temperature field within the vessel wall is evaluated. The transient structural mechanical calculations are performed using a new numerical approach which avoids the use of a single creep law employing constants derived from the data for a limited stress and temperature range. Instead of this a three-dimensional array is developed where the creep strain rate is evaluated according to the values of the actual total strain, temperature and equivalent stress. Care has to be exercised in the comparison of the measured data and the numerical results. Considering the FOREVER-C2 experiment, for example, the recorded creep process appeared to be tertiary at the first glance. But it could be shown that a small temperature increase during the creep deformation caused the observed progressive behaviour. Such

considerations provide insight and better predictive capability for the vessel creep behaviour during prototypic severe accident scenarios. The work has been performed in cooperation with KTH Stockholm (Prof. Sehgal).

E. Altstadt
T. Mössner
T. Repp
R. Weiß

Water hammers in pipelines

The pressure waves induced by a sudden slow down of the fluid flow in a pipeline are modelled on the base of the finite element method. Special attention is put on the influence of fluid-structure interaction if the pipe diameter is relatively large in comparison with the wall thickness. The FE-codes ADINA and ANSYS are used for modelling. The transient velocity and pressure distribution is calculated in a straight pipe and in a 90° elbow assuming a slightly compressible fluid. The coupling between the elastic pipe wall and the fluid is realized by boundary elements. It is shown that there are local stresses in the elbow which are higher than those calculated with conventional uncoupled calculations. It was also found that pressure waves propagate in radial direction. These calculations have to be validated. Therefore, at the FZR a cold water hammer test facility has been installed. Pressure amplitudes of up to 200 bars can be generated. First tests have shown that it works as expected. A one-dimensional model for the acceleration of the fluid was developed and validated with the results of the first experiments. The bouncing velocity is predicted quite well by this model, whereas the pressure amplitude is over_estimated by some 30-50% since the effect of the junction coupling is not yet included. The work is supported by the EC (5th frame work programme).

supported by
VDEW

M. Werner
E. Altstadt
S. Perov

Finite Element-Modelling of crack propagation and material damage

A 3-dimensional FE-Model of a Charpy specimen has been developed. This model includes the kinematics of the roll bearings as well as the crack opening mechanism. Additionally the influence of the elastic deformation of the test facility is considered. This might be of importance for the correction of experimentally determined compliance functions. Two different methods of crack modelling were used: (i) the substructure technique based on the concept of linear-elastic fracture mechanics and (ii) the elastic-plastic material behaviour coupled with a simple damage based criterion for crack opening (crack opening is realized by the node unlocking concept). In the latter concept the crack opening is simulated in a time dependent calculation. The numerical stability was found to be a problem in some cases with large plastic strain. This might be due to the node unlocking concept. Therefore, an element deactivation concept is now being tested.

In a parallel work the plasticity model of Gurson, Needleman and Tveergard was integrated into the finite element code ANSYS. With that model the description of porosity (development of mesoscaled cavities) just before the ductile fracture is possible.

Simulation of particle and radiation fields

R. Koch

Prototypical nuclear data libraries for the European Pressurised Reactor

The new version 1.6 of the neutron and gamma transport code HELIOS for cell and depletion calculations was installed, tested and debugged. In addition, some Fortran 90 programs and UNIX-shell scripts have been written to automate the processing with different data and to extract the results of HELIOS runs. With the help of HELIOS and this auxiliary programs 310 two-groups sets, each for seven depletion steps, were calculated and prepared for the use in reactor-dynamic calculations with the DYN3D code. To analyse the cross-sections and other data calculated with the Program HELIOS 1.6, a module was implemented to import and plot these results. This module automates the graphical representation of cross sections over depletion as 2D-plots.

R. Küchler
K. Noack
T. Zorn

Transport of radio-nuclides in the unsaturated zone

In recent years numerical codes have been developed and were used for transport calculations of water and chemical species of radio-nuclides through the unsaturated soil. Now the mathematical models of the various physical and geo-chemical phenomena and the parameters required by them have to be verified by appropriate experiments. Therefore, a laboratory was built which allows to carry out batch and column experiments. The columns are filled with modelled mixtures consisting of sea sand as quasi-inert matrix and certain minerals which are of great importance for the radio-nuclide transport in the dumps of the former uranium mining in Saxony. At present, research is focused on the dissolution rates of those minerals under unsaturated conditions. Additionally to the collection of samples of the leaking solution at the feet of the columns the stand for the column experiments is equipped with in-situ measuring techniques of the electrolytic conductivity and of the pH-value. In the first series of experiments the dissolution behaviour of gypsum and calcite was determined and compared with results of calculations based on published dissolution rates. The developed data acquisition and experiment control proved to work stable over the experiment time of some months.

*work performed in
cooperation with
the Institute of
Radiochemistry of
FZR*

K. Noack
A. Rogov*

Neutron Laboratory at ELBE

The neutron laboratory at the electron accelerator ELBE will be equipped with a photo-neutron source. The target material stops the electrons which produce Bremsstrahlung the photons of which then generate neutrons by photo-nuclear reactions. The production of photo-neutrons was calculated for different directions around a specified target by means of the Monte Carlo code MCNP-4B and the results compared to those which were independently achieved with the code FLUKA by the TU Dresden. In contrast to FLUKA the MCNP code does not yet allow an automatic run simulating the three coupled particle transports. So, the task was solved by two steps: first, the photon flux distribution inside the target was calculated in an electron/photon transport problem and, second, applying a published reaction model the distribution of

Visitor to Forschungszentrum Rossendorf

emitted photo-neutrons was calculated and used as source in the subsequent neutron transport simulation. The results of both codes showed a very good agreement so that both can be used for target optimisation further on.

B. Böhmer
J. Konheiser
H. Kumpf
P. Vladimirov

Neutron and Gamma dosimetry of reactor pressure vessels

As contribution to the BMWi project „Influence of the gamma irradiation on the deterioration of reactor pressure vessel materials and on reactor dosimetry measurements" neutron and gamma flux spectra have been calculated for two Russian and two German reactor types, partly in co-operation with Russian scientists. Using the calculated flux spectra damage parameters for the highest flux regions of the reactor pressure vessels have been obtained. More detailed investigations of the impact of high gamma fluences on the pressure vessel embrittlement were prepared. Additionally, a model of the development of atomic displacement cascades, the formation of copper precipitates, and of the influence of gamma irradiation on these processes has been developed.

The recently upgraded geometrical module of the Rossendorf Monte Carlo code TRAMO was successfully tested through fluence calculations for the irradiation experiment at the Russian VVER-1000 Novovonesh-5. The work was carried out within the EU TACIS project SRR2/95. The obtained calculation results were compared with experimental values and with results of independent calculations. In both cases a reasonable agreement was found.

B. Böhmer
J. Konheiser
H. Kumpf
K. Noack

Increasing the accuracy of neutron and gamma fluence determination

A new research project was started that aims at extension and verification of TRAMO for solving neutron-gamma transport problems and at testing nuclear data libraries. In this project which is supported by DFG partners are involved from the TU Dresden (TUD) and from the HTWS Zittau/Görlitz. First test measurements of neutron and gamma spectra were performed at the horizontal neutron beam channel of the training reactor of the TUD. The measurements were performed in the open beam as well as behind iron and water layers. Calculations with the code MCNP were used to optimise the measurement set-up. The code TRAMO was qualified for coupled neutron-gamma calculations and for an improved treatment of thermal neutrons. The needed thermal scattering matrices were calculated with the code NJOY.

Publications

Publications in scientific and technical journals and in conference proceedings

Altstadt, E.; Willschuetz, H.-G.
Creep Modelling for Complex Geometries with Highly Non-uniform Temperature Fields
26. MPA-Seminar "Sicherheit und Verfügbarkeit in der Energietechnik", Staatliche Materialprüfanstalt Stuttgart, Proc. S. 9.1-9.13, 5.-6.10.2000, Stuttgart

Altstadt, E.; Willschütz, H.-G.
Applying ANSYS/Multiphysics with Extended Creep Capabilities to an Integral Severe Nuclear Accident Experiment
18. CAD-FEM Users´ Meeting, 20.-22. September 2000, Friedrichshafen am Bodensee, Germany, Proceedings Vol.2, 2.5.5.

Anikeev, A. V.; Bagryansky, P. A.; Ivanov, A. A.; Karpushov, A. N.; Korepanov, S. A.; Maximov, V. V.; Murakhtin, S. V.; Smirnov, A. Yu.; Noack, K.; Otto, G.
Fast Ion Relaxation and Confinement in the Gas Dynamic Trap
Nuclear Fusion 40 (2000) 753-765

Aszodi, A.; Krepper, E.; Prasser, H.-M.
Experimental and numerical investigation of one and two phase natural convection in storage tanks
Heat and Mass Transfer 36 (2000) 6, 497-504

Barz, H.-U.; Böhmer, B.; Konheiser, J.; Stephan, I.
Monte Carlo Calculations of Neutron Fluence Spectra, Activation Measurements, Uncertainty Analysis and Spectrum Adjustment for the KORPUS Dosimetry Benchmark
Tenth International Symposium on Reactordosimetry, 12.- 17. 9. 1999, Osaka, Japan, ASTM STP 1398

Beyer, M.; Carl, H.; Schumann, P.; Seidel, A.; Weiß, F.-P.; Zschau, J.; Nowak, K.
Support of the Ukrainian supervisory authority in establishing a modern nuclear power plant monitoring
Kerntechnik Vol. 65; No.1; Februar 2000; Seiten 23 - 27

Boehmert, J.; Ulbricht, A.; Kruykov, A.; Nikolaev, Y.; Dmitry, E.
Composition Effects on the Radiation Embrittlement of Iron Alloys
Effects of Radiation on Materials: 20th International Symposium, June 2000, ASTM STP 1405, S.T. Rosinski, M. L. Grossbeck, T. R. Allen and A. S. Kumar, Eds.

Böhmer, B.; Borodkin, G. I.; Manturov, G. N.
Improved Covariance Analysis and Spectrum Adjustment for VVER-1000 Pressure Vessel Fluences
Tenth International Symposium on Reactordosimetry, 12.- 17. 9. 1999, Osaka, Japan, ASTM STP 1398

Böhmer, B.; Manturov, G.
Neutron Flux Uncertainty and Covariances for Spectrum Adjustment and Estimations of Pressure Vessel Fluences
Tenth Symposium of AER on VVER Reactor Physics and Reactor Safety 2000, Moscow (Russia), 18.-22. September 2000, Proceedings pp. p. 345-351

Böhmert, J.; Große, M.
Characterization of the Deformation Field Near the Crack-Tip after Bending by Small Angle X-ray Scattering
Conference of the Federation of European Material Societies EUROMAT'99, Sept. 1999, Munich, Microstructural Investigation and Analysis, EUROMAT, Vol. 4, B. Jouffrey and J. Svejcar (Editors), DGM, Weinheim, 2000, pp. 114-120

Böhmert, J.; Viehrig, H.-W.; Richter, H.
Bestrahlungsverhalten von WWER-Druckbehälterstählen - Erste Ergebnisse aus dem Bestrahlungsprogramm Rheinsberg
Jahrestagung Kerntechnik 2000, Bonn, 23.-25. Mai, Tagungsbericht S. 591

Borodkin, G.; Böhmer, B.
Validation of 3D Synthesis RPV Neutron Fluence Calculations using VVER-1000 Ex-Vessel Reference Dosimetry Results (Invited Paper)
2000 ANS Annual Meeting, San Diego, California, June 4-8 2000, Trans. Am. Nucl. Soc. Vol.82,p.223-225 (2000)

Borodkin, G. I.; Kovalevich, O. M.; Barz, H.-U.; Böhmer, B.; Stephan, I.; Ait Abderrahim, H.; Voorbraak, W.; Hogel, J.; Polke, E.; Schweighofer, W.; Seren, T.; Borodin, A. V.; Vikhrov, V. I.; Lichadeev, V. V.; Markina, N. V.; Grigoriev, E. I.; Troshin, V. S.; Penev, I.; Kinova, L.
Balakovo-3 Ex-vessel Exercise: Intercomparison of Results
Tenth International Symposium on Reactordosimetry, 12.- 17. 9. 1999, Osaka, Japan, ASTM STP 1398

Brodkin, E.; Egorov, A.; Zaritsky, S.; Böhmer, B.
CONTRIBUTION OF GAMMA IRRADIATION TO MATERIAL DAMAGE AT VVER PRESSURE VESSELS
Jahrestagung Kerntechnik 2000, 23.-25.Mai 2000, Bonn, Tagungsbericht S. 597-600

Cramer, A.; Gerbeth, G.; Bojarevics, A.; Gelfgat, Y.
Stabilizing the direct melt extraction of intermetallic fibres by magnetic fields
The 3rd International Symposium on Electromagnetic Processing of Materials (EPM2000) April 3-6 / Nagoya, Japan, Published by: The Iron and Steel Institute of Japan, pp 147-152

Cumblidge, Stephen E.; Catchen, Gary L.; Motta, Arthur T.; Brauer, G.; Boehmert, J.
Effects of Neutron Irradiation and Thermal Annealing on Model Alloys using Positron Annihilation Techniques
Effects of Radiation on Materials: 20th International Symposium, June 2000, ASTM STP 1405, S. T. Rosinski, M. L. Grossbeck, T. R. Allen and A. S. Kumar (Eds.)

Dudlik, A.; Hagemann, O.; Fahlenkamp, H.; Prasser, H.-M.
Innovative Maßnahmen zur Vermeidung von Druckstößen und Kavitationsschlägen
3R international 39 (2000) 11, S. 673-677.

Eckert, S.; Gerbeth, G.
Anwendung des Ultraschall-Doppler Verfahrens zur Bestimmung von Geschwindigkeitsprofilen in Flüssigmetallströmungen
5. Seminar für Strömungssensorik an der Universität Rostock, 28./29.09.2000, Shaker-Verlag
ISBN 3-8265-8163-6

Eckert, S.; Gerbeth, G.; Lielausis, O.
The behaviour of gas bubbles in a turbulent liquid metal MHD flow - Part I: Dispersion in quasi-two-dimensional MHD turbulence.
International Journal of Multiphase Flow (2000), Vol. 26/1, 45-66

Eckert, S.; Gerbeth, G.; Lielausis, O.
The behaviour of gas bubbles in a turbulent liquid metal MHD flow, Part II: The influence of an external magnetic field on the slip ratio in a liquid metal bubbly flow
International Journal of Multiphase Flow (2000), Vol. 26/1, 67-82

Eckert, S.; Witke, W.; Gerbeth, G.
Measuring techniques for model experiments in liquid metal alloys
EPM2000, The 3rd International Symposium on Electromagnetic Processing of materials, April 3-6, Nagoya, Japan, Published by: The Iron and Steel Institute of Japan, pp. 43-48

Eckert, S.; Witke, W.; Gerbeth, G.
A new mechano-optical technique to measure local velocities in opaque fluids
Flow Measurement and Instrumentation, Vol. 11/2 (2000) 71-78

Gailitis, A.; Lielausis, O.; Dementiev, S.; Platacis, E.; Cifersons, A.; Gerbeth, G.; Gundrum, T.; Stefani, F.; Christen, M.; Hänel, H.; Will, G.
Detection of a flow induced magnetic field eigenmode in the Riga dynamo facility
Physical Review Letters Vol 84, No 19, (2000) 4365-4368

Gelfgat, Yu. M.; Mikelsons, A.; Romancuks, A.; Gerbeth, G.
Stability of levitation of solid and liquid conducting spheres in high frequency electromagnetic field
Magnetohydrodynamics, Vol.36, No.2, 167-179, 2000

Gerbeth, G.; Priede, J.
Spin-up instability of electromagnetically levitated spherical bodies
IEEE Transactions on Magnetics, Vol. 36. No. 1, Januar 2000

Große, M.; Denner, V.; Böhmert, J.; Mathon, M.-H.
Irradiation-induced structural changes in surveillance material of VVER 440-type weld metal
Journal of Nuclear Materials 277 (2000) 280-287

Große, M.; Gokhman, A.; Böhmert, J.
Dependence of the Ratio between Magnetic and Nuclear Small Angle Neutron Scattering on the Size of the Heterogeneities
Nuclear Instruments and Methods in Physics Research B 160 (2000) 515-520

Grundmann, U.; Rohde, U.; Mittag, S.
DYN3D - Three Dimensional Core Model for Steady-State and Transient Analysis of Thermal Reactors
PHYSOR 2000 - Advances in Reactor Physics and Mathematics and Computation into the Next Millennium, Pittsburgh (USA), May 7-12, 2000, Proceedings on CD-ROM, ANS Order No. 2700281

Grundmann, U.; Rohde, U.; Tietsch, W.
3D-Kernberechnungen bei Borverdünnung nach kleinen Lecks
Tagungsband der Fachtagung der KTG: "Wechselwirkungen Neutronenphysik und Thermofluiddynamik", pp. 5-26 bis 5-38, Forschungszentrum Rossendorf, 31. Januar - 1. Februar 2000

Grunwald, G.; Höhne, T.; Prasser, H.-M.
Investigation of coolant mixing in pressurized water reactors at the Rossendorf mixing test facility ROCOM
Tagungsband der Fachtagung der KTG: "Wechselwirkungen Neutronenphysik und Thermofluiddynamik", pp. 71-77, Forschungszentrum Rossendorf, 31. Januar – 1. Februar 2000

Grunwald, G.; Höhne, T.; Prasser, H.-M.
Investigation of coolant mixing in pressurized water reactors at the Rossendorf mixing test facility ROCOM
8th International Conference on Nuclear Engineering (ICONE8), Baltimore, USA, April 2-6, 2000, Conference CD

Grunwald, G.; Höhne, T.; Prasser, H.-M.; Weiß, F.-P.
Coolant Mixing in Pressurized Water Reactors at Constant Coolant Flow in the Primary Circuit
Jahrestagung Kerntechnik 2000, 23.-25. Mai 2000, Bonn, Proceedings pp. 109-114.

Hainoun, A.; Schaffrath, A.
Nachrechnung der Oak Ridge Versuche (THTL) zur thermohydraulischen Instabilität
Jahrestagung Kerntechnik 2000, Bonn, 23.-25. Mai 2000, Tagungsbericht S. 523-529

Hensel, F.
Investigation of a Density Measurement Technique using Positron Radiation
Applied Radiation and Isotopes 53 (2000) 617-624

Hessel, G.; Kryk, H.; Schmitt, W.; Seiler, T.; Weiß, F.-P.; Deerberg, G.; Neumann, J.
Assessment and Identification of Undesired States in Chemical Semibatch Reactors Using Neural Networks
Proceedings of IFAC Symposium on Fault Detection, Supervision and Safety for Technical Processes - SAFEPROCESS'2000, Budapest, 14-16 June, 2000, pp. 458-461

Hinssen, H.-K.; Krüssenberg, A.-K.; Moormann, R.; Wu, C.-H.
Oxidation of innovative carbon based materials for future energy systems
in: High Temperature Materials Chemistry, ed. by K. Hilpert, F.W. Froben, L. Singheiser,
Schriften des Forschungszentrums Jülich, Series Energy Technology, (2000), Volume 10,
ISBN 3-89336-259-2

Höhne, T.
Untersuchung der Kühlmittelvermischung in Druckwasserreaktoren
atw 12, S. 774-775

Höhne, T.; Grunwald, G.; Prasser, H.-M.
Experimental Investigations on the Four-Loop Test Facility ROCOM
Kerntechnik 65/5-6, S. 212-215

Ivanov, A. A.; Anikeev, A. V.; Bagryansky, P. A.; Karpushov, A. N.; Kornilov, V. N.;
Maximov, V. V.; Noack, K.
Axial Distribution of DD-Neutron Yield in GDT under Skew Injection of Deuterium
Neutral Beams
International Conference on Open Systems for Plasma Confinement, July 3-6, 2000, Tsukuba,
Japan, Proc. in Transactions of Fusion Technology Vol. 39, p. 213 (2001)

Karpushov, Alexander N.; Anikeev, Andrey V.; Noack, K.; Strogalova, Svetlana L.
Integrated Transport Code Sytem for Multicomponent High-ß Plasmas in the Gas
Dynamic Trap
EPS 27th Conference on Controlled Fusion and Plasma Physics, Budapest, Hungary, 12-16
June 2000, Poster P3.019, Proceedings will be published

Kern, T.; Prasser, H.-M.
Study of the Foaming Behaviour of a Bubble Column
5th German-Japanese Symposium "Bubble Columns", 28-30 May 2000, Dresden, Germany,
proceedings pp. 162-167.

Kliem, M.
3D flow simulation for a reactor core modelled as porous body by CFX - 4.2 code
Jahrestagung Kerntechnik 2000, Bonn, 23.-25. Mai 2000, Tagungsbericht S. 69-73

Kliem, S.; Grundmann, U.; Höhne, T.; Rohde, U.
Importance of coolant mixing for accident analyses using coupled codes using the
coupled code DYN3D/ATHLET
Tagungsband der Fachtagung der KTG: "Wechselwirkungen Neutronenphysik und
Thermofluiddynamik", pp. 513-525, Forschungszentrum Rossendorf, Januar 2000

Kliem, S.; Grundmann, U.; Rohde, U.
Analysis of the OECD MSLB Benchmark using the coupled code DYN3D/ATHLET
Jahrestagung Kerntechnik 2000, Bonn, 23.-25. Mai 2000, Tagungsbericht S. 7-10

Kliem, S.; Grundmann, U.; Rohde, U.
Analysis of the OECD MSLB Benchmark using the Coupled Code DYN3D/ATHLET
Eighth International Conference on Nuclear Engineering (ICONE-8) 2000, Baltimore (USA), 2.-6. April 2000, Proceedings (CD-ROM) paper 8696

Kliem, S.; Seidel, A.; Grundmann, U.
Definition of the 6th Dynamic AER Benchmark - Main Steam Line Break in a NPP with VVER-440
Tenth Symposium of AER on VVER Reactor Physics and Reactor Safety 2000, Moscow (Russia), 18.-22. September 2000, Proceedings pp. 749-762

Kozmenkov, Y.; Orekhov, Y.; Grundmann, U.; Kliem, S.; Rohde, U.; Seidel, A.
Benchmarking of DYN3D/RELAP5 Code Package using the Fifth AER Dynamic Problem for Coupled Codes
Tenth Symposium of AER on VVER Reactor Physics and Reactor Safety 2000, Moscow (Russia), 18.-22. September 2000, Proceedings pp. 1043-1048

Krepper, E.; Aszodi, A.
Experimental and numerical investigation of one and two phase natural convection in large pools
3rd European Thermal Science Conference, Heidelberg, September 2000, Proceedings edited by E.W.P. Hahne, W. Heidemann and K. Spindler, 2000 ETS Pisa, Vol. II, pp. 1075-1080, ISBN 88-467-0305-7

Krepper, E.; Prasser, H.-M.
Measurements and CFX-simulations of a bubbly flow in a vertical pipe
3rd Int. Conf. on Advances in Fluid Mechanics, Montreal May 2000; in: M. Rahman, C.A. Brebbia (Ed.): Advances in Fluid Mechanics III, pp. 23-31, WITPress Southampton, Boston 2000, ISBN 1-85312-813-9

Krepper, E.; Prasser, H.-M.
Measurements and CFX-simulations of a bubbly flow in a vertical pipe
AMIF-ESF Workshop:"Computing methods for two-phase flow", Aussois, January 12-14, 2000, Conference-CD

Krepper, E.; Schaffrath, A.; Aszódi, A.
Numerical Simulation of the Emergency Condenser of the SWR1000
Nuclear Science and Engineering 135 (2000) No.3 267-279

Krüssenberg, A.-K.; Prasser, H.-M.; Schaffrath, A.
A New Criterion for the Bubble Slug Transition in Vertical Tubes
Kerntechnik 65/1 (2000) 7-13
NURETH-9, San Francisco, California, USA, October 3-8, 1999

Lucas, D.
BRICK - a one-dimensional simulation tool for multiphase flow in vessels
Chemical Engineering and Technology 23(2000)845-849

Lucas, D.; Krepper, E.; Prasser, H.-M.
Influence of the bubble size distribution on radial gas fraction profiles in vertical pipe flow
Second Japanese-European Two-Phase Flow Group Meeting, Tsukuba, Japan, September 25-29, 2000, Proceedings on CD-ROM: K-2.pdf

Lucas, D.; Krepper, E.; Prasser, H.-M.
Radial Gas Profiles in Vertical Pipe Flow in Dependence on the Bubble Size Distribution
38th European Two-Phase Flow Group Meeting, May, 29-31 2000, Karlsruhe, Germany, Paper G4

Mittag, S.; Kliem, S.; Weiß, F.-P.; Kyrki-Rajamäki, R.; Hämäläinen, A.; Langenbuch, S.; Danilin, S.; Hadek, J.; Hegyi, G.; Kuchin, A.; Panayotov, D.
Validation of Coupled Codes for VVER Reactors by Analysis of Plant Transients
Tagungsband der Fachtagung der KTG: "Wechselwirkungen Neutronenphysik und Thermofluiddynamik", pp. 4-55 bis 4-66, Forschungszentrum Rossendorf, 31. Januar - 1. Februar 2000

Mittag, S.; Kliem, S.; Weiß, F.-P.; Kyrki-Rajamäki, R.; Hämäläinen, A.; Langenbuch, S.; Danilin, S.; Hadek, J.; Hegyi, G.; Kuchin, A.; Panayotov, D.
Validation of Coupled Codes for VVERs by Analysis of Plant Transients
Proceedings of OECD / CSNI workshop on Advanced Thermal-Hydraulic and Neutronic Codes Application, Barcelona (Spain), 10-13 April, 2000, Conference CD

Mittag, S.; Kliem, S.; Weiß, F.-P.; Kyrki-Rajamäki, R.; Hämäläinen, A.; Langenbuch, S.; Danilin, S.; Hadek, J.; Hegyi, G.; Kuchin, A.; Panayotov, D.
Validation of coupled neutron-kinetic/thermal-hydraulic codes for VVERs
Proc. of Tenth Symposium of AER on VVER Reactor Physics and Reactor Safety, Moscow, Russia, September 18-22, 2000, 763-781

Mönch, I.; Stephan, I.; Köthe, A.
High-purity niobium for neutron activation detectors
Tagung Ultra High Purity Base 1999 Metals, Sendai, Japan
Material Transactions JIM Vol. 41, 1 (2000) 1ff

Moormann, R.; Hinssen, H.-K.; Latge, Ch.; Dumesnil, J.; Veltkamp, A. C.; Grabon, V.; Beech, D.; Buckthorpe, D.; Dominguez, T.; Krüssenberg, A.-K.; Wu, C. H.
Oxidation of carbon based materials for innovative energy systems (HTR, fusion reactor): Status and further needs
Proc. First Meeting: Survey on Basic Studies in the Field of High Temperature Engineering (including Safety Studies), Paris, France, 27-29 September 1999, 161-172

Noack, K.
Monte Carlo Simulations of Neutral Gas and Fast Ion Dynamics in GDT Experiments
Monte Carlo 2000, International Conference on Advanced Monte Carlo for Radiation Physics, Particle Transport Simulation and Applications, October 23-26, 2000 - Lisbon, Portugal; Proc. will be published by Springer-Verlag

Parts, Ü.; Avilov, V.; Koivuniemi, J. H.; Kopnin, N. B.; Krusius, M.; Ruohio, J. J.; Ruutu, V. M. H.
Coexistence of single and double quantum vortex lines
Physical Review B, Vol. 62, No. 9, pp. 5865-5876, 1 September 2000-I

Perov, S.; Altstadt, E.; Weiss, F.-P.; Werner, M.
ANALYSIS OF FLUID-STRUCTURE INTERACTION AT WWER-1000 TYPE REACTORS
8th International Conference on Nuclear Engineering ICONE8 Baltimore, MD U.S.A., April 2-6, 2000, Proceedings on CD-ROM, Paper No. 8446

Perov, S.; Altstadt, E.; Werner, M.
Vibration analysis of the pressure vessel internal of WWER-1000 type reactors with consideration of fluid-structure interaction
Annals of Nucl. Energy 27 (2000) 1441-1457

Prasser, H.-M.; Krepper, E.; Lucas, D.
Fast wire-mesh sensors for gas-liquid flows and decomposition of gas fraction profiles according to bubble size classes
Second Japanese-European Two-Phase Flow Group Meeting, Tsukuba, Japan, September 25-29, 2000, proceedings on CD-ROM: D-3.pdf

Prasser, H.-M.; Zippe, C.
Measurement of Bubble Size Distributions with Wire-Mesh Sensors
5th German/Japanese Symposium "Bubble Columns", Dresden, May 28 - 30, 2000, proceedings pp. 223 - 228

Priede, J.; Gerbeth, G.
Oscillatory instability of electromagnetically levitated solid bodies
Journal IEEE Transactions on Magnetics, USA, Vol. 36. No. 1, pp. 354-357, January 2000

Priede, J.; Gerbeth, G.; Mikelsons, A.; Gelfgat, Y.
Instabilities of electromagnetically levitated bodies and its prevention
International Symposium on Electromagnetic Processing of Materials, Nagoya, Japan, April 3-6, 2000, Published by: The Iron and Steel Institute of Japan, pp 352-357

Repp, T.
Fluiddynamic Waterhammer Simulations with Consideration of Fluid-Structure Interaction
Sammelband Workshop Kompetenzerhalt Kerntechnik, Jahrestagung Kerntechnik, 18.-21. Mai 1999, Karlsruhe; Haag, G. (Ed.), 2000

Rindelhardt, U.; Teichmann, G.
Energieertrag von netzgekoppelten Photovoltaikanlagen
Erneuerbare Energien Heft 5(Mai)2000, S.50-52

Rindelhardt, U.; Teichmann, G.
Performance Ratio im Detail: PV-Generatorleistung und Anlagenertrag
Tagungsband 15. Symposium Photovoltaische Solarenergie, 15.-17. März 2000, Staffelstein, S. 331

Rohde, U.; Hensel, F.
Measurement and Simulation of the Turbulent Dispersion of a Radioactive Tracer in a Two-Phase Flow System
5th German-japanese Symposium on Bubble Columns, May 28 - 30, 2000, Dresden Proc. pp. 235-240

Rohde, U.; Kliem, S.; Seidel, A.; Khalimonchuk, V.; Kuchin, A.
On usage of coupled neutron-kinetic and thermal-hydraulic computer code DYN3D/ATHLET to study safety of VVER-1000 type reactors under transient and emergency operational modes
Tenth Symposium of AER on VVER Reactor Physics and Reactor Safety 2000, Moscow (Russia), 18.-22. September 2000, Proceedings pp. 913-920

Schaffrath, A.; Krüssenberg, A.-K.
Neue Instrumente der Kommunikation: Internet
Jahrestagung Kerntechnik 2000 - Fachsitzung "Kommunikation mit der Öffentlichkeit - Communication with the Public"; Juni 2000, INFORUM Verlags- und Verwaltungsgesellschaft, Bonn, S. 59-69

Schmitt, W.; Hessel, G.; Kryk, H.; Hulzer, G.
Kalorimetrische und FTIR-Untersuchungen zur sicheren Betriebsführung einer Grignardreaktion
5. Fachtagung "Anlagen-, Arbeits- und Umweltsicherheit", Köthen 9./10. Nov. 2000, S. 347-352

Stefani, F.; Gerbeth, G.
A contactless method for velocity reconstruction in electrically conducting fluids
Measurement science and technology 11 (2000) 758-765

Stefani, F.; Gerbeth, G.
Can we look inside a dynamo?
Astronomische Nachrichten (2000) 235-248

Stefani, F.; Gerbeth, G.
On the uniqueness of velocity reconstruction in conducting fluids from measurements of induced electromagnetic fields
Inverse Problems 16 (2000), pp. 1-9

Stefani, F.; Gerbeth, G.; Rädler, K.-H.
Steady dynamos in finite domains: an integral equation approach
Astronomische Nachrichten 321 (2000) 65-73

Ulbricht, A.; Böhmert, J.; Große, M.; Strunz, P.
Small Angle Scattering Study Concerning the Effect of Residual Elements on the Radiation Behaviour of Iron Alloys
ECNS'99, 2. European Conference on Neutron Scattering, Sept. 1999, Budapest, PHYSICA B 276-278 (2000) 936-938
Physica B 276-278 (2000) 936-938

Ulbricht, A.; Böhmert, J.; Nikolaev, Y.
Nachweis und Analyse neutroneninduzierter Defektstrukturen in Eisenlegierungen
Jahrestagung Kerntechnik 2000, Bonn, 23.-25. Mai, Tagungsbericht S. 587

Viehrig, H.-W.; Boehmert, J.; Dzugan, J.
Beitrag zur Bewertung des Bestrahlungsverhaltens russischer WWER Reaktordruckbehälterstähle
26. MPA-Seminar "Sicherheit und Verfügbarkeit in der Energietechnik", Staatliche Materialprüfanstalt Stuttgart, Universität Stuttgart, 5.-6. Oktober 2000, Sammelband, S. 20.1-20.20

Viehrig, H.-W.; Böhmert, J.; Richter, H.; Valo, M.
Use of Instrumented Charpy Test for Determination of Ductile Crack Initiation Toughness
Pendulum Impact Testing: A Century of Progress, ASTM STP 1380, T. Siewert ans M.P. Manahan, Sr., Eds., American Society for Testing and Materials, West Conshohocken, PA, 2000, pp. 354-365

Weier, T.; Fey, U.; Gerbeth, G.; Mutschke, G.; Avilov, V.
Boundary layer control by means of electromagnetic forces
ERCOFTAC bulletin, No. 44, pp. 36-40, March 2000

Weiß, F.-P.; Rohde, U.; Grundmann, U.; Teschendorff, V.; Burtak, F.
Aufgabenstellung - Validierung - Anwendung von gekoppelten 3D-Kernmodellen und Systemcodes
atw 45. Jg. (2000) Heft 6 - Juni

Willschuetz, H.-G.; Altstadt, E.; Weiss, F.-P.; Sehgal, B. R.
A Finite Element model for pre- and posttest calculations of the forever-experiments
8th International Conference on Nuclear Engineering (ICONE-8) Baltimore, MD U.S.A., April 2-6, 2000, Proceedings on CD-ROM, Paper No. 8542

Other oral and poster presentations

Avilov, V.
Thermal diffusion in laser beam welding of metals
Kolloquium Thermo- und Fluiddynamik an der Technischen Universität Ilmenau, November 7, 2000

Cramer, A.; Gerbeth, G.; Bojarevics, A.; Gelfgat;, Y.
Stabilisation of the melt extraction process by magnetic fields
International Workshop "Electromagnetic Control of Free Surface Flows in Materials Processing" (EFMP 2000) June 4-7, 2000, Ilmenau, Germany

Danilin, S.; Ilieva, B.; Khalimonchuk, V.; Mittag, S.; Weiß, F.-P.
Three VVER-1000 Tests Suitable for the Validation of Coupled Neutronic / Thermal-hydraulic Codes
NEA/NSC Workshop on the Preservation of Experimental Integral Reactor Physics Data, 18-19 May 2000, Budapest, Hungary

Eckert, S.; Gerbeth, G.; Witke, W.; Langenbrunner, H.
MHD turbulence measurements in a sodium channel flow exposed to a transverse magnetic field
International Symposium on Turbulence, Heat and Mass Transfer, Nagoya, Japan, April 3-6, 2000

Gailitis, A.; Lielausis, O.; Platacis, E.; Gerbeth, G.; Stefani, F.
Riga Dynamo Experiment
NATO Advanced Research Workshop "DYNAMO AND DYNAMICS, A MATHEMATICAL CHALLENGE" August 21-26, 2000,Cargese, France

Gailitis, A.; Lielausis, O.; Platacis, E.; Stefani, F.; Gerbeth, G.
The Riga Dynamo Experiment: Prognoses, Results, Interpretation
SEDI2000 The 7th Symposium of the Study of the Earth's Deep Interior University of Exeter, UK, 30th July - 4th August 2000

Galindo, V.; Gerbeth, G.
Crystal growth melt flow control by means of magnetic fields
4th International Conference "MHD at dawn of 3rd Millennium", Presqu'ile de Giens, France, September 18-22, 2000

Gerbeth, G.
Magnetfeldeinsatz bei Kristallzüchtungen aus der Schmelze - Beispiele und Perspektiven
Einladungsvortrag am 19.05.00 am Institut für Kristallzüchtung Berlin

Gerbeth, G.
Strukturbildung unter Berücksichtigung der Hydrodynamik bei der Erstarrung von Nd-Fe-B-Schmelzen; Teilprojekt: Strömungskontrolle über Magnetfelder
Kick-Off-Meeting-Meeting zum DFG-Schwerpunktprogramm 1120: Phasenumwandlungen in mehrkomponentigen Schmelzen 30./31.10.2000, Bonn

Gerbeth, G.; Stefani, F.; Gailitis, A.; Lielausis, O.; Platacis, E.
Das Rigaer Dynamo-Experiment
im Greifswalder Physikalischen Kolloquium, Greifswald, 19.10.2000

Gerbeth, G.; Stefani, F.; Gailitis, A.; Lielausis, O.; Platacis, E.
Magnetic field self-excitation in the Riga dynamo experiment
ICTAM 2000, 20th Int. Congress of Theoretical and Applied Mechanics, Chicago, USA, 27.8.-2.9.00

Grants, I.; Gerbeth, G.
Rotating magnetic field driven flow: Multiple steady solutions and stability
4th International Conference "MHD at dawn of 3rd Millennium", Presqu'ile de Giens, France, September 18-22, 2000

Grants, I.; Gerbeth, G.; Pätzold, O.; Wunderwald, U.; Jenkner, K.
Linearization approaches in VGF models: decoupling global radiation transfer and the Stefan problem
DGKK-Jahrestagung, Freiberg, 11-12.10.00

Hicken, Enno-F.; Jaegers, H.; Schaffrath, A.; Weiß, F.-P.
The NOKO/TOPFLOW Facility for Natural Convection Flow
TCM Meeting in Vienna (Austria), July 18-21, 2000

Kryk, H.; Hessel, G.; Schmitt, W.; Seiler, T.; Willms, T.
Investigations on exothermic semi-batch reactions as a basis of the prevention of dangerous operating states
Fall 2000 DIERS Users Group meeting, October 16-18, Brookline (Boston), MA

Mönch, I.; Stephan, I.; Köthe, A.
High-purity niobium for neutron activation detectors
Tagung Ultra High Purity Base 1999 Metals, Sendai, Japan

Priede, J.; Cramer, A.; Bojarevics, A.; Gerbeth, G.
Experimental and numerical study of anomalous thermocapillary convection in liquid gallium
International Workshop "Electromagnetic Control of Free Surface Flows in Materials Processing" (EFMP 2000) June 4-7, 2000, Ilmenau, Germany

Priede, J.; Gerbeth, G.
Effect of AC magnetic field on the damping of shape oscillationsof liquid metal droplets
4th International Conference "MHD at dawn of 3rd Millennium", Presqu'ile de Giens, France, September 18-22, 2000

Priede, J.; Gerbeth, G.; Hermann, R.; Behr, G.; Schultz, L.
Control of floating-zone crystal growth in high-frequency magnetic field
4th International Conference "MHD at dawn of 3rd Millennium", Presqu'ile de Giens, France, September 18-22, 2000

Schaffrath, A.; Krüssenberg, A.-K.
Investigation on multiphase and multicomponent flows - experiments and measurement devices
Politecnico di Milano, Dipartimento di Ingegneria Nucleare (2000) Milano, Italy

Shatrov, V.; Galindo, V.; Gerbeth, G.
Stability analysis of the flow inside an electromagnetically levitated drop
4th International Conference "MHD at dawn of 3rd Millennium", Presqu'ile de Giens, France, September 18-22, 2000

Stefani, F.; Gerbeth, G.
A toy model for inverse dynamo theory
SEDI2000 The 7th Symposium of the Study of the Earth's Deep Interior University of Exeter, UK, 30th July - 4th August 2000

Stefani, F.; Gerbeth, G.
On some inverse problems in MHD
4th International Conference "MHD at dawn of 3rd Millennium", Presqu'ile de Giens, France, September 18-22, 2000

Viehrig, H.-W.; Boehmert, J.; Richter, H.
Common German/Russian Irradiation Experiment at Rheinsberg NPP - Results of the Mechanical Testing
Workshop on VVER-RPV Integrity Assessment - methods and Applications February 23 - 25, 2000 at GSR in Cologne (Germany)

Weier, T.; Fey, U.; Gerbeth, G.; Mutschke, G.; Lielausis, O.; Platacis, E.
Boundary layer control by means of wall parallel Lorentz forces
4th International Conference "MHD at dawn of 3rd Millennium", Presqu'ile de Giens, France, September 18-22, 2000

FZR-Reports and other publications

Altstadt, E.; Mössner, T.
Extension of the ANSYS® creep and damage simulation capabilities
Wissenschaftlich-Technische Berichte / Forschungszentrum Rossendorf; FZR-296 Juli 2000

Altstadt, E.; Willschütz, H.-G.
Development of an Integral Finite Element Model for the Simulation of Scaled Core-Meltdown-Experiments
Wissenschaftlich-Technische Berichte / Forschungszentrum Rossendorf; FZR-292; April 2000

Beyer, M.; Carl, H.; Reitz, T.
Unterstützung der ukrainischen Aufsichtsbehörde bei der Einrichtung einer verbesserten betrieblichen Überwachung für das gesamte KKW Saporoshje
Wissenschaftlich-Technische Berichte / Forschungszentrum Rossendorf; FZR-297 Juli 2000

Chochlov, V. N.; Duncev, A.; Ivanov, V. V.; Kontelev, V. V.; Melnikov, V. I.; Stoppel, L. K.; Prasser, H.-M.; Zippe, W.; Zschau, J.; Zboray, R.
Local and integral ultrasonic gauges for two-phase flow instrumentation in nuclear reactor and safety technology
Wissenschaftlich-Technische Berichte / Forschungszentrum Rossendorf; FZR-303 November 2000

Gokhman, A.; Boehmert, J.; Ulbricht, A.
Contribution to the Determination of Microstructural Parameters from Small Angle Scattering Experiments at Reactor Pressure Vessel Steels
Wissenschaftlich-Technische Berichte / Forschungszentrum Rossendorf, FZR-288 Februar 2000

Grahn, A.; Prasser, H.-M.
Dissipative Strukturbildung bei exothermen Grenzflächenreaktionen
Wissenschaftlich-Technische Berichte / Forschungszentrum Rossendorf; FZR-307 Dezember 2000

Grundmann, U.; Kliem, S.; Mittag, S.; Rohde, U.; Seidel, A.; Kozmenkov, Y.; Kumayev, V.
Störfallablaufanalysen für neue Reaktorkonzepte und WWER-Reaktoren mit neuem Brennstoffdesign - WTZ mit Russland
Wissenschaftlich-Technische Berichte / Forschungszentrum Rossendorf; FZR-302 Oktober 2000

Grundmann, U.; Kliem, S.; Rohde, U.; Seidel, A.; Khalimonchuk, V.; Kuchin, A.
Beiträge zur Validierung fortgeschrittener Störfallanalysecodes mit 3D Neutronenkinetik - WTZ mit der Ukraine
Wissenschaftlich-Technische Berichte / Forschungszentrum Rossendorf; FZR-301 Oktober 2000

Hoppe, D.
Methodische Grundlagen für die Tomographie durch gefilterte Rückprojektion an einer Axialpumpe
Wissenschaftlich-Technische Berichte / Forschungszentrum Rossendorf; FZR-306 November 2000

Krepper, E.; Schäfer, F.
Verifikation des ATHLET-Rechenprogrammes anhand der Nachanalyse zweier Experimente an der CCTF-Versuchsanlage
Wissenschaftlich-Technische Berichte / Forschungszentrum Rossendorf; FZR-315, März 2001

Müller, G.; Böhmert, J.
Metallographic Post Test Investigations for the Scaled Core-Meltdown-Experiments FOREVER-1 and -2
Wissenschaftlich-Technische Berichte / Forschungszentrum Rossendorf, August 2000, FZR-298

Richter, H.
Ermittlung zähbruchmechanischer Kennwerte unter schlagartiger Belastung mittels Schallemission
Wissenschaftlich-Technische Berichte / Forschungszentrum Rossendorf; FZR-299 September 2000

Schaffrath, A.; Ringel, H.
Modelle zur Bestimmung der Relativbewegung der Phasen in einer Zweiphasenstroemung - Stand der Technik
Wissenschaftlich-Technische Berichte / Forschungszentrum Rossendorf, FZR-294 Juni 2000

Scholz, D.
Bewertung der Genauigkeit eines Gittersensors zur Visualisierung einer Zweiphasenströmung durch Vergleich mit optischen Hochgeschwindigkeitsaufnahmen
Wissenschaftlich-Technische Berichte / Forschungszentrum Rossendorf; FZR-300 September 2000

Schumann, P.
Nutzung der Rauschdiagnostik für Nachweis und Überwachung der Schwingungen von Reaktordruckbehältereinbauten und zur Aufklärung ihrer Ursachen in ostdeutschen Kernkraftwerken mit WWER-440/230-Reaktoren der russischen Baureihe
Wissenschaftlich-Technische Berichte / Forschungszentrum Rossendorf, FZR-304, Oktober 2000

Weiß, F.-P.; Rindelhardt, U. (Editors)
Anual Report 1999 Institute of Safety Research
Wissenschaftlich-Technische Berichte/Forschungszentrum Rossendorf; FZR-284 Februar 2000

Patents

Patents

Hoppe, D.; Giera, H.-D.
Anordnung zur akustischen Volumenbestimmung
DE 198 30 442 A1

Lindau, B.
Vorrichtung zum Fördern von Schüttgut mittels Vibrationsförderung
DE 198 35 530A1

Rindelhardt, U.; Teichmann, G.
Verfahren und Schaltungsanordnung zur Maximum-Power-Point-Steuerung von Solargeneratoren
DE 199 04 561 A1

Stefani, F.; Gerbeth, G.; Priede, J.; Thess, A.; Cramer, A.; Eckert, S.
Verfahren und Anordnung zur Bestimmung von räumlichen Geschwindigkeitsverteilungen in elektrisch leitfähigen Flüssigkeiten
DE 199 22 311 A1

Witke, W.; Gerbeth, G.; Eckert, S.
Einrichtung zur lokalen Messung von Strömungsgeschwindigkeiten
DE 199 13 484 A1

Guests

Guests

Knebel, Joachim
Forschungszentrum Karlsruhe, Institut für Kern- und Energietechnik
01.03.2000 – 03.03.2000

Ilieva, Bonka
Institute for Nuclear Research and Nuclear Energy Sofia, Bulgaria
13.03.2000 – 03.04.2000
03.07.2000 – 10.07.2000
19.10.2000 – 15.12.2000

Dr. Panayotov, Dobromir
Institute for Nuclear Research and Nuclear Energy Sofia, Bulgaria
13.03.2000 – 03.04.2000
03.07.2000 – 10.07.2000

Dr. Perov, Sergey
Bauman University Moscow, Russia
13.03.2000 – 16.04.2000
05.06.2000 – 10.06.2000
09.11.2000 – 16.12.2000

Dr. Platacis, Ernest
Institute of Physics Riga, Latvia
15.03.2000 – 25.03.2000

Prof. Dr Gailitis, Agris
Institute of Physics Riga, Latvia
15.03.2000 – 25.03.2000
13.08.2000 –16.09.2000

Prof. Dr. Lielausis, Olgerts
Institute of Physics Riga, Latvia
15.03.2000 – 20.04.2000
26.11.2000 – 22.12.2000

Dr. Priede, Janis
Institute of Physics Riga, Latvia
15.03.2000 – 21.04.2000
11.9.2000 – 20.10.2000

Dr. Ivanov, Vadim
Center of Scientific and Technical Services NUKLID Ltd., Russia
20.03.2000 – 31.03.2000
24.11.2000 – 09.12.2000

Prof. Melnikov, Vladimir
Center of Scientific and Technical Services NUKLID Ltd., Russia
20.03.2000 – 31.03.2000

24.11.2000 – 09.12.2000

Chornousova, Lyubov
Umweltministerium, Kiew, Ukraina
04.04.2000 – 07.04.2000

Lukýanskyy, Vladislav
Umweltministerium, Kiew, Ukraina
04.04.2000 – 07.04.2000

Borodkin, Gennady
SEC NRS of GOSATOMNADZOR Moskau, Russia
24.04.2000 – 22.06.2000
01.11.2000 – 15.12.2000

Maximov, Vladimir
Budker-Institute Novosibirsk, Russia
25.04.2000 – 22.05.2000

Dr. Karpuchov, Alexandre
Budker-Institute Novosibirsk, Russia
25.04.2000 – 22.05.2000

Schmidt, Paul
Auburn University, USA
24.05.2000 – 15.07.2000

Khrennikov, Nikolay
SEC NRS of GOSATOMNADZOR Moskau, Russia
29.05.2000 – 04.06.2000

Dr. Oussanov, Alexandre
VNIIAES Moscow, Russia
05.06.2000 –10.06.2000

Egorova, Tatjana
VNIIAES Moscow, Russia
05.06.2000 –10.06.2000

Gutsev, Dmitri
VNIIAES Moscow, Russia
05.06.2000 –10.06.2000

Mikhailovich, Boris
Ben-Gurion-University of the Negev, Beer-Sheva Israel
08.06.2000 – 15.06.2000

Dr. Kozmenkov, Yaroslav
Institute of Physics and Power Engineering Obninsk, Russia
09.07.2000 – 05.08.2000

Dr. Kumayev, Vladimir
Institute of Physics and Power Engineering Obninsk, Russia
09.07.2000 – 05.08.2000

Prof. Gad-el-Hak, Mohamed
University of Notre Dame, USA
20.07.2000 – 23.07.2000

Voskoboinikov, Roman
Kurchatov Institut Moskau, Russia
14.08.2000 – 10.09.2000

Dr. Anikeev, Andrei
Budker Institut Novosibirsk, Russia
12.09.2000 – 06.10.2000

Dr. Manturov, Guennadi
IPPE Obninsk, Russia
08.10.2000 – 25.10.2000

Prof. Gokhman, Alexander
South Ukrainian Pedagigical University K.D. Ushinski, Dpt. of Physics Odessa, Ukraina
10.11.2000 – 21.12.2000

Dr. Waskaas, Magne
Telemark University Porsgrunn, Norwegen
02.12.2000 – 05.12.2000

Matveyev, Inger Hedvig
Telemark University Porsgrunn, Norwegen
02.12.2000 – 05.12.2000

Kozlov, Oleh
Kernkraftwerk Rovno, Ukraina
07.12.2000 – 10.12.2000

Scholz, Danilo
HTWS Zittau/Görlitz
01.09.2000 – 30.11.2000
01.12.2000 – 31.12.2000

Kuchin, Alexander
Umweltministerium, Kiew, Ukraina
30.01.2000 03.02.2000

Chochlov, Valeryi
TU Nizhny Novgorod, Russia
24.07.2000 – 31.07.2000

Poetefi, Gabor
TU Budapest, Hungary
08.10.2000 – 11.10.2000

Aszodi, Attila
TU Budapest, Hungary
08.10.2000 – 11.10.2000

Boros, Ildiko
TU Budapest, Hungary
08.10.2000 – 11.10.2000

Dr. Wagenknecht, Michael
IPM an der HTWS Zittau/Görlitz
01.11.2000 – 30.11.2000

Dr. Hadek, Jan
NRI Rez, Czech Republic
01.11.2000 – 15.12.2000

Gocht, Thoralf
IPM an der HTWS Zittau/Görlitz
01.11.2000 – 31.12.2000

Prof. Ivanov, Alexandre
Budker Institut Novosibirsk, Russia
06.11.2000 – 17.11.2000

Meetings and workshops

Meetings und workshops

Fachtagung der KTG-Fachgruppen „Thermo- und Fluiddynamik" und „Reaktorphysik und Berechnungsmethoden"
Rossendorf, 31. 01. – 01. 02. 2000

Project Meeting „Vibration Modelling of VVER Type Reactor"
Rossendorf, 05. 06. – 07. 06. 2000

4. Workshop „Messtechnik für stationäre und transiente Mehrphasenströmungen"
Rossendorf. 16. 11. – 17. 11. 2000

Seminars of the Institute

Seminars

Dr. K. Noack, G. Otto, Prof. E. Collatz
Stand der Forschungen zum Projekt einer Neutronenquelle für die Fusionsmaterialforschung auf der Grundlage einer gasdynamischen Falle
13.01.00

H.-G. Willschütz, Dr. E. Altstadt
Nachrechnungen der FOREVER-Experimente mit dem FEM-Code ANSYS
27.01.00

C. Beckert
Entwicklung und Anwendung des deterministischen 3D-Neutronentransportprogramms TransRay
11.02.00

Dr. F. Stefani, Dr. G. Gerbeth, T. Gundrum
Erste Ergebnisse des Riager Dynamo-Experiments
29.02.00

Dr. J. U. Knebel (FZK)
Übersicht über die FZK-Arbeiten zum ADS
02.03.00

S. Kliem, Dr. U. Grundmann
Die Lösung einer Benchmarkaufgabe der OECD zu einem Störfallszenarium mit Frischdampfleck
23.03.00

Dr. C. Zippe
Gasgehaltsverteilungen in rotierenden Turbomaschinen
06.04.00

Dr. V. Lelek (NRI Rez)
End of nuclear fuel cycle
13.04.00

Dr. S. Mittag
Validierung gekoppelter neutronenkinetisch-thermohydraulischer Systemcodes
11.05.00

Dr. S. Langenbuch (GRS München)
Brennstabverhalten unter Störfallbedingungen bei hohem Abbrand
16.05.00

C. Schneider
Reaktionskinetik und Stofftransport der Hydrier- und Oxidationsstufe des Anthrachinon-Prozesses
08.06.00

Dr. H.-M. Prasser
Wechselwirkung der Gittersensoren mit der Zweiphasenströmung – Rückwirkung und Messgenauigkeit
22.06.00

Prof. B. R. Sehgal (Royal Institute of Technology, Stockholm)
Recent results from LWR severe accident research at the Royal Institute of Technology
30.06.00

Prof. M. Gad-el-Hak (University of Notre Dame, USA)
The fluid mechanics of microdevices
21.07.00

Dr. A. Cramer
Experimentelle Untersuchung von reverser Marangoni-Konvektion in Gallium
24.08.00

Dr. D. Lucas
Berechnung radialer Gasgehaltsprofile aus gemessenen Blasengrößenverteilungen in vertikaler Rohrströmung
08.09.00

S. Yokobori (Toshiba Nuclear Engineering Laboratory)
Experimental investigation of the heat removal performance of passive safety systems in the GIRAFFE test facility
14.09.00

Dr. F. Bergner (TU Dresden)
Charakterisierung der Ermüdungsrissausbreitung metallischer Werkstoffe
21.09.00

Dr. T. Willms
HPLC-Konzentrationsmessungen bei Hydrierung in Dreiphasensystemen
29.09.00

Dr. E. Altstadt
Eine Versuchsanlage für Druckschläge (Wasserhammer) – Konzept und erste Versuchsergebnisse
19.10.00

F. Schäfer, Dr. E. Krepper
Nachrechnung thermohydraulischer Experimente an der Versuchsanlage CCTF mit dem Code ATHLET
02.11.00

Dr. H.-W. Viehrig
Bewertung der Probenrekonstitutionstechnik im internationalen Vergleich
16.11.00

A. Grahn
Dissipative Strukturbildung bei exothermen Grenzflächenreaktionen
07.12.00

Dr. P. Vladimirov (RCC Kurchatov-Institute Moscow)
Effect von γ-radiation on the RPV steel embrittlement
14.12.00

Lecture courses

Lectures

Frank-Peter Weiß
Zuverlässigkeit und Sicherheit technischer Systeme
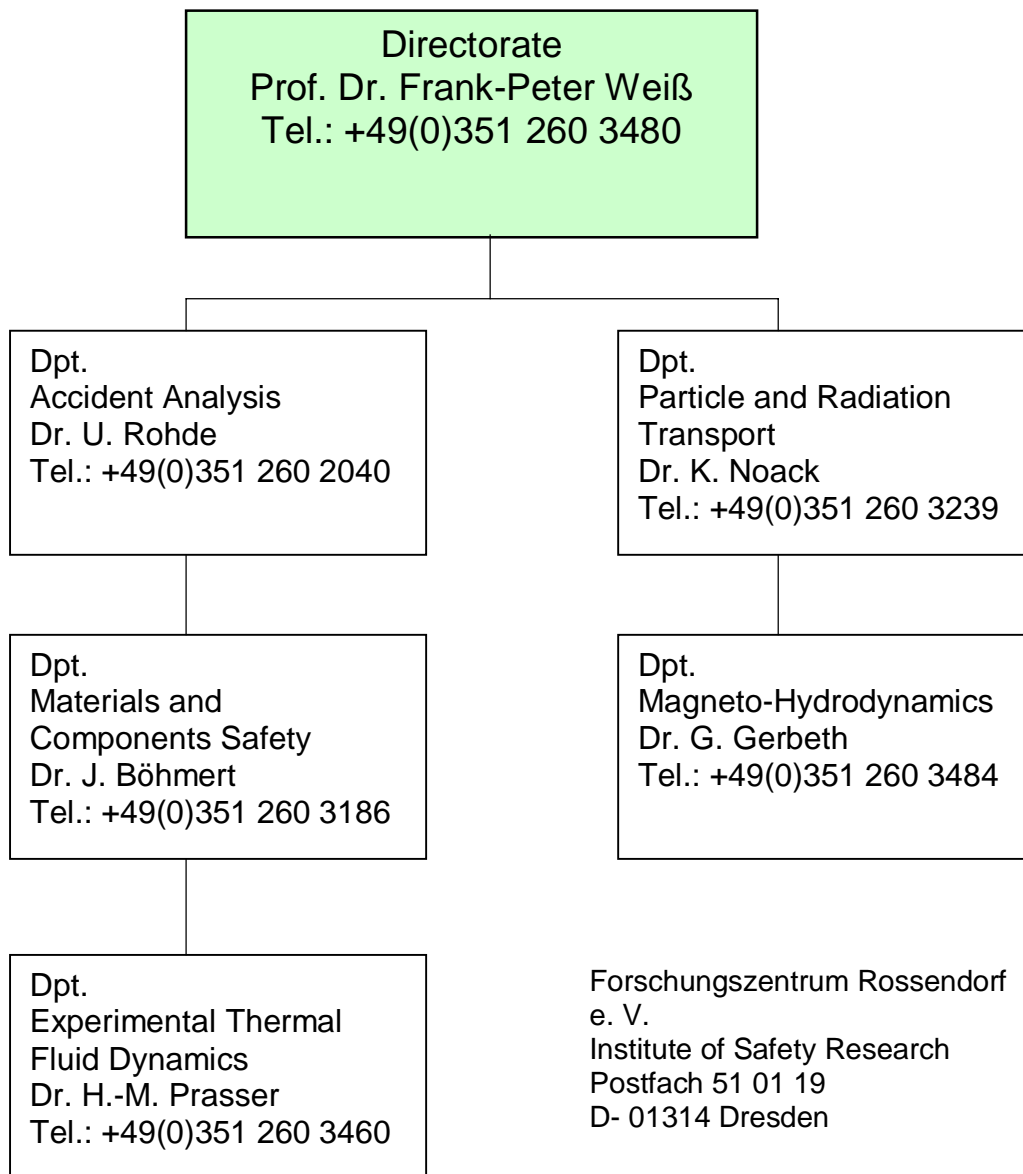TU Dresden, Fakultät Maschinenwesen
SS 2000 und WS 2000

Udo Rindelhardt
Erneuerbare Energien I und II
Universität Leipzig, Fakultät für Physik und Geowissenschaften
SS 2000 und WS 2000

Departments of the Institute

Institute of Safety Research

```
                    Directorate
              Prof. Dr. Frank-Peter Weiß
               Tel.: +49(0)351 260 3480
```

Dpt.
Accident Analysis
Dr. U. Rohde
Tel.: +49(0)351 260 2040

Dpt.
Particle and Radiation
Transport
Dr. K. Noack
Tel.: +49(0)351 260 3239

Dpt.
Materials and
Components Safety
Dr. J. Böhmert
Tel.: +49(0)351 260 3186

Dpt.
Magneto-Hydrodynamics
Dr. G. Gerbeth
Tel.: +49(0)351 260 3484

Dpt.
Experimental Thermal
Fluid Dynamics
Dr. H.-M. Prasser
Tel.: +49(0)351 260 3460

Forschungszentrum Rossendorf
e. V.
Institute of Safety Research
Postfach 51 01 19
D- 01314 Dresden

Organigram / 30.01.2001

Personnel

Director: Prof. Dr. F.-P. Weiß

Scientific Staff

Altstadt, Eberhard Dr.
Beyer, Matthias
Böhmer, Bertram
Böhmert, Jürgen Dr.
Böttger, Arnd
Carl, Helmar Dr.
Cramer, Andreas Dr.
Eckert, Sven Dr.
Erlebach, Stephan
Fey, Uwe, Dr.
Fietz, Jürgen Dr.
Galindo, Vladimir Dr.
Gerbeth, Günter Dr.
Grants, Ilmars Dr.
Grundmann, Ulrich Dr.
Grunwald, Gerhard Dr.
Hensel, Frank Dr.
Hessel, Günter
Hoppe, Dietrich Dr.
Hüller, Jürgen Dr.
Kliem, Sören
Koch, Reinhard Dr.
Konheiser, Jörg
Krepper, Eckhard Dr.
Krüssenberg, Anne-Kathrin Dr.
Kryk, Holger Dr.
Küchler, Roland Dr.
Lindau, Bernd Dr.
Lucas, Dirk Dr.
Mittag, Siegfried Dr.
Mössner, Thomas
Müller, Gudrun, Dr.
Mutschke, Gerd
Noack, Klaus Dr.
Prasser, Horst-Michael Dr.
Richter, Holger Dr.
Rindelhardt, Udo PD Dr.
Rohde, Ulrich Dr.

Schaffrath, Andreas Dr.
Schmitt, Wilfried Dr.
Schütz, Peter
Seidel, Andre
Stephan, Ingrid Dr.
Stephani, Frank Dr.
Viehrig, Hans-Werner Dr.
Werner, Matthias Dr.
Willms, Thomas Dr.
Willschütz, Hans-Georg
Witke, Willy
Zschau, Jochen Dr.
Zippe, Winfried Dr.
Zippe, Cornelius Dr.

PhD Students

Beckert, Carsten
Grahn, Alexander
Höhne, Thomas
Kern, Tommy
Kliem, Margarita
Repp, Thomas
Schäfer, Frank
Ulbricht, Andreas
Weier, Tom

Technical Staff

Baldauf, Dieter
Behrens, Sieglinde
Bombis, Doris
Borchardt, Steffen
Eichhorn, Christine
Forker, Klaus
Futterschneider, Hein
Gundrum, Thomas
Kunadt, Heiko
Leonhardt, Wolf-Dietrich
Leuner, Bernd
Losinski, Claudia
Mansel, Catrin
Nowak, Bernd
Opitz, Ruth
Otto, Gerlind
Pietzsch, Jens
Richter, Annett
Richter, Henry
Richter, Joachim
Richter, Karl-Heinz
Richter, Petra
Rott, Sonja
Russig, Heiko
Schleßiger, Heike
Schneider, Gisela
Seidler, Christa
Seiler, Torsten
Skorupa, Ulrich
Tamme, Marko
Tamme, Günther
Webersinke, Steffen
Weiß, Rainer
Zimmermann, Wilfried